Compréhension des mécanismes d'interaction entre des nanotubes de carbone et une membrane biologique : effets toxiques et vecteurs de médicaments potentiels

Sebastian Kraszewski

▶ **To cite this version:**

Sebastian Kraszewski. Compréhension des mécanismes d'interaction entre des nanotubes de carbone et une membrane biologique : effets toxiques et vecteurs de médicaments potentiels. Modélisation et simulation. Université de Franche-Comté, 2010. Français. NNT : . tel-00642770

HAL Id: tel-00642770

https://theses.hal.science/tel-00642770

Submitted on 18 Nov 2011

HAL is a multi-disciplinary open access archive for the deposit and dissemination of scientific research documents, whether they are published or not. The documents may come from teaching and research institutions in France or abroad, or from public or private research centers.

L'archive ouverte pluridisciplinaire **HAL**, est destinée au dépôt et à la diffusion de documents scientifiques de niveau recherche, publiés ou non, émanant des établissements d'enseignement et de recherche français ou étrangers, des laboratoires publics ou privés.

Université de Franche-Comté

École Doctorale Louis Pasteur

Institut UTINAM

Thèse de Doctorat

Spécialité Physique

présenté par

Sebastian Kraszewski

Compréhension des mécanismes d'interaction entre des nanotubes de carbone et une membrane biologique : effets toxiques et vecteurs de médicaments potentiels

Thèse dirigée par Christophe Ramseyer et Mounir Tarek

soutenue le 17 septembre 2010

Jury :

Président :	Alberto BIANCO	Directeur de Recherche CNRS – Université de Strasbourg
Rapporteurs :	François HENN	Professeur – Université Montpelier 2
	Patrick SENET	Professeur – Université de Bourgogne
Examinateurs :	Emmanuel FLAHAUT	Chargé de Recherche CNRS – Université Paul Sabatier – Toulouse III
	Christophe RAMSEYER	Professeur – Université de Franche-Comté
	Mounir TAREK	Directeur de Recherche CNRS – Université Henri Poincaré – Nancy 1

A ma famille :
Irmina, Justyna
et mes parents

"If you don't dare to think you might, you won't."
Terry Pratchett, *Nation* (Chapter 14)

"Just because it's inexplicted doesn't mean it's inexplicable…"
Gregory House in *Hosue, M.D.* - TV series (Season 3 Episode 15)

REMERCIEMENTS

Toute mon estime et mes premiers remerciements vont à mes deux directeurs de thèse, Pr. Christophe Ramseyer et Dr. Mounir Tarek. Je voudrais leur adresser toute ma reconnaissance pour leur rigueur scientifique, leur passion et leurs encouragements qui, durant toutes ces années de travail, m'ont permis de trouver les ressources nécessaires pour mener à bien ce travail. Je voudrais leur exprimer également ma très sincère reconnaissance pour leur disponibilité et leurs qualités pédagogiques. J'ai beaucoup appris à leurs côtés et je leur adresse toute ma gratitude pour m'avoir fait découvrir la simulation numérique et surtout pour leur confiance et l'autonomie qu'ils m'ont laissée.

Ce travail est un travail d'équipe et je tiens à remercier surtout Céline Boiteux qui m'a beaucoup aidé pendant les simulations des canaux ioniques.

Je remercie Pr. Claude Girardet directeur du Laboratoire de Physique Moléculaire, qui m'a accueilli dans son laboratoire ainsi que tous les permanents du laboratoire : Béatrice Bussery-Honvault, Pascal Honvault, Fabien Picaud, Jean-Marie Vigoureux.

Je remercie vivement l'ensemble des membres du jury pour avoir accepté de lire ce travail et de participer à la soutenance de cette thèse.

Un grand merci au Pr. François Henn et Pr. Patrick Senet d'avoir accepté de relire, de corriger et de juger ce manuscrit.

Je tiens à remercier également le Centre Informatique National de l'Enseignement Supérieur à Montpellier - CINES, et le Mésocentre de Franche-Comté pour les nombreuses heures de calculs attribuées à ce travail.

Je n'oublie pas de remercier mes parents pour leur confiance inestimable envers moi, et pour leur soutien permanent depuis toujours.

Enfin, je voudrais remercier tout particulièrement la femme de ma vie Justyna car elle a eu la patience et m'a encouragé lors des moments les plus difficiles. Merci pour tout.

Table des matières

I INTRODUCTION 8

1 Nanomédecine 8

2 Objectifs de la thèse 10

II OUTILS NUMERIQUES 12

1 Buts des simulations moléculaires 12

2 Calculs de Mécanique Quantique (QM) 12

2.1 Méthodes purement quantiques 13
2.2 Méthodes hybrides QM/MM 13
2.3 Calcul des charges partielles 14
2.3.1 Analyse de populations de MULLIKEN 14
2.3.2 Charges dérivées du potentiel électrostatique (ESPD) 15
2.4 Fonctions d'ondes et fonctions de base 20
2.5 Théorie de la fonctionnelle de la densité (DFT) 22

3 Calculs par Dynamique Moléculaire (DM) tout-atomes 23

3.1 Le Champ de Force 23
3.1.1 Expression 23
3.1.2 Interactions intramoléculaires – « liées » 24
3.1.3 Interactions intermoléculaires - « non liées » 24
3.2 Evaluation des Interactions non liées 26
3.2.1 Distance de troncature – cutoff 26
3.2.2 Double cutoff 26
3.2.3 Interactions à Longues Distances (ILD) 27
3.3 Minimisation de l'énergie 30
3.4 Principes de la Dynamique Moléculaire classique 31
3.4.1 Résolution des équations de NEWTON : algorithme de VERLET 31
3.4.2 Contrôle de la température T 33
3.4.3 Contrôle de la pression P 33
3.5 Dynamique sous contraintes 34
3.5.1 Algorithme SHAKE 34
3.5.2 Conditions périodiques 35

4 Dynamique Moléculaire « Gros Grains » 36

5 Simulation statistiques Monte Carlo (MC) 37

6 Calculs d'énergie libre dans un système classique 37
6.1 La méthode des perturbations 38
6.1.1 Umbrella Sampling 39
6.2 La méthode de l'intégration thermodynamique 39
6.2.1 Adaptive Biasing Force (ABF) 40
6.3 Linear Interaction Energy (LIE) 41

III NANOSTRUCTURES DE CARBONE 43

1 Description moléculaire 43
1.1 Fullerène C60 43
1.2 Nanotubes de carbone (CNT) 44

2 Utilisation des CNT dans le domaine biomédical 46
2.1 Utilisation des CNT pour l'imagerie et le diagnostic 46
2.2 Utilisation des CNT pour les biocapteurs 47
2.3 Utilisation des CNT pour la distribution des médicaments 48
2.4 Solubilité et fonctionnalisation des CNT 49

3 Biocompatibilité et cytotoxicité des nanostructures de carbone 50
3.1 Biocompatibilité des nanostructures de carbone 50
3.2 Cytotoxicité des fullerènes 51
3.3 Cytotoxicité des nanotubes 51

IV CIBLES ETUDIEES 53

1 Membrane cellulaire 53
1.1 Propriétés générales 53
1.2 Structure des composants de la membrane 53
1.2.1 Lipides 53
1.2.2 Protéines membranaires 54
1.2.3 Stabilisation de la membrane 54
1.3 Membrane cellulaire en tant que barrière sélective 55
1.4 Polarité de la membrane 57

2 Canaux ioniques 58
2.1 Rôle biologique 59
2.2 Structure détaillée 60
2.3 Les canaux étudiés pendant la thèse 60
2.4 Etudes approfondies du canal KcsA 62

3 Résultats obtenus sur le fonctionnement des canaux 78
3.1 Origine de la perméation des ions dans le KcsA 78
3.1.1 Quantification du « knock-on » 78
3.1.2 L'aspect dynamique du filtre est-il important ? 87
3.2 Origine de la sélectivité dans le KcsA 95
3.2.1 Rôle des effets de polarisation 95

V INTERACTIONS DES NANOSTRUCTURES DE CARBONE 105

1 Interactions des fullerènes avec les protéines membranaires 105

2 Interactions des fullerènes avec la membrane cellulaire 121

3 Interactions des CNT avec la membrane cellulaire 139

3.1 Endocytose ou diffusion passive ? 140

3.2 La fonctionnalisation joue-t-elle un rôle ? 141

3.3 Quel est l'effet de la longueur des CNT sur l'inclusion ? 141

3.4 Comment différencier la membrane nucléaire et la membrane cellulaire ? 142

VI CONCLUSIONS ET PERSPECTIVES 160

VII BIBLIOGRAPHIE 163

Table des articles

1. *Ion conductance vs. pore gating and selectivity in KcsA channel: Modeling achievements and perspectives* 63

2. *Insight into the origins of the barrier-less knock-on conduction in the KcsA channel: molecular dynamics simulations and* ab initio *calculations* 80

3. *Is the mobility of the pore walls and water molecules in the selectivity filter of KcsA channel functionally important?* 88

4. *Determination of the charge profile in the KcsA selectivity filter using* ab initio *calculations and molecular dynamics simulations* 97

5. *Affinity of C60 Neat Fullerenes with Membrane Proteins: a Computational Study on Potassium Channels* 108

6. Supplementary Information: *Affinity of C60 Neat Fullerenes with Membrane Proteins: a Computational Study on Potassium Channels* 108

7. *Uptake and translocation mechanisms of cationic amino derivatives functionalized on pristine C60 by lipid membranes: A molecular dynamics simulation study* 123

8. Supplementary Information: *Uptake and translocation mechanisms of cationic amino derivatives functionalized on pristine C60 by lipid membranes: A molecular dynamics simulation study* 130

9. *Uptake mechanism of single-walled carbon nanotubes by lipid bilayer. Passive diffusion and role of functionalization derivatives revealed by extensive molecular dynamics simulations.* 144

I Introduction

1 Nanomédecine

La dernière décennie a vu la naissance des nanosciences et nanotechnologies. Ces sciences sont avant tout des domaines interdisciplinaires touchant pratiquement toutes les disciplines scientifiques traditionnelles. Les nanosciences concernent en théorie les études effectuées sur les systèmes dont au moins une dimension est nanométrique. La nanotechnologie est relative à la production et à l'application des procédés physiques, chimiques et biologiques à des échelles aussi petites que la taille d'atomes (ou de molécules) jusqu'à des dimensions pouvant atteindre le dixième de micron, ainsi que l'intégration des nanostructures dans des systèmes plus complexes. Aujourd'hui la nanotechnologie est souvent citée pour avoir un impact potentiel profond sur l'économie et la société du 21ème siècle, comparable à ce qu'ont apporté les microtechniques en sciences de l'information. La recherche en nanoscience promet jusqu'à présent des révolutions dans de nombreux domaines traditionnels tels que les matériaux, l'énergie et la médecine. Mon travail s'insère directement dans le domaine de la nanomédecine.

L'impact des nanotechnologies sur les domaines biomédicaux est relativement récent et commence tout juste à gagner en importance comme le démontre une analyse récente des publications scientifiques dans ce domaine. Sur le nombre total de publications liées aux nanotechnologies (environ 8000 entre 2005—2010), seulement 20% d'entre elles sont liées aux sciences biomédicales. Pour comparer, seulement 10% des publications pour la période 2002-2004 sur un total de 2500 publications étaient dédiées à ces domaines. Même si l'effet des nanotechnologies sur le domaine biomédical est lent, il prend de l'ampleur chaque jour et devrait être majeur dans les années à venir. En effet, il faut rappeler que les nanomatériaux et nano-dispositifs développés ont des tailles moléculaires et ont donc un potentiel d'interaction direct avec les cellules et les macromolécules qui constituent le monde vivant. Si les nanomatériaux sont susceptibles d'avoir un énorme impact sur la médecine, la compréhension de la biologie avec l'aide des nanosciences permettra aussi la production de matériaux biomimétiques nanométriques. L'utilisation de nanomatériaux biologiques intégrant des anticorps, des protéines et d'autres substrats ouvrira certainement la voie à de nombreuses applications biomédicales dans le futur. Ces dernières années, la communauté biomédicale a ainsi découvert que les caractéristiques physiques et les nouvelles propriétés des nanoparticules pourraient ouvrir des voies jusqu'alors inexplorées. Citons par exemple, leur rapport surface/volume extraordinairement élevé, l'émission optique

réglable, le comportement magnétique, qui peuvent être exploités pour des utilisations allant de la délivrance des médicaments jusqu'aux biocapteurs.

La nanomédecine, à savoir le recours à des nanosciences dans le domaine de la médecine, demande encore à être pleinement exploitée. Les chercheurs nourrissent en particulier l'espoir de développer un système qui permettrait de diagnostiquer, d'opérer et d'administrer le traitement destiné à combattre une maladie particulière à l'aide d'un nano-objet contrôlé de l'extérieur du patient. À titre d'exemple, dans un cancer, les dosages de médicaments seraient administrés en ciblant les cellules uniquement tumorales, permettant ainsi de réduire la posologie des médicaments utilisés actuellement. En marge d'un intérêt économique évident, un autre avantage consisterait à réduire les effets secondaires qui se manifestent couramment lorsque les techniques de chimiothérapie et de radiothérapie actuelles sont utilisées. D'après les experts en nanomédecine, ces effets secondaires indésirables, associés à la mauvaise solubilité des médicaments, constituent parfois les facteurs qui limitent l'utilisation étendue des traitements actuels contre le cancer et surtout qui empêchent la commercialisation de principes actifs connus, plus efficaces mais impossible à utiliser à cause de ces inconvénients.

L'application des nanotechnologies au domaine de la délivrance des médicaments est donc un domaine de recherche très actif qui pourrait changer le paysage de l'industrie pharmaceutique et de la recherche médicale dans le futur [1-8]. Grâce aux nanotechnologies, nous devrions être capables de réaliser en particulier :

a) l'amélioration de la livraison des médicaments faiblement solubles ; l'administration ciblée de médicaments dans une cellule ou un tissu de manière spécifique ;
b) la transcytose de médicaments à travers les barrières épithéliales et endothéliales étanches ;
c) la livraison de médicaments macromoléculaires aux sites intracellulaires de l'action ;
d) la co-livraison de deux médicaments ou plus, ou d'une modalité thérapeutique, pour un traitement d'association ;
e) la visualisation des sites d'administration de médicaments par la combinaison d'agents thérapeutiques avec des modalités d'imagerie [9] ; et
f) la surveillance de l'efficacité *in vivo* d'un agent thérapeutique en temps réel [3].

A court et moyen terme, on peut donc s'attendre à voir l'émergence de l'administration des médicaments véhiculés par des nanoparticules de carbone, des liposomes, des nanoshells, des dendrimères, des nanoparticules superparamagnétiques, etc. Bien que les technologies organiques et inorganiques soient en cours de développement, les technologies polymériques et les liposomes sont beaucoup plus exploitées pour l'instant et vont probablement continuer à avoir le plus d'impact clinique à court terme. Nous vivons une époque passionnante pour la recherche et le rythme des

découvertes scientifiques dans le domaine médical prend de plus en plus d'ampleur. Il est très largement admis maintenant que le domaine de la délivrance des médicaments sera un bénéficiaire important des nanotechnologies dans les années à venir.

2 Objectifs de la thèse

L'objectif de ma thèse était donc d'étudier spécifiquement les mécanismes d'interaction de nanostructures à base de carbone avec les membranes cellulaires, constituant l'essentiel des cellules vivantes. Ce sujet est très complexe compte tenu de la pluridisciplinarité de la thématique. Nous avons volontairement partagé ce travail en deux parties distinctes. Nous avons d'abord étudié le fonctionnement des canaux ioniques qui sont d'une part des protéines membranaires essentielles pour la fonction cellulaire. D'autre part, elles constituent aussi des cibles thérapeutiques fréquentes dans la recherche des nouveaux médicaments. C'est pour cette deuxième raison que nous nous y sommes particulièrement intéressés. Dans une seconde partie, nous avons étudié le comportement d'espèces carbonées en présence de la membrane cellulaire en analysant finement le mécanisme d'ingestion (ang. *uptake*) de ces vecteurs de médicaments potentiels par les membranes biologiques. Nous avons ensuite tenté de mettre en évidence le rôle toxique que peuvent présentées certaines nanostructures vis-à-vis des protéines membranaires précédemment étudiées.

Ce travail a été essentiellement réalisé à l'aide de simulations numériques. Très vite, nous nous sommes rendu compte qu'il fallait non seulement faire des études en dynamique moléculaire sur des temps très longs (> 100 ns) et sur des systèmes très vastes pour bien comprendre les phénomènes mis en jeu mais également, compte tenu des dimensions nanométriques des canaux ioniques (notamment au niveau du filtre de sélectivité), mené des études *ab-initio* connues également pour être très lourdes. *In fine*, ce travail a duré 4 ans. Pour le mener à terme, nous avons pu bénéficier de temps de calculs sur les grands ordinateurs nationaux (CINES et IDRIS), régionaux (Mésocentre de Franche-Comté) et locaux (calculateur HPC de l'institut UTINAM). Il est à préciser que ce ne sont pas moins de trois siècles de calculs qui ont été effectués sur ces machines lors de mon travail de thèse !

Pour ne pas alourdir le manuscrit mais également parce que la langue française n'est pas ma langue maternelle, j'ai préféré construire mon rapport de thèse sur la base des articles de recherche publiés ou soumis à ce jour. Le manuscrit est donc constitué d'abord par une énumération des outils numériques utilisés. Ensuite, les membranes (constituées essentiellement de lipides et de protéines membranaires) sont présentées en terme de cibles potentielles pour les nanostructures carbonées. Un premier article visant à faire l'état de l'art sur le canal ionique montre combien travailler sur les canaux ioniques est complexe. Trois articles viennent ensuite pour approfondir nos connaissances sur les canaux ioniques. Nous avons en particulier cherché à comprendre la sélectivité du canal, le

rôle des charges ioniques dans le filtre de sélectivité et la dynamique du filtre. La deuxième partie du manuscrit est l'étude proprement dite des interactions des fullerènes et des nanotubes de carbone avec les cibles. Le premier article montre comment les fullerènes bloquent une grande variété de canaux ioniques tandis que le second et troisième concernent l'étude du transport des fullerènes et nanotubes au travers des membranes.

II Outils numériques

1 Buts des simulations moléculaires

Les simulations numériques réalisées à l'aide d'ordinateurs puissants sont appelées parfois expériences *in silico*. Elles permettent de comprendre les propriétés d'assemblages moléculaires en fonction de leur structure et des interactions microscopiques mises en jeu. Elles servent de complément aux expériences classiques (*in vitro* et *in vivo*) et donnent des informations cruciales, inaccessibles autrement. Les simulations numériques à l'échelle moléculaire constituent ainsi un pont entre ce qui se passe à l'échelle atomique et le monde macroscopique du laboratoire. Il s'agit d'une analyse quasi exacte dans le sens où les simulations peuvent être aussi précises qu'on le souhaite, sous réserve des limitations imposées par les outils (interactions et ordinateurs) utilisés. Pour effectuer des simulations numériques en biophysique, il est nécessaire d'effectuer deux opérations majeures. La première consiste à valider le modèle d'interactions utilisé. De nombreuses équipes dans le monde travaillent sur ce sujet et il suffit souvent d'utiliser les champs de force mis à notre disposition pour répondre à cette contrainte. Parfois, en revanche il faut quand même avoir recours à des calculs quantiques (QM) pour raffiner les modèles utilisés. La seconde étape consiste à résoudre, dans des conditions de température et de pression données, les mouvements couplés des macromolécules (réduits à leur cœur atomique) pendant des temps comparables à l'expérience.

2 Calculs de Mécanique Quantique (QM)

Les calculs quantiques consistent essentiellement à résoudre l'équation de SCHRÖDINGER d'un système multiélectronique afin de déterminer la fonction d'onde du système ou plus précisément sa densité électronique. Différentes approches existent selon les modèles. Grossièrement, on peut utiliser une description sur la base de la densité électronique à l'aide de la théorie de la fonctionnelle de la densité (DFT) ou sur la base de la fonction d'onde multiélectronique avec des bases localisées type orbitales moléculaires, gaussiennes... Il existe plusieurs manières de traiter tout ou partie d'un système biologique de façon quantique, le choix de la méthode dépendant des grandeurs que l'on souhaite déterminer.

2.1 Méthodes purement quantiques

Les méthodes quantiques *ab initio* sont des méthodes de calculs fondées sur la chimie quantique. Le terme *ab initio* indique qu'aucune donnée empirique n'est utilisée. Le type de calcul *ab initio* le plus simple est la méthode HARTREE-FOCK (HF) (*voir section 2.4*), dans laquelle les répulsions instantanées électron-électron ne sont pas spécifiquement prises en compte. Seuls les effets moyens (champ moyen) sont inclus dans ce calcul. C'est une procédure variationnelle par conséquent, les énergies approximativement obtenues sont toujours égales ou supérieures à la quantité exacte et tendent vers une valeur limite appelée la limite de HARTREE-FOCK. Il existe un panel de méthodes pour tenir compte des corrélations électroniques dont nous ne donnerons pas la liste ici. En particulier nous avons utilisé largement la théorie de la fonctionnelle de la densité électronique pour résoudre nos problèmes. Celle-ci traite les électrons en terme de densité plutôt qu'en particules indépendantes.

Enfin, il faut signaler que les calculs quantiques peuvent aussi prendre en compte les phénomènes de polarisation et de transferts de charge qui se manifestent tout particulièrement dans les milieux confinés, ou dans le cas d'interactions fortes entre un ligand et son environnement. Ces conditions sont typiquement celles rencontrées dans les protéines membranaires. Il était donc intéressant d'étudier le rôle que peut jouer la structure électronique sur leurs fonctions. Nous tenterons de répondre à cette problématique dans le chapitre IV.

Dans cette thèse, les calculs *ab initio* ont été effectués avec le logiciel Gaussian 03 [10] et MOPAC 2000 [11] à différents niveaux de théorie selon les systèmes traités (*voir articles correspondants*).

2.2 Méthodes hybrides QM/MM

Les méthodes mixtes sont actuellement en plein essor. Elles marient les méthodes quantique (DFT) et classique (DM) en traitant spécifiquement les différentes parties d'un système complexe. Elles sont tout particulièrement intéressantes dans l'étude des processus chimiques en phase liquide, ou encore des phénomènes de catalyse enzymatique, quand seules certaines zones restreintes constituent des sites réactifs. Elles ont été récemment appliquées aux protéines membranaires telles que les canaux ioniques [12-13], afin d'optimiser la structure de quelques acides aminés et de quantifier les phénomènes de polarisation. Ces méthodes donnent d'excellents résultats mais sont parfois difficiles à mettre en œuvre et à interpréter. En particulier, les zones frontières entre quantique et classique doivent être choisies avec soin, à l'écart de toute densité de charge trop importante, ce qui n'est pas toujours facile. De plus, elles demandent un long travail de paramétrisation afin d'évaluer correctement les interactions entre domaine classique et domaine quantique et sont très coûteuses en terme de ressources matérielles.

2.3 Calcul des charges partielles

L'une des manifestations communes des phénomènes d'induction est la polarisation. Celle-ci est liée à la déformation des nuages électroniques. D'autre part, l'induction peut se traduire par des transferts de charge entre ligands, et être interprétée en terme de densité électronique déplacée, ou plus précisément en terme de charges partielles. En particulier, l'atome étudié ne porte plus une charge entière mais partielle, qui traduit la délocalisation des électrons dans un milieu confiné. Ces calculs de charges partielles peuvent être effectués par des méthodes quantiques, en travaillant sur des configurations issues de la DM (situation précise d'un système a un instant donné) d'une partie du système, restreinte de façon totalement indépendante du reste. Cette approche est évidemment plus approximative que les méthodes hybrides QM/MM, mais est beaucoup plus simple, plus rapide et permet de traiter de façon quantique des systèmes assez vastes (de l'ordre de 200 atomes).

Bien que les charges atomiques soient des grandeurs très couramment utilisées en physique et en chimie, ce ne sont pas des observables au sens quantique du terme. Leur valeur n'est pas mesurable expérimentalement. De nombreuses méthodes de calcul ont donc été mises au point afin d'estimer leur valeur. La méthode employée dépend principalement des propriétés du système que l'on souhaite déterminer. Ainsi, il est possible de déterminer ces charges par dynamique moléculaire ou par simulation de type Monte-Carlo, en visant à reproduire les propriétés thermodynamiques d'un système. Leurs valeurs sont alors modifiées de manière itérative jusqu'à ce que la simulation et l'expérience concordent de façon acceptable. Cette méthode simple, qui donne des résultats corrects, n'est toutefois applicable qu'à des systèmes de taille réduite (quelques acides aminés). Dans la plupart des cas, ce sont les propriétés électrostatiques que l'on cherche à estimer à partir de ces charges. Ces propriétés étant directement liées aux positions des électrons et des noyaux au sein d'une molécule, on peut raisonnablement envisager de calculer les charges partielles grâce à la mécanique quantique.

Un grand nombre de méthodes basées sur ce principe ont été proposées et leurs mérites respectifs sont encore discutés. Néanmoins, certaines d'entre elles sont plus répandues, du fait de leur simplicité ou de leur efficacité.

2.3.1 Analyse de populations de MULLIKEN

L'analyse de populations (PA) est presque aussi répandue que critiquée dans le cadre du calcul de charges partielles à partir de la fonction d'onde d'un système. Son principe fut initialement proposé par MULLIKEN en 1955 [14]. Il suggéra de répartir les électrons d'une molécule en une population nette n_r dans le jeu de fonctions de base χ_r d'une part, et une population de recouvrement n_{r-s} sur toutes les paires possibles de fonctions de base d'autre part.

Ainsi, chaque orbitale moléculaire (OM) φ_i peut être considérée comme une combinaison linéaire des fonctions de bases χ_r (orbitales atomiques) :

$$\varphi_i = \sum_r c_{r,i}\chi_r \qquad (1)$$

et, en considérant φ_i et χ_r normalisées, la densité de probabilité attachée à un électron s'écrit :

$$|\varphi_i|^2 = c_{1,i}^2 + c_{2,i}^2 + \cdots + 2c_{1,i}^2 c_{2,i}^2 S_{12} + 2c_{2,i}^2 c_{3,i}^2 S_{23} + \cdots \qquad (2)$$

où les termes S_{rs} sont des intégrales de recouvrement de type $S_{rs} = \iint \chi_r \chi_s dv_1 dv_2$.

MULLIKEN proposa la répartition suivante : un électron de l'OM φ_i contribue pour $c_{1,i}^2$ à la population nette de χ_1, pour $c_{2,i}^2$ à la population nette de χ_2 et pour $2c_{1,i}^2 c_{2,i}^2 S_{12}$ à la population de recouvrement entre χ_1 et χ_2 … Ainsi, s'il y a n_i électrons dans l'OM φ_i, la population nette sera $n_{r,i} = n_i c_{r,i}^2$ et la population de recouvrement $n_{r-s,i} = n_i\left(2c_{r,i}c_{s,i}S_{rs}\right)$. L'analyse de population par MULLIKEN calcule les charges en divisant le recouvrement orbital de deux atomes impliqués de façon égale.

Cette méthode est couramment utilisée en première approximation car très simple à mettre en œuvre une fois connue la fonction d'onde du système, mais elle présente de nombreuses limites. Tout d'abord, elle est évidemment extrêmement dépendante du jeu de fonctions de base utilisées. Ensuite, la répartition arbitraire des populations de recouvrement par moitié introduite par MULLIKEN peut se justifier pour des orbitales atomiques simples, mais devient nettement plus discutable dans d'autres cas, notamment lorsque les orbitales de diffusion sont très délocalisées, et peuvent être situées très loin du noyau auquel elles sont rattachées.

Des améliorations ont été apportées à cette méthode, et d'autres techniques d'analyse de populations, basées sur le même principe, ont été proposées, telles que la LPA (LÖDWIN Population Analysis) ou la NPA (Natural Population Analysis), mais elles restent très dépendantes du jeu de fonctions de base utilisées, et le raffinement de ce dernier permet difficilement d'obtenir une convergence des résultats obtenus, même avec ces techniques améliorées.

Il faut de plus noter que les charges obtenues par analyse des populations reproduisent souvent mal les propriétés électrostatiques des molécules, et il est nécessaire pour les étudier d'avoir recours à des méthodes plus performantes, comme la dérivation de charges à partir du potentiel électrostatique.

2.3.2 Charges dérivées du potentiel électrostatique (ESPD)

Le potentiel électrostatique en un point est un potentiel agissant sur une charge positive unitaire et ponctuelle en ce point. C'est une observable qui peut être déterminée à partir de la fonction d'onde d'un système :

$$V(r) \propto \sum_{A=1}^{N} \frac{Z_A}{|r - R_A|} - \int \frac{\rho(r')}{|r - r'|} dr' \qquad (3)$$

où Z_A est le numéro atomique de l'atome A, R_A sa position, N le nombre d'atomes dans le système, et $\rho(r')$ la densité électronique au point r', avec :

$$\rho(r')dr' \equiv \int \dots \int \psi(r')\psi^*(r')dr' \qquad (4)$$

où ψ est la fonction d'onde du système total.

Le potentiel $V(r)$ est continu et difficile à représenter à l'aide d'une fonction analytique. Dans le cadre d'une étude numérique, il sera donc représenté de façon discrète, en certains points choisis selon la méthode de calcul. L'objectif est alors de déterminer un jeu de charges partielles localisées sur les atomes du système qui reproduit au mieux le potentiel électrostatique pour ces points :

$$V_{calc}(r) = \sum_{i=1}^{N} \frac{q_i}{|r - R_i|} \qquad (5)$$

où q_i et R_i représentent respectivement la charge partielle et la position de l'atome i, N étant le nombre total d'atomes.

Une solution à ce problème a été proposée par COX et WILLIAMS en 1981 [56], sous la forme d'un ajustement par moindres carrés du potentiel calculé grâce aux charges partielles *(éq. 5)* sur le potentiel obtenu à partir de la fonction d'onde *(éq. 3)* :

$$\chi^2 = \sum_{j=1}^{n} \left[V_{calc}(r_j) - V_{ref}(r_j)\right]^2 \qquad (6)$$

où les n points $r_j (j = 1, \dots, n)$ sont ceux où le potentiel de référence est évalué, choisis hors des sphères de VAN DER WAALS des atomes, χ^2 est une fonction à minimiser. De nombreuses techniques basées sur ce principe ont depuis été mises au point. Elles diffèrent principalement par le choix des points de calculs du potentiel de référence et par la méthode de résolution de l'équation aux moindres carrés *(éq. 6)*.

2.3.2.a Méthode de MERZ-KOLLMAN (MK)

Initialement proposée en 1984 par SINGH et KOLLMAN [15], puis dans sa version finale par BESLER, MERZ et KOLLMAN en 1990 [16], la méthode dite de MERZ-KOLLMAN échantillonne les points de calculs sur les surfaces de CONNOLY, soit à des distances de 1.4, 1.6, 1.8 et 2.0 fois le rayon de VAN DER WAALS, avec une densité de 1 point/Å^2.

Partant de l'équation aux moindres carrés *(éq. 6)*, les auteurs proposent de prendre en compte les contraintes (g) imposées au système via des multiplicateurs de LAGRANGE (λ). La fonction à minimiser devient, en considérant ω contraintes :

$$z = \chi^2 + \lambda_1 g_1 + \lambda_2 g_2 + \dots + \lambda_\omega g_\omega \qquad (7)$$

où les contraintes doivent être des fonctions de la valeur des charges afin de conserver une équation linéaire. Le minimum de la fonction z et les charges correspondantes peuvent alors être déterminées en résolvant le système d'équations suivant :

$$\begin{cases} \sum_{k=1}^{n} \frac{\partial z}{\partial q_k} = 0 \\ \sum_{l=1}^{\omega} \frac{\partial z}{\partial \lambda_l} = g_l \end{cases} \quad (8)$$

Dans le cadre de cette étude, la seule contrainte imposée au système ($\omega = 1$) est la valeur de la charge totale :

$$g_1 = \sum_{j=1}^{N} q_j - q_{tot} = 0 \quad (9)$$

En prenant cette contrainte en compte, l'équation *(7)* devient :

$$z = \sum_{i=1}^{n} \left(V_{ref}(r_i) - \sum_{j=1}^{N} \frac{q_j}{r_{ij}} \right)^2 - 2\lambda \left(\sum_{j=1}^{N} q_j - q_{tot} \right) \quad (10)$$

où n est le nombre total de points de calcul du potentiel, N le nombre d'atomes dans le système et λ une constante arbitraire. Le système d'équations *(8)* devient :

$$\begin{cases} \frac{\partial z}{\partial \lambda} = 0 = \sum_{j=1}^{n} q_j - q_{tot} \\ \frac{\partial z}{\partial q_k} = 0 = \sum_{i=1}^{n} \frac{2}{r_{ik}} \left(V_{ref}(r_i) - \sum_{j=1}^{N} \frac{q_j}{r_{ij}} \right) + \lambda \end{cases} \quad (11)$$

soit, en simplifiant :

$$\begin{cases} \sum_{j=1}^{n} q_j = q_{tot} \\ \sum_{j=1}^{N} \sum_{i=1}^{n} \frac{q_j}{r_{ij} r_{ik}} = \sum_{i=1}^{n} \frac{V_{ref}(r_i)}{r_{ik}} + \lambda \end{cases} \quad (12)$$

On peut définir

$$A_{jk} = \sum_{i=1}^{n} \frac{1}{r_{ij} r_{ik}} \quad et \quad B_k = \sum_{i=1}^{n} \frac{V_{ref}(r_i)}{r_{ik}} \quad (13)$$

qui sont les termes de l'équation matricielle Aq = B :

$$\begin{pmatrix} A_{11} & A_{12} & \cdots & A_{1n} & -1 \\ A_{21} & A_{22} & \cdots & A_{2n} & -1 \\ \vdots & \vdots & \ddots & \vdots & -1 \\ A_{n1} & A_{n2} & \cdots & A_{nn} & -1 \\ 1 & 1 & 1 & 1 & 0 \end{pmatrix} \begin{pmatrix} q_1 \\ q_2 \\ \vdots \\ q_n \\ \lambda \end{pmatrix} = \begin{pmatrix} B_1 \\ B_2 \\ \vdots \\ B_n \\ q_{tot} \end{pmatrix} \quad (14)$$

Les charges sont alors déterminées par résolution de l'équation $q = A^{-1}B$.

2.3.2.b CHarge from ELectrostatic Potential (CHELP)

Dans la méthode CHELP, développée en 1987 par CHIRLIAN et FRANCL [17], les points sont choisis de façon symétrique autour de chaque atome, sur des enveloppes sphériques à des distances de 2.5, 3.5, 4.5, 5.5 et 6.5 Å. La technique de détermination des charges q_j est identique à celle décrite dans la méthode de MERZ-KOLLMAN.

2.3.2.c CHarge from ELectrostatic Potential, Grid method (GHELPG)

La méthode CHELPG est une version améliorée de la méthode CHELP, publiée en 1990 par BRENEMAN et WIBERG [18]. Les points de calculs du potentiel électrostatique y sont choisis régulièrement sur une grille cubique de pas 0.3 Å, sur une distance allant de 0 à 2.8 Å au delà du rayon de VAN DER WAALS, avec une densité jusqu'à 1000 fois plus importante que pour la méthode CHELP.

Ces trois méthodes ne diffèrent que par le choix des points de calculs du potentiel électrostatique, mais cette unique différence introduit des variations significatives dans les valeurs des charges obtenues et, d'une manière générale, les méthodes CHELPG et MK donnent des résultats plus valables que la méthode CHELP. Afin d'améliorer la qualité des résultats obtenus, il a été suggéré de choisir de façon aléatoire les points de calculs autour de la molécule. Cela permet d'annuler toute dépendance au système de coordonnées. Les calculs sont alors rendus plus simples dans le sens où aucune surface particulière ne doit être préalablement déterminée.

2.3.2.d Restrained Electrostatic Potential (RESP)

La méthode RESP, mise au point en 1993 par l'équipe de PETER KOLLMAN [19], est une version améliorée de la technique de MERZ-KOLLMAN, plus particulièrement destinée à déterminer des charges utilisables par les logiciels de dynamiques moléculaires comme AMBER. Elle constitue une réponse au problème de dépendance des charges vis-à-vis de la conformation de la molécule que présentaient les autres méthodes. Du fait de sa nature statistique, la détermination de charges dérivées du potentiel électrostatique (charges ESPD) s'accompagne nécessairement d'imprécisions, certaines charges étant déterminées au détriment d'autres. En particulier, les *« buried atoms »*, littéralement atomes enterrés, c'est-à-dire les atomes isolés du solvant par ceux auxquels ils sont liés, ou par leur voisins (carbones sp^3 par exemple), sont particulièrement mal traités par ces méthodes. En effet, le choix des points de calcul du potentiel excluant les sphères de VAN DER WAALS, les points proches de ces atomes restent éloignés du solvant, mais en général sont suffisamment trop proches d'un autre atome, pour obtenir des valeurs de charges satisfaisantes. D'une façon générale, moins un atome est exposé au solvant, moins la valeur de sa charge sera calculée de façon

satisfaisante. Une première réponse à ce problème a été proposée par REYNOLDS *et coll.* [20]. Elle consistait à déterminer les charges ESPD pour les différentes conformations d'une molécule, puis à effectuer pour chaque centre atomique une moyenne pondérée statistiquement. Si cette solution représente un moyen efficace de trouver un jeu de charges partielles indépendant de la conformation, elle est évidemment très lourde en terme de temps de calcul. Par conséquent, elle peut difficilement être appliquée à des systèmes de grandes tailles dont il faudrait d'une part, déterminer le jeu de conformères approprié, et d'autre part, calculer les charges ESPD à un niveau de théorie suffisant pour chaque conformère.

La méthode RESP repose sur une autre idée. Elle consiste à imposer une contrainte anharmonique χ^2_{rst} supplémentaire dans la procédure d'ajustement des charges par moindres carrés, sous la forme d'une charge de référence imposée à tous les atomes sauf ceux d'hydrogène. Le terme χ^2 *(éq. 6)* à minimiser devient :

$$\chi^2 = \chi^2_{esp} + \chi^2_{rst} \qquad (15)$$

avec

$$\chi^2_{esp} = \sum_j \left[V_{calc}(r_j) - V_{ref}(r_j)\right]^2 \qquad (16)$$

Le minimum de cette fonction χ^2 est alors, pour chaque atome j :

$$\frac{\partial(\chi^2)}{\partial q_j} = \frac{\partial\left(\chi^2_{esp}\right)}{\partial q_j} + \frac{\partial(\chi^2_{rst})}{\partial q_j} = 0 \qquad (17)$$

Selon les auteurs, la fonction de contrainte qui donne les meilleurs résultats est de forme hyperbolique [19] :

$$\chi^2_{esp} = a \sum_j \left(\sqrt{q_j^2 + b^2} - b\right) \qquad (18)$$

où a est un facteur multiplicatif qui définit la limite asymptotique de l'intensité de la contrainte et b définit l'écrasement de l'hyperbole autour de son minimum. Le second terme de l'équation *(17)* devient alors :

$$\frac{\partial(\chi^2_{rst})}{\partial q_j} = \frac{a q_j}{\sqrt{q_j^2 + b^2}} \qquad (19)$$

La résolution du système d'équations défini par l'équation *(17)* se fait alors sur le même principe que pour les méthodes précédemment citées, en résolvant l'équation matricielle :

$$\mathrm{A}q = \mathrm{B} \qquad (20)$$

où les termes non-diagonaux de la matrice A sont toujours de la forme :

$$A_{jk} = \sum_i \frac{1}{r_{ij} r_{ik}} \qquad (21)$$

mais où les termes diagonaux de A prennent désormais en compte la contrainte :

$$A_{jj} = \sum_i \frac{1}{r_{ij}^2} + \frac{\partial(\chi_{rst}^2)}{\partial q_j} \qquad (22)$$

De même, les termes de la matrice B restent de la forme :

$$B_j = \sum_i \frac{V_{ref}(r_i)}{r_{ij}} \qquad (23)$$

Cette méthode permet d'obtenir des résultats quasiment invariants pour les atomes dont la charge ESPD était bien déterminée par les méthodes antérieures, mais donne des valeurs significativement différentes et plus raisonnables pour les atomes intérieurs, précédemment mal traités. De plus, ces charges sont moins dépendantes de la conformation du système, et restent relativement stables lors de changement de symétrie ou d'orientation.

Cette non dépendance à la conformation fait des charges RESP les charges les mieux adaptées aux dynamiques moléculaires. En effet, durant les simulations par DM, la conformation des différents éléments du système change rapidement, et il serait numériquement impossible de recalculer les charges atomiques partielles à chaque pas de simulation. Or, l'évolution d'un système traité par DM est fortement dépendante des interactions coulombiennes, et donc de la valeur des charges. Les charges RESP, calculées préalablement sur des molécules restreintes de façon indépendante (acides aminés, molécule d'eau...), constituent en ce sens un bon compromis, même si elles ne permettent pas de rendre compte des configurations à polarisation spécifique qui peuvent apparaître spontanément au cours d'une simulation.

2.4 Fonctions d'ondes et fonctions de base

La résolution de l'équation de SCHRÖDINGER d'un système quantique nécessite une base de fonctions d'onde adaptée. L'équation de SCHRÖDINGER est linéaire et, par conséquent toute combinaison linéaire de ses solutions est également solution. De plus, la détermination d'une solution générique passe en général par la recherche de solutions particulières, telles que les états propres de l'opérateur hamiltonien. Malheureusement, il est impossible d'obtenir des solutions de ces équations aux valeurs propres pour des systèmes de plus de 2 ou 3 particules, et il faut avoir recours à un certain nombre d'approximations sur l'hamiltonien moléculaire pour les résoudre.

En 1927, HARTREE proposa de découpler la fonction d'onde d'un système à plusieurs corps en un produit de fonctions d'onde monoélectroniques orthogonales et normalisées, également appelées orbitales moléculaires, puis de résoudre l'équation de SCHRÖDINGER pour chaque électron se déplaçant dans ce potentiel, en partant du principe que chaque électron se déplace dans un champ moyen créé par les autres électrons et les noyaux. En 1930, SLATER et FOCK proposèrent une alternative à la méthode de HARTREE en approximant la fonction d'onde d'un système complexe

d'électrons par un déterminant de SLATER des spin-orbitales monoélectroniques. Depuis ce temps-là, dès lors que des fonctions d'onde monoélectroniques interviennent dans le cadre de la résolution de l'équation de SCHRÖDINGER on parle de la méthode HARTREE-FOCK. Par conséquent, il convient d'utiliser un jeu de fonctions de base suffisamment large pour obtenir des résultats fiables, sans pour autant augmenter de façon déraisonnable les temps de calcul, compte tenu de la taille du système.

Les fonctions de bases sont les expressions mathématiques des orbitales atomiques, qui décrivent la portion de l'espace où l'on peut trouver un électron autour d'un atome. Initialement les orbitales atomiques étaient décrites rigoureusement comme des orbitales de SLATER, fonctions décroissant exponentiellement à mesure que la distance au noyau augmente. Mais d'un point de vue mathématique, l'exponentielle pose un certain nombre de problèmes, en particulier pour le calcul des intégrales dans un système de plus de deux atomes. Désormais, elles sont approximées par des combinaisons linéaires de gaussiennes, en général 3, plus faciles et plus rapides à traiter numériquement, sans perte significative de précision sur les résultats si le jeu des fonctions de base est suffisamment étendu.

Il existe en effet un grand nombre de jeu de fonctions de base, et plus ils sont complets, plus les résultats obtenus sont réalistes. Les jeux les plus simples possèdent le nombre minimal de fonctions de base nécessaire pour représenter tous les électrons d'un atome. L'hydrogène par exemple peut être décrit par une seule gaussienne, pour son unique électron, qui correspond à l'orbitale *1s*. Quand le nombre d'électrons augmente, on attribue au moins une fonction de base supplémentaire pour chaque orbitale atomique : *1s, 2s,* $2p_x$, $2p_y$, $2p_z$, *3s*...

Les jeux de base minimaux de type STO-xG (pour *Slater Type Orbital x Gaussian*), décrivent chaque orbitale atomique comme une combinaison linéaire de *x* gaussiennes. Ces jeux sont, de toute évidence, insuffisants pour obtenir des résultats utilisables, et ils peuvent être améliorés de plusieurs façons, en traitant différemment les orbitales selon leur éloignement au noyau.

Tout d'abord, concernant les orbitales de cœur où les électrons sont très proches du noyau, l'énergie est donc très sensible à leur position. Par conséquent il est plus rigoureux d'utiliser un nombre plus important de gaussiennes pour les représenter. Ensuite, viennent les orbitales de valence, où se situent les électrons impliqués dans les liaisons interatomiques. La densité électronique y est délocalisée entre plusieurs atomes et perd donc sa symétrie sphérique. Leur description peut être améliorée de deux façons :

a) par *démultiplication de la couche de valence*, où l'on utilisera par exemple deux orbitales *s* de valence au lieu d'une et six orbitales *p* au lieu de trois. Ces jeux sont notés X-YZg, X représentant le nombre de gaussiennes primitives composant les orbitales de cœur, Y et Z signifiant que les orbitales de valence sont représentées par deux fonctions de base, elles-

mêmes combinaisons linéaires de Y et Z gaussiennes primitives. Il est également possible de définir sur le même principe, des jeux de type X-YZWg ou encore X-YZWVg ;

b) une *fonction de polarisation* peut également être ajoutée afin d'autoriser la déformation des orbitales de valence. Cela revient à ajouter aux couches de valence des orbitales de nombre quantique secondaire *l* plus élevé (*p* ou *d* pour l'atome d'hydrogène, *d, f* ou *g* pour les atomes plus gros...).

Enfin, les électrons les plus éloignés du noyau peuvent être décrits par ajout de *fonction de diffusion,* qui leur accorde plus d'espace que les simples gaussiennes. Les orbitales diffuses sont particulièrement importantes quand les systèmes traités font intervenir des anions, dont la probabilité de présence d'électron supplémentaire est beaucoup plus large.

2.5 Théorie de la fonctionnelle de la densité (DFT)

De plus en plus la théorie de la fonctionnelle de la densité électronique (ang. *Density Functional Theory* - DFT) est utilisée en physique et chimie pour étudier la structure électronique de systèmes à plusieurs corps, notamment en phase condensée. Les propriétés d'un système à plusieurs électrons peuvent être déterminées en utilisant des fonctionnelles, i.e. des fonctions d'une autre fonction, qui est dans ce cas la densité d'électrons dépendante de l'espace. La DFT a commencé à être populaire dans les années 1970. Dans de nombreux cas, les résultats des calculs DFT pour les systèmes semi-conducteurs sont tout à fait satisfaisants. En outre, les coûts de calculs sont relativement faibles par rapport aux méthodes traditionnelles qui étaient basées sur la fonction d'onde complexe à plusieurs électrons, comme la théorie HARTREE-FOCK et ses dérivées. Toutefois, la DFT est souvent jugée imprécise et des améliorations supplémentaires ont été ajoutées pour mieux modéliser les interactions d'échange et de corrélation. La DFT est maintenant une méthode largement utilisée pour les calculs de structure électronique en chimie et en physique du solide. Malgré ces améliorations, il y a encore des difficultés pour décrire correctement les interactions intermoléculaires, en particulier les forces de VAN DER WAALS (dispersion), le transfert de charges lors d'une excitation (ce qui est actuellement traité par la fonctionnelle dépendante du temps TD-DFT), ou encore les états de transition. Le mauvais traitement de la dispersion rend la DFT parfois inappropriée pour les systèmes dominés par ces interactions (comme l'interaction entre atomes neutres) ou lorsque la contribution de dispersion est en concurrence de manière significative avec d'autres effets (ce qui peut arriver dans des biomolécules). Le développement de nouvelles méthodes DFT, destinées à résoudre ce problème par des altérations de la fonction ou par l'inclusion de termes additifs, est un sujet de recherche actuel en plein développement.

3 Calculs par Dynamique Moléculaire (DM) tout-atomes

La dynamique moléculaire permet de simuler, à partir des lois de la mécanique classique, les trajectoires des atomes en phase cristalline, en solution ou en phase gazeuse [21-23]. Elle décrit donc l'évolution d'un système au cours du temps. Une résolution numérique des équations classiques du mouvement est utilisée pour calculer l'énergie du système le long de son parcours sur la surface de potentiel du système.

Ainsi, une macromolécule est considérée comme un ensemble d'atomes dont les interactions mutuelles peuvent être décrites par une fonction d'énergie potentielle. C'est le « champ de force » qui est implicitement dérivé des calculs quantiques précédemment expliqués. La distribution des électrons, considérée comme implicite, est localisée sur les liaisons du système et est représentée par la distribution de charges sur les atomes de chaque molécule. Ces charges, comme nous l'avons vu précédemment, peuvent être calculées de façon à reproduire le moment dipolaire de la molécule ou la surface de potentiel électrostatique obtenue par les calculs *ab initio*.

Une simulation de dynamique moléculaire (DM) n'est valable que si on échantillonne l'espace et le temps correctement. La taille d'un système simulé (nombre de particules N), le pas de temps d'intégration (Δt) et la durée totale de la simulation doivent être choisis de manière à ce que le calcul puisse se terminer dans un délai raisonnable. Il faut aussi veiller à ce que les simulations soient suffisamment pertinentes aux échelles de temps des processus naturels à l'étude. Ainsi, pour déduire des conclusions statistiquement valables à partir des simulations, la durée de temps simulée doit correspondre à la cinétique du processus naturel étudié.

La mise en œuvre d'une simulation comprend différentes étapes : après avoir construit le système et immergé celui-ci dans son solvant, l'ensemble du système est tout d'abord relaxé afin de minimiser les tensions (phase d'équilibration), puis commence la dynamique moléculaire proprement dite avec la phase de production.

3.1 Le Champ de Force

3.1.1 Expression

Nous avons effectué l'ensemble des calculs de Dynamique Moléculaires (DM) avec les logiciels AMBER 8 [24] et NAMD 2.6 et 2.7 [25]. Ils utilisent tous les deux une représentation empirique de l'énergie potentielle dont l'expression la plus simple est :

$$U = \sum_{liaisons} k_b(b - b_0)^2 + \sum_{angles} k_\theta(\theta - \theta_0)^2 \qquad (24)$$

$$+ \sum_{dièdres} \sum_{n} V_n[1 + cos(n\varphi - \gamma)] + \sum_{i<j} \left[\frac{q_i q_j}{r_{ij}} - 2\varepsilon_{ij} \left(\frac{r_{ij}^*}{r_{ij}} \right)^6 + \varepsilon_{ij} \left(\frac{r_{ij}^*}{r_{ij}} \right)^{12} \right]$$

Cette énergie se décompose en contributions intra et intermoléculaires.

3.1.2 Interactions intramoléculaires – « liées »

Les déformations des liaisons et des angles sont modélisées par un oscillateur harmonique en sommant soit sur toutes les liaisons covalentes, soit sur tous les angles entre atomes liés de façon covalent.

L'énergie potentielle de ***déformation des liaisons*** s'exprime :

$$\sum_{liaisons} k_b(b - b_0)^2 \qquad (25)$$

où b est la longueur de la liaison instantanée (en Å), b_0 celle de la liaison à l'équilibre et k_b la constante de force (en kcal.mol^{-1}.Å^{-1})

Dans le cas de la ***déformation des angles*** on exprime l'énergie potentielle comme :

$$\sum_{angles} k_\theta(\theta - \theta_0)^2 \qquad (26)$$

où θ est l'angle instantané (en °), θ_0 sa valeur à l'équilibre (en °) et k_θ la constante de force associée (en kcal.mol^{-1}).

Le terme énergétique de ***déformation des dièdres*** φ concerne trois liaisons et donc quatre atomes A, B, C et D consécutifs. L'angle dièdre φ correspond à l'angle entre les liaisons AB et CD, et permet donc la rotation autour de la liaison BC. Ce terme contribue à la barrière d'énergie rencontrée lors de la rotation d'une liaison. Il est défini de la manière suivante :

$$\sum_{dièdres} \sum_{n} V_n[1 + cos(n\varphi - \gamma)] \qquad (27)$$

où V_n est la valeur de la barrière de rotation d'ordre n (en kcal.mol^{-1}), γ la phase (en °) et φ la valeur instantanée du dièdre (en °).

Chaque terme correspondant à un angle dièdre φ contient plusieurs ordres en V_n : l'ordre 1 (V_1) correspond à une rotation complète autour de la liaison, l'ordre 2 (V_2) à un demi-tour etc. En général seul l'ordre prépondérant est utilisé. Par exemple on ne conservera que l'ordre 3 (V_3) dans le cas d'une barrière d'ordre 3.

3.1.3 Interactions intermoléculaires - « non liées »

Toutes les interactions non liées concernent les atomes qui appartiennent à des molécules différentes ou qui sont liés par plus de trois liaisons covalentes. Ces interactions sont décrites par deux termes : un terme dit de LENNARD-JONES, aussi appelé terme de VAN DER WAALS et un terme électrostatique, appelé aussi terme coulombien.

3.1.3.a Interactions de VAN DER WAALS

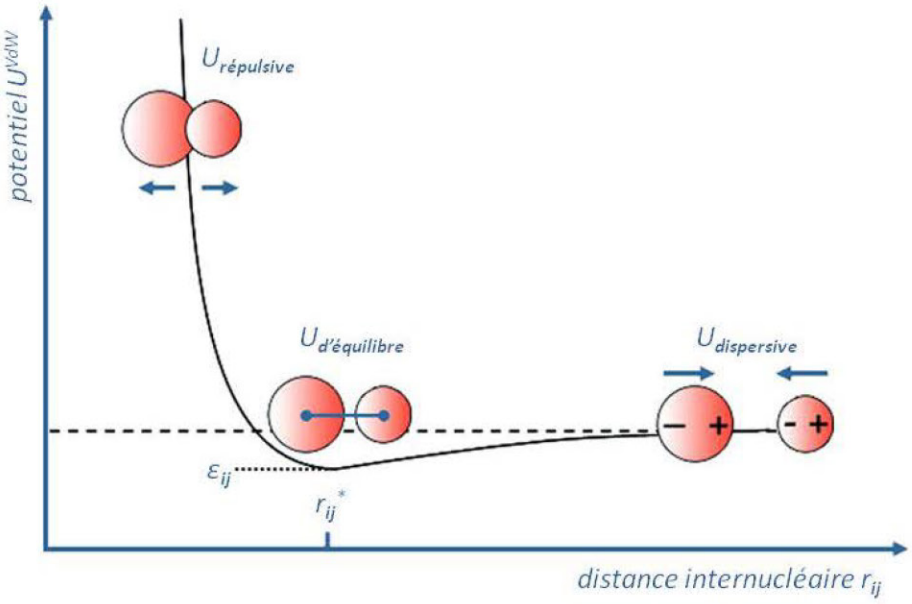

Figure II.1 Energie potentielle des interactions de VAN DER WAALS

Les interactions de VAN DER WAALS sont représentées par une énergie potentielle U^{VdW} dont l'expression prend la forme suivante :

$$U^{VdW} = \sum_{i<j} \sum_{j} 2\varepsilon_{ij} \left[\frac{1}{2} \left(\frac{r_{ij}^*}{r_{ij}} \right)^{12} - \left(\frac{r_{ij}^*}{r_{ij}} \right)^{6} \right] \qquad (28)$$

où ε_{ij} et r_{ij}^* sont les paramètres de LENNARD-JONES pour les interactions entre les atomes i et j. ε_{ij} représente la profondeur du puits de VAN DER WAALS à la distance r_{ij}^* (*voir Figure II.1*). Le terme en r_{ij}^{-6} représente la dispersion attractive de LONDON entre deux atomes et celui en r_{ij}^{-12} la répulsion due à l'exclusion de PAULI [26].

Pour deux atomes i et j différents, on applique les règles de combinaison de LORENTZ-BERTHELOT :

$$\varepsilon_{ij} = \sqrt{\varepsilon_{ii} \times \varepsilon_{jj}} \qquad (29)$$

$$r_{ij}^* = \frac{r_{ii}^* + r_{jj}^*}{2} \qquad (30)$$

3.1.3.b Interactions électrostatiques

Les interactions coulombiennes sont limitées aux interactions entre charges partielles et s'écrivent :

$$\sum_{i<j} \sum_{j} \frac{q_i q_j}{r_{ij}} \qquad (31)$$

où q_i et q_j sont les charges partielles des atomes i et j.

3.2 Evaluation des Interactions non liées

3.2.1 *Distance de troncature – cutoff*

La sommation des interactions non liées de l'énergie potentielle totale porte sur toutes les paires d'atomes non liées du système, soit $N(N-1)/2$. Les autres composantes de l'énergie étant proportionnelles à N, il est nécessaire, pour limiter le temps de calcul, de réduire cette sommation aux contributions les plus importantes. Pour ce faire, une distance de troncature (ang. *cutoff*) est introduite. Au delà de cette distance, les interactions non liées ne sont plus calculées.

Les calculs standards utilisent un *cutoff* basé sur une distance définie. A l'intérieur d'un résidu, les interactions entre tous les atomes qui le constituent sont toujours calculées, quelle que soit la distance qui les sépare. Dans le cas de deux résidus distincts, on ne calcule les interactions non liées entre toutes les paires atomiques de ces deux résidus, que s'il existe une paire d'atomes séparée d'une distance inférieure au *cutoff.* Dans le cas des interactions avec le solvant, ces distances ne sont testées que pour l'atome d'oxygène de la molécule de solvant (de l'eau). Si cette méthode est satisfaisante pour traiter l'interaction VAN DER WAALS, elle ne l'est pas en général pour la contribution électrostatique qui converge très mal.

3.2.2 *Double cutoff*

La méthode du *double cutoff* a été introduite par BERENDSEN *et coll*. en 1985 [27], pour gagner du temps sur le calcul des interactions non liées. On utilise cette fois deux rayons de *cutoff* R_{C1} et R_{C2} (*voir Figure II.2*). Pour un atome i, les atomes j se trouvant à une distance inférieure à R_{C1} sont stockés dans un tableau « *pair-list* » PL_i de cet atome (comprenant l'ensemble des atomes j interagissant de manière non liée avec l'atome i). Les énergies d'interactions des atomes k pour lesquels $R_{C1} < r_{ik} < R_{C2}$ (*zone grisée, voir Figure II.2*) sont stockées dans une variable E_k^{ILD} appelée Energie à Longues Distances.

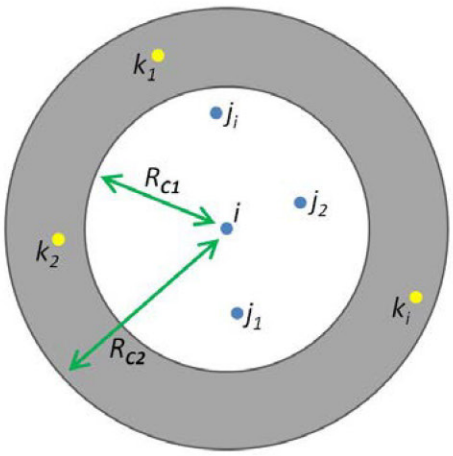

Figure II.2 Méthode du double *cutoff*

A chaque pas Δt de dynamique, les énergies d'interactions *non liées* sont la somme de deux contributions : les interactions à courtes distances entre i et PL_i calculées en utilisant les positions des atomes au moment t et l'énergie E_k^{ILD} qui, elle, est maintenue constante pendant un certain nombre de pas (PL_i et E_k^{ILD} sont généralement renouvelées simultanément tous les 10 à 50 pas de dynamique environ).

3.2.3 *Interactions à Longues Distances (ILD)*

La discontinuité brutale de l'énergie à la distance du *cutoff* cause des artefacts dans les mouvements, les conformations [28-30] ou dans les énergies calculées [31-35]. Afin de corriger cet artefact, il est possible d'estimer les interactions au delà du *cutoff* (en utilisant par exemple la *sommation d'EWALD*), et en même temps de faire tendre vers zéro les interactions pour des distances légèrement inferieurs au *cutoff* (en utilisant par exemple des *fonctions de commutation* (ang. *switching functions*)).

3.2.3.a Sommation d'EWALD – PME

La méthode de la sommation d'EWALD a été conçue en 1921 [36] pour traiter un peu mieux les problèmes liés au calcul de l'énergie électrostatique et en particulier pour évaluer les énergies d'interaction à l'intérieur des milieux ioniques. Elle suppose qu'une particule de la boîte (« maille ») interagit avec toutes les particules de la boîte et avec toutes leurs images se trouvant dans une matrice infinie de boîtes périodiques, construite en translatant la maille initiale suivant les trois directions *x, y* et *z* de l'espace [21, 37]. A l'infini, le système global tend vers une forme quasi-sphérique (*voir schéma en 2D, Figure II.3*).

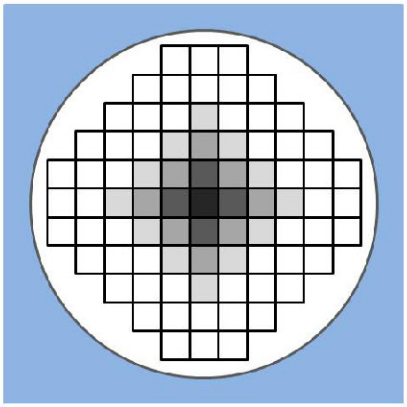

Figure II.3 Construction d'un système de cellules périodiques par la méthode d'EWALD

En tenant compte de cette périodicité, l'expression de l'énergie coulombienne à l'intérieur de la boîte est la suivante :

$$U = \frac{1}{2}\sum_{i=1}^{N}\sum_{\substack{j=1 \\ j\neq i}}^{N}\frac{q_i q_j}{r_{ij}} \qquad (32)$$

et avec les boîtes images :

$$U = \frac{1}{2}\sum_{|n|}^{\infty}\sum_{i=1}^{N}\sum_{\substack{j=1 \\ j\neq i}}^{N}\frac{q_i q_j}{|r_{ij}+n|} \qquad (33)$$

où N est le nombre de particules dans chaque boîte, r_{ij} la distance entre les particules i et j, q_i et q_j leurs charges et n la distance à la boîte centrale avec, $n = n_x L_x + n_y L_y + n_z L_z$ où L_x, L_y, L_z sont les dimensions de la cellule.

Cependant, la convergence de ces deux sommes *(32)* et *(33)* est relativement lente et incertaine. La méthode d'EWALD réexprime U en une somme convergeant rapidement afin de pouvoir calculer aisément les interactions à longues distances.

La distribution de charge $Q_i(r)$ est un ensemble infini de charges ponctuelles q_i représentée par la fonction δ :

$$Q_i(r) = q_i\delta(r - r_i) \qquad (34)$$

Toutes les charges ponctuelles q_i sont alors entourées d'une distribution gaussienne de charges de même amplitude α mais de signe opposé :

$$Q_i^G(r) = -q_i\left(\frac{\alpha}{\sqrt{\pi}}\right)^3 e^{-\alpha^2|r-r_i|^2} \qquad (35)$$

On a alors la distribution de charges globale :

$$Q_i^S(r) = Q_i(r) + Q_i^G(r) \qquad (36)$$

L'expression de U faisant intervenir cette répartition de charges converge plus rapidement grâce à l'introduction de la fonction d'erreur $erfc(x)$:

$$U^S = \frac{1}{2}\sum_{n=0}^{\infty}\sum_{i=1}^{N}\sum_{\substack{j=1 \\ j\neq i}}^{N}\frac{q_i q_j}{|r_{ij}+n|}erfc\left(\alpha|r_{ij}+n|\right) \qquad (37)$$

où $erfc(x) = \frac{2}{\sqrt{\pi}}\int_x^{\infty} e^{-t}dt$

On ajoute un terme supplémentaire afin d'annuler l'interaction entre gaussiennes :

$$U^G = \frac{1}{2}\sum_{k\neq 0}\sum_{i=1}^{N}\sum_{\substack{j=1 \\ j\neq i}}^{N}\frac{q_i q_j}{\pi L^3}\frac{4\pi^2}{k^2}e^{\frac{-k^2}{4\alpha^2}}\cos\left(\vec{k}\cdot\vec{r}_{ij}\right) \qquad (38)$$

où $k = 2\pi n/L^2$

Il est aussi nécessaire de soustraire le terme d'auto-couplage des gaussiennes :

$$U^{auto} = -\frac{\alpha}{\sqrt{\pi}} \sum_{k=1}^{N} q_k^2 \qquad (39)$$

L'expression globale du potentiel électrostatique est alors la suivante :

$$U = \frac{1}{2} \sum_{i=1}^{N} \sum_{\substack{j=1 \\ j \neq i}}^{N} \left\{ \sum_{n=0}^{\infty} q_i q_j \frac{erfc(\alpha |r_{ij} + n|)}{|r_{ij} + n|} + \sum_{k \neq 0} \frac{q_i q_j}{\pi L^3} \frac{4\pi^2}{k^2} e^{\frac{-k^2}{4\alpha^2}} cos(\vec{k} \cdot \vec{r}_{ij}) - \frac{\alpha}{\sqrt{\pi}} \sum_{k=1}^{N} q_k^2 \right\} \qquad (40)$$

La présence de la fonction exponentielle permet d'approximer cette somme sur le réseau infini par une somme finie. Le paramètre α est choisi de manière à optimiser la convergence vers 0 de $erfc(\alpha R_C)/R_C$. En pratique, on choisit α tel que U^S soit nulle à la distance du *cutoff*. Dans le cas d'un système électriquement neutre, on calcule le potentiel provenant de la distribution de charges sur le réseau sans approximation. Par contre, dans le cas d'un système chargé, on introduit un plasma uniforme de charges opposées sur tout l'espace pour que la somme *(39)* puisse converger.

Lors des simulations, nous avons utilisé la méthode *Particle Mesh Ewald (PME)*, algorithme rapide en $N \log(N)$ développé par DARDEN et PEDERSEN [38].

3.2.3.b Fonctions de Commutations

Pour gérer la coupure des termes électrostatique et VAN DER WAALS au *cutoff* il existe principalement deux méthodes. La première façon par défaut est tout simplement de tronquer les forces à zéro au delà de la distance de *cutoff*. Cette méthode entraîne une discontinuité dans le champ de force si le *cutoff* est trop petit ou devient très gourmande en temps d'exécution si le *cutoff* est très grand. L'autre moyen de faire face à cette coupure est fourni par les fonctions de commutation (ang. *switching functions*). Ces fonctions permettent un lissage doux des forces et des énergies qui tendent vers zéro a partir de la distance R_{on} jusqu'à la distance de R_{off} (*cutoff*) pour éviter toute discontinuité dans le champ de force.

Il existe différentes fonctions de commutation utilisées pour l'électrostatique et pour le terme de VAN DER WAALS. Pour l'électrostatique, la fonction d'énergie est modifiée pour devenir :

$$E_{elec}^{ij} = \frac{q_i q_j}{|\vec{r}_{ij}|} S_{elec}(|\vec{r}_{ij}|) \qquad (41)$$

avec la fonction de commutation définie par :

$$S_{elec}(|\vec{r}_{ij}|) = \begin{cases} \left(1 - \frac{|\vec{r}_{ij}|^2}{{R_{off}}^2}\right)^2 & \text{si } |\vec{r}_{ij}| < R_{off} \\ 0 & \text{si } R_{off} \leq |\vec{r}_{ij}| \end{cases} \qquad (42)$$

Pour les interactions de VAN DER WAALS, la modification d'énergie s'écrit :

$$E_{vdw} = \left(\frac{A}{|\vec{r}_{ij}|^{12}} - \frac{B}{|\vec{r}_{ij}|^6} \right) S_{vdw}(|\vec{r}_{ij}|) \qquad (43)$$

où la fonction de commutation est définie par :

$$S_{vdw}(|\vec{r}_{ij}|) = \begin{cases} 1 & si\ |\vec{r}_{ij}| \leq R_{on} \\ \frac{\left({R_{off}}^2 - |\vec{r}_{ij}|^2\right)^2 \left({R_{off}}^2 + 2|\vec{r}_{ij}|^2 - 3{R_{on}}^2\right)}{\left({R_{off}}^2 - {R_{on}}^2\right)^3} & si\ R_{on} < |\vec{r}_{ij}| < R_{off} \\ 0 & si\ R_{off} \leq |\vec{r}_{ij}| \end{cases} \quad (44)$$

3.3 Minimisation de l'énergie

Afin d'éviter de générer des trajectoires aberrantes (quand les forces initiales sont trop importantes), il est nécessaire de « minimiser » (plus précisément de relaxer) l'énergie totale du système. Pour cela, nous avons utilisé le minimiseur par défaut implémenté dans NAMD qui utilise soit la méthode du *gradient conjugué* sophistiqué, soit un algorithme de recherche *de la plus grande pente*. Ces deux méthodes sont basées sur la dérivée de l'énergie potentielle U par rapport aux coordonnées de chaque atome i :

$$\vec{F}_i = -\left(\overrightarrow{grad U}\right)_{\vec{r}_i} \quad (45)$$

Chaque atome est déplacé selon la force qui s'exerce sur lui en suivant la pente de l'hypersurface énergétique (*voir Figure II.4*). Il est donc par ce biais emmené vers le minimum local le plus proche de la configuration initiale. Ceci ne permet pas, quand même, de franchir toutes les barrières d'énergie et d'arriver à converger vers le minimum absolu.

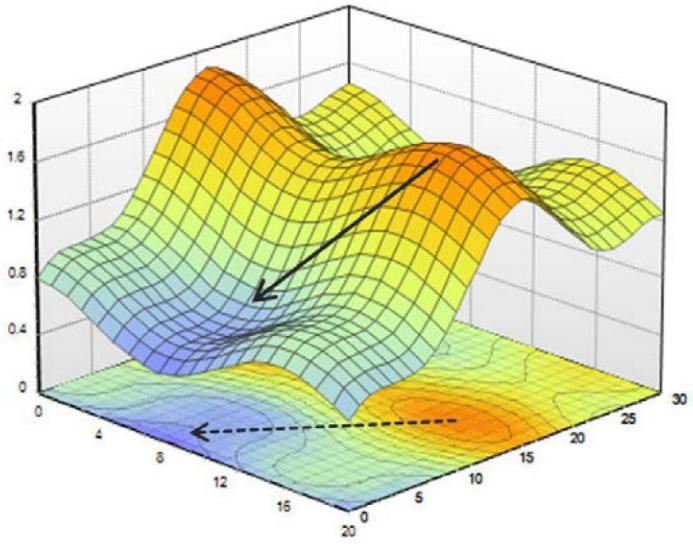

Figure II.4 Exemple de surface énergétique (source : http://www.cyber-wit.com/images/gallery/surface1_b.png)

A chaque itération k, le système de N atomes est décrit par un vecteur $\overrightarrow{X_k}$, de dimension $3N$. Si on définit une direction de descente $\overrightarrow{S_k}$ et la taille du pas de déplacement λ_k. Les coordonnées $\overrightarrow{X_{k+1}}$ à l'itération k+1 sont alors :

$$\overrightarrow{X_{k+1}} = \overrightarrow{X_k} + \lambda_{k+1}\overrightarrow{S_{k+1}} \quad (46)$$

Dans le cas de la *méthode de la plus grande pente*, la direction de pente $\overrightarrow{S_k}$ est définie par le vecteur unitaire :

$$\overrightarrow{S_k} = \frac{\overrightarrow{F_k}}{\|\overrightarrow{F_k}\|} \qquad (47)$$

Au premier pas, λ est choisi arbitrairement, puis il est augmenté (ou diminué) suivant que l'énergie potentielle U décroît (ou croît). Cette méthode est très efficace pour s'approcher très rapidement d'un minimum local. Elle est utilisée uniquement en début de minimisation.

La *méthode des gradients conjugués* converge plus doucement, mais permet d'atteindre un minimum local si l'énergie est quadratique. Dans ce cas, le gradient calculé à chaque pas est conjugué au précédent par la relation suivante :

$$\overrightarrow{S_k} = -\overrightarrow{grad U} + b_k \overrightarrow{S_{k-1}} \qquad (48)$$

où b_k est le facteur pondérant les gradients courant et précédent. La méthode des gradients conjugués est utilisée pour sélectionner les directions de recherche successives qui éliminent la minimisation répétée le long de la même direction.

3.4 Principes de la Dynamique Moléculaire classique

En Dynamique Moléculaire classique (DM) les différentes configurations du système sont générées par intégration des équations de mécanique classique de NEWTON. Le résultat de cette intégration donne les positions (trajectoires) et les vitesses des atomes au cours du temps. L'algorithme permettant une telle opération repose sur la deuxième loi de NEWTON donnant l'accélération $\vec{a}_i$ d'un atome i de masse m_i soumis à la force externe $\vec{F}_i$:

$$\vec{F}_i = m_i \times \vec{a}_i \qquad (49)$$

La force dérivant de l'énergie potentielle totale U, on obtient :

$$\vec{F}_i = -\left(\overrightarrow{grad U}\right)_{\vec{r}_i} \qquad (50)$$

La température instantanée du système T est calculée à partir de l'équation de CLAUSIUS basée sur la *théorie de l'équipartition de l'énergie* reliant l'énergie cinématique à T :

$$E_c = \sum_{i=1}^{N} \frac{1}{2} m_i v_i^2(t) = \frac{1}{2} N_{dl} k_B T(t) \qquad (51)$$

où N_{dl} est le nombre de degrés de liberté du système, k_B la constante de BOLTZMANN, v_i la vitesse de l'atome i.

3.4.1 *Résolution des équations de NEWTON : algorithme de VERLET*

La résolution d'un système couplé de grande taille n'est pas si simple. Il existe de nombreuses méthodes analytiques de résolution des équations de NEWTON [22, 39]. Toutes supposent que les

positions des atomes et les propriétés dynamiques du système (vitesses et accélérations) peuvent être développées en séries de TAYLOR sur des pas de temps d'intégration suffisamment petits :

$$\vec{r}(t+\Delta t) = \vec{r}(t) + \Delta t\vec{v}(t) + \frac{1}{2}\Delta t^2\vec{a}(t) + \frac{1}{6}\Delta t^3\vec{b}(t) + \cdots \quad (52)$$

$$\vec{v}(t+\Delta t) = \vec{v}(t) + \Delta t\vec{a}(t) + \frac{1}{2}\Delta t^2\vec{b}(t) + \frac{1}{6}\Delta t^3\vec{c}(t) + \cdots \quad (53)$$

$$\vec{a}(t+\Delta t) = \vec{a}(t) + \Delta t\vec{b}(t) + \frac{1}{2}\Delta t^2\vec{c}(t) + \cdots \quad (54)$$

où $\vec{r}$ est le vecteur des positions, $\vec{v}$ celui des vitesses et $\vec{a}$ celui des accélérations.

On peut aussi écrire un développement quasi-identique pour l'intervalle $[t-\Delta t, t]$:

$$\vec{r}_i(t+\Delta t) = \vec{r}_i(t) + \Delta t\vec{v}_i(t) + \frac{1}{2}\Delta t^2\vec{a}_i(t) + \cdots \quad (55)$$

Dans ce cas, le vecteur $\vec{r}_i$ à l'instant $(t-\Delta t)$ s'écrit :

$$\vec{r}_i(t-\Delta t) = \vec{r}_i(t) - \Delta t\vec{v}_i(t) + \frac{1}{2}\Delta t^2\vec{a}_i(t) - \cdots \quad (56)$$

Si on additionne les deux équations ci-dessus, on obtient alors :

$$\vec{r}_i(t+\Delta t) = 2\vec{r}_i(t) - \vec{r}_i(t-\Delta t) + \frac{1}{2}\Delta t^2\vec{a}_i(t) \quad (57)$$

En remplaçant l'accélération $\vec{a}_i(t)$ par son expression *(éq. 54)* on obtient l'expression de *l'algorithme de VERLET* :

$$\vec{r}_i(t+\Delta t) = 2\vec{r}_i(t) - \vec{r}_i(t-\Delta t) + \frac{\vec{F}_i}{m_i}\Delta t^2 \quad (58)$$

La particularité de cet algorithme est que l'expression des vitesses n'y apparaît pas explicitement et que le couplage de la température au temps $(t+\Delta t)$ s'effectue avec les vitesses à $(t-\Delta t/2)$:

$$\vec{v}_i(t+\Delta t) = \vec{v}_i(t) + \frac{\vec{a}_i(t) + \vec{a}_i(t+\Delta t)}{2}\Delta t \quad (59)$$

Le temps de calcul est directement lié au pas d'intégration Δt. Plus celui-ci va être « élevé » plus le temps de calcul sera court. Ce pas doit cependant rester suffisamment petit devant la période de vibration la plus faible dans le système (en général les vibrations des liaisons X-H), soit une valeur de Δt de l'ordre de 10^{-15} s = 1 fs.

En principe, l'intégration des équations de NEWTON conserve l'énergie totale du système. Ainsi, si le volume V de la boîte ainsi que le nombre d'atomes N sont maintenus constants, on génère un ensemble microcanonique (N,V,E). Souvent, durant la dynamique, il est préférable de maintenir constantes la température, ensemble (N,V,T), ou la pression, ensemble (N,P,T), plutôt que l'énergie totale. On couple alors le système à un bain thermique ou de pression. Dans ce cas la température ou la pression deviennent des variables indépendantes dont on peut choisir la valeur, comme indiqué dans les deux paragraphes suivants.

3.4.2 Contrôle de la température T

Nous avons utilisé la méthode dite de *faible couplage à un bain thermique* (ang. *weak coupling method*) développée par BERENDSEN *et coll.* [39]. Cette méthode est basée sur la modification de l'équation des mouvements des atomes afin d'obtenir une relaxation du premier ordre de la température T vers la température de référence T_0.

$$\frac{dT(t)}{dt} = \frac{1}{\tau_T}[T_0 - T(t)] \qquad (60)$$

où τ_T est le temps de relaxation de la température.

Comme la température d'un ensemble à N_{dl} degrés de liberté peut être déterminée, d'après la théorie de l'équipartition de l'énergie cinétique, par l'équation de CLAUSIUS *(51)*, le contrôle de la température du système s'effectue en adaptant les vitesses des atomes à l'aide d'un facteur de correction $\lambda(t)$:

$$\lambda(t) = \sqrt{\left[1 + \frac{\Delta t}{\tau_T}\left(\frac{T_0}{T(t)} - 1\right)\right]} \qquad (61)$$

Le paramètre de relaxation τ_T peut-être ajusté en fonction du système. Il doit être choisi suffisamment petit de manière à maintenir la température moyenne proche de T_0, mais suffisamment grand pour permettre des fluctuations.

Dans la majorité des cas, nous avons fixé la température de référence à 300 K (température expérimentale) et les temps de relaxation à 0,1 ps.

3.4.3 Contrôle de la pression P

Le contrôle de la pression s'effectue de manière analogue à celui de la température. Dans ce cas, la correction est appliquée au volume global et donc à la position des atomes. On modifie l'équation du mouvement des atomes afin d'obtenir une relaxation du premier ordre de la pression P par rapport à la pression de référence P_0 :

$$\frac{dP(t)}{dt} = \frac{1}{\tau_P}[P_0 - P(t)] \qquad (62)$$

où τ_P est le temps de relaxation de la pression.

La pression instantanée peut être obtenue à l'aide du viriel des forces θ et de l'énergie cinétique du système :

$$P(t) = \frac{2}{3V_{xyz}(t)}[E_c(t) - \theta(t)] \qquad (63)$$

où $V_{xyz}(t)$ est la taille de la boîte de simulation à l'instant t et θ est le viriel des forces :

$$\theta(t) = \frac{1}{2}\sum_{i<j} \vec{r}_{ij}(t) \cdot \vec{F}_{ij}(t) \qquad (64)$$

Ici $\vec{r}_{ij}(t)$ est la distance entre les atomes i et j et $\vec{F}_{ij}(t)$ la force d'interaction de i sur j.

La pression est modifiée par un ajustementdu volume de la boîte. Cette variation est reliée à la compressibilité isotherme κ. Le couplage s'effectue donc par ajustement de la valeur des coordonnées atomiques et de la taille de la boîte de simulation grâce à un facteur d'homothétie μ (pour la taille de boîte) et $\mu^{1/3}$ (pour les coordonnées) :

$$\mu(t) = \left[1 - \frac{\Delta t}{\tau_P'}\left(P_0 - P(t)\right)\right] \qquad (65)$$

avec $\tau_P' = \tau_p/\kappa$. Le temps de relaxation τ_P étant un paramètre adaptable, il n'est pas nécessaire de connaître la valeur de κ avec précision (dans le cas d'un liquide peu compressible, comme l'eau, κ = 4,591.10^{-4} MPa^{-1}).

Pour nos calculs à pression constante, nous avons choisi une pression de référence P_0 de 1 bar et un temps de relaxation τ_P de 0,1 ps.

3.5 Dynamique sous contraintes

L'application de contraintes dans les simulations de DM peut souvent aider à raccourcir les temps de calcul mais peut aussi entraîner des complications et des erreurs de calculs. Pour que la dynamique sous contraintes soit physiquement raisonnable et valable, il faut considérer plusieurs aspects. Les fréquences des degrés de liberté « gelés » doivent être (considérablement) plus grandes que les autres pour permettre une augmentation notable du pas d'intégration Δt. Il faut également s'assurer que ces degrés de liberté soient faiblement couplés aux autres afin de ne pas affecter le mouvement des molécules par l'application des contraintes.

3.5.1 Algorithme SHAKE

En Dynamique Moléculaire, la valeur du pas Δt est limitée par les vibrations internes de plus hautes fréquences caractérisées par des pas de temps très petits (typiquement 10^{-12} s). Pour réduire le temps de calcul des mouvements globaux du système, on peut contraire ces liaisons. Il existe de nombreux algorithmes (SHAKE, RATTLE, SETTLE ...), permettant d'appliquer des contraintes de distance. Nous avons utilisé la méthode SHAKE, illustrée par la Figure II.5.

Si l'on considère deux atomes i et j, l'expression rigoureuse de la contrainte sur leur distance est :

$$\vec{r}_{ij}^{\,2}(t) - \vec{r}_{ij}^{\,2}(0) = 0 \qquad (66)$$

où $\vec{r}_{ij}(t)$ est le vecteur instantané entre les deux atomes i et j et $\vec{r}_{ij}(0)$ la distance interatomique de référence entre ces 2 atomes.

La correction sur les positions s'effectue à chaque pas de dynamique. L'équation *(66)* est résolue par la méthode des multiplicateurs de LAGRANGE. Cependant, numériquement une telle égalité n'est généralement pas vérifiée, c'est pourquoi les équations sont résolues itérativement et le calcul

s'arrête, si l'on atteint un certain seuil de tolérance (typiquement, de l'ordre de 10^{-5} Å), ou si le nombre d'itérations est trop important, ou bien encore si le déplacement à effectuer lors du pas de contrainte est trop grand (cas d'erreur).

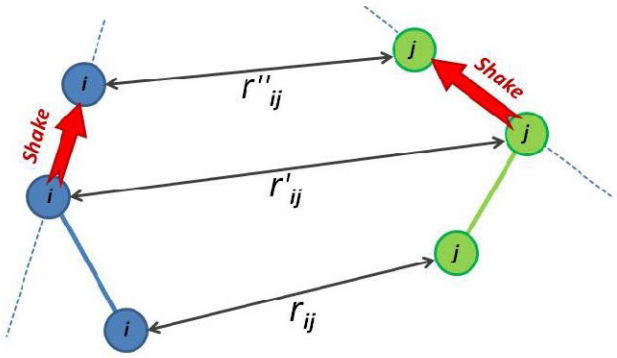

Figure II.5 Algorithme SHAKE

Le gain de temps dû à cet algorithme est appréciable dans notre cas. Le fait de passer d'une simulation sans SHAKE avec un Δt de 1 fs à une simulation avec SHAKE et un Δt de 2 fs a permis de réduire pratiquement de moitié le temps de calcul. En pratique, nous avons appliqué l'algorithme SHAKE à toutes les liaisons faisant intervenir des atomes d'hydrogène.

3.5.2 *Conditions périodiques*

Les conditions périodiques sont utilisées afin d'éviter les effets de bord tout en ayant un système contenant un nombre fini de particules [22].

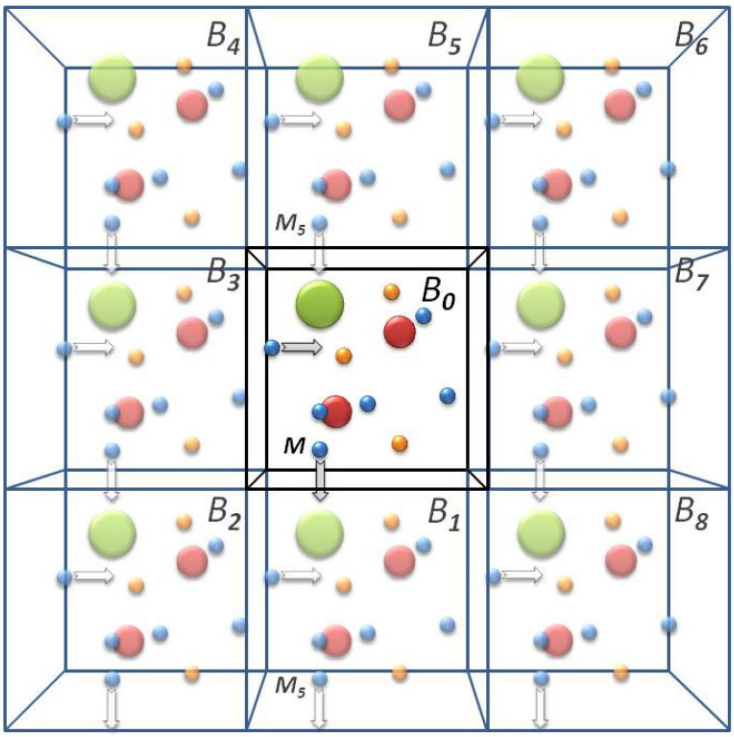

Figure II.6 Périodicité de la boîte suivant 2 dimensions

Les atomes du système simulé sont introduits dans une boîte parallélépipédique entourée de 26 boîtes identiques, images l'une de l'autre par translation de la boîte initiale (B_0) dans les trois directions de l'espace. Elles forment un parallélépipède de trois boîtes de côté (*voir Figure II.6*). Ainsi les molécules proches des bords de la boîte centrale sont entourées de molécules de solvant de la même manière qu'une molécule se trouvant au centre de la boîte. Pour qu'un atome A_0 n'interagisse avec aucune de ses images A_i ou simultanément avec un atome B_0 et l'une de ses images B_i, il faut que les dimensions R_x, R_y et R_z de la boîte centrale soient supérieures au double de la valeur du *cutoff*, augmentées de la taille des résidus.

Lorsqu'une molécule M sort de la boîte centrale B_0, et pénètre dans une boîte voisine B_1, elle est aussitôt remplacée dans la boîte B_0 par son image M_5 provenant de la boîte B_5. Ce processus s'applique à l'ensemble des 27 boîtes images (en 3D).

Il faut noter que la taille de la boîte centrale doit rester suffisamment grande afin d'éviter les effets de bord dont les conséquences sont dramatiques. Dans notre cas, la taille standard est de 100 Å de côté.

4 Dynamique Moléculaire « Gros Grains »

Un des principaux problèmes en suspens dans les sciences biologiques est l'écart entre l'échelle de temps et de longueur qu'il existe entre les simulations numériques et les expériences effectuées sur des systèmes biologiques. L'observation expérimentale non-invasive de ces processus dynamiques serait grandement appréciée pour comprendre comment fonctionne la vie. Cependant, les techniques expérimentales habituelles ne donnent pas la bonne résolution moléculaire et surtout regardent des temps généralement longs. Nous avons vu précédemment que des méthodes comme la DM, permettent la description des systèmes biologiques avec une vue tout-atomes. Toutefois, jusqu'à présent, ces approches sont limitées à des temps de simulation inferieurs à 100 ns et des tailles de systèmes de moins de 10 nm, respectivement. Une manière d'étendre la modélisation moléculaire et de combler l'écart avec les techniques expérimentales est d'utiliser la méthode de « gros grains » (ang. *coarse-grain*) [40-42]. On représente le système par un nombre réduit (en comparaison avec une description tout-atomes) de degrés de liberté, en particulier en substituant quelques atomes par un seul nouveau site avec le moins d'interactions possibles. En raison de la réduction des degrés de liberté et de l'élimination des détails d'interactions fines, la simulation du système en gros grains requiert bien moins de ressources. Elle est donc plus rapide que celle du même système représenté en tout-atomes. En conséquence, une augmentation des ordres de grandeur dans le temps simulé et des échelles de longueur peut être atteinte. Malheureusement, suite à la description grossière du système traité, celui-ci nécessite un champ de forces spécialement

adapté [43-49]. Pour la majorité des molécules, il est encore en développement et malgré les premiers paramètres récemment proposés pour des espèces carbonés [50-51] nous ne nous sommes pas impliqués dans ce type des simulations.

5 Simulation statistiques Monte Carlo (MC)

La méthode Monte Carlo (MC), proposée en 1949 par N. METROPOLIS et S. ULAM [52], est souvent appliquée à la modélisation mathématique des processus très complexes afin de prédire les résultats en utilisant des approches statistiques. Pour prédire des moyennes correctes des observables, la sélection aléatoire des valeurs qui caractérisent le processus doit être faite soigneusement. Le tirage doit être effectué en conformité avec des règles prédéfinies pour pouvoir générer des configurations finales. Pour chacun des facteurs, un grand nombre de tirages aléatoires est effectué dans les distributions de probabilité déterminées précédemment, afin de trouver la probabilité d'occurrence de chacun des résultats. En suivant cette procédure, nous pouvons obtenir une description complète d'un processus complexe. Après avoir recueilli un nombre suffisant des tirages, les informations obtenues peuvent être comparé aux résultats expérimentaux. Nous pouvons ainsi confirmer ou nier les hypothèses, les règles et les procédures appliqués dans ce modèle statistique. La précision du résultat obtenu par cette méthode dépend de la quantité des tirages et de la qualité du générateur de nombres aléatoires utilisés. L'augmentation du nombre d'essais n'est pas toujours sensé d'augmenter la précision du résultat, parce que le générateur possède une quantité fini de nombres aléatoires. Cette méthode est souvent utilisée dans les cas où la rapidité d'acquisition des résultats est plus importante que sa précision (par exemple pour les calculs techniques).

6 Calculs d'énergie libre dans un système classique

L'énergie libre F d'un système classique s'exprime à l'aide de la fonction de partition configurationnelle Z :

$$F = -k_B T \, ln \, Z \tag{67}$$

où :

$$Z = \int \dots \int e^{-\beta E(X)} dX \tag{68}$$

et $\beta = k_B T$. Dans l'équation *(68)*, X signifie l'ensemble des coordonnées et l'intégrale est effectuée dans l'espace de configuration du système. La différence d'énergie libre entre deux états du système, 1 et 2, a donc l'expression :

$$F_2 - F_1 = -k_B T \ln \frac{Z_2}{Z_1} \tag{69}$$

En pratique, l'intégrale dans l'équation *(68)* est remplacée par une somme sur un ensemble de configurations représentatif du système généré par la dynamique moléculaire. Pour être exact, il faudrait théoriquement réaliser le calcul des intégrales en sommant sur toutes les configurations du système possibles. Ceci est totalement impossible pour des gros systèmes. Afin de limiter les erreurs dues à un échantillonnage du système qui est toujours partiel, il existe deux méthodes pratiques de calcul des différences d'énergie libre, la méthode des perturbations et la méthode de l'intégration thermodynamique.

6.1 La méthode des perturbations

La théorie de la perturbation de l'énergie libre (ang. *Free Energy Perturbation* - FEP) est une méthode assez utilisée dans la chimie computationnelle. La méthode FEP a été présentée par R.W. ZWANZIG en 1954 [53-54].

En partant de l'équation *(68)* on obtient :

$$\frac{Z_2}{Z_1} = \frac{\int \dots \int e^{-\beta E_2(X)}\, dX}{\int \dots \int e^{-\beta E_1(X)}\, dX} \qquad (70)$$

En multipliant l'intégrant du numérateur par le facteur unité $1 = e^{+\beta E_1(X)} e^{-\beta E_1(X)}$ on peut écrire :

$$\frac{Z_2}{Z_1} = \frac{\int \dots \int e^{-\beta E_2(X)} e^{+\beta E_1(X)} e^{-\beta E_1(X)}\, dX}{\int \dots \int e^{-\beta E_1(X)}\, dX} \qquad (71)$$

d'où résulte :

$$\frac{Z_2}{Z_1} = \int \dots \int e^{-\beta [E_2(X) - E_1(X)]}\, P_1(X) dX \qquad (72)$$

où P_1 est la fonction de probabilité de Boltzmann. Alors l'équation *(71)* devient :

$$\frac{Z_B}{Z_A} = \langle e^{-\beta \Delta E(X)} \rangle_1 \qquad (73)$$

Ici l'indice 1 indique que la moyenne est calculée dans l'état initial du système. En conclusion :

$$\Delta F = -k_B T \ln \langle e^{-\beta \Delta E(X)} \rangle_1 \qquad (74)$$

et

$$\Delta F = -k_B T \ln \langle e^{+\beta \Delta E(X)} \rangle_2 \qquad (75)$$

Cette approche sera précise seulement si les états 1 et 2 sont très proches l'un par rapport à l'autre. Dans le cas contraire, il est généralement nécessaire de diviser une perturbation dans une série de petites « fenêtres », qui sont calculées de manière indépendante. Le calcul peut être effectué en plusieurs pas en utilisant une coordonnée λ de dosage des deux états. La variation d'énergie libre est obtenue ensuite par l'addition des contributions de chaque pas :

$$\Delta F = \sum_{i=0}^{n-1} \Delta F_i(\lambda_i \rightarrow \lambda_{i+1}) \qquad (76)$$

Comme il n'y a pas de nécessité d'une communication constante entre la simulation pour une fenêtre et l'autre, le processus peut être trivialement parallélisé en exécutant chaque fenêtre dans un processeur différent.

Les calculs FEP sont souvent utilisés pour étudier l'énergie des liaisons (ang. *binding energy*), les prévisions de pKa, l'effet de solvant sur les réactions et les réactions enzymatiques, pour lesquels le ΔG obtenu est une « mutation » d'une molécule vers l'autre. On obtient souvent une carte d'énergie libre le long d'une ou des plusieurs coordonnées de réaction. Cette carte d'énergie libre est également connue comme le potentiel de force moyenne (ang. *Potential Mean Force* – PMF) [55]. Le PMF présente un intérêt particulier lorsque la coordonnée choisie est la coordonnée de réaction : dans ce cas le profil obtenu peut être vu comme une moyenne effectuée sur tous les chemins de réaction possibles. Cela ne doit pas être confondu avec le chemin de réaction le plus probable, qui correspond à la barrière d'énergie minimum.

6.1.1 *Umbrella Sampling*

L'efficacité de l'échantillonnage peut être augmentée en utilisant une technique appelée *Umbrella Sampling*. C'est une technique de calcul d'énergie libre suggérée par TORRIE et VALLEAU en 1977 [56]. Cela concerne surtout les endroits où une barrière d'énergie sépare deux régions de l'espace de configuration. Dans ce cas, l'échantillonnage est très pauvre car la probabilité de surmonter la barrière de potentiel est faible et peut laisser de coté bon nombre de configurations inaccessibles. Dans ce cas, le système est forcé d'évoluer au voisinage d'une certaine valeur, ξ_c, de la coordonnée de réaction par l'ajout d'une contrainte harmonique :

$$U(\xi) = \frac{1}{2} K(\xi - \xi_c)^2 \qquad (77)$$

Plusieurs fenêtres d'échantillonnage sont alors générées en modifiant la valeur de la contrainte K. Les effets des contraintes sont corrigés dans le traitement final des résultats. Dans la limite d'une contrainte infinie forte cette méthode est équivalente à l'intégration thermodynamique. La technique *Umbrella Sampling* est généralement utilisée pour le calcul de la variation d'énergie libre associée à un changement des coordonnées de position. Elle peut également être utilisée pour une transformation chimique où les coordonnées chimiques sont traitées comme des variables dynamiques.

6.2 La méthode de l'intégration thermodynamique

La méthode de l'intégration thermodynamique (ang. *Thermodynamic Integration* – TI) peut être appliquée même dans le cas où les deux états, 1 et 2, sont très différents. Dans cette méthode, le

calcul est basé sur des simulations de dynamique moléculaire effectuées pour des systèmes hybrides dont l'énergie est une combinaison des énergies des deux états, 1 et 2. Le mélange des deux états est dosé à l'aide d'un paramètre λ qui peut varier entre 0 et 1. Dans le cas le plus simple d'un mélange linéaire on peut écrire :

$$E(X,\lambda) = (1-\lambda)E_1(X) + \lambda E_2(X) \qquad (78)$$

Formellement, la différence d'énergie libre entre les deux états s'exprime alors de la manière suivante :

$$F_2 - F_1 = F(2) - F(1) = \int_0^1 \frac{\partial F(\lambda)}{\partial \lambda} d\lambda \qquad (79)$$

Les équations *(67)*, *(68)* et *(78)* conduisent à la relation :

$$\frac{\partial F(\lambda)}{\partial \lambda} = \langle \frac{\partial E(X,\lambda)}{\partial \lambda} \rangle_\lambda \qquad (80)$$

La notation $\langle\ \rangle_\lambda$ représente une moyenne effectuée sur l'ensemble statistique des configurations d'un système hybride de paramètre d'ordre λ donné.

Afin d'évaluer par voie numérique l'intégrale intervenant dans l'équation *(79)*, plusieurs simulations de dynamique moléculaire sont effectuées pour différentes valeurs de λ situées dans l'intervalle [A,B]. La variation de l'énergie libre est alors obtenue en utilisant la relation :

$$F_2 - F_1 = \sum_i \langle \frac{\partial F(\lambda)}{\partial \lambda} \rangle_{\lambda_i} \Delta\lambda_i \qquad (81)$$

Dans le cas d'une combinaison linéaire d'énergies *(éq. 78)* on peut écrire :

$$\frac{\partial F(\lambda)}{\partial \lambda} = \langle E_2(X) - E_1(X) \rangle_\lambda \qquad (82)$$

donc :

$$F_2 - F_1 = \sum_i \langle E_2 - E_1 \rangle_\lambda \Delta\lambda_i \qquad (83)$$

6.2.1 Adaptive Biasing Force (ABF)

Le principe de la méthode ABF proposé en 2001 par DARVE et POHORILLE [57] consiste à modifier le potentiel au cours de la simulation, afin d'éliminer les caractéristiques de la dynamique métastable simple, tout en se rapprochant de l'énergie libre. Le lien entre la dérivée de l'énergie libre par rapport au paramètre d'ordre et les forces exercées sur celui-ci peut être écrit comme :

$$\frac{\partial F(\lambda)}{\partial \lambda} = \langle \frac{\partial V(X)}{\partial \lambda} \rangle_\lambda - \frac{1}{\beta} \langle \frac{\partial\, ln\, X}{\partial \lambda} \rangle_\lambda = -\langle \mathbb{F}_\lambda \rangle_\lambda \qquad (84)$$

Le premier terme correspond à des forces physiques exercées sur le système, qui sont les dérivées de la fonction d'énergie potentielle $V(X)$. La seconde contribution est une correction purement géométrique qui tient compte des différences de disponibilité de l'espace de phase quand le

paramètre d'ordre λ varie. Contrairement à sa composante instantanée, $\mathbb{F}_\lambda$, seulement la force moyenne, $\langle \mathbb{F}_\lambda \rangle_\lambda$ est physiquement significative.

Dans le cadre de la méthode ABF la force $\mathbb{F}_\lambda$ est accumulée dans de petites fenêtres ou des *bins* de taille finie, $\delta\lambda$, fournissant ainsi une estimation de la dérivée $\frac{\partial F(\lambda)}{\partial \lambda}$ défini dans l'équation *(84)*. La force appliquée le long du paramètre d'ordre λ afin de surmonter les barrières d'énergie libre est défini comme suit :

$$\mathbb{F}^{ABF} = -\langle \mathbb{F}_\lambda \rangle_\lambda \nabla_\lambda \lambda \qquad (85)$$

La force biaisée (ang. *biasing force*) $\mathbb{F}^{ABF}$, introduite dans les équations du mouvement, garantie que pour le paramètre λ donnée, la force qui agit tout le long du paramètre d'ordre moyenne à zéro au fil du temps. L'évolution du système est donc régie principalement par ses propriétés d'autodiffusion.

Une caractéristique particulière de la force instantanée, est sa tendance à fluctuer de façon significative. En conséquence, au début d'une simulation de l'ABF, la moyenne accumulée pour chaque coordonné de réaction prend généralement les valeurs grandes et inexactes. Dans ces circonstances, l'application de la force biaisée peut gravement perturber la dynamique du système, en déplaçant artificiellement la moyenne acquise, et, par conséquent, entraver la convergence. Pour éviter ces effets indésirables, aucune force de contrainte n'est appliquée jusqu'à ce qu'un nombre raisonnable d'échantillons soient recueillies. Lorsque le nombre minimal d'échantillons défini par l'utilisateur est atteint, la force de contrainte est introduite progressivement, sous la forme d'une rampe linéaire. Pour une efficacité optimale, ce nombre minimal d'échantillons doit être ajusté sur une base dépendante du système.

En outre, pour atténuer les effets préjudiciables causés par les variations brusques de la force, les fluctuations correspondantes sont lissées, en utilisant une moyenne pondérée. Il est cependant crucial de vérifier que le profil d'énergie libre varie régulièrement dans l'intervalle, sur laquelle la moyenne est effectuée. Pour obtenir un échantillonnage adéquat dans les temps de simulation raisonnable, il est recommandé de séparer les voies d'une longue coordonné de réaction en intervalles consécutifs plus courtes. En contraste avec les méthodes probabilistes, l'ABF n'exige pas que ces fenêtres se chevauchent en vertu de la continuité de la force dans la voie de la réaction.

6.3 Linear Interaction Energy (LIE)

Cette simple méthode de quantification d'énergie libre des liaisons a été proposée initialement par AQVIST *et coll.* [58-59] pour étudier le blocage des canaux ioniques par les ions ammonium comme le tetraethylammonium (TEA) ou par des anesthésiant locaux. L'approche est basée sur une

estimation des différences entre deux simulations de la DM, l'une (l'état 1) avec le ligand libre dans son environnement et l'autre (l'état 2) où le ligand est lié à la protéine.

La moyenne de l'énergie libre de liaison est calculée comme suit :

$$\Delta G = \alpha\left(\langle V_{\ell-e}^{VdW}\rangle_{bind} - \langle V_{\ell-e}^{VdW}\rangle_{free}\right) + \beta\left(\langle V_{\ell-e}^{el}\rangle_{bind} - \langle V_{\ell-e}^{el}\rangle_{free}\right) \qquad (86)$$

où ΔG est l'enthalpie libre de liaison, $V_{\ell-e}^{VdW}$ et $V_{\ell-e}^{el}$ sont les interactions ***ℓ***igand- ***e***nvironnement de Lennard-Jones et de Coulomb. Les indices *free* et *bind* décrivent la valeur du potentiel pour le ligand libre ou lié. α et β sont des facteurs empiriques qui permettent d'ajuster le résultat pour s'approcher au mieux des valeurs expérimentales et sont calculés d'après des règles bien définies en fonction du type de molécules impliquées [60-61]. Très souvent $\alpha = 0{,}18$ et β prend une valeur proche de $0{,}50$.

III Nanostructures de Carbone

Le carbone est un élément de base, présent sur toute la terre, qui peut s'organiser au niveau moléculaire pour donner aux matériaux des propriétés physiques uniques. Le graphite est un élément très conducteur et relativement mou (comme en atteste la « solidité » réduite des mines de crayons de papier par exemple) alors que le diamant, lui aussi composé de carbone, est un isolant extrêmement dur. Depuis très longtemps, ces matériaux massifs sont utilisés en médecine pour leurs propriétés mécaniques et pour leur excellente biocompatibilité.

Parmi les formes de carbone découvertes récemment en nanosciences, il en existe de très originales et de très stables d'un point de vue chimique et thermique. Les plus connues sont les fullerènes C60 semblables à un ballon de football et construit à partir de 60 atomes de carbone. Les formes plus allongées et cylindriques, découvertes en 1991, sont appelés nanotubes. Les nanotubes de carbone (CNT) et les fullerènes présentent aussi des propriétés chimiques et électroniques exceptionnelles. Ils ont des résistances mécaniques remarquables malgré leur formidable légèreté. Ces caractéristiques ont mené les scientifiques à proposer bon nombre d'applications et ce, dans des domaines variés, allant de l'électronique (nouveaux transistors), la mécanique (nouvelles fibres pour les raquettes de tennis), la chimie (nouveaux catalyseurs) et jusqu'au domaine biomédical [62]. Dans ce dernier, il s'agit de mettre au point des bio-détecteurs, de délivrer des médicaments et des vaccins ou d'élaborer de nouveaux matériaux biocompatibles, tels que les polymères renforcés. Cependant, avant que de tels matériaux puissent être incorporés avec succès aux implants biomédicaux, ou que des médicaments ou des vaccins puissent être véhiculés par des CNT ou des fullerènes, la biocompatibilité et la toxicité de ces espèces doivent être établies [63]. Malgré cela, les nanostructures de carbone méritent une grande considération pour différentes applications thérapeutiques, notamment comme vecteurs pour le traitement anticancéreux local ciblé.

1 Description moléculaire

1.1 Fullerène C60

Les C60 – buckminsterfullerène ou buckyball - comportent 60 atomes de carbone dans une structure analogue à un « ballon de football ». Dans cette structure les atomes de carbone forment une coque comportant 20 hexagones et 12 pentagones. Cette proportion est requise pour assurer l'équilibre de la boule. Les 12 pentagones doivent être obligatoirement présents pour tenir la

structure en coquille fermée faite à partir d'un plan d'atomes de carbone disposés en nid d'abeilles hexagonale. De plus gros fullerènes existent (C70, C82, etc.) et ont des structures similaires contenant aussi 12 pentagones nécessaires à la fermeture, mais un nombre différent d'hexagones.

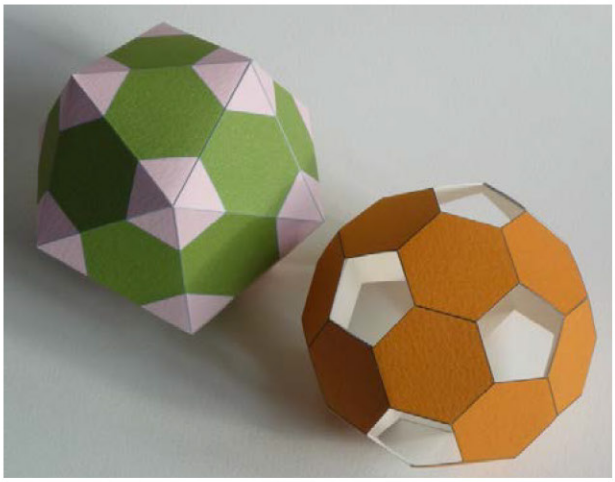

Figure III.1 Icosaèdre (à gauche) et icosaèdre tronqué (à droite)
(source : http://leblogdeclaudelothier.blogspot.com/2009_05_01_archive.html)

Pour illustrer la structure cristalline du C60, il suffit de considérer un icosaèdre tronqué par un processus de coupure qui coupe chacun des 12 sommets (*voir Figure III.1*). Chaque sommet est remplacé par un pentagone. Ce processus convertit également chacune des 20 faces triangulaires en cycle à six carbones (hexagones). Dans la structure proposée, chacun des sommets de l'icosaèdre tronqué est occupé par un atome de carbone et chaque carbone a une triple coordination, similaire à la coordination dans le graphite à l'exception de la courbure introduite par les pentagones dans le réseau. Cette structure particulière des C60 est normalement extraite de la suie produite par l'arc électrique entre deux électrodes de graphite. Cette suie ne contient que de très petites fractions de fullerènes. L'extraction se fait alors en utilisant des solvants organiques dans lesquels les fullerènes sont solubles.

1.2 Nanotubes de carbone (CNT)

Les nanotubes de carbone (CNT) sont des cylindres nanométriques construits à partir de plans d'atomes de carbone à l'hybridation sp^2. Les nanotubes de carbone sont dérivés de feuilles de graphène sans défaut qui sont enroulées en tubes [64-65]. Les nanotubes fermés sont terminés par des extrémités faites de fullerènes avec six pentagones aux deux extrémités. Les propriétés uniques mécaniques et électriques de ces nanotubes de carbone sont directement liées aux caractéristiques du réseau de carbone et à l'organisation des atomes dans le réseau tubulaire. Les nanotubes se distinguent par le nombre de couches qui composent leurs parois cylindriques : les nanotubes à paroi simple (SWNT) et les nanotubes multi-parois (MWNT). La Figure III.2 présente des modèles et des

images de SWNT et de MWNT obtenues par microscopie électronique à haute résolution (HRTEM). Le long de l'axe du tube, les nanotubes de carbone montrent d'excellentes propriétés de résistance mécanique dues à la nature de la forte liaison C-C et de la structure sans défaut. La propriété la plus intrigante des CNT vient de leur structure électronique particulière. Selon le diamètre et la chiralité des tubes, les nanotubes de carbone peuvent être soient métalliques, soient semi-conducteurs avec une bande interdite (ou « gap ») variable. Ils montrent aussi une bonne conductivité thermique et une grande stabilité chimique.

Il existe de nombreuses méthodes de synthèse de préparation des CNT. Les trois techniques principales pour la synthèse des deux types de nanotubes de carbone sont la méthode de décharge électrique (l'arc électrique), l'ablation laser (vaporisation sous laser pulsé) et la CVD (dépôt chimique en phase vapeur).

En raison de leur incroyable panel de propriétés, les nanotubes de carbone sont des matériaux prometteurs pour diverses applications et ont été proposés pour intervenir dans des dispositifs pour la nanoélectronique, pour le stockage d'énergie, pour les nano-capteurs, et bien d'autres encore. Une description détaillée de cet aspect peut être trouvée dans les Refs. [64-66]. Vue la portée de cette thèse, nous ne donnerons ici qu'un bref aperçu de l'utilisation des nanotubes dans le domaine biomédical.

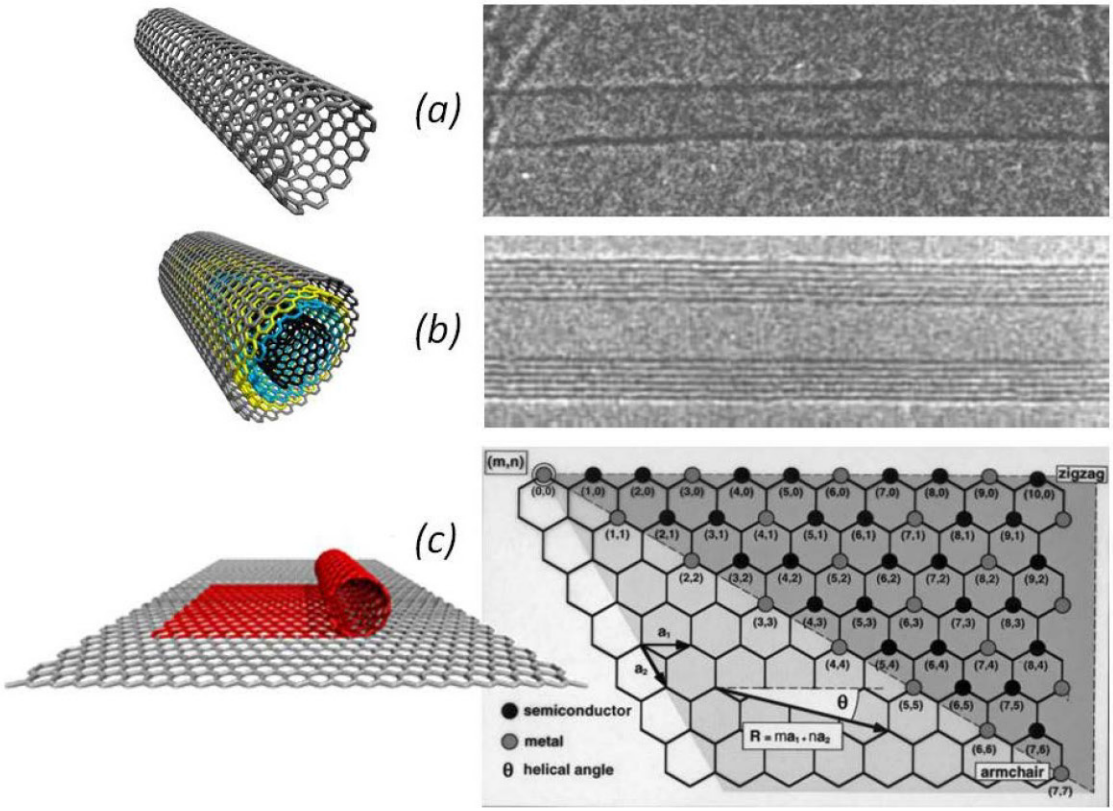

Figure III.2 Structures de nanotubes de carbone. (a) SWNT, modèle à gauche et image HRTEM à droite. (b) MWNT, modèle à gauche et image HRTEM à droite. (c) Les indices pour différents types d'enroulement sont spécifiques selon la nature des CNT (semi-conducteurs ou métalliques). (Images de droite d'après AJAYAN [64])

2 Utilisation des CNT dans le domaine biomédical

2.1 Utilisation des CNT pour l'imagerie et le diagnostic

Comme les CNT sont très fins et relativement longs, ils peuvent être utilisés comme pointe dans les microscopes à champ proche. L'avantage de la pointe faite d'un nanotube repose sur sa structure ordonnée mais surtout sur sa finesse et donc sa capacité à imager des objets qui sont presque impossibles à voir avec les meilleures pointes métalliques. Un bel exemple est montré sur la Figure III.3, où un MWNT attaché à l'extrémité d'une pointe de microscope-sonde à balayage peut servir pour l'imagerie des biomolécules [67]. Grâce à cela, des molécules biologiques telles que les immunoglobulines M (IgM) ont pu être facilement imagées à une résolution très élevée en utilisant des nanotubes à la place des pointes. Les pointes à MWNT et à SWNT ont été aussi utilisées en mode « tapping » pour imager des molécules biologiques telles que l'amyloïde-β-protofibrilles (lié à la maladie d'Alzheimer) avec une résolution jamais atteinte auparavant [67].

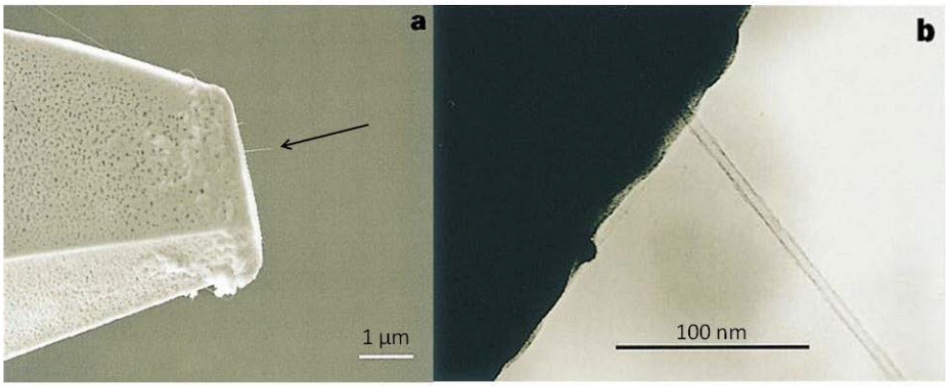

Figure III.3 Pointe faite de MWNT déposé avec la méthode CVD. (a) Les nanotubes ont grandi à partir d'une structure poreuse déposée directement sur la pointe. (b) Zoom sur l'assemblage pointe-CNT (Images d'après HAFNER *et coll.* [67])

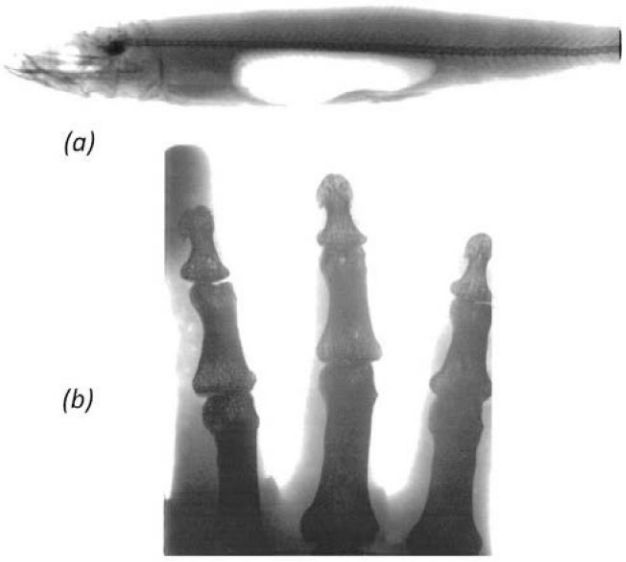

Figure III.4 Images obtenues par rayonnement X (a) d'un poisson et (b) d'une main humaine à l'aide d'une source basée sur des CNT (Images d'après YUE *et coll.* [68])

Un autre exemple lié à l'imagerie médicale est le rayonnement X provenant des nanotubes [68]. L'intensité des rayons X générés par cette source est suffisante pour imager des zones minces (*voir Figure III.4*). L'appareil peut facilement produire à la fois des rayons X continus et pulsés avec une forme d'onde et des fréquences programmables. Les rayons X pulsés avec une fréquence supérieure à 100 kHz ont été facilement atteints. La technologie des rayons X à cathode froide basée sur des CNT peut donc potentiellement conduire à des sources de rayons X portables et miniaturisées pour des applications industrielles et médicales dans le futur.

2.2 Utilisation des CNT pour les biocapteurs

Les nanotubes de carbone peuvent être également utilisés pour détecter des espèces chimiques. Ils permettent aussi de surveiller l'activité chimique comme les processus enzymatiques. La détection de molécules comme des protéines s'attachant à la surface externe des CNT a déjà été effectuée [69]. La Figure III.5 illustre l'utilisation des SWNT semi-conducteurs comme biocapteurs polyvalents [70]. L'attachement contrôlé des enzymes redox de glucose-oxydase (GOx) sur la paroi latérale d'un nanotube induit un changement net de la conductance. Les tubes recouverts des enzymes agissent comme un capteur de pH car de grands changements réversibles de la conductance sont observés lorsque le pH est modifié. Après l'addition de glucose, la réponse peut être même surveillée en temps réel, ce qui indique que le capteur est capable de mesurer l'activité enzymatique même à l'aide d'un seul nanotube. Cette démonstration de biocapteurs basés sur des nanotubes fournit donc un nouvel outil pour les études enzymatiques et ouvre la voie à des diagnostics biomoléculaires.

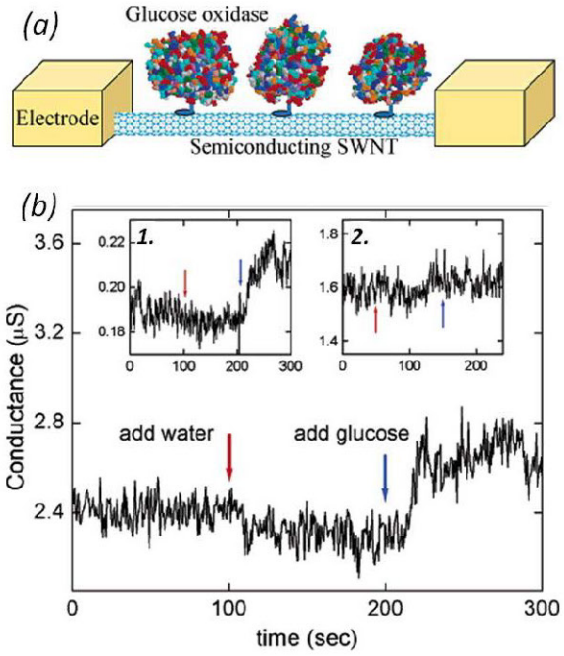

Figure III.5 (a) Schéma de deux électrodes liant un SWNT semi-conducteur avec des enzymes GOx adsorbées sur sa surface. (b) Mesure de la conductance en temps réel dans l'eau purifié et déionisé (Milli-Q®). (b.1) La même mesure sur un second dispositif où la conductance est 10 fois inférieure. (b.2) Les mêmes mesures mais sans GOx (Image d'après BESTEMAN *et coll.* [70])

2.3 Utilisation des CNT pour la distribution des médicaments

Les technologies de libération de médicaments sont généralement protégées par des brevets décrivant les méthodes de formulation qui modifient le profil de libération du médicament, l'absorption, la distribution et l'élimination au profit de l'amélioration de l'efficacité du produit et la sécurité, ainsi que le confort des patients et la conformité au loi. Il existe des méthodes de livraison reconnues incluant les voies non-invasives orales (par la bouche), transcutanées (par la peau), transmuqueuses (nasale, buccale/sublinguale, vaginale, oculaire ou rectale) et par inhalation. Beaucoup de médicaments tels que des peptides et des protéines, des anticorps, des vaccins et des médicaments à base de gènes, ne peuvent cependant pas être distribués en utilisant ces voies parce qu'ils pourraient être sensibles à la dégradation enzymatique ou parce qu'ils ne peuvent pas être absorbés efficacement en raison de leur taille moléculaire et de la charge qu'ils présentent, nécessaire à l'efficacité thérapeutique. Pour cette raison, de nombreuses protéines et peptides médicamenteux doivent être administrés par injection. Par exemple, l'administration de vaccins basés sur des protéines étant antigènes de surface, est toujours réalisée par injection.

De plus, les efforts actuels dans le domaine de l'administration de médicaments concernent l'élaboration d'**administration ciblée** dans lequel le médicament est uniquement actif dans la zone cible du corps (par exemple, dans les tissus cancéreux). Elle est souvent basée sur des formulations à libération prolongée dans lesquelles le médicament est libéré sur une période de temps contrôlée par un type de formulation. Ce type de formulation à libération prolongée peut se faire à l'aide de liposomes, de microsphères biodégradables chargées en médicaments, ou avec des conjugués polymère-médicament. Très récemment les nanotubes de carbone ont aussi été proposés comme vecteurs d'administration ciblée potentiels [71].

Puisque les nanotubes de carbone présentent une solubilité importante dans les membranes biologiques (ce qui facilite la pénétration des cellules par ces agents), une des voies de recherche concerne l'utilisation des CNT afin d'améliorer la délivrance des médicaments à l'intérieur des cellules. BIANCO *et coll.* ont observé expérimentalement que les nanotubes de carbone sont en mesure d'interagir avec les membranes plasmiques et de pénétrer dans le cytoplasme sans le besoin apparent d'énergie supplémentaire pour faciliter le transport intracellulaire. Dans ces premières études, les CNT fonctionnalisés ont été en mesure de faciliter le transport de plasmide d'ADN (*pDNA*) intracellulaire [72-73]. Un autre exemple prometteur concerne l'encapsulation de molécules anticancéreuses comme le cisplatine par des agents ciblant spécifiquement les membranes cellulaires cancéreuses [74-75]. Ce composé est reconnu comme un des produits majeurs de la chimiothérapie anticancéreuse courante mais ne présente aucune spécificité. Les sels de platine forment des liens chimiques très forts entre les différents brins de l'ADN et à l'intérieur d'un brin

d'ADN lui-même altérant ainsi le code génétique de la cellule. C'est pour cela qu'ils doivent être administrés jusqu'à l'intérieur de la cellule et seulement aux cellules cancéreuses. Le traitement traditionnel par cisplatine s'effectue par perfusion intraveineuse en exposant toutes les cellules du patient à la réactivité de cet agent. Ceci engendre un taux important de toxicité digestive, rénale, neurologique, auditive ou même allergisante. Pour minimiser les effets indésirables et diminuer les doses administrées, la livraison ciblée du cisplatine par sa vectorisation avec des nanomatériaux pourrait donc répondre aux besoins.

2.4 Solubilité et fonctionnalisation des CNT

En général, le potentiel de bio-réactivité des nanoparticules augmente avec la diminution de taille des particules en raison de deux facteurs inhérents : (i) plus petite est la particule - plus grande est la surface par unité de masse [76-77], et (ii) la caractéristique de la surface des particules [78-79]. En vertu des applications des nanoparticules pour la délivrance des médicaments et d'imagerie, celles-ci ont été intentionnellement chimiquement recouvertes avec différents agents comme des tensioactifs, des anticorps monoclonaux, des protéines purifiées, de l'ADN ou des molécules organiques pour le ciblage spécifique des organes ou des cellules souhaitées, ou encore pour rendre ces nanoparticules biocompatibles. On parle alors de fonctionnalisation. Ces nanoparticules nouvellement conçues avec des complexes attachés à leur surface créent de nouveaux matériaux qui peuvent être plus réactifs avec les cellules vivantes, réagir différemment avec chaque type de cellules, d'hormones ou de facteurs immunitaires rencontrés dans l'organisme vivant.

Pour rendre les CNT solubles dans l'eau, on les fonctionnalise par des liaisons covalentes selon deux approches principales : (i) estérification ou amidation des tubes oxydés, ou (ii) attachement covalent sur les parois de groupes fonctionnels [80]. En ce qui concerne la première approche, le processus d'oxydation est réalisé dans des conditions fortement acides, qui provoquent l'ouverture des extrémités des CNT, générant ainsi des groupes carboxyliques, appropriés pour la fonctionnalisation suivante. Les fonctions carboxyliques sont aussi créées là où des défauts sont présents dans la paroi latérale des nanotubes. D'autre part, la fonctionnalisation directe des parois des CNT avec des groupes organiques est aussi possible en utilisant des espèces réactives, telles que les nitrènes et les carbènes. Des azotures d'alkyle, des sels d'imidazolium, et des radicaux perfluoroalkyles ont aussi été employés comme réactifs efficaces. Une autre stratégie pour fonctionnaliser des parois de nanotubes de carbone, afin d'obtenir la solubilisation, le marquage ou d'autres propriétés requises, est d'utiliser la cycloaddition dipolaire d'ylures d'azométhine [81]. Sur la Figure III.6, sont indiquées plusieurs fonctionnalisations qui rendent des nanotubes solubles ou qui offrent d'autres propriétés. Dans cette thèse, seules les amino-fonctionnelles ont été considérées (*voir Figure III.6*).

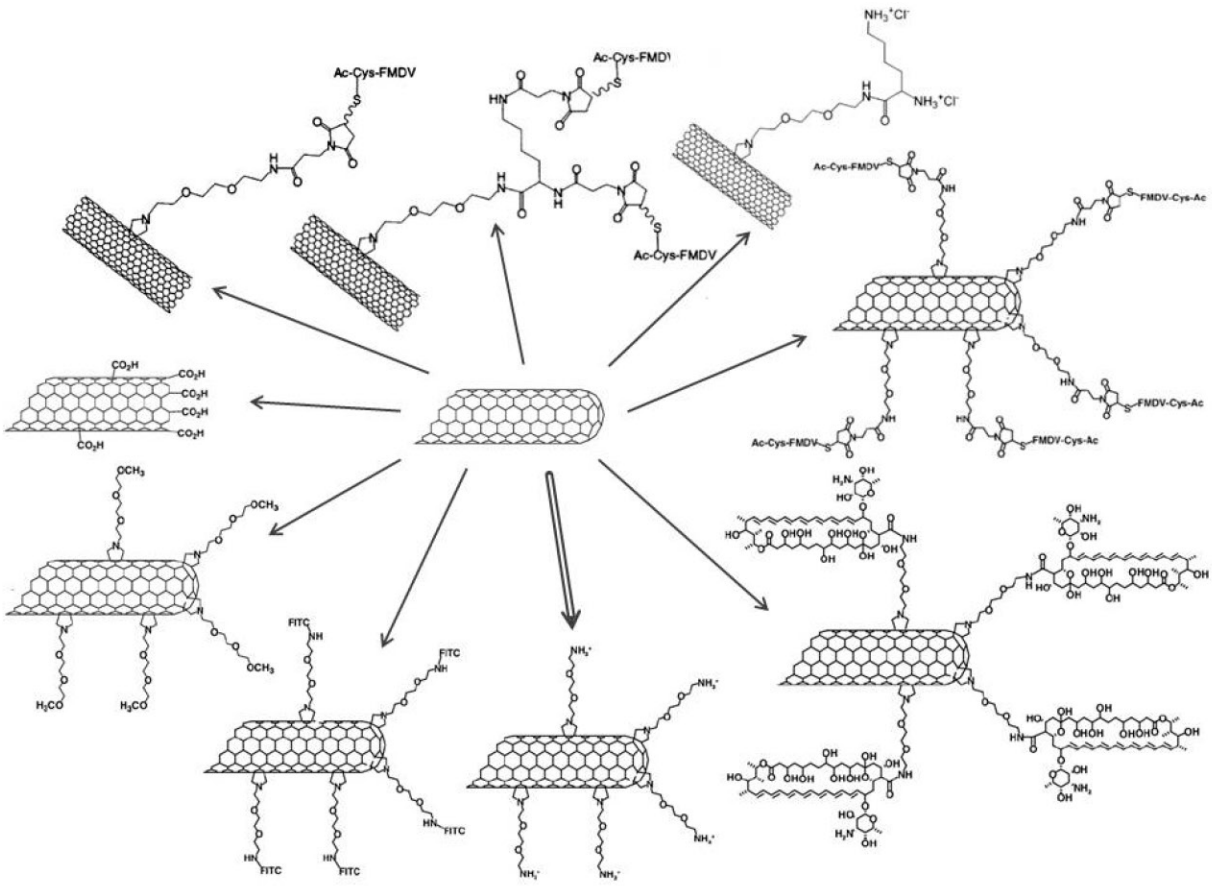

Figure III.6 Différents types de fonctionnalisations permettant aux CNT d'être solubles dans l'eau ou d'avoir des propriétés supplémentaires. La double flèche indique une amino-fonctionnelle utilisée dans cette thèse. (Images d'après A. BIANCO *et coll.* [82-84])

3 Biocompatibilité et cytotoxicité des nanostructures de carbone

3.1 Biocompatibilité des nanostructures de carbone

D'après le dictionnaire international de médecine, la biocompatibilité est la capacité d'un objet implanté dans le corps d'exister en harmonie avec les tissus sans provoquer de changements néfastes [85]. Pour être biocompatible, les vecteurs de médicaments à base de nanoparticules doivent donc non seulement ne pas provoquer de réactions inflammatoires mais aussi rester suffisamment longtemps dans l'organisme pour avoir la possibilité d'atteindre les zones cibles avant qu'ils soient reconnus comme des corps étrangers et éliminés de la circulation sanguine ou excrétés par d'autres voies. Le problème de compatibilité des fullerènes et des CNT avec l'environnement biologique a été soulevé en inspectant leurs interactions avec les cellules vivantes. Par exemple, des nanotubes fonctionnalisés semblent être biocompatibles (ne pas provoquer de réactions inflammatoires) avec les cellules du système immunitaire comme lymphocytes B, T ainsi que les macrophages [86]. L'absence de réponse immunitaire au CNT est d'une importance fondamentale en vue de leur utilisation comme un système de délivrance des antigènes. En outre, les études récentes

de la biodistribution ont montré que les CNT sont rapidement excrétés par les reins et visualisés dans l'urine [87]. Cette fonctionnalité rend donc les CNT potentiellement utiles pour diverses applications thérapeutiques.

3.2 Cytotoxicité des fullerènes

Compte tenu de leur taille nanométrique et de la facilité à les produire, les fullerènes ont ouvert des perspectives uniques dans les domaines de l'électronique, de l'optique et de la biomédecine [88]. Les premières recherches à des fins médicales ont montré le pouvoir inhibant des C60 sur les virus de l'immunodéficience humaine (VIH). En s'attachant au virus, les C60 empêchent ainsi sa réplication [89-90]. D'autres applications potentielles des fullerènes ont vu le jour [91] mais à chaque fois la question de leur toxicité a été posée. SAYES *et coll.* [92] ont démontré par exemple que les C60 avaient une cytotoxicité significative sur des cellules de culture de tissus *in vitro*, alors que les fullerènes très hydroxylés, $C60(OH)_{24}$, n'ont produit aucune preuve de cytotoxicité dans les mêmes conditions. Plus récemment encore, les mêmes auteurs ont rapporté que la cytotoxicité causée par les C60 était due à la peroxydation lipidique des membranes cellulaires (des membranes non-mitochondriales) dans des fibroblastes dermiques humains, des cellules de carcinome du foie humain (HepG2), et des astrocytes neuronaux après 48 heures d'exposition [93]. OBERDORSTER [94], de même, a signalé le stress oxydatif et la peroxydation des lipides des tissus du cerveau après une exposition aux fullerènes, ainsi que la translocation de nanoparticules tout au long des neurones du système nerveux central. En dépit d'une utilité potentielle des fullerènes il n'y a pas d'applications pratiques à l'heure actuelle compte tenu de cet aspect toxique. Toutefois, des modifications chimiques apportées aux fullerènes pourraient finalement aboutir à leurs applications dans les domaines pharmaceutiques et biochimiques [95].

3.3 Cytotoxicité des nanotubes

De la même manière que les fullerènes, la question de toxicité des tubes vis-à-vis des cellules vivantes doit être posée. Si les nanotubes de carbone doivent être utilisés pour administrer le médicament ou être utilisés pour l'imagerie, la compréhension de la réponse des cellules aux nanomatériaux est essentielle. Les deux types de cellules sanguines phagocytaires (les macrophages, les monocytes, les neutrophiles) et non-phagocytaires (les lymphocytes, les érythrocytes) et les plaquettes participent à la reconnaissance de corps étrangers dans le sang, et pourraient donc constituer un obstacle majeur au transport des nanoparticules via le système circulatoire. Les premières informations de biocompatibilité des CNT sont assez controversées. Ils existent des études *in vitro* effectuées sur des cellules immunitaires, des cellules neuronales et des ostéoblastes [86] et sur des canaux ioniques [96] démontrant que les CNT ne sont pas toxiques. Néanmoins, les réactions

inflammatoires au niveau des poumons de certains rongeurs ont été constatées [97-99]. MATTSON *et coll.* [100] ont montré que les nanotubes de carbone peuvent inhiber la croissance de neurones embryonnaires du cerveau d'un rat. Une cytotoxicité similaire a été signalée dans les kératinocytes exposés à des SWNT [101-102]. CUI *et coll.* [103] ont trouvé des preuves de l'altération de la régulation des gènes dans les cellules rénales embryonnaires humaines (HEK293) induite par une exposition à SWNT. MONTEIRO-RIVIERE *et coll.* [104] ont rapporté que les cytokines pro-inflammatoires ont été libérées de kératinocytes humaines incubées avec des MWNT, similairement aux résultats des autres en utilisant les mêmes cellules exposées aux SWNT [101]. BOTTINI *et coll.* [105] ont étudié la toxicité des MWNT purs (hydrophobes) et oxydés avec les lymphocytes T humains. Bien que ces cellules sanguines soient très sensibles aux corps étrangers, les MWNT hydrophobes sont moins toxiques que les MWNT oxydés. Ces MWNT oxydés induisent visiblement une perte significative de la viabilité cellulaire (apoptose) à des doses de 400 $\mu g.ml^{-1}$ (10 millions des CNT par cellule). Il apparaît que la toxicité de ces MWNT dans ces études ne dépende pas seulement du temps d'exposition et de la concentration, mais aussi du type de cellules utilisé, ainsi que des caractéristiques de surface des nanotubes. Comme mentionné dans la plupart des études décrites précédemment, en réduisant les temps d'exposition et en utilisant de concentrations plus faibles des nanoparticules de carbone, on réduit la cytotoxicité [105].

IV Cibles étudiées

1 Membrane cellulaire

1.1 Propriétés générales

La membrane cytoplasmique est une partie de la cellule qui entoure directement le cytoplasme. Elle est peut-être la structure la mieux conservée dans toutes les cellules vivantes. Chaque être vivant a un certain type de membrane. Les membranes sont des structures minces, mesurant environ 8 nm d'épaisseur. Elles sont des barrières fonctionnelles de la cellule, qui séparent l'intérieur de celle-ci du monde extérieur. Les membranes cellulaires sont composées majoritairement de phospholipides et de protéines. Cette structure permet aux cellules de communiquer sélectivement avec leur environnement. Les membranes sont très organisées avec des géométries généralement asymétriques. Les deux surfaces qui les composent ont des topologies et des fonctions différentes. Les membranes sont également très dynamiques, s'adaptant constamment à l'évolution des conditions environnementales.

1.2 Structure des composants de la membrane

1.2.1 Lipides

Les phospholipides de la membrane contiennent un groupe chargé ou polaire (souvent un groupe phosphate) attaché à un glycérol contenant 3 carbones dans sa chaîne. Deux chaînes d'acides gras attachées aux autres carbones du glycérol complètent la molécule. Un côté de la molécule est hydrophile (côté phosphate) et l'autre hydrophobe (côté chaînes d'acides gras).

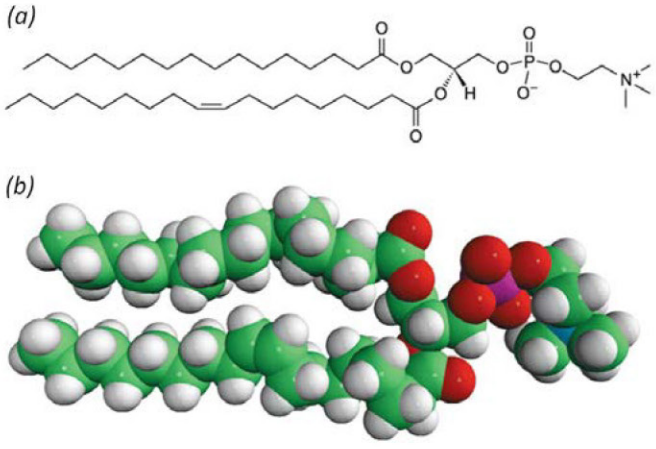

Figure IV.1 Molécule de lipide type POPC. (a) structure chimique $C_{42}H_{82}NO_8P$ et (b) vue 3D en prenant en compte le rayon de VAN DER WAALS de chaque atome constituant la molécule.

La Figure IV.1 montre la structure de la L-α-phosphatidylcholine (POPC) couramment utilisée dans nos simulations. Ces molécules s'auto-organisent entre elles pour former la bicouche lipidique de la membrane.

1.2.2 Protéines membranaires

Les membranes contiennent aussi des protéines. Généralement 20-30% d'entre elles sont peu liées, alors que 70-80% sont enfouies dans la membrane (protéines transmembranaires) (*voir Table IV.1*). Ces protéines sont aussi souvent des molécules amphipathiques (contenant à la fois des fractions hydrophobes et hydrophiles). Les acides aminés se distribuent dans la membrane de sorte que les acides aminés hydrophobes s'associent aux lipides de la membrane et les acides aminés hydrophiles se placent à l'extérieur de la membrane en interagissant soit avec le cytoplasme soit avec le périplasme.

Table IV.1 Caractérisation des protéines membranaires.

Type	***Description***	***Exemples***
Les protéines intégrales ou transmembranaires	Traversent la membrane et possèdent : - un domaine cytoplasmique hydrophile qui interagit avec les molécules de l'intérieur ; - un domaine transmembranaire hydrophobe permettant l'ancrage de la protéine dans la membrane ; - un domaine extracellulaire hydrophile qui interagit avec les molécules de l'extérieur. Le domaine hydrophobe se compose d'une ou de plusieurs α-hélices, ou d'une combinaison de α-hélices et de feuillets β.	Canaux ioniques ; Pompes à protons ; Récepteurs couplés aux protéines G
Les protéines ancrées dans les lipides	Liées de manière covalente à une ou à plusieurs molécules lipidiques. La protéine elle-même n'est pas en contact avec la membrane.	Protéines G
Les protéines périphériques	Attachées aux protéines membranaires intégrales, ou associées avec les régions périphériques de la bicouche lipidique. Ces protéines ont tendance à avoir des interactions seulement temporaires avec les membranes biologiques, et, après avoir réagi avec la molécule cible, elles se dissocient pour poursuivre les travaux dans le cytoplasme.	Certaines enzymes ; Certaines hormones

1.2.3 Stabilisation de la membrane

La membrane cytoplasmique est stabilisée par les interactions hydrophobes des liaisons hydrogène entre les lipides voisins. Les liaisons hydrogène peuvent également se former entre les protéines membranaires et les lipides. La stabilité peut aussi provenir des charges négatives des protéines membranaires qui conduisent à des interactions électrostatiques fortes avec les cations divalents tels que Mg^{2+} et Ca^{2+} ou encore avec les têtes hydrophiles des lipides.

Certaines protéines peuvent également bouger dans le plan de la membrane tandis que d'autres sont ancrées dans sa structure. Le résultat est tel que la membrane est en fait fluide et visqueuse (sa consistance s'apparente à une huile de faible qualité). La membrane lipidique a souvent été qualifiée de mosaïque fluide ; mosaïque parce qu'il existe des domaines bien définis qu'on appelle communément des radeaux lipidiques, et fluide parce que les radeaux lipidiques sont libres de circuler de chaque côté de la membrane. Les lipides ne sautent pas en général de l'extérieur vers l'intérieur, ou de l'intérieur vers l'extérieur de la membrane, en raison d'une barrière énergétique importante de 20 à 50 kcal.mol^{-1} [106]. Ce phénomène connu comme le flip-flop passif confère un certain nombre de propriétés à la membrane qui lui permettent d'effectuer de nombreuses fonctions.

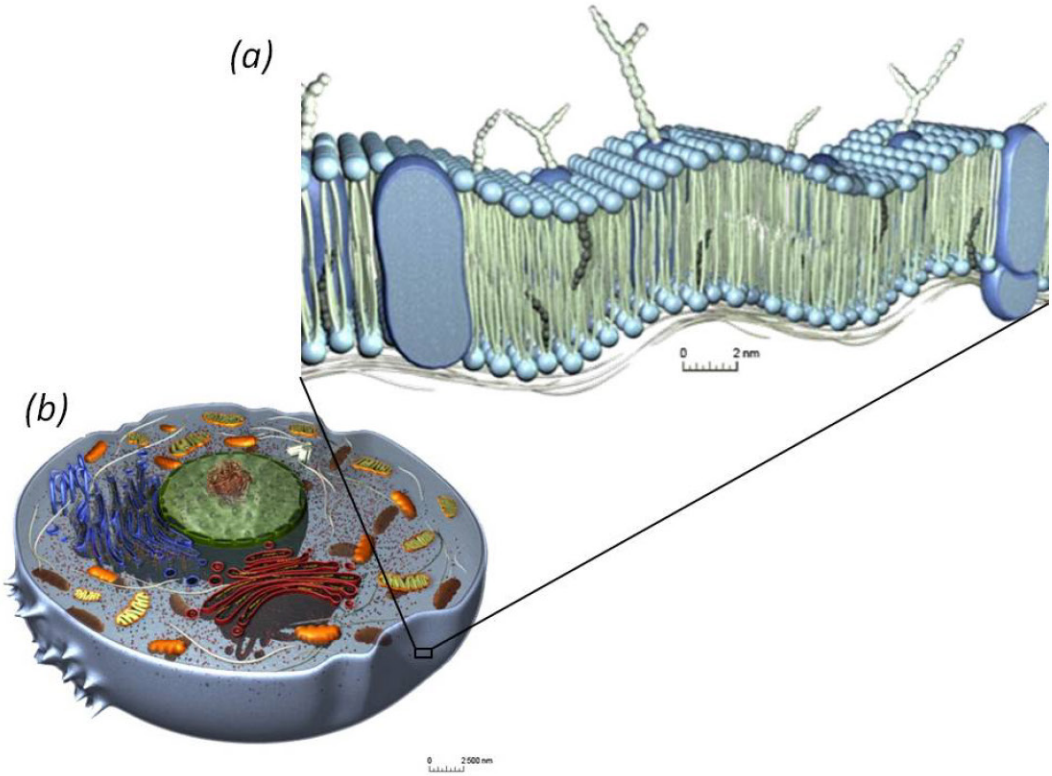

Figure IV.2 (a) Vue sur la membrane cellulaire avec les protéines transmembranaires et (b) sur la cellule. Certaines protéines traversent la membrane (protéines intégrales), tandis que d'autres se trouvent à l'extérieur ou l'intérieur (protéines périphériques). Beaucoup de protéines membranaires sont impliquées dans le transport de molécules ou d'ions ou dans la production d'énergie (canaux, pompes, moteurs moléculaires, etc.).
(œuvre modifiée, Mélanie Villeneuve, © La cellule animale, CCDMD, source : http://www.ccdmd.qc.ca/ri/cellule/)

1.3 Membrane cellulaire en tant que barrière sélective

Les concentrations des solutés, des sucres, des ions, etc. sont beaucoup plus élevées au sein de la cellule qu'au dehors. La membrane cellulaire prévient ainsi la libre circulation des molécules. Elle constitue donc une barrière osmotique qui empêche l'équilibration naturelle de ces espèces et lutte contre les gradients naturels de concentration.

Bien que la cellule soit séparée de son environnement, elle a cependant besoin d'obtenir des nutriments et de sortir ses déchets. La membrane doit donc être en mesure de permettre le transport d'espèces. Elle agit ainsi comme une barrière sélective. Certaines molécules peuvent traverser la membrane sans aucun apport d'énergie (diffusion passive), mais la plupart d'entre elles ne le peut pas. L'eau, les molécules non polaires et certaines petites molécules polaires peuvent la traverser selon ce principe passif. Les molécules non polaires pénètrent en particulier en se dissolvant dans la bicouche lipidique. La plupart des résidus polaires tels que les acides aminés, les acides organiques et les sels inorganiques ne sont pas autorisés à entrer. Ils peuvent alors être sélectivement transportés à l'aide des protéines membranaires (transport facilité ou transport actif). Ces protéines généralement transmembranaires nécessitent souvent une dépense d'énergie pour aider les molécules à traverser la membrane.

Il existe principalement quatre types de systèmes de transport (*voir Table IV.2*) :

a) **la diffusion passive** qui n'est pas spécifique. Il n'y a pas de protéines de transport dans ce cas, et l'apport d'énergie n'est pas nécessaire. Un gradient de concentration de ces molécules ne peut pas être donc généré entre les deux côtés de la membrane ;

b) **la diffusion facilitée** qui implique une protéine facilitant le transport de la molécule sans apport d'énergie. Les protéines de transport passif permettent souvent le passage d'un seul type de molécule selon le gradient de concentration. Il s'agit d'ailleurs des canaux ioniques sélectifs à une seule entité comme les canaux à potassium ;

c) **la translocation des groupes** qui implique une modification chimique de la molécule transportée une fois liée à la protéine spécifique du transport. Ce type de transport exige un apport d'énergie et est souvent utilisé dans des voies cataboliques pour amener les deux substrats vers la cellule ;

d) **le transport actif** qui provoque une accumulation importante du produit d'un côté de la membrane avec des concentrations qui peuvent atteindre plusieurs fois la concentration existant de l'autre côté, notamment grâce aux pompes moléculaires. Ceci nécessite un apport d'énergie évident.

Table IV.2 Comparaison des quatre systèmes de transport transmembranaire présents dans les cellules.

Propriétés	***Diffusion passive***	***Diffusion facilitée***	***Translocation des groupes***	***Transport active***
Transporteur-médié	-	+	+	+
Concentration contre le gradient	-	-	*néant*	+
Sélectivité	-	+	+	+
Apport d'énergie	-	-	+	+
Modification au cours du transport	-	-	+	-

1.4 Polarité de la membrane

Parce que la membrane est faite de molécules lipidiques, la membrane plasmique a intrinsèquement une résistivité électrique élevée, en d'autres termes une faible perméabilité aux ions. Toutefois, certaines molécules incorporées dans la membrane sont capables soit de transporter activement des ions d'un côté de la membrane vers l'autre, soit de fournir des canaux par lesquels ils peuvent se déplacer. Le fluide des deux côtés de la membrane contient de fortes concentrations d'ions mobiles, dont le sodium (Na^+), le potassium (K^+), le chlore (Cl^-) et le calcium (Ca^{2+}) présents en majorité. Le potentiel membranaire résulte de la différence en concentration d'ions du côté intracellulaire et extracellulaire de la membrane.

Le potentiel membranaire a deux fonctions de base. Premièrement, il permet à la cellule de fonctionner comme une batterie, fournissant le courant nécessaire à l'exploitation d'une variété de « dispositifs moléculaires » intégrés dans la membrane. Deuxièmement, dans les cellules excitables électriquement comme les neurones, il est utilisé pour transmettre des signaux entre les différentes parties d'une cellule. L'ouverture ou la fermeture des canaux ioniques produit un changement local dans le potentiel de la membrane, qui provoque un courant électrique rapide qui circule ensuite vers d'autres points de la membrane.

Dans les cellules non excitables et dans les cellules excitables dans leur état électrique de base, le potentiel membranaire est maintenu à une valeur relativement stable, appelé potentiel de repos. Parce que l'épaisseur de la membrane est d'environ 7-8 nm, une très grande tension transmembranaire n'est pas nécessaire pour créer un fort champ électrique en son sein. Les potentiels membranaires typiques dans les cellules animales sont de l'ordre de 100 millivolts, mais les calculs montrent qu'ils génèrent un champ électrique proche de la limite maximum supportée par la membrane. Il a été calculé qu'une tension dépassant 200 millivolts pourrait provoquer une rupture diélectrique, c'est-à-dire provoquer un arc électrique à travers la membrane. Pour les neurones, la gamme des valeurs typiques du potentiel de repos est de -70 à -80 millivolts. L'intérieur de la cellule a une tension de base négative de presque un dixième de volt inferieur par rapport à l'extérieur. L'ouverture et la fermeture des canaux ioniques peut provoquer une rupture de ce potentiel de repos, appelée dépolarisation si la tension de l'intérieur monte (disons de -70 mV à -65 mV), ou hyperpolarisation si la tension intérieure devient encore plus négative (par exemple de -70 mV à -80 mV). Dans les cellules excitables, une dépolarisation suffisamment importante peut évoquer un événement de courte durée appelé potentiel d'action, dans lequel la valeur du potentiel membranaire subit très rapidement un grand changement, souvent inversant brièvement son signe (*voir Figure IV.3*).

Les potentiels d'action sont générés par des canaux ioniques particuliers, dépendants de la tension. Les canaux ioniques voltage-dépendants sont donc contrôlés par le potentiel de membrane, tandis que le potentiel de membrane est lui-même en partie contrôlé par ces mêmes canaux ioniques. Les boucles de rétroaction qui apparaissent permettent de gérer la dynamique complexe du potentiel d'action, y compris les oscillations et les événements régénératifs.

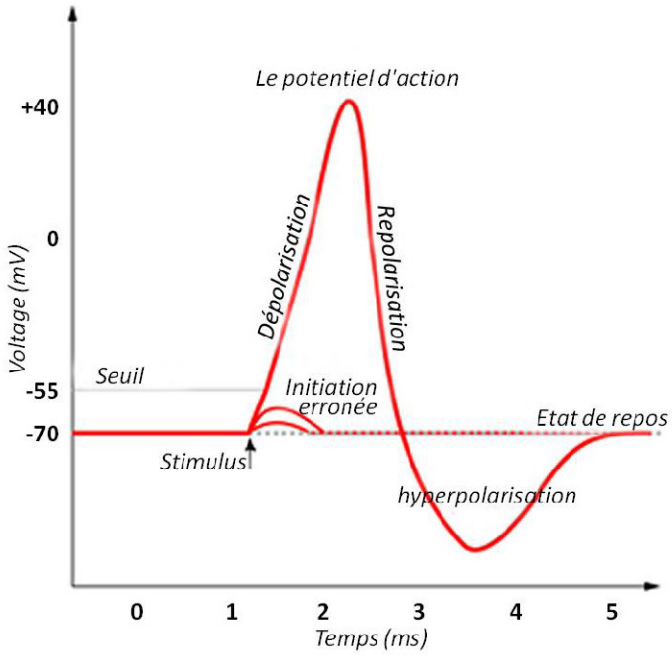

Figure IV.3 Schéma illustrant les changements du potentiel membranaire des cellules excitables au cours du potentiel d'action. Le potentiel d'action se compose de plusieurs phases : (i) forte augmentation du potentiel membranaire (dépolarisation), (ii) baisse plus lente du potentiel membranaire (repolarisation), et (iii) période où le potentiel membranaire est inférieur au potentiel de repos (hyperpolarisation).

2 Canaux ioniques

Comme nous venons de le voir, les canaux ioniques sont des protéines qui aident à établir et à contrôler le petit gradient de tension existant à travers la membrane plasmique des cellules vivantes (*voir section Polarité de la membrane*) en permettant le flux d'ions grâce aux gradients électrochimiques locaux [107]. L'étude expérimentale des canaux ioniques (ang. *channelomics*) fait appel à de nombreuses techniques telles que l'électrophysiologie de tension (notamment la technique dite de « patch clamp »), l'immunohistochimie, et les réactions en chaîne par polymérase en temps réel (RT-PCR).

Les canaux ioniques sont des protéines membranaires intégrales, ou, plus généralement, un assemblage de plusieurs protéines. Ces ensembles de « multi-unités » impliquent habituellement un auto-arrangement de protéines identiques ou homologues sous la forme d'un pore rempli d'eau traversant la bicouche lipidique [108-109]. Dans la plupart des canaux ioniques voltage-dépendants, les sous-unités formant le pore central sont appelées les sous-unités α, tandis que les sous-unités

auxiliaires sont notés β, γ, et ainsi de suite. Certains canaux permettent le passage des ions uniquement en fonction de leur charge positive (cations) ou négative (anions). D'autres jouent sur l'empêchement stérique et sont sélectifs à des ions de tailles différentes tels que le sodium ou le potassium. Dans certains canaux ioniques, le passage des ions à travers le pore est régulé par une « porte », qui peut être ouverte ou fermée par des moyens chimiques, des signaux électriques, la température ou même une force mécanique. La Figure IV.4 donne une image générale du fonctionnement d'un canal ionique.

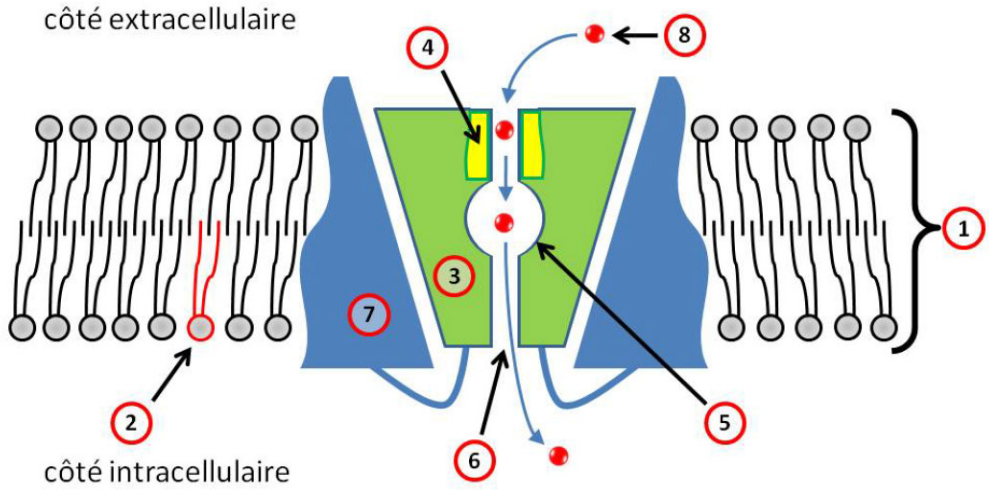

Figure IV.4 Schéma d'un canal ionique inséré dans la membrane cellulaire (1). Celle-ci est composée de deux couches de lipides (2). La partie transmembranaire de la protéine (3) contient le filtre de sélectivité (4), la cavité interne (5) et la porte intracellulaire (6), gérée par les domaines sensibles à la tension électrique de la membrane (7). Cette porte permet ou empêche le passage des ions (8) dans le pore.

2.1 Rôle biologique

Puisque les canaux voltage-dépendants sont à la base de l'influx nerveux, et parce que les canaux activés par un ligand gèrent aussi la conduction à travers les synapses, ces pores sont des composants particulièrement importants du système nerveux. Ce n'est d'ailleurs pas un hasard si la plupart des toxines offensives ou défensives secrétées par certains prédateurs ou proies (par exemple, le venin produit par les araignées, les scorpions, les serpents, les poissons, les abeilles, les escargots de mer et autres) agissent soit pour arrêter, soit pour moduler la conductance des canaux ioniques. En outre, les canaux ioniques sont des éléments clés dans une grande variété de processus biologiques qui impliquent des changements rapides dans les cellules, tels que la contraction cardiaque, squelettique et musculaire, les transports épithéliaux de nutriments et d'ions, l'activation des cellules T et la sécrétion d'insuline des cellules bêta-pancréatiques. Dans la recherche de nouveaux médicaments, les canaux ioniques sont donc des cibles fréquentes [110-112]. C'est donc pour cela que nous nous y sommes intéressés particulièrement dans cette thèse.

2.2 Structure détaillée

Les canaux peuvent être classés selon différents critères : selon les ions qu'ils laissent passer (Na^+, K^+, Cl^-, …), selon la manière dont ils peuvent être régulés (pH, voltage transmembranaire, …), ou selon le nombre de sous-unités dont ils sont composés et d'autres aspects de leur structure. Les canaux appartenant à la plus grande classe sont les canaux voltage-dépendants qui sont à la base de l'influx nerveux. Ils se composent de quatre sous-unités avec six hélices transmembranaires chacune. Les canaux voltage-dépendants s'ouvrent et se ferment en fonction du gradient de tension à travers la membrane plasmique, tandis que les canaux ioniques ligand-dépendants s'ouvrent et se ferment en fonction des ligands liés au canal. A l'activation, ces hélices bougent légèrement pour ouvrir le pore. Deux de ces six hélices sont séparées par une boucle (appelé boucle P) qui est le principal déterminant de la sélectivité ionique et de la conductivité dans cette classe de canaux. Les boucles P s'arrangent entre elles pour former la partie cylindrique la plus étroite du canal (filtre de sélectivité). L'existence et le mécanisme de la sélectivité ionique ont été postulés dans les années 1960 par CLAY ARMSTRONG [113]. Cet auteur a suggéré que la composition chimique du pore pouvait remplacer efficacement les molécules d'eau qui hydratent normalement les ions potassium, contrairement aux autres ions. Ce mécanisme a finalement été confirmé lorsque la structure de la chaîne (et donc la boucle P) a été élucidée. Il existe en effet des canaux très simples en structure où les sous-unités ne sont composées que de cette boucle P et de deux hélices transmembranaires, comme le canal KcsA par exemple. La détermination de leur structure moléculaire par cristallographie aux rayons X [114] a d'ailleurs été récompensée par le prix NOBEL de chimie attribué en 2003 à RODERICK MACKINNON.

Il aura fallu de longues années pour confirmer les hypothèses premières de C. AMSTRONG. Ceci s'explique en partie en raison de la petite taille des canaux et à cause de la difficulté de cristallisation des protéines transmembranaires pour l'analyse en rayons X. De plus, comme la cristallographie nécessite l'extraction des canaux de leur membrane à l'aide de détergent, beaucoup de chercheurs ne pouvaient considérer les images obtenues que comme provisoires. L'ambiguïté inévitable, au sujet de ces structures, est basée sur le fait que la conformation des chaînes change pendant leur fonctionnement (la protéine s'ouvre et se ferme, par exemple), et donc que la structure cristalline pourrait ne représenter qu'un état quelconque du canal étudié. R. MACKINNON a levé cette ambiguïté en élucidant deux structures (ouverte et fermée) de canaux analogues. D'autres études sur le fonctionnement des canaux, et donc sur leur structure, peuvent être aussi conduites grâce à l'électrophysiologie, à la biochimie, à la comparaison de séquences de gènes et à la mutagénèse [107, 115].

2.3 Les canaux étudiés pendant la thèse

Au cours de cette thèse, trois canaux ioniques ont été étudiés (*voir Figure IV.5*) :

a) le KcsA (pdb code 1BL8 [116] ou 1K4C [117]) : canal bactérien à potassium (à partir de *Streptomyces lividans*) cristallisé sous forme fermée et appartenant à la famille de canaux potassiques rectifiant intérieurement (ang. *inwardly rectifying potassium channels*), en passant le courant (charge positif) plus facilement vers l'intérieur de la cellule. À ce jour, sept sous-familles ont été identifiées dans divers types de cellules de mammifères [118]. Ils sont les cibles de multiples toxines et le dysfonctionnement des canaux a été reconnu être à l'origine de plusieurs maladies [119].

b) le MthK (pdb code 1LNQ [120]) : canal bactérien à potassium (de *Methanobacterium thermoautotrophicum*) cristallisé dans l'état ouvert et appartenant à la famille des canaux à potassium activés par le calcium [121]. Cette famille de canaux ioniques contient chez les mammifères seulement 8 membres connus.

c) le Kv1.2 (pdb code 2A79 [122]) : canal appartenant à la famille des canaux potassiques voltage-dépendants (K_V). Cette famille regroupe près de 40 membres, qui sont subdivisés en 12 sous-familles. Ces canaux sont connus surtout pour leur rôle dans la repolarisation de la membrane cellulaire suivant les potentiels d'action. Chaque sous-unité α a six segments transmembranaires, homologues à un seul domaine des canaux à sodium. En conséquence, ils se rassemblent en tétramères pour produire un canal fonctionnel.

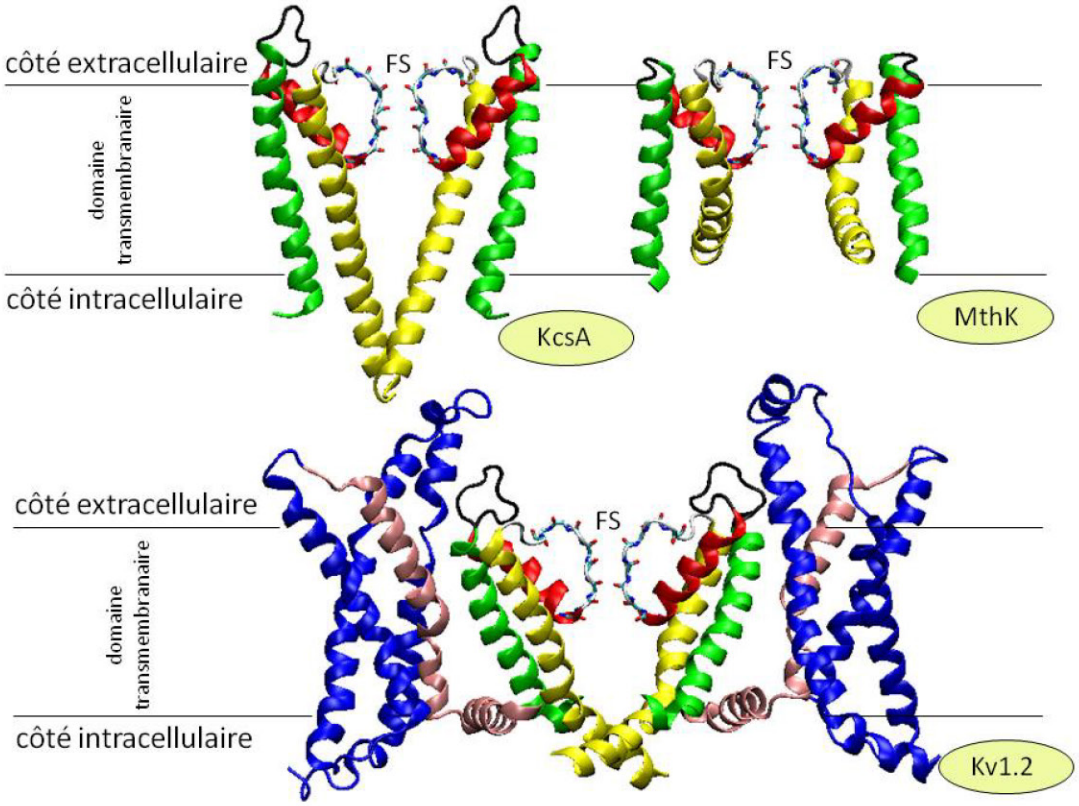

Figure IV.5 Trois modèles atomistiques des canaux ioniques étudiés dans cette thèse : KcsA, MthK et Kv1.2. (FS) filtre de sélectivité sur la boucle P. Par souci de clarté, seulement deux des quatre sous-unités présentes dans chaque protéine sont présentées.

2.4 Etudes approfondies du canal KcsA

Le canal à potassium KcsA appartient à une vaste famille de protéines allostériques qui commutent entre les conformations fermée et ouverte en réponse à un stimulus, et agissent comme un régulateur de l'activité de cations dans les cellules vivantes. Le mécanisme d'ouverture de la porte et la sélectivité vis-à-vis des cations de ce canal ont été abondamment étudiés dans la littérature, avec un regain notoire ces dernières années (en raison de la publication de la structure cristallisée du KcsA). Malgré le nombre croissant de recherche et de synthèse sur ces sujets, l'interprétation quantitative de ces processus à l'échelle atomique est loin d'être atteinte. Dans l'article suivant *« Ion conductance vs. pore gating and selectivity in KcsA channel: Modeling achievements and perspectives »*, nous avons examiné les progrès dans ce domaine d'activité sur la base des données expérimentales et théoriques les plus récentes, et en incluant nos résultats. Nous avons discuté les faiblesses et les lacunes qui doivent être résolues dans l'avenir. Dans cette étude bibliographique, nous avons envisagé successivement le filtre, la cavité et les milieux extra- et intracellulaires, afin d'analyser séparément la spécificité de chaque région. Nous portons une attention particulière à l'étude de la sélectivité et de la perméation des ions à l'échelle atomique. L'influence de l'eau est vue comme une composante structurelle et dynamique des propriétés du canal dans ses états fermé et ouvert, ainsi que dans les mouvements séquentiels des cations. Les résultats obtenus à l'aide des simulations de dynamique moléculaire et des calculs *ab initio* sont analysées plus spécifiquement.

J Mol Model (2007) 13:699–713
DOI 10.1007/s00894-007-0202-y

ORIGINAL PAPER

Ion conductance vs. pore gating and selectivity in KcsA channel: Modeling achievements and perspectives

Céline Boiteux · Sebastian Kraszewski · Christophe Ramseyer · Claude Girardet

Received: 16 November 2006 / Accepted: 19 March 2007 / Published online: 6 April 2007
© Springer-Verlag 2007

Abstract KcsA potassium channel belongs to a wide family of allosteric proteins that switch between closed and open states conformations in response to a stimulus, and act as a regulator of cation activity in living cells. The gating mechanism and cation selectivity of such channels have been extensively studied in the literature, with a revival emphasis these latter years, due to the publication of the crystallized structure of KcsA. Despite the increasing number of research and review papers on these topics, quantitative interpretation of these processes at the atomic scale is far from achieved. On the basis of available experimental and theoretical data, and by including our recent results, we review the progresses in this field of activity and discuss the weaknesses that should be corrected. In this spirit, we partition the channel into the filter, cavity, extra and intracellular media, in order to analyze separately the specificity of each region. Special emphasis is brought to the study of an open state for the channel and to the different properties generated by the opening. The influence of water as a structural and dynamical component of the channel properties in closed and open states, as well as in the sequential motions of the cations, is analyzed using molecular dynamics simulations and *ab initio* calculations. The polarization and charge transfer effects on the ions' dynamics and kinetics are discussed in terms of partial charge models.

Keywords Ionic channels · Selectivity · Gating Molecular dynamics · Ab initio calculations

C. Boiteux · S. Kraszewski · C. Ramseyer · C. Girardet (✉)
Laboratoire de Physique Moléculaire UMR CNRS 6624,
Université de Franche-Comté,
La Bouloie,
25030 Besançon Cedex, France
e-mail: claude.girardet@univ-fcomte.fr

Introduction

Ion channels are proteins inserted in the membrane lipidic bilayer of a cell which form aqueous pores. They allow ions to cross the hydrophobic barrier of the core membrane, guaranteeing to the cell exchange of ionized particles. There are many different families of ion channels which all possess the same basic properties. They can open or close the ion conduction in a controlled way and they are furthermore selective to an ion or to a range of ions. The first property corresponds to the gating, the second to the selectivity.

The gating mechanism was set in the late 1960s, with Armstrong's studies on voltage dependent channels, showing that ammonium compounds blocked potassium currents [1]. Important improvements in the knowledge of the gating were done in the late 1990s, when the x-ray structure of the transmembrane part of the bacterial potassium channel KcsA was established [2] and, a few years later, when the open form of the MthK channel was compared to the KcsA structure [3, 4]. At the same time, Electron Paramagnetism Resonance (EPR) and Site Directed Spin Labelling (SDSL) methods provided, together with restrained energy minimization of the structure, a model for the 3D fold of full-length KcsA including N and C termini in the cytoplasmic region [5]. It was suggested that, while these termini do not play a fundamental role in ion permeation, they could act as sensors to modulate the pH-dependent gating of the channel [5]. Then, the gating of a voltage dependent Kv channel was explored in the context of the MthK structure to determine the nature and magnitude of the structural changes induced by the gate opening [3–7]. Very recently, it has been shown that to open the conduction pathway of KcsA, two gates at least should act simultaneously [8–11]. This illustrates the difficulty in presently understanding the

gating mechanism, which seems not to be unique for all the potassium channels [12, 13].

The selectivity of sodium ion channels was experimentally revealed at nearly the same time as the investigations on the gating mechanism [14, 15], and it was then evidenced for the potassium channels a few years later [16, 17]. An attempt has been made to interpret the origin of this process in terms of differences in the coordination cage for K^+ and Na^+ ions in the channel. Such a model was then exploited on the basis of more precise information on the KcsA structure [2] and widely used in several studies based on molecular dynamics (MD) or brownian dynamics (BD) simulations [18–22]. Other hypotheses implying the ion hydration/dehydration mechanism at the mouths of the channel were also proposed [23]. Transition state theory has also been exploited to describe the ion transport and selectivity by determining the free energy variation for an ion entering the filter [24–27]. Unfortunately, no well-established microscopic mechanism can actually explain the selectivity of potassium channels.

Several interesting reviews on the potassium channels occurred since 2000, which all describe in detail the progresses carried out on our understanding of gating and selectivity mechanisms, either based on experimental arguments, especially by comparing pH and voltage-gated channels [28–30], or based on calculations [31–35]. The goal of this paper is to introduce, in the discussion of these reviews, additional information obtained from molecular dynamics and quantum calculations on the KcsA. These additional data concern the ions correlation in the permeation mechanism and the influence of water on the ionic conduction. These topics were widely discussed for the closed state of the K channel, and they are extended here to an atomic description of an open state. They also describe polarization effects on ions and protein walls, especially the occurrence of different partial charges on K^+ and Na^+ ions, which could be at the origin of channel selectivity.

Basis of the channel structure

General information from experiments

The primary function of an ion channel is thus to permit the controlled and selective diffusion of ions across the membrane from the cell interior to the extracellular medium. Understanding this feature requires atomistic information on the protein structure embedded in the lipidic membrane. Such information, although still partial, is available for a small set of voltage and ligand-gated ion channels [6, 36, 37] and has reached a high standard for the KcsA channel, with the x-rays crystallized structure at 2.0 Å resolution (pdb 1K4C) [38], 3 years after a previously published structure at a lower resolution by the same group (pdb 1BL8) [2].

The basic structure of KcsA consists of four subunits that form a symmetric tetramer (Fig. 1a). Each subunit is made up of one outer (M_1) and one inner (M_2) transmembrane helices connected by a re-entrant P loop (Fig. 1b), made by a descending P helix and an ascending F region containing the TVGYG (Threonine, Valine, Glycine, Tyrosine, Glycine) sequence common to all K^+ channels [39–41] and responsible for selectivity [42] (Fig. 2). This latter region forms the filter at the outermost part of the membrane. This narrow part, of radius 1.4 Å and around 12 Å long, opens on a rather large outer mouth limited by the M_2 helices, which form an inverted tepee-like structure at the intracellular part of the pore. The widest part of this structure consists of a hydrated cavity C, which can be approximated by a sphere of 5–6 Å radius forming the inner vestibule, while the narrowest part corresponds to the gate G with a radius of about 2 Å (Fig. 2a). The cytoplasmic part is constituted by NH_2 termini which form α-helices anchored at the membrane-water interface, while the COOH termini form a right-handed four helices bundle that extend towards the cell cytoplasm (Fig. 3).

Fifty years before the experimental determination of the channel structure by MacKinnon and collaborators [2], Hodgkin and Keynes [43] had shown that the filter contains two to three K^+ ions and that permeation involves single-file ion motions across the membrane (Fig. 2b). Such a feature has been corroborated by the x-ray data, and information on the ion sites in the entire pore is now relatively well-established [44, 45]. Seven sites have been determined at relatively high K^+ concentration, S_{ext} and S_0 located at the outer mouth of the filter, S_1 to S_4 inside the filter and S_{cav} in the cavity [40, 46]. S_1 to S_4 are between planes defined by carbonyl and hydroxyl oxygen atoms of Y78, C77, V76 and T75 residues in such a way each K^+ ion is solvated by 8 oxygen atoms.

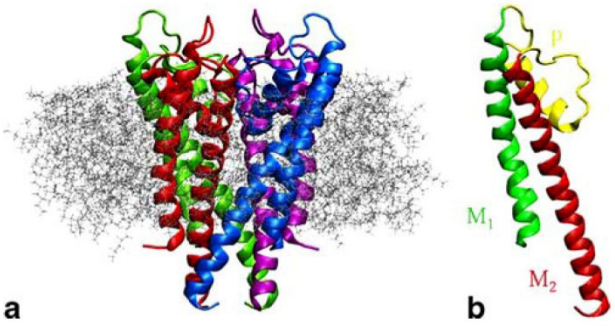

Fig. 1 **a** Structure of the KcsA protein embedded in the octane slab mimicking the lipid membrane. The four subunits forming the channel are drawn in different colors. **b** Structure of one monomer formed by the two transmembrane helices M_1 and M_2, and the P loop

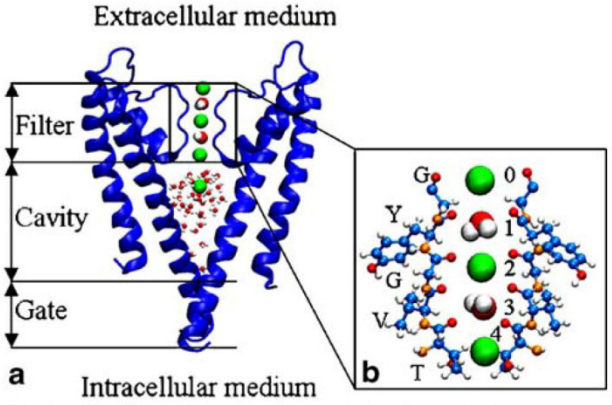

Fig. 2 **a** Partition of the closed state of the channel, using only two monomers for clarity. *Green circles* represent cations, in alternation with water molecules (oxygen in *red* and hydrogen in *white*). **b** Zoom of the filter part describing the TVGYG sequence. Sites created by carbonyl groups are labelled by number 0 to 4 (carbon in *blue*)

Numerical methods

Using structural data, theoretical approaches can help the confirmation of experimental models on the permeation dynamics, channel conductance and selectivity [46]. Two limiting factors prevent an accurate development of theoretical methodologies. Firstly, the number of atoms that can be considered in these approaches to interpret permeation and gating mechanisms is in general too small regarding the size of the protein and the closer parts of the membrane. Secondly, times which are relevant to describe the gating and the ion diffusion through the pore are very long when compared to the ion dynamics.

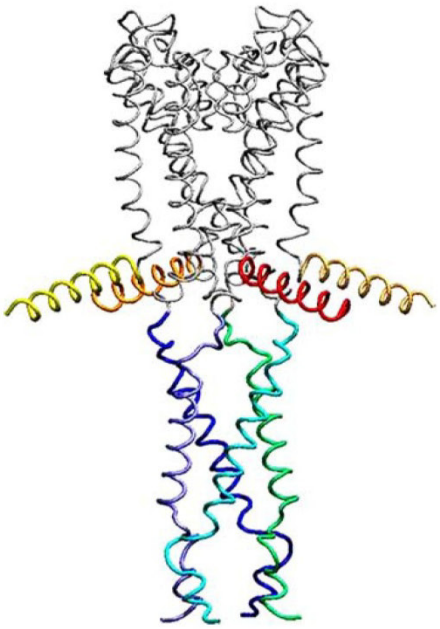

Fig. 3 Full-length KcsA structure including the cytoplasmic region (pdb 1F6G). N (from *yellow* to *red*) and C (from *green* to *blue*) termini are shown on this figure, in addition to the membrane part (in *grey*) of the KcsA

Ab initio calculations based on first principles are therefore unable to describe these phenomena since the maximum number of involved atoms ($<10^3$) is dramatically small when compared to the system size ($\geq 10^7$ to 10^9 atoms). Such calculations can nevertheless provide information on a very limited part of the protein, for instance inside the filter [47–51], to interpret possible mechanisms for the Na^+/K^+ selectivity.

At the opposite side, the continuum electrostatics methodologies avoid the atomic description of the system by replacing the discrete matter by dielectric continua with rigid boundaries. While such calculations are simple and practical to analyze the influence of the protein electric field on the ions' behavior, they appear to be rather artificial and totally unadapted to the description of concerted motions of ions and protein walls [52].

The most used methods are Molecular Dynamics (MD) and Brownian Dynamics (BD), which are very complementary as much in time scale as in size scale. MD allows simulations to be performed by including reasonably large numbers of atoms ($\approx 10^5$) when classical force fields (AMBER [53], CHARMM [54], GROMACS [55], NAMD [56]) are used. Free energies, protein relaxation and diffusion coefficients can be determined, even if this method is very expensive in terms of computational time, but it cannot include physical times longer than a few tens of nanoseconds. This weakness of the MD is the strength of the BD since microsecond scale can be easily reached to simulate the whole ion diffusion in the channel. The counterpart is the poor description of the protein in terms of continuum and the use of parameters that should be calculated independently. MD can nevertheless provide parameters such as diffusion coefficients and information on the modification of the electric field due to the channel distortion, and, in this sense, both simulation methods are complementary.

Because continuum approaches also including BD simulations are too much parameterized, thus introducing inaccuracies in the results, and because MD simulations are very restrictive in terms of the system size and also dependent on the classical force field used to describe electrical properties of the protein, no direct path perfectly exists to analyze the ion permeation of the membrane. Therefore, aside from these conventional methodologies, some physical and numerical ansatzs have been used to reduce computational times and, sometimes, extend the validity limits of the method. As a first example, octane, which is known to have roughly the same dielectric properties as the lipidic bilayer but a much lower viscosity, can be substituted to describe the membrane surrounding the protein in order to favor relaxations, and more generally motions, of protein atoms [57]. As a second example, to

artificially decrease gating time, constraints can be applied to various parts of the pore. As a third example, the cytoplasmic part containing the N and C residues is generally disregarded, at least in the gating process. Such approximations, although sometimes unavoidable in practice, lay some doubts on the accuracy of the calculations.

The results presented in this paper were obtained from MD simulations using AMBER 8 suite of programs [53]. We used a 75 Å side periodic simulation box, containing nearly 6,300 atoms, forming the membrane part of the protein (pdb 1K4C), embedded in a 29 Å thickness octane slab. The extra and intracellular media are constituted by more than 6,200 TIP3P water molecules, and around 30 ions and counterions, forming two slabs of 22 Å of thickness. Simulations were conducted at constant temperature T (300 K) and atom number N. Quantum calculations on restrained part of the channel were performed by using Gaussian03 [58], at the Hartree-Fock 6–31G(*d*) level of theory.

Conductance and gating

While the diffusion model based on an ionic single file is now well-admitted [2, 27, 34, 59–61], it is not known whether the general structure of the protein controls the conductance or whether this latter is limited at one or several locations in the channel. As discussed above, since a complete description of the pore properties is not computationally possible, most of the studies have been devoted to a selected part of the channel. Moreover, permeation through the channel is gated and, at a minimum, one gate should open or close on command to regulate the ion flux. Here again, no complete information on the gating mechanism exists. In particular, no clear answer is, up to now, given to the following questions:

- What are the atomic structures of the open against closed states of the protein? And what are the consequences of opening on the ion properties?
- Are there one, two or even several activation gates which act in an independent way or being strongly correlated? Which pore part(s) finally control(s) the ion diffusion?
- What is the role of water in the ion conduction mechanism?

Attempts to give partial explanations to these features are available in the literature via studies focused on various levels of the pore structure, with different methodologies presented in the following sections of the paper.

The opening mechanism

When the crystallized structure of the KcsA was first published, paramagnetic spin resonance studies, associated with pH-dependence analysis indicated that it corresponds to a close conduction state and that the transmembrane helices forming the intracellular pore can move away from the channel axis to induce gating [37, 62]. A series of studies have thus been conducted, using MD and BD simulations, to interpret the influence of conductance with pore opening [57, 63–66]. A preliminary work in all these studies was to create a more or less stable open state of the pore. This is possible by using several methodologies. Steered MD has been independently performed by two groups [64, 65], by artificially stabilizing the aperture at the desired configuration, using a repulsive cylinder inside the pore or by placing a Van der Waals balloon at the intracellular mouth of the channel and gradually inflating and displacing it. The KcsA gating was also studied by a normal mode analysis (NMA), by considering mainly the lowest frequency modes responsible for the largest displacements [67]. A similar approach, on the basis of collective motion analysis named PCA (principal component analysis), was proposed to extract the functionally relevant motions of the protein from the simulation noise due to atomic fluctuations [68]. Homology with Ca^{+}-gated channel MthK and voltage-dependent channel KvAP has also been extensively discussed; these channels being assumed to nicely represent the open conformation of KcsA [3, 4, 7, 29, 37, 41]. However, we can wonder whether the open state of MthK mimics in a convenient way the open state of KcsA.

Targeted MD have been recently developed to study, via an all-atom description, the opening of the pore [69]. Starting from the skeleton of the crystallized close state of KcsA modelled on the basis of x-rays experiments, large constraints were applied to ions and water molecules in the filter to avoid their escape and thus to keep them at their electrostatic sites. In contrast, C_α carbon atoms of transmembrane helices M_1 and M_2 were progressively stretched to new positions, some of them being derived from an open state issued from EPR experiments (pdb 1JQ1) [70], while the others were free to move consistently with the surrounding structure. The results of these simulations have shown that the external transmembrane M_1 was not significantly perturbed by the gating mechanism. In contrast, the inner transmembrane helices M_2 moved significantly to open the channel, with root mean square displacements around 1.25 Å instead of 0.5 Å for the closed state. It may be noted that these values are only averages over all C_α atoms of M_2 helices and they do not give information on the detail of the opening, in particular what part of these helices in the cavity are mainly concerned with the gating, and how and where the pore opens first.

The study of distance variation between homoresidues in the tetrameric backbone located at the bottom of the cavity and in the intracellular medium demonstrates that channel opening proceeds as a zip [71]. Indeed, the narrowest part

of the tepee forming the gate does not open first: the opening initiates from residues located at the inner end of M_2 helices, i.e. located in the cytoplasm, with an abrupt increase of the distance between His124 and 227 of about 15 Å when submitted to the restraint. Once this increase has been stimulated, it is sufficient to open the gate zone (around Leu110 and 213) by about 4 Å, with an asymmetrical behavior for the other two monomers.

In contrast, the intra-cavity part of M_2 helices does not distort significantly and a hinge point around Met96 is obtained. The subsequent question that arises is the stability of the open state. By releasing the constraints, an asymmetric relaxation of the C termini in the M_2 helices proceeds, indicating that two monomers get closer (His-His distance equal to 19 Å) whereas the other two monomers stay roughly open (His-His distance equal to 30 Å). In the gate region, although the distance between homoresidues Leu-Leu decreases, the conformation still corresponds rather to the open state than to the closed one (Fig. 4).

The analysis of the low-frequency vibration modes of the protein has revealed that M_1 and M_2 transmembrane helices undergo totally concerted tilting and rotational motions [67]. However, M_1 motions do not directly modulate the size of the cavity, in contrast with M_2 helices. Two pivots were identified near Met96 and Thr107. The first pivot divides the KcsA subunit into a highly rigid part including the small-pore helix and the TVGYG sequence of the filter, and a much more flexible portion containing M_1 and M_2 helices (Fig. 4). The second pivot allows the swinging motion of M_2 helices and leads to an enlargement of the intracellular gate without loosening up the integrity of the protein structure. Such results are comparable with those issued from the targeted MD, which give hinge points at Met96 and Leu110 (closed to Thr107) although they do not take into account the influence, probably dominant, of the cytoplasmic part of the M_2 helix ends (Fig. 3).

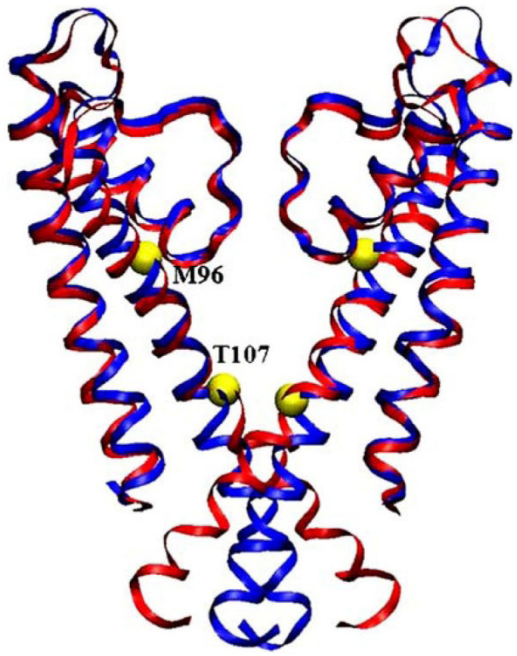

Fig. 4 Superimposed structures of the closed (*blue*) and open states (*red*) of the channel. *Yellow spheres* correspond to hinge points (Met96 and thr107). Note the strong deformation of the terminal M_2 helices

It may be noted that the magnitude of the KcsA pore opening found in the targeted simulation is much smaller than expected from the MthK homology, although the Met96 hinge point corresponds for the two channels. However, this opening is sufficient to allow for large displacements of the K^+ ions and thus to favor diffusion, as demonstrated in BD simulations [63].

The cavity

As a consequence of the large deformation of the M_2 helices, the cavity they form is the most influenced part of the pore during the opening. This inverted tepee-like structure forming a hydrophobic cavity filled by 20–40 water molecules is known to receive a well-hydrated K^+ ion. Due to its hydrophobicity and to the strong electric field it generates via the COOH termini of the α-helices of the pore, the cavity contributes to stabilize the ions in the channel and to focus K_{cav} along the pore axis, favoring the throughput. The cavity properties have thus been associated to the gating mechanism which was at the basis of the channel conductance.

When the M_2 helices move away, the volume of the bottom part of the cavity near the Leu110 increases by 15% with respect to the closed state, and the volume of the intracellular gate region increases by a factor 8 [65, 71]. This structural change in the M_2 helices conformation is followed by drastic modifications in the electrostatic field created by the protein on the K_{cav} ion (Fig. 5). Indeed, in the closed state, the cation experiences a positive field everywhere along the cavity axis, which tends to stabilize it at the top of the cavity. When the gate opens, the influence of the electric field becomes less significant, with a loss in the ion stability inside the cavity. At the cavity bottom, i.e. at the gate, the electric field displays two opposite peaks (one negative and one positive) in the closed state, which prevent the ion diffusion in both directions. On the contrary, this field remains positive in the open state and tends to favor the diffusion toward the filter. These effects are then magnified by the presence of water.

Indeed, water plays crucial structural and dynamical roles in the cavity [72, 73]. In the closed state of the pore, the S_{cav} site is revealed by the organization of the confined water molecules inside the hydrophobic cavity, while the

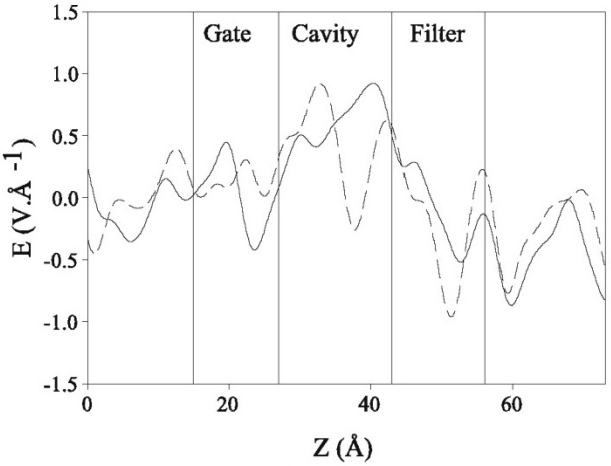

Fig. 5 Behavior of the electric field versus the z position of the ion along the channel axis for the closed (*full curve*) and open (*dashed curve*) states of the channel

electric field of the protein itself does not create such a stable site. Statistically, this site is closer to the filter mouth than to the middle of the cavity, while the water molecules tend to bolster the K_{cav} ion in this conformation by creating an electric dipole moment directed toward the gate (Fig. 6a). In the open state, the K_{cav} ion tends to move toward the gate, being surrounded by the water molecules which create a dipole oriented toward the filter (Fig. 6b). The change of electric field promoted by the water molecules in the cavity during the opening appears therefore drastic and should influence the ionic conduction. Homology studies have corroborated the fact that a cation located in the cavity is less stable in the open state than in the closed state, due to a high dielectric environment in the vicinity of the cavity ion [37].

Water also appears as a major dynamical element in the cavity due to its high mobility. Opening the gate induces a large mobility of water molecules from the intracellular to the cavity and vice-versa. The number of water molecules in the open cavity fluctuates slightly around 38 instead of 32 in the closed state (Fig. 7). It may be noted in addition that the molecules can exit or enter the cavity, and although the total number is conserved, a third of these molecules was changed in 1 nanosecond. This is a contrasted situation with the closed state, in which the water molecules cannot escape the cavity. The water molecules are strongly correlated to the K_{cav} ion motions in order to create a hydration sphere (Fig. 8), but this correlation does not prevent water molecules from moving in the cavity by creating/breaking hydrogen bonds, and even escaping from their hydration sphere to leave the cavity in the open state. There are in fact permanent exchanges of water molecules in the solvation sphere of the K_{cav} ion [73].

Since gating of the KcsA is activated by a drop in pH, *ab initio* calculations have been conducted to study the role of

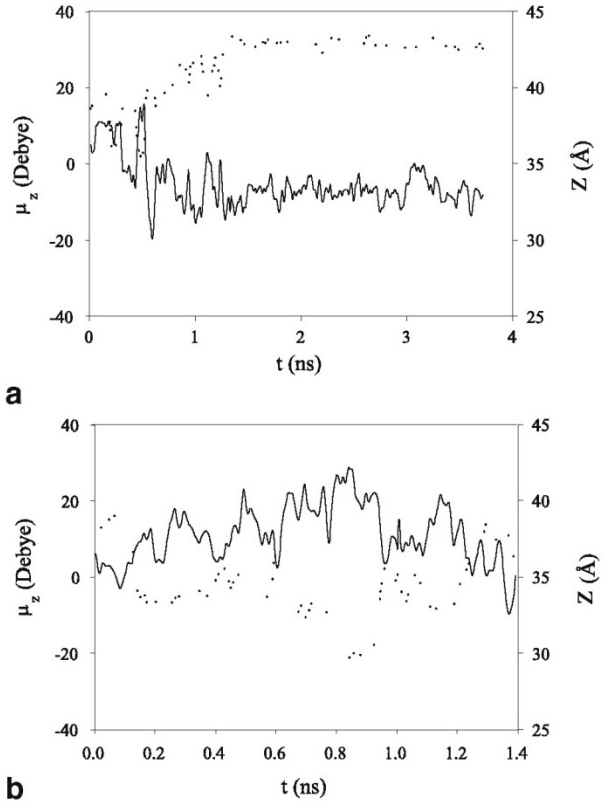

Fig. 6 Behavior of the component μ_z of the dipole moment created by the water molecules inside the cavity (*full curve*) as a function of the simulation time. The corresponding position of K_{cav} along the z axis inside the cavity is drawn versus the time (*dotted curve*) for closed (**a**) and open (**b**) states of the channel

water at bundle crossing of M_2 helices in the cavity. Results suggest that an H_5O_2 group, partially charged, would connect or disconnect glutamate residues in the gating

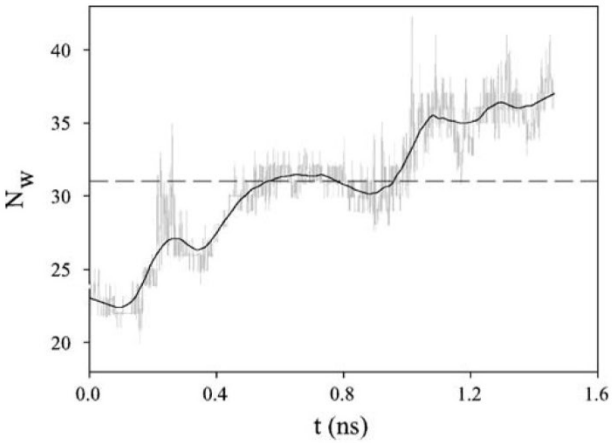

Fig. 7 Number of water molecules in the cavity versus the simulation time for closed (*dashed line*) and open (*full curve*) channel. The curve represents smoothed data of the grey curve including the instantaneous variations of the number of molecules. In the closed state this number is constant, there is no exchange of water with the intracellular medium, whereas it increases during the opening of the channel

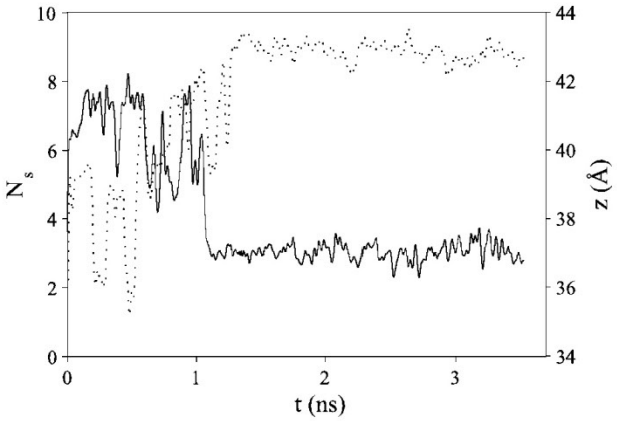

Fig. 8 Behavior of the number of water molecules in the first hydration shell (*dotted curve*) versus the simulation time and of the corresponding position of the ion along the z axis (*full curve*) in the closed state

region, depending on the net charge of the four residues (respectively −2e or −1e, where e is the electronic charge). The arrival of a proton responsible for the change of residue charge would in fact lead to weak H-bonds insufficient to hold the gate closed. Such a mechanism could be at the origin of the gating process [74, 75]. In fact, recent publications have shown that two gates should open simultaneously to permit the conduction of KcsA. The main gate formed by the bundle crossing of the transmembrane M_2 helices at the innermost part of the cavity is open by a pH decrease [62] as indicated before, while the second gate, connected to destabilizing interactions between residues in P loop (mainly Asp80 and GLu71), is promoted by Glu71 that acts as a gating charge depending on variations of the membrane field [9, 10, 76, 77].

The filter

During the opening of the pore by targeted MD, the C_α carbon atoms of the filter do not show strong deviations from their equilibrium position since the root mean square displacement does not exceed 0.2 Å, while the protein displacement is clearly much important (around 1.3 Å) [69]. Moreover, a drastic event such as the sudden switch from NVT to NPT distribution (where the constraint on the volume V of the simulation box is released to a process at constant pressure P) does not perturb the filter backbone, even if the filter plays a crucial role in the conductance control.

The filter is the best known region of the pore at the atomic level from x-rays experiments. This narrowest part of the channel, formed by residues corresponding to the sequence TVGYG, creates through carbonyl oxygen atoms ideal solvation sites for nearly dehydrated K^+ ions. The rate-limiting step in the ion conduction mechanism, which was elaborated many years ago [43] and then adapted according to improvements in the knowledge of the protein structure [2], is the concept of translocation. This translocation was then described as totally concerted barrierless motions of dehydrated ions in single file which recover, via the sites formed by carbonyls, solvated states [59, 60].

However, since x-rays data are static, performed at 77 K, and for the closed state of the channel, simulations have been extensively developed to reproduce channel conditions at 300 K, including protein motions and distortions correlated with ion diffusion. Simulations generally start from initial atomic coordinates obtained by embedding the protein structure in a pre-equilibrated membrane and then adding water molecules and ions at 300 K. When applied to the filter part of the channel, they have corroborated that permeation occurs via concerted single-file motion of K^+ and water molecules. They have furthermore shown that the innermost walls of the filter undergo small changes, with the oxygen atoms of the carbonyls lining the pore moving as the ions switch along the sites. The correlated motions of carbonyls and ions, indicating that the filter should be reasonably flexible, have been invoked to explain the rapid ion flux across the pore [21, 33, 78]. Conformational dynamics of the filter has also been considered for occasional distortions implying peptide bond flips, where some carbonyls change their orientations. The results suggest that such distortions, which can be controlled by pH change [9], could have an influence on the permeation mechanism. Indeed as shown in crystallized structure of KcsA, high K^+ concentrations lead to an equilibrated, rigid, structure with well-organized carbonyl groups, while low K^+ concentrations tend to destabilize carbonyl arrangement (CO flips are observed at the Valine level) [38]. Models have been proposed to explain ion kinetics across the filter by stating that diffusion proceeds via a concerted switch of K^+ ions at the four filter sites S_1-S_4 [79–81].

At present, the MD simulations tend to prove that diffusion occurs via a knock-on process. This mechanism consists in the alternation of two or three ions occupation states in the filter [27, 43, 61]. Most of the time there are only two ions in the filter, which occupy alternately the sites S_1-S_3 or S_2-S_4. While the sites S_1-S_3 are filled, it is possible for an ion located in the cavity to enter the S_4 site of the filter leading to a sudden contraction of the file and to the displacement of ions in sites S_0 and S_2. This transition state S_0-S_2-S_4 is followed by a rapid dissociation and the departure of the S_0 ion to the extracellular side. The efficiency of such a transition has been estimated using molecular dynamics simulations by considering concerted fluctuations of the ion positions in the file and cavity. It was shown in a recent paper that such a process occurs each nanosecond, a value that could be compared to the experimental estimation of 10^8 diffusing ions per nanosecond [82].

The role of water molecules confined in the filter, the number of which is in fact restricted to the two molecules

placed in alternation with the two K^+ ions [38, 45], has long been limited to a screening of the repulsive interactions between ions and to a completion of the solvation of the K^+ ions in the filter. In fact, in single file transport, it has been shown that water molecules are more than just spacer molecules. Molecular dynamics simulations supported by electrostatic calculations have shown that water molecules act as a structural element for the K^+ ions inside the filter. Indeed, water tends to enhance the depth of the wells occupied by the K^+ ions, which themselves stabilize the protein, and creates a new well in the cavity (Fig. 9) [83].

Moreover, water molecules are constrained to move with the K^+ ions through the filter, their motions being strongly correlated [83, 84]. The couple K_0-W_1 corresponding to a K^+ ion in site S_0 and a water molecule in site S_1 move in a concerted way, as does the couple K_4-W_3, when an event tends to modify the constraints imposed to the protein (Fig. 10). These concerted motions are consistent in magnitude as well as in the slope of the displacement versus time (velocity drift). A strong correlation between the couples K-W (Fig. 11) and the oxygen atoms of the carbonyl groups closer to these couples is also observed. This is the case for K_0-W_1 and the oxygen of Tyr78 in a monomer, which exhibit displacements with nearly the same amplitude (Fig. 10a). It may however be noted that the two couples K_0-W_1 and K_4-W_3 appear to be in phase opposition under the switch NVT/NPT, instead to be in phase concerted.

Water molecules can also play a significant role at the two mouths of the filter. On the extracellular side of the channel, the K^+ ion located in the site S_0 has been detected in the 2.0 Å resolution x-rays structure to be rather fully hydrated [38]. In contrast, simulations have shown that this ion is only partially coordinated to water molecules and

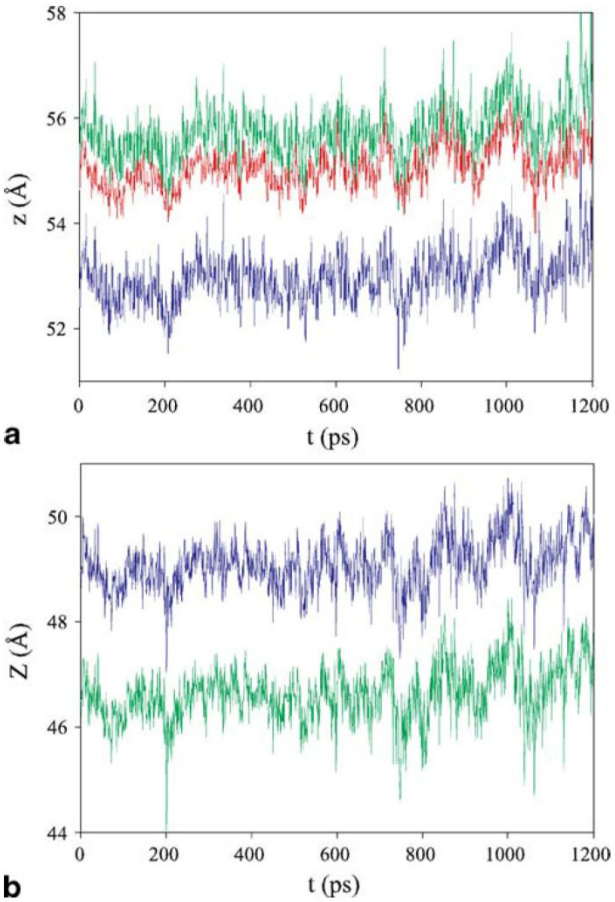

Fig. 10 Time evolution of the position of various atoms in the filter. **a** K_0 ion (*green curve*), W_1 water (*blue*) and mean positions of carbonyl oxygen atoms of the four Tyr78 (*red*). **b** K_4 ion (*green*) and W_3 water (*blue*)

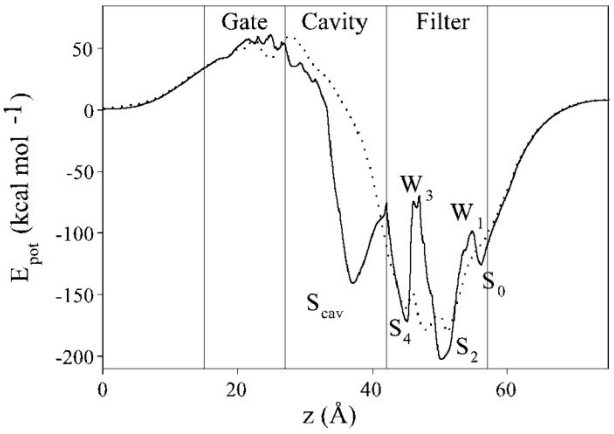

Fig. 9 Behavior of the potential energy due to the protein experienced by a single K^+ ion moving along the channel (*dotted curve*) compared to the potential energy of the same ion when water is included in the channel (*full curve*). Sites S_1 and S_3 are filled by water while S_0, S_2 and S_4 correspond to the ion location

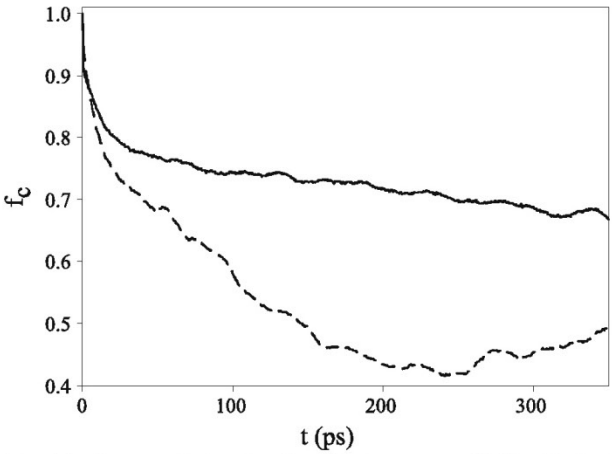

Fig. 11 Time correlation function for the couples K_0-W_1 (*dashed curve*) and K_4-W_3 (*full curve*). Note the difference in the correlation of the two couples due to the fact that K_0 ion tends to exit the filter while K_4 prefers to enter the filter

transiently solvated by the carbonyl oxygen atoms of Tyr78 [27, 35, 46]. At the inner mouth of the filter, i.e. close to the cavity, simulations found two adjacent sites for K_4 ion, which allow its back and forth motions at the filter entry. The K_4 ion is also very partially hydrated and solvated by the carbonyl oxygen atoms of Thr75. From a structural point of view, the surrounding water molecules act thus by revealing S_0 and S_4 sites (Fig. 9).

Moreover, entry/exit of these ions in the inner/outer mouths of the filter have been suggested by experiments and simulations to be a key determinant of conductance magnitude. Two reasons have been invoked. The first is based on hydration/dehydration energy required to exit/enter the filter [16, 23, 85]. The second relies on the structural confinement of water. Due to geometrical confinements in the selectivity filter, (1) liquid–vapor oscillations occur where the file of molecules embedded in the channel (the liquid) cooperatively exits the channel, leaving behind a near vacuum (the vapor) [86, 87], and (2) dielectric properties of confined water are distant from those of the bulk, with a permitivity constant that can be reduced by a factor 2, and the corresponding electric fields are dramatically changed [88, 89]. This second argument is reinforced by the hydrophobic character of the inner and outer mouths of the filter. This tends to stabilize H-bonds between water molecules over times which can be increased by a factor 10. As a result, proton transfer is favored and this latter process can promote specific bindings at filter mouths influencing the conductance.

The cytoplasmic region

Little attention has been paid to C and N terminal domains of K^+ channel in cytoplasm, probably due to a lack of understanding of structural relationship of these two domains to the rest of the channel. While N termini are probably responsible for the anchoring of channel to membrane, C termini form with transmembrane helices M_2 a large water filled cavity which appears as a natural path for ion permeation (Fig. 3) [5]. The few simulations available to date, to our knowledge, have demonstrated that these domains have no direct effect on ion conduction in KcsA but that they could influence the gating, through in particular the electrostatic field they create under local rearrangements [90, 91].

Conductance and selectivity

Since transmembrane ion channels partition the exterior from the interior of the cell in order to maintain, in particular, the proper ionic gradient in the cell, it must be highly selective, allowing some ions to pass while blocking other species. To discriminate between the different ions with different charge values, the protein electrostatic potential must analyze the ion charge to decide whether the ion can cross or not the membrane. In the KcsA channel, the selectivity is ensured by charged carbonyl oxygen atoms that attract monovalent cations and repel anions [92, 93]. However, for monovalent cations with the same charge, such as K^+ and Na^+, the selectivity appears to be a more subtle phenomenon. Most studies on the Na^+ versus K^+ selectivity of the KcsA channel have been devoted to the filter [18, 20, 21, 94], which is recognized as the dominant part of the pore selectivity, but the other zones can also promote selectivity through their specific properties [95, 96]. In analogy with what has been done for the gating, we will thus explore the different parts of the pore to discuss selectivity.

The filter

The selectivity filter has received considerable experimental attention since the pioneering studies by Chandler et al. [14], Hille [17] and Armstrong [1]. To interpret the selectivity of this narrow part of the pore, they postulated that Na^+ was too small to fit well in the coordination cages provided by the K channel, in comparison with the water molecules forming the hydration sphere of the cation. This model was then renewed when the crystallized structure of KcsA was published [2]. It was shown that eight carbonyl oxygen atoms in the filter play the role of water in hydration sphere for a cation K^+ in each site S_1, S_2 and S_3. The preference for K^+ over Na^+ was thus explained as the result of a nearly perfect compensation of the K^+ dehydration by the channel carbonyl solvation, while such compensation was not possible for a smaller ion, such as Na^+ [18, 22] (Fig. 12).

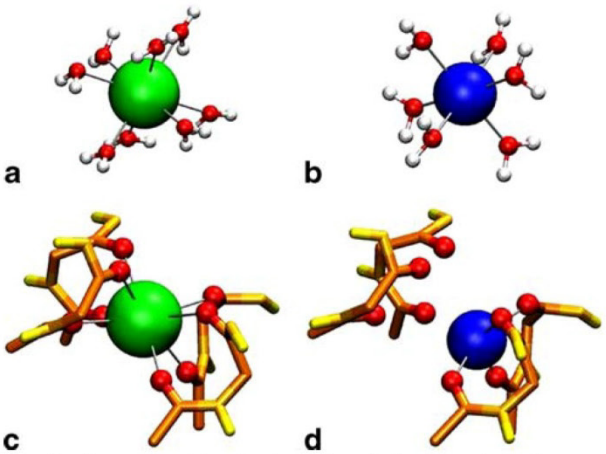

Fig. 12 Geometry of the first hydration shell of ions in bulk water, octahedral geometry for potassium (**a**) and tetrahedral one for sodium (**b**). First solvation shell of potassium ion (**c**) and sodium ion (**d**) in the site S_2 of the filter

In some papers [21, 78], and in particular in a more recent one [97], it was nevertheless argued that the size difference between K^+ and Na^+ radii (0.38 Å) is too small to be retained as an argument to explain selectivity if we consider that proteins are "soft materials displaying structural flexibility". In particular, it was shown, in a simple model including the eight carbonyl groups, that the C=O dipoles are very dynamic, and their electrostatic properties, rather than their structural conformation, control the cation selectivity by increasing or decreasing the resulting dipole moments of the protein walls. In contrast, experiments conducted on Na^+/K^+ selectivity of NaK channel, which shares high sequence homology and similar structure with the KcsA channel, tend to demonstrate that the electrostatic repulsion between carbonyls would not explain the selectivity [98]. From these results, the size-selectivity through geometric constraints was privileged. However, recent additional calculations based on the dynamical role of the C=O dipoles have shown that thermodynamic exclusion of Na^+ relative to K^+ was due to the scarcity of favorable binding configurations for Na^+ compared to K^+ in the filter. The enhanced fluctuations of the binding energy for the smaller cation could thus be at the origin of this selectivity [99].

The incidence on selectivity of polarizations and charge transfers between the cations in the filter has recently been discussed. Previous DFT (Density Functional Theory) calculations showed that, during the translocation process from one site to another one in the filter, the K^+ ion significantly polarizes its ligands, the carbonyl groups and the neighboring water molecule(s) [47, 100]. These results were contradicted by other authors who compared *ab initio* Hartree-Fock and DFT calculations of partial charge for K^+ ion in the filter, from a study of the electrostatic potential experienced by the cation [48, 51]. This comparison suggested that the DFT method overemphasizes the importance of polarization. The electronic structure of the selectivity filter polarized by the electrostatic field of the environment was investigated using DFT and QM/MM methods. It was shown that the carbonyl groups were largely polarized and that a charge transfer took place between the backbone and the cations, with a more pronounced effect for Na^+ than for K^+ in the cation sites explored.

A more extensive analysis of the incidence of partial charge on the pore selectivity has been carried out in our group. In a first paper [49], *ab initio* calculations were performed to calculate the atomic charges in the selectivity filter according to Merz-Kollman-Singh (MKS) scheme [101, 102]. Emphasis was mainly devoted to the determination of the charges of (1) the oxygen atoms in the two water molecules, (2) the two K^+ ions in the filter, (3) the nitrogen, the carbon and the oxygen atoms in peptide bonds and (4) the carbon and the oxygen atoms of the CHOH part of the Thr74 lateral chain. Significant decreases of the K^+ charges in sites S_2 and S_4 up to about 0.31 e were observed, while the charges of oxygen in water molecules decrease by 0.20 to 0.25. Similar changes were calculated for the atoms belonging to peptide bonds and hydroxyl groups of Threonine, with a strong dependence on the proximity with a given site (S_2 or S_4). These results, obtained for K^+ only, needed to be extended to Na^+. This was done in a second paper [50], using two methods for charge partitioning from the knowledge of the electrostatic potential. These two methods (MKS and HR [103]) allowed us to be confident that determination of partial charges was not too dependent on the choice of the partitioning. Four situations were then considered, which correspond to water–cation sequences in S_1 to S_4 sites of the filter. The WKWK sequence, for which the two water molecules are located in S_1 and S_3 sites while K^+ ions occupy the other two sites, could be compared with situations for which one or two sodium ions are substituted to potassium. The results showed, in both charge partitioning methods, that the mean partial charge for K^+ is always much more affected by charge transfer process, with a value which is smaller by 25% than the electronic charge, instead of less than 10% for Na^+ in the S_2 and S_4 sites. The values of the partial charges depend on the position of the two cations species in the sequence, with a charge decrease which is more pronounced in S_4 site than in S_2 for both K^+ and Na^+. The corresponding partial charges on the oxygen atom of water molecules in S_1 and S_3 sites also significantly decreased, up to 30% for S_1, while this change was much smaller for S_3.

In terms of electrostatic potential experienced by any cation in a given sequence, the charge transfer process did not change the overall shape of the potential curves, indicating that the four sites were in general well defined. In contrast, the depth of the wells connected to those four sites was shown to depend on the cation species in the sequence. In the calculations, it was found that the energy difference in the wells can reach 40 kcal mol^{-1} when a Na^+ cation is substituted to a K^+ one. This value is dramatically larger (by a factor of 4) than the value calculated by considering the electronic charge for the two cations, and it could be at the origin of the K^+/Na^+ selectivity of the KcsA channel. Unfortunately, this value led to a selectivity ratio unrealistically large, using the model of Nelson [79].

The main problem to estimate the selectivity in this charge partitioning method is the use of a constant partial charge for the cation along the filter and a common structure of the protein for the two species. Indeed, the charge should depend on the position of the cations in the filter and on the possible distortion of the filter conformation by changing K^+ to Na^+, particularly regarding the orientation of carbonyl groups. This variation has been

taken into account for a more accurate estimation of the selectivity ratio P_{K^+}/P_{Na^+} in a third paper.

We have performed targeted molecular dynamics simulations to mimic the diffusion of a water-cation sequence from sites S_4 to S_0. The sequence $K_0W_1K_2W_3K_4$ was moved along the filter to reach the $W_0K_1W_2K_3W_4$ occupation, which was sufficient to determine the partial charges for each site (Fig. 13a). A similar procedure was then applied to the sequence containing one Na^+, which was moved in the two directions from S_2 to S_4 or S_2 to S_0 in order to explore every site (Fig. 13b). The quasi continuum behavior of the Na^+ and K^+ charges in the sequences moving along the filter was then analyzed, showing that these partial charges fluctuate significantly when the ion transits from a given site to another one. Including the filter distortion, disregarding in a first step the charge fluctuations and considering only a mean behavior that reflects the value of the partial charge in the five sites (S_0-S_4), we see (Fig. 14) that the Na^+ charge is equal to the electronic charge in site S_0 and decreases by less than 8% in site S_1. For K^+, while the charge is close to the electronic charge in S_0 and S_4, it decreases by 16% for S_2. From these results, the calculated selectivity ratio P_{K^+}/P_{Na^+} was estimated to be around 10^6, a value which appears closer to the experimental value equal to 10^4. The energy difference between Na^+ and K^+ now ranges between 6 and 12 kcal mol^{-1} (Fig. 15). These values are still too high by a factor of 2 in order to explain the experimental data. In fact, such values should be corrected to account for the entropic contribution, i.e. by calculating the free energy difference within the transition state theory [24–27] and not the potential energy difference. Such a calculation is in progress. However, without anticipating the results, it may be noted that inclusion of this entropic term should significantly reduce this difference and probably provide a better agreement with experiments.

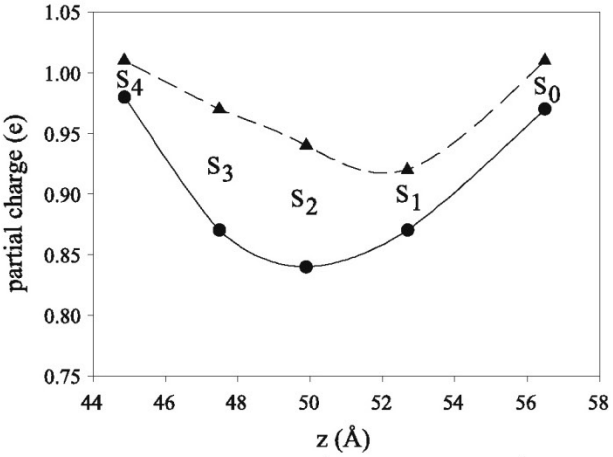

Fig. 14 Mean partial charge of K^+ (*full curve*) and Na^+ (*dashed curve*) ions along the axis of the filter

The polarization and charge transfer processes are thus clearly phenomena that must be accounted for to interpret conductance and selectivity of KcsA channel. In the filter, these processes are magnified due to atom confinement, and we can also wonder whether they could explain the cavity selectivity, which is discussed in the following section. An accurate calculation of the selectivity ratio should in fact include a set of selectivity processes involving the filter, its inner and outer mouths and the cavity. In contrast, the selective role of the cytoplasmic region of the protein is not known. In the very scarce studies of this protein part, it seems to serve rather as a receptor of cytoplasmic activators [5, 91, 92]. However, the fact that large electrostatic fields are generated by this part could suggest other influences.

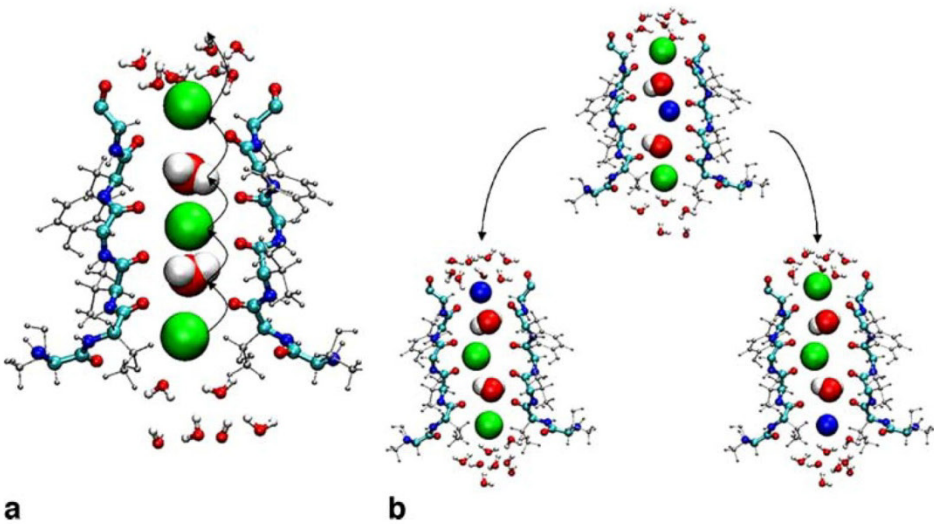

Fig. 13 **a** Diffusion of the KWKWK sequence along the filter. **b** Diffusion of the Na^+ ion (*blue sphere*) in the sequence, toward the outer part of filter (*left*) and toward the inner part (*right*)

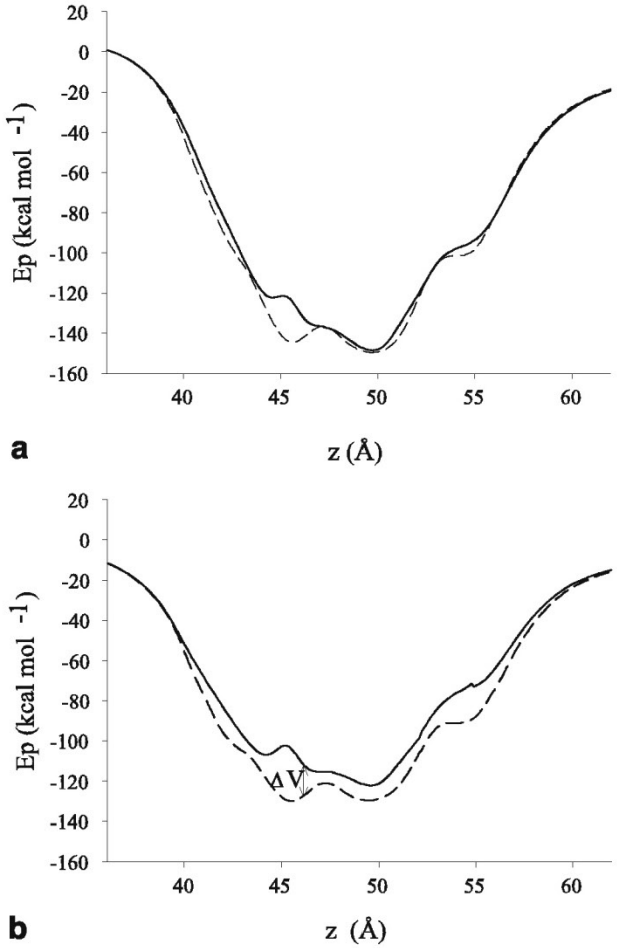

Fig. 15 Potential energy experienced by K^+ (*full curve*) and Na^+ (*dashed curve*) along the filter using either the standard charges (**a**) or the partial charges (**b**) for ions and filter atoms. ΔV characterizes the energy difference which is used to determine the selectivity ratio (see text)

The outer and inner mouths of the filter

Aside from the binding site S_0 located on the extracellular side of the channel, which corresponds to the partial hydration by three to four water molecules and to the additional coordination with carbonyl oxygen atoms of Tyr78 of the K^+ ion occupying this site, there exists another site S_{ext} in the outer mouth of the filter, for which the ion is more hydrated [27]. Crystallographic data have demonstrated the existence of these two different positions which could represent the transition sites corresponding to dehydration/rehydration, as a cation enters/exits the filter. Since this mechanism is about 18 kcal mol^{-1} more energetic for Na^+ ion than for K^+ ion in bulk water, it could be invoked to explain the selectivity ratio K^+/Na^+. However, the ability of the cation to dehydrate or rehydrate at a specific location should also depend on an intimate interaction with the protein. No calculations are presently available to estimate this hydration energy of the two cations in a confined water medium submitted to the influence of strong electrostatic field of the protein.

Moreover, experiments conducted on voltage-gated K^+ channels have shown that protonated Histidine influences selectivity K^+/Na^+ independently of the filter [85]. In particular, mutation of this residue to neutral amino acids increases the selectivity of K^+ over Na^+, increases K^+ current through the pore and blocks Na^+. Here again, no extensive atomic scale analysis of this pore region has been performed.

Although the outer and inner mouths of the filter do not display symmetrical structures, it can be noted that the cations seem to occupy two positions at the inner mouth of the filter. These two positions, which are not discriminated in terms of sites since they are labelled under the same name S_4, correspond to situations where the cation is partially hydrated and partially coordinated with carbonyls (the outer position in the filter) and where cations are nearly dehydrated and mainly solvated by the carbonyl oxygen atoms (the inner position). This process corresponding to dehydration/solvation of the cation looks like the one which occurs at the level of sites S_0 and S_{ext} of the outer mouth.

The cavity

Although in a much smaller proportion, the cavity is known for a long time to display K^+/Na^+ selectivity. K^+ in the S_{cav} site is surrounded by eight water molecules, while the hydration structure around Na^+ is not ordered at the same level (Figs. 8 and 12). Free energy perturbation calculations for a single K^+ over Na^+ ion moving throughout the cavity up to the gate have shown energy differences ranging between 2–4 kT (1.2–2.4 kcal mol^{-1}), instead of 6–8 kT inside the filter, demonstrating the discriminatory role of the cavity [19].

Electrophysiological experiments have been performed, leading to a 5- to 7-fold preference for K^+ over Na^+, equivalent to 1 kcal mol^{-1} [95]. Using Tl^+, a monovalent cation displaying a good analogy with K^+, instead of K^+, to determine the cavity selectivity, the Tl^+/Na^+ binding affinity was estimated to be 7-fold, favoring Tl^+ over Na^+ [104]. The consistency between structural and functional data, and the additional information provided by homology with open channel, have demonstrated that this selectivity does not fundamentally depend on the open or closed state of the pore, and that it can be considered as an intrinsic property of the K^+ channels. The origin of such selectivity is not really known, and it is suggested that the electrostatic interaction between the cation and the channel, alone, cannot explain it [96].

In fact, the role of water in the cavity is probably more important than generally discussed. MD simulations have

shown that the cation occupation is different according to whether the pore is in its open or closed state [73]. Moreover, it has also been demonstrated that the hydration sphere is less structured around Na^+ than K^+ [22, 38]. These features could explain a difference in the effective charge of the two cations at the origin of the selectivity. Calculations of partial charge of the cations Na^+ and K^+ in the cavity should probably provide an answer to this remark.

Conclusion

KcsA constitutes a potassium channel that shows high conduction and selectivity of cations, as observed in permeation experiments [105]. Electropermeation experiments typically measure currents on millisecond time scales, which are clearly well beyond the possibilities offered by MD (typically around a few tens of nanoseconds), and describe conductance as a function of concentration and voltage, which cannot be satisfactorily interpreted in terms of BD.

Kinetic models based on single file ion diffusion in the filter of the channel have been proposed using stochastic processes to describe the ion configurations in terms of occupancy states and the transitions between these states. While the models differ by the description of the translocation mechanism in the filter (strongly concerted ion motions [79], knock-on mechanism based [81] on quasi-ion diffusion and ion-ion fluctuations [80]), they all agree that the permeation limiting rate corresponds to the ion entry entry/exit from the filter. This phenomenon is itself the result of association/dissociation of the ions due to the superimposition of the two effects: the electric field created by the protein at the entry/exit (a feature observed for a large class of channels [106]) of the filter and the dehydration/hydration mechanism of the cation, followed by its solvation via oxygen of carbonyls.

These models can in principle roughly explain both ion conductance and selectivity in the filter, which strongly depend on the depth of the filter well and on the hydration energy. However, these quantities themselves are sensitive to the ion, water and protein dynamics and to the configuration (closed or open state) of the channel, and they are generally considered as parameters. Therefore, only qualitative comparisons with the electrophysiological data can be made. Progress in this analysis would require a more detailed knowledge of the channel to describe the concerted dynamics of the ions and the protein in the various parts of the pore (filter, outer and inner mouths of the filter, cavity, gate and cytoplasmic region), depending on the closed and open state conformation.

Channel gating and its real influence on the pore conductance and selectivity remains an unresolved problem at the atomic scale. The very different time scales that are involved in the various processes implied in ion conductance, ranging from picoseconds for ion dynamics, nanoseconds for ion diffusion, milliseconds for ionic current to seconds for the whole gating and inactivation mechanism, prevent, furthermore, any general interpretation of the behavior of these channels in terms of numerical simulations.

Therefore, an understanding of these phenomena should be taken into account in improved versions of permeation models. These improvements would concern (1) a continuous description of the partial charges of the cations and the filter wall atoms during the ion translocation in the pore via q(z) dependence, (2) an atomic description of the water medium implying both the confinement influence and the effect of strong electrostatic forces, (3) the role of charge transfer and electric field created by the cytoplasmic termini on the rest of the protein, (4) the inclusion of the slow dynamics of the channel opening under the influence of pH changes and extra against intra cellular ion concentration variations. Moreover, (5) the activation and inactivation mechanisms in the protein, which have been evidenced using substitution residues in various voltage and pH-gated channels, could be included in an accurate theoretical interpretation of these mechanisms.

References

1. Armstrong CM (1969) J Gen Physiol 54:553–575
2. Doyle DA, Cabral JM, Pfuetzner RA, Kuo A, Gulbis JM, Cohen SL et al (1998) Science 280:69–77
3. Jiang Y, Lee A, Chen J, Cadene M, Chait BT, MacKinnon R (2002) Nature 417:515–522
4. Jiang Y, Lee A, Chen J, Cadene M, Chait BT, MacKinnon R (2002) Nature 417:523–526
5. Cortes DM, Cuello LG, Perozo E (2001) J Gen Physiol 117:165–180
6. Yellen G (2002) Nature 419:35–42
7. Jiang Y, Lee A, Chen J, Ruta V, Cadene M, Chait BT, MacKinnon R (2003) Nature 423:33–41
8. Bernèche S, Roux B (2005) Structure 13:591–600
9. Cordero-Morales JF, Cuello LG, Perozo E (2006) Nat Struct Mol Biol 13:319–322
10. Cordero-Morales JF, Cuello LG, Zhao Y, Jogini V, Cortes DM, Roux B, Perozo E (2006) Nat Struct Mol Biol 13:311–318
11. Kuruta HT, Fedida D (2006) Biophys Mol Biol 92:185–208
12. Doyle DA (2004) Trends Neurosci 27:298–302
13. Swartz KJ (2004) Nat Struct Mol Biol 11:499–502
14. Chandler WK, Meves H (1965) J Physiol 180:788–820
15. Meves H, Chandler WK (1965) J Gen Physiol 48:31–33
16. Bezanilla F, Armstrong CM (1972) J Gen Physiol 60:588–608
17. Hille B (1973) J Gen Physiol 61:669–686
18. Allen TW, Hoyles M, Kuyucak S, Chung SH (1999) Chem Phys Lett 313:358–365
19. Allen TW, Bliznyuk A, Rendell AP, Kuyucak S, Chung SH (2000) J Chem Phys 112:8191–8204
20. Biggin PC, Smith GR, Shrivastava I, Choe S, Sansom MSP (2001) Biochim Biophys Acta 1510:1–9
21. Shrivastava IH, Tieleman DP, Biggin PC, Sansom MSP (2002) Biophys J 83:633–645

22. Domene C, Sansom MSP (2003) Biophys J 85:2787–2800
23. Guidoni L, Torre V, Carloni P (1999) Biochemistry 38:8599–8604
24. Olsson MHM, Mavri J, Warshel A (2006) Philos Trans R Soc Lond B 361:1417–1432
25. Braun-Sand S, Burykin A, Tao Chu Z, Warshel A (2005) J Phys Chem B 109:583–592
26. Luzhkov VB, Åqvist J (2005) Biochim Biophys Acta 1747:109–120
27. Bernèche S, Roux B (2001) Nature 414:73–77
28. MacKinnon R (2003) FEBS Lett 555:62–65
29. Gulbis J, Doyle DA (2004) Curr Opin Struct Biol 14:440–446
30. Korn SJ, Trapani JG (2005) IEEE Trans Nanobio 4:21–33
31. Sansom MSP, Shrivastava IH, Ranatunga KM, Smith GR (2000) Trends Biochem Sci 25:368–374
32. Chung SH, Kuyucak S (2002) Biochim Biophys Acta 1565:267–286
33. Sansom MSP, Shrivastava IH, Bright JN, Tate J, Capener CE, Biggin PC (2002) Biochim Biophys Acta 1565:294–307
34. Miloshevsky GV, Jordan PC (2004) TRENDS Neurosci 27:308–314
35. Roux B (2005) Annu Rev Biophys Biomol Struct 34:153–171
36. Roux B (2002) Curr Opin Struct Biol 12:182–189
37. Jogini V, Roux B (2005) J Mol Biol 354:272–288
38. Zhou Y, Morais-Cabral JH, Kaufman A, Mackinnon R (2001) Nature 414:43–48
39. Heginbotham L, Abramson T, MacKinnon R (1992) Science 258:1152–1155
40. Heginbotham L, Lu Z, Abramson T, MacKinnon R (1994) Biophys J 66:1061–1067
41. Nimigean CM, Chappie JS, Miller C (2003) Biochemistry 42:9263–9268
42. Chapman ML, Krovetz HS, VanDongen AMJ (2001) J Physiol 530:21–33
43. Hodgkin AL, Keynes RD (1955) J Physiol 128:61–88
44. Zhou Y, MacKinnon R (2003) J Mol Biol 333:965–975
45. Zhou M, MacKinnon R (2004) J Mol Biol 338:839–846
46. Roux B, Allen T, Bernèche S, Im W (2004) Q Rev Biophys 37:15–103
47. Guidoni L, Carloni P (2002) Biochim Biophys Acta 1563:1–6
48. Blizniuk AA, Rendell AP (2004) J Phys Chem B 108:13866–13873
49. Compoint M, Ramseyer C, Huetz P (2004) Chem Phys Lett 397:510–515
50. Huetz P, Boiteux C, Compoint M, Ramseyer C, Girardet C (2006) J Chem Phys 124:44703–44712
51. Bucher D, Raugei S, Guidoni L, Dal Peraro M, Rothlisberger U, Carloni P, Klein ML (2006) Biophys Chem 124:292–301
52. Roux B, Bernèche S, Im W (2000) Biochemistry 39:13295–13306
53. Case DA, Darden TA, Cheatham TE III, Simmerling CL, Wang J, Duke RE, Luo R, Merz KM, Wang B, Pearlman DA, Crowley M, Brozell S, Tsui V, Gohlke H, Mongan J, Hornak V, Cui G, Broza P, Schafmeister C, Caldwell JW, Ross WS, Kollman PA (2004) AMBER 8. University of California, San Francisco
54. Brooks BR, Bruccoleri RE, Olafson BD, States DJ, Swaminathan S, Karplus M (1983) J Comp Chem 4:187–217
55. Bekker H, Berendsen HJC, Dijkstra FJ, Achterop S, van Drunen R, van der Spoel D, Sijbers A, Keegstra H, Reitsma B, Renardus MKR (1993) Gromacs: A parallel computer for molecular dynamics simulations In: de Groot RA, Nadrchal J (eds) Physics computing 92, World Scientific, Singapore
56. Phillips JC, Braun R, Wang W, Gumbart J, Tajkhorshid E, Villa E, Chipot C, Skeel RD, Kale L, Schulten K (2005) J Comp Chem 26:1781–1802
57. Holyoake J, Domene C, Bright JN, Sansom MSP (2004) Eur Biophys J 33:238–246
58. Frisch MJ, Trucks GW, Schlegel HB, Scuseria GE, Robb MA, Cheeseman JR, Montgomery Jr JA, Vreven T, Kudin KN, Burant JC, Millam JM, Iyengar SS, Tomasi J, Barone V, Mennucci B, Cossi M, Scalmani G, Rega N, Petersson GA, Nakatsuji H, Hada M, Ehara M, Toyota K, Fukuda R, Hasegawa J, Ishida M, Nakajima T, Honda Y, Kitao O, Nakai H, Klene M, Li X, Knox JE, Hratchian HP, Cross JB, Bakken V, Adamo C, Jaramillo J, Gomperts R, Stratmann RE, Yazyev O, Austin AJ, Cammi R, Pomelli C, Ochterski JW, Ayala PY, Morokuma K, Voth GA, Salvador P, Dannenberg JJ, Zakrzewski VG, Dapprich S, Daniels AD, Strain MC, Farkas O, Malick DK, Rabuck AD, Raghavachari K, Foresman JB, Ortiz JV, Cui Q, Baboul AG, Clifford S, Cioslowski J, Stefanov BB, Liu G, Liashenko A, Piskorz P, Komaromi I, Martin RL, Fox DJ, Keith T, Al-Laham MA, Peng CY, Nanayakkara A, Challacombe M, Gill PM W, Johnson B, Chen W, Wong MW, Gonzalez C, Pople JA (2004) Gaussian 03, Revision C02, Gaussian, Wallingford CT
59. Åqvist J, Luzhkov V (2000) Nature 404:881–884
60. Morais-Cabral JH, Zhou Y, MacKinnon R (2001) Nature 414:37–40
61. Bernèche S, Roux B (2003) Proc Natl Acad Sci USA 100:8644–8648
62. Perozo E, Cortes DM, Cuello LG (1999) Science 285:73–78
63. Allen TW, Chung SH (2001) Biochim Biophys Acta 1515:83–91
64. Chung SH, Allen TW, Kuyucak S (2002) Biophys J 82:628–645
65. Biggin PC, Sansom MSP (2002) Biophys J 83:1867–1876
66. Shrivastava IH, Sansom MSP (2002) Eur Biophys J 31:207–216
67. Shen Y, Kong Y, Ma J (2002) Proc Natl Acad Sci USA 99:1949–1953
68. Grottesi A, Domene C, Haider S, Sansom MSP (2005) IEEE Trans Nanobio 4:112–120
69. Compoint M, Picaud F, Ramseyer C, Girardet, C (2005) J Chem Phys 122:134707–134715
70. Liu YS, Sompornpisut P, Perozo E (2001) Nat Struct Biol 8:883–887
71. Compoint M, Picaud F, Ramseyer C, Girardet C (2005) Chem Phys Lett 407:199–204
72. Guidoni L, Torre V, Carloni P (2000) FEBS Lett 477:37–42
73. Compoint M, Boiteux C, Huetz P, Ramseyer C, Girardet C (2005) Phys Chem Chem Phys 7:4138–4145
74. Green ME (2002) J Biomol Struct Dyn 19:725–730
75. Sapronova A, Bystrov V, Green ME (2003) Theochem 630:297–307
76. Bernèche S, Roux B (2002) Biophys J 82:772–780
77. VanDongen AMJ (2004) Proc Natl Acad Sci USA 101:3248–3252
78. Bernèche S, Roux B (2000) Biophys J 78:2900–2917
79. Nelson PH (2002) J Chem Phys 117:11396–11403
80. Mafé S, Pellicer J, Cervera J (2005) J Chem Phys 122:204712–204720
81. Yesylevskyy SO, Kharkyanen VN (2004) Phys Chem Chem Phys 6:3111–3122
82. Kraszewski S, Boiteux C, Langner M, Ramseyer C (2006) Phys Chem Chem Phys 9:1219–1225
83. Boiteux C, Compoint M, Huetz P, Ramseyer C, Girardet C (2005) IEJMD 4:1–14
84. Compoint M, Carloni P, Ramseyer C, Girardet C (2004) Biochim Biophys Acta 1661:26–39
85. Consiglio JF, Andalib P, Korn SJ (2003) J Gen Physiol 121:111–124
86. Beckstein O, Sansom MSP (2003) Proc Natl Acad Sci USA 100:7063–7068
87. Saparov SM, Pohl P (2004) Proc Natl Acad Sci USA 101:4805–4809

88. Roux B, MacKinnon R (1999) Science 285:100–102
89. Senapati S, Chandra A (2001) J Phys Chem B 105:5106–5109
90. Molina ML, Encinar JA, Barrera FN, Fernandez-Ballester G, Riquelme G, Gonzalez-Ros JM (2004) Biochemistry 43:14924–14931
91. Encinar JA, Molina ML, Poveda JA, Barrera FN, Renart ML, Fernandez AM, Gonzalez-Ros JM (2004) FEBS Lett 579:5199–5204
92. Corry B, Vora T, Chung SH (2005) Biochim Biophys Acta 1711:72–86
93. Corry B, Chung SH (2006) Cell Mol Life Sci 63:301–315
94. Luzhkov VB, Åqvist J (2001) Biochim Biophys Acta 1548:194–202
95. Nimigean CM, Miller C (2002) J Gen Physiol 120:323–335
96. Bichet D, Grabe M, Jan YN, Jan LY (2006) Proc Natl Acad Sci USA 103:14355–14360
97. Noskov SY, Bernèche S, Roux B (2004) Nature 431:830–834
98. Shi N, Ye S, Alam A, Chen L, Jiang Y (2006) Nature 440:570–574
99. Asthagiri D, Pratt R, Paulaitis ME (2006) J Chem Phys 125: 24701–24707
100. Ban F, Kusalik P, Weaver DF (2004) J Am Chem Soc 126:4711–4716
101. Singh UC, Kollman PA (1984) J Comp Chem 5:129–145
102. Besler BH, Merz KM, Kollman PA (1990) J Comp Chem 11:431–439
103. Hinsen K, Roux B (1997) J Comp Chem 18:368–380
104. Zhou Y, MacKinnon R (2004) Biochemistry 43:4978–4982
105. LeMasurier M, Heginbotham L, Miller C (2001) J Gen Physiol 118:303–313
106. Treptow W, Tarek M (2006) Biophys J 91:L26–L28

3 Résultats obtenus sur le fonctionnement des canaux

3.1 Origine de la perméation des ions dans le KcsA

3.1.1 Quantification du « knock-on »

Pour comprendre l'origine de la perméation, c'est-à-dire la manière dont les ions passent dans le canal ionique, il a fallut focaliser nos études au filtre de sélectivité. Celui-ci, grâce à ses dimensions (diamètre ≈ 3 Å, longueur ≈ 14 Å), fournit les propriétés nécessaires à la perméation et la sélectivité. Très généralement, la séquence d'acides aminés TVGYG qui constitue le filtre crée un puits attractif pour les cations. Cela facilite l'entrée de ces ions dans le pore, mais en revanche une autre force est nécessaire pour vaincre cette attraction et donner un flux (donc une efficacité) convenable au canal (courant de l'ordre de 10 pA, c'est-à-dire 1 ion toutes les 10 ns). Historiquement et jusqu'à présent, il était généralement admis que c'est la répulsion entre les ions dans le filtre qui compensait cette attractivité et qui déclenchait la diffusion. Cette hypothèse connue sous le nom de « knock-on » demandait à être clarifiée et quantifiée. Pour cela, nous avons envisagé une alternance de deux séquences contenant 2 ou 3 ions qui ont presque les mêmes énergies potentielles (*voir Figure IV.6*). Dans l'article suivant *« Insight into the origins of the barrier-less knock-on conduction in the KcsA channel: molecular dynamics simulations and* ab initio *calculations »*, nous avons effectué des simulations de dynamique moléculaire effectuées à l'échelle des nanosecondes afin d'identifier de tels événements de répulsion.

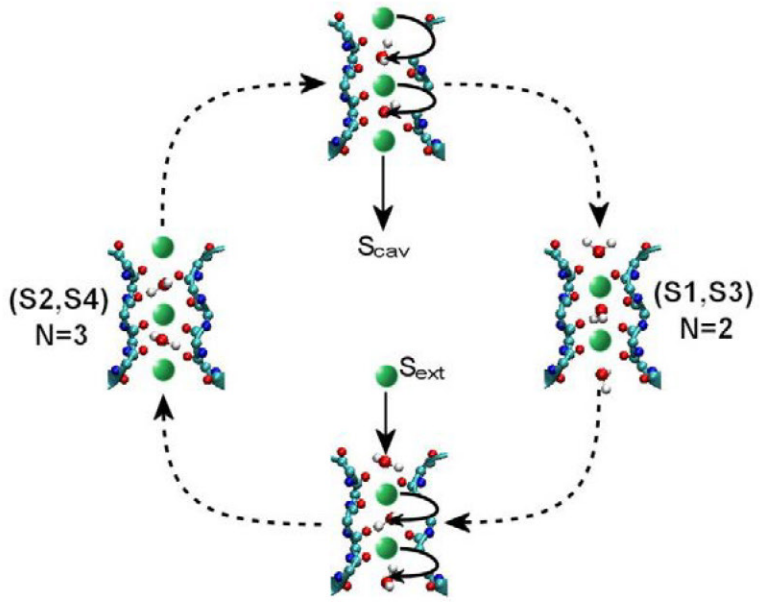

Figure IV.6 Représentation schématique du mécanisme « knock-on » dans le filtre de sélectivité de KcsA. Un ion pénètre dans le canal (vue en bas) qui contient déjà deux ions et les pousse le long du pore. En conséquence, l'état d'une triple occupation (S2, S4) est formé (vue à gauche). Ensuite l'ion du côté opposé s'échappe dans la solution (vue en haut) et l'état d'une double occupation (S1, S3) est restauré (vue à droite). Il faut noter que les ions K^+ dans chacune des deux séquences sont toujours disposés en alternance avec des molécules d'eau.

Nous avons clairement illustré le fait que les mouvements thermiques à l'intérieur du filtre peuvent conduire au mécanisme particulier du « knock-on » (*voir Figure IV.7*). Nous montrons que les contractions du fil à deux ions et la dilatation du fil à trois ions sont à l'origine du passage d'une séquence à l'autre. La comparaison entre le taux de diffusion observé expérimentalement et la fréquence de ces contractions/dilatations confirme qu'il y a suffisamment d'événements pour provoquer un changement de séquence d'ions. Les critères proposés démontrent que 5 à 500 processus de « knock-on » prennent place pendant qu'un seul processus de diffusion d'un ion puisse subvenir. En conséquence, une diminution de 11% de la distance d'équilibre entre les ions dans la séquence (S1, S3) (ou augmentation dans la séquence (S2, S4)) permet à un autre ion de venir à l'intérieur (s'échapper à l'extérieur) du filtre de sélectivité de KcsA. Cette efficacité est renforcée par les effets de polarisation que nous avons étudiés à l'aide de calculs *ab initio*. Ces calculs sont détaillés plus spécifiquement dans l'article dédié aux charges partielles (*voir page 97*).

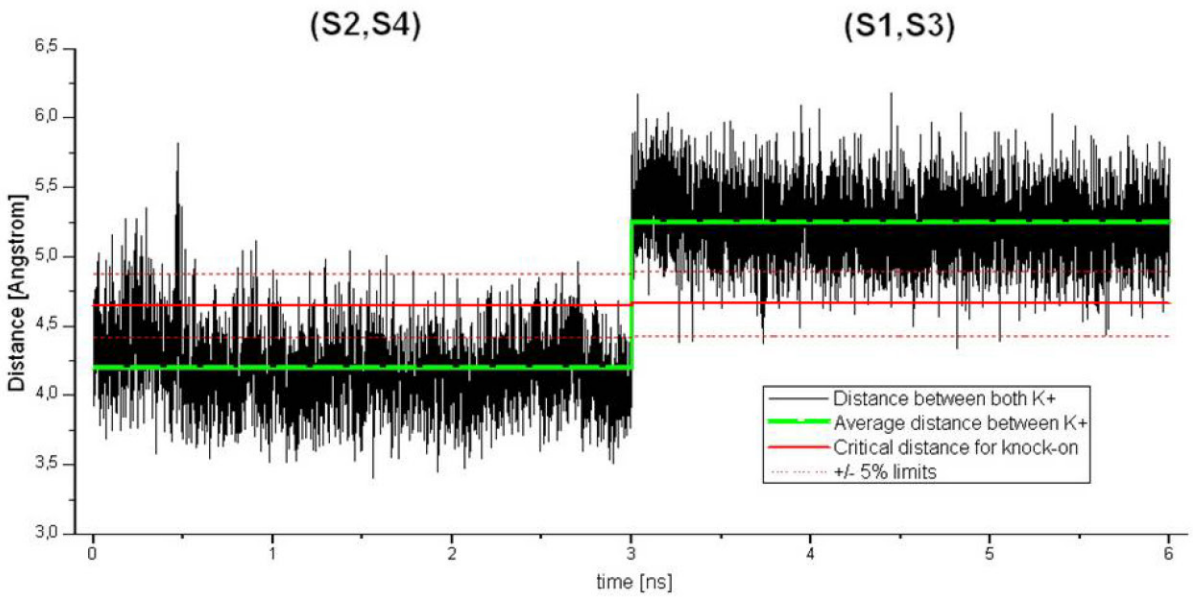

Figure IV.7 Distance entre les ions K^+ en fonction du temps dans le filtre de sélectivité de KcsA. Les 3 premières nanosecondes (ns) correspondent à la distance K2-K4 de la séquence (S2, S4) alors que la distance K1-K3 de la séquence (S1, S3) est indiquée sur les 3 autres ns. Les distances moyennes (trait vert) sont égales à 4.19 Å dans (S2, S4) et à 5,24 Å dans (S1, S3). La ligne rouge indique la condition nécessaire à l'augmentation ou à la diminution des distances pour que le processus de « knock-on » intervienne dans les deux séquences. Des barres d'erreur de 5% sont également considérées (lignes rouges en pointillés).

Insight into the origins of the barrier-less knock-on conduction in the KcsA channel: molecular dynamics simulations and *ab initio* calculations†

Sebastian Kraszewski,*[a] Céline Boiteux,[b] Marek Langner[a] and Christophe Ramseyer[b]

Received 22nd September 2006, Accepted 19th December 2006
First published as an Advance Article on the web 22nd January 2007
DOI: 10.1039/b613668k

Since the pioneering work of Zhou *et al.* (Y. Zhou, J. H. Morais-Cabral, A. Kaufman and R. MacKinnon, *Nature*, 2001, **414**, 43–48) it is now well established that the *streptomyces lividans* potassium channel (KcsA) can accommodate more than one ion, namely between 2 and 3. As a result, it is usually assumed that the conduction of ions proceeds through a barrier-less knock-on mechanism. This one is an alternation of two sequences containing either 2 or 3 ions which have nearly the same energies. However, the origin of such knock-on mechanism is not clearly known. The entry and the exit of ion in or out of the selectivity filter are suspected to be due to the repulsive interactions between ions. In this work, molecular dynamics simulations running over nanoseconds have been done in order to identify such events. Two specific situations, namely (S_1, S_3) containing 2 ions and (S_2, S_4) containing 3 ions, have been investigated regarding the different locations that ions can occupy during their diffusion through the selectivity filter of KcsA. We show that contractions of the (S_1, S_3) file and dilation of the (S_2, S_4) file are at the origin of the passage from one sequence to the other. The comparison between the experimentally observed diffusion rate and the occurrence's frequency of such contractions or dilation confirm the importance of such events. *Ab initio* calculations have also been conducted in order to examine the effect of ion polarization in the filter of KcsA. During the contraction of the ion/water file, one charge at the extra-cellular mouth of the channel strongly deviates from the others. This behavior could guide the diffusion direction to a certain extent since the contraction of the (S_1, S_3) is favored.

1. Introduction

Ion channels are proteins inserted in the membrane lipid bilayer of cells that form aqueous pores. Ion permeation is crucial for a variety of biological functions such as nervous signal transmission and osmotic regulation. They allow ions to cross the hydrophobic barrier of the core membrane, guaranteeing to the cell a controlled exchange of ionized particles.[1,2] As all membrane proteins, ionic channels are difficult to crystallize and up to 1995, no high resolution structures of a potassium channel were available. In 1995, the cloning of the first bacterial gene from *streptomyces lividans* encoding for a potassium selective channels (the KcsA gene)[3] opened the way to large production of purified K^+ channel and led in 1998 to the KcsA channel crystallization.[4] Research in ion channels, as in other areas of biology, has long had a strong experimental tradition with relatively little input from theory. The reason for this imbalance between theory and experiment is usually attributed to the complexity of both the biological processes and the underlying molecular structure involved in their execution. Rapid advances in two frontiers, that is determination of the tertiary structures of macromolecules from X-ray diffraction and NMR, and an exponential increase in computational power allowing large-scale simulations of biological processes now give hope that theory and experimental studies will be complementary. Studies of ionic channels witness these complementarities. Indeed, the publication of the crystal structure of the KcsA channel at 3.2 Å resolution[4] and its refinement at 2.0 Å[5,6] gave rise to a large effervescence in this field of research. These high-resolution X-ray structures of the bacterial KcsA K^+ channel brought a new insight into the ion channel science. It was established that the most important feature in KcsA structure is a narrow (*ca.* 3 Å) filter. It is responsible for selectivity and conduction[5–9] and possibly for the fast gating of the channels.[10–15] Aside, a large number of molecular dynamics (MD) or Brownian dynamics (BD) simulations[16,17–22,24–26] provided an opportunity to relate with experiments. In particular, these simulations were able to give some insights into the various physiological functions associated to channels (selectivity, gating, permeation,...). Experimentally, the pore was found to be occupied by more than one

[a] *Department of Physics, Wyb. Wyspiańskiego 27, Wrocław University of Technology, 50-370 Wrocław, Poland*
[b] *Laboratoire de Physique Moléculaire—UMR CNRS 6624-Faculté des Sciences, la Bouloie, Université de Franche-Comté, 25030 Besançon Cedex, France*
† The HTML version of this article has been enhanced with colour images.

This journal is © the Owner Societies 2007

ion, that is between 2 and 3. Ion locations of the binding sites of K^+ ions and water molecules in or near the selectivity filter were also undoubtedly observed. Recent MD results revealed barrier-less "knock-on" conduction in the filter.[7,16] This mechanism can be briefly explained as follows. If we consider the channel which initially contains N ions, the translocation is first due to the entry of the $N + 1$th ion from one side of the filter which pushes them through the pore until the ion from the opposite side escapes the solution. In this case, the translocation of the ion is an alternation of the states N and $N + 1$ ions. In the case of KcsA channel $N = 2$. The ion translocation in the filter follows a barrier-less[5] mechanism in the sense that the energy of the system remains almost the same during the entry or exit of ions inside or outside the filter. S. Bernèche and B. Roux[7] found a small free energy barrier ranging between 2 and 3 kcal mol^{-1}. It was also recently argued that this knock-on barrier-less conduction can be considered a universal mechanism of ion translocation in ion channels with multiple occupancy[26] since it can allow the maximal current flow that a given channel can support. Finally, we have reported in one of our previous study that concerted motions between ions and water molecules inside the filter occur.[24] Through the calculation of correlation functions, the motion of this species as a whole (file motion) has been postulated accordingly to the quasi-ion model developed by Yesylevskyy and Kharkyanen.[26]

In this paper, we want to address some more specific features that concern mostly this knock-on mechanism. In section 2, we give an overview of our numerical methods while section 3 is devoted first to the origins of such mechanism, namely the structural and dynamical reasons which can explain such translocation. In this section, we will also make the statistics of knock-on events, in order to test their efficiency. Since knock-on diffusion leads to small distances between the ions in the filter (and hence strong repulsive interactions), we have also analyzed the role of polarization, *i.e.* distortion of electronic clouds, in terms of partial charges.

2. Methods

2.1 Molecular dynamics simulations

Our model of membrane channel was built in order to reproduce as well as possible the experimental conformation deduced from X-ray at 2.0 Å resolution,[6] namely 1K4C structure. We have also taken into account the surroundings of the protein. The lipid bilayer of the cellular membrane is modeled by an octane box which has been proved to be efficient to mimic the membrane hydrophobic behavior.[19] We have thus considered a box of about 73 $Å^3$ where we have immersed the portion of protein ranging from Trp66 and Trp92 inside an octane slab of 29 Å of thickness. The rest of the protein is hydrated with water molecules. On each part of the octane slab, the extracellular and intracellular sides are mimicked also by a slab of 22 Å thickness of water. Note that water must also hydrate the protein's cavity since the presence of water in that zone has been proved by EPR experiments.[27] Finally, it should be mentioned that we must distinguish the water molecules which constitute the solvent (intra- and extracellular area) from the ones which hydrate the cavity. In fact, the water density of the bulk water has been chosen for molecules in the extra- and intracellular sides while the density of water molecules in the cavity was determined by evaluating the Connolly surface.[28]

The channel is mostly constituted of three main regions (filter, cavity and gate). In this paper, we focus on the narrowest part of the pore which acts as a selectivity filter for the K^+ ions. It is represented in Fig. 1 with different ion occupations during the translocation. It is formed by the backbone carbonyl oxygens of the TVGYG sequence, an amino acid sequence commonly seen in potassium channels. It extends over about 12 Å with a mean radius of about 1.4 Å. At the membrane center, the size of the pore increases to form a 5 Å radius hydrophobic cavity, which can contain up to 40 water molecules. As already mentioned, the pore axis, at the filter level, contains both K^+ ions and water molecules. In agreement with Zhou *et al.*,[6] six of the seven ionic sites elucidated, namely, 2 extra cellular sites S_0 and S_{EXT} and 5 sites S_1 to S_{CAV} inside the channel were filled by two distinct alternate sequences of K^+ ions and water molecules. These sequences, namely WKWKW and KWKWK are shown in Fig. 1. They contain the occupancies of interest, namely 2 and 3 ions, respectively. For clarity and for homogeneity reasons with respect to the literature, these ones will be called (S_1, S_3) and (S_2, S_4), respectively. These sequences describe successive states of the translocation of K^+ ions in the filter during the diffusion process (see Fig. 1). In a previous study, we have already conducted MD calculations on the (S_2, S_4) sequence.[25] In the present paper, we have also investigated the second sequence. It is important to note that the passage from one sequence to the other is not observable in our simulation but only the initial stages of these can be elucidated. We refer the

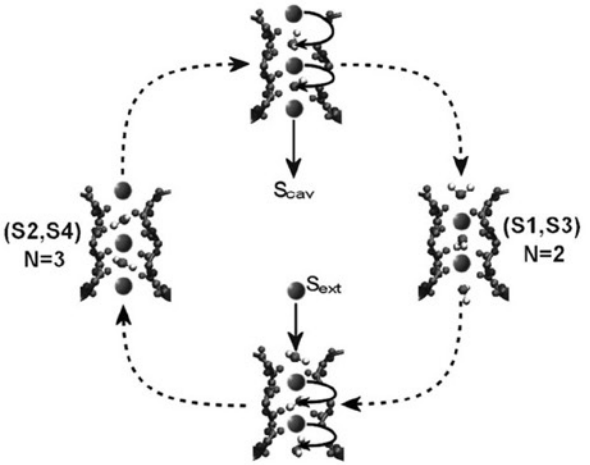

Fig. 1 Schematic representation of the barrier-less knock-on mechanism in the KcsA selectivity filter. An ion enters the channel (bottom view), which already contains two ions and pushes them along the pore. As a result, the state of triple occupancy (S_2, S_4) (or KWKWK) is formed (left view). The ion from opposite side escapes to solution (top view) and the state of double occupancy (S_1, S_3) (or WKWKW) is restored (right view). Note that the two sequences modeled here are constituted of an alternation of K^+ ions and water molecules.

This journal is © the Owner Societies 2007

reader to previous works[24,25] if modeling and equilibration of the channel details are required. All MD calculations were carried out using the AMBER suite of programs using the AMBER8 force fields.[29] The coulomb interactions were treated using the particle mesh Ewald method.[30] Water molecules were treated using the TIP3P model.[31] In order to be consistent with our previous simulations, the polarization interactions were switched off.[24] They will be investigated more precisely in the following by direct *ab initio* calculations. The integration of Newton's equations was made using a time step of 1 fs in order to take into account all motions including the fastest water rotations. The protein was first relaxed with the (S_2, S_4) sequence during at least 3 ns. The first sequence was then replaced by the (S_1, S_3) configuration and the whole system was equilibrated again for 3 ns.

2.2 Quantum calculations

We have conducted quantum calculations on conformations generated by these two classical MD simulations. At present, it is not possible to calculate the entire protein electronic structure from first-principles methods. Therefore, we have restricted our analysis to the filter region, namely, on a system representing a reasonable description of the K^+–protein interactions.[32] We choose to more specifically look at S_1 to S_4 sites, and therefore we have truncated KcsA structure at the level of the four Gly79 residues, where the peptide bond with Asp80 was cut (oxygen forming a double bond with carbon atom) and near the cavity below the four Thr74, –NH of the amide bond was completed to NH2. The portion considered was thus (Thr74-Thr75-Val76-Gly77-Tyr78-Gly79). No lipidic or water environment constitutive of the MD construct was considered, and the total number of atoms was 332. The electrostatic potential energy surfaces were computed using GAUSSIAN-03[33] at Hartree–Fock at the 6-31G(d) level of theory, without any further energy minimization, in order to be strictly consistent with the MD snapshot pictures. We have determined the Merz–Kollman (MK) partial charges[34] which have been proved to reflect quite well the polarization effects.[35] Indeed, the charges derived from the potential generally reproduce the first multipole moments well and optimally also intermolecular interactions. A number of studies have shown the superiority of such charges compared to those derived from other methods and, among them, it is generally assumed that the MK method gives the best values according to electrostatic criteria. They are conformation dependent but don't depend on the choice of the basis set.

3. Results and discussion

Fig. 2 exhibits the locations of K^+ ions and water molecules along the pore axis z as a function of time. The first 3 ns correspond to the (S_2, S_4) sequence containing $N = 3$ ions while in the last 3 ns, the (S_1, S_3) sequence with $N = 2$ is investigated. All these species located in the selectivity filter remain stable in the nanosecond time scale. This corroborates again the occurrence of 4 binding sites in the filter observed experimentally.[5,6] Nevertheless, the locations of these sites can differ from one sequence to another. Indeed, one site which is occupied by K^+ ion in a given sequence is occupied by a water in the other sequence and *vice-versa*. It is obvious that due to the strength of the electrostatics in such a protein system, the equilibrium sites can be shifted. The root mean square deviations (rmsd) of the corresponding positions along z do not exhibit large values, indicating again the stability of the sites. Indeed, we found rmsd's of 0.4 Å in almost each site and in the two sequences whatever the site is occupied by a water molecule or a potassium ion. As a comparison, the closest water molecule from the filter mouth in the cavity side exhibits a rmsd of 2.8 Å in the (S_2, S_4) sequence while it reaches only 0.8 Å for the other molecule in the extracellular side. These values are still larger than those obtained in the inner part of the filter. It should also be mentioned here, even if it has already been observed and analyzed in the (S_2, S_4) sequence, that correlated motions take place in the two sequences. Indeed, the shapes of each motions of water molecules and ions are closely related, especially in the (S_2, S_4) sequence during the first 3 ns.

The root mean square deviation (rmsd) of the protein remains also very small (less than 1.5 Å) in the presence of such files of ions trying to keep them inside the filter.[24] Only

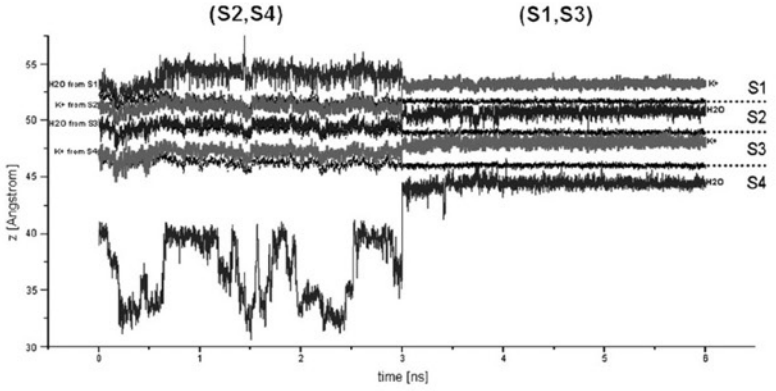

Fig. 2 Location of K^+ ions and water molecules along the pore axis z as a function of time. The 3 first ns corresponds to MD results for the (S_2, S_4) sequence while (S_1, S_3) sequence is investigated between 3 and 6 ns of simulation. Four binding sites are still observed. Small shifts of the site locations are obtained when comparing both sequences.

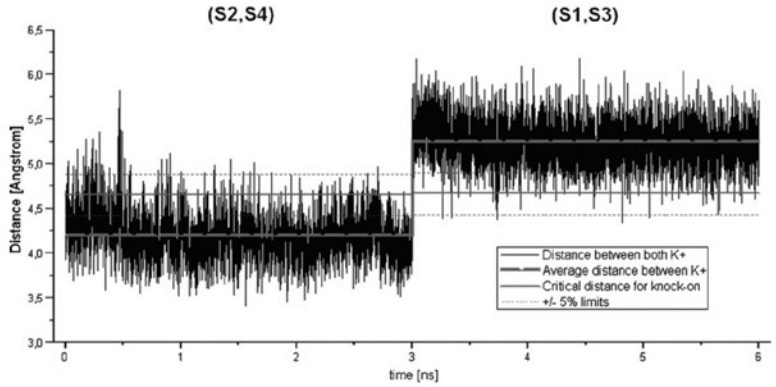

Fig. 3 Distance between K^+ ions as a function of time in the selectivity filter of KcsA. The first 3 ns correspond to the K_2–K_4 distance in the (S_2, S_4) sequence while K_1–K_3 distance of the (S_1, S_3) sequence is shown on the remaining 3 ns. The average distances (thick line) are equal to 4.19 Å in (S_2, S_4) and to 5.24 Å in (S_1, S_3). The thin line indicates the necessary condition of increase or decrease of distances for the knock-on process for both sequences. Error bars of 5% are also considered (dashed lines).

rare and sudden situations, known to be at the origin of the knock-on diffusion can disturb this well-equilibrated structure. An intuitive view of the knock-on is usually assumed: since at room temperature, atoms have energies proportional to thermal energy (the proportion depends only on their degrees of freedom), they can make large deviation around their equilibrium positions. These atoms can thus sometimes explore repulsive interactions and behave very differently. In the case of ions in the channel, the knock-on diffusion or, more precisely, the passage from the $N = 2$ to $N = 3$ configurations should be due to a sudden contraction of the ion–ion distance while the passage from the $N = 3$ to $N = 2$ configurations should be due to a sudden increase of the ionic distances. Fig. 3 shows the distance between K_2 and K_4 in (S_2, S_4) and between K_1 and K_3 in (S_1, S_3) sequence. The average distances are found to be equal to 4.19 Å in (S_2, S_4) with a rmsd of 0.28 Å and to 5.24 Å in (S_1, S_3) with a rmsd of 0.24 Å. The equilibrium distances shown here result from a subtle balance between the interactions of the ions and between the ions with the rest of the system (protein, membrane and water). Some peaks corresponding to large deviations (increase or decrease of the distance) from the average distance can be observed in Fig. 3. They clearly reflect the knock-on condition. It is however difficult to extract a good criteria to discriminate which event is part of the knock-on diffusion and qualitative arguments should be used at this point. If one assumes that the total potential can be modeled as a Lennard-Jones form with characteristic equilibrium distance R_{eq}, then the distances R at which repulsions take place should be such that $R < \frac{R_{eq}}{\sqrt[6]{2}}$, *i.e.* 89% of the equilibrium distance. This assumption appears licit with respect to the short distance discussed here. For the contraction expected in the (S_1, S_3), a knock-on event should occur for $R < 4.66$ Å. Since this criterion is intuitive and the total potential could not behave as a simple Lennard-Jones form, we have also drawn in Fig. 3 some error bars (5% from this value). For the second sequence (S_2, S_4), we expect an increase of the distance which could lead to the exit of one ion from the filter. We have used the same criteria, namely, an increase of 11% of the equilibrium distance. Since $R_{eq} = 4.19$ Å, knock-on is found to occur for $R > 4.65$ Å. As one can see, the two critical distances (4.66 and 4.65 Å) are very close. This surprising fact certainly reinforces our criteria to discriminate such events. Again, an error bar of 5% is used to make sure that our potential form assumption is correct and that results can be discussed in a more quantitative way.

Within these criteria, we have calculated the frequency of such events. For the (S_1, S_3) sequence, 46 contractions occur during the 3 ns for $R < 4.66$ Å and only 5 remain if R is chosen in the lower limit $R < 4.43$ Å. For the (S_2, S_4) sequence, 150 increases of the ionic distance occur during the 3 ns for $R > 4.65$ Å and 47 still remain if R is chosen at its upper limit $R > 4.88$ Å. This features show that the contraction of the sequence even with 2 ions is less probable than the dilation of the sequence containing 3 ions. There are 3 times more (9 if we consider the limits) events in the (S_2, S_4) than in the (S_1, S_3). It is, in fact, rather obvious that a system where repulsive interactions should take place are less probable than other guided by attractive interactions and dissociations mainly. Finally, we can compare these frequencies of events with the observed experimental diffusion. Indeed, it is often reported that 10^7 ions can cross the channel each second.[7] This means that on average only 1 diffusion of ion occurs each 10 ns. As a result, there are enough situations which can promote the knock-on diffusion. The efficiency of the diffusion process is the number of contraction/dilation events for a single diffusion. It can reach 1/5 to 1/150 each 3 ns, depending on the sequence and on the criteria used here.

At this step, we have clearly illustrated the fact that thermal motions inside the filter can lead to the particular knock-on mechanism. This view is certainly correct but is still reinforced by another reason which is specific to KcsA. Indeed, a metastable site located at the intracellular side of the filter near Thr74 and Thr75 residues has been highlighted by several authors.[7,24] In the (S_2, S_4), the electrostatic interactions of a K^+ ion in S_4 site with Thr75 residue were shown to be more favorable than those with Thr74 residues. Nevertheless, it is less hydrated when it faces the Thr75 residues than when it faces Thr74. This subtle competition between hydration and

 This journal is © the Owner Societies 2007

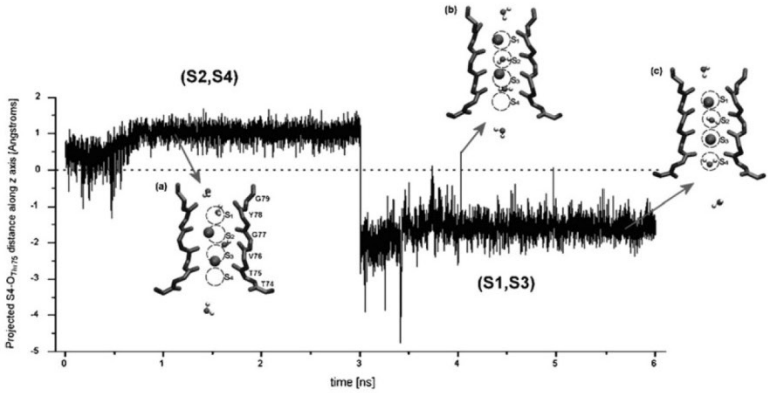

Fig. 4 During the first 3 nanoseconds, the projected distance along the pore axis between K_4 ion in the (S_2, S_4) sequence and average position of oxygens of Thr75 is represented as a function of time. For the remaining time (between 3 and 6 ns), the projected distance along the pore axis between oxygen of water molecule W_4 in the (S_1, S_3) sequence and average position of oxygens of Thr75 is also represented. Dashed line indicates the average position of the oxygen atoms of Thr75 residues. In the (S_2, S_4) sequence, positive values indicate the stable site of K^+ ion on top of the Thr75 residues, that is out of the mean S_4 site (a). For the (S_1, S_3) sequence, only few situations where the water molecule W_4 escapes from the S_4 site are observed (b) when compared to the mean configuration (c).

electrostatics leads finally to a particular behavior where K^+ ion in S_4 can undergo large motions due to thermal energy but also because it has to explore these two non-equivalent configurations. We have also focused on such events. Fig. 4 exhibits the time dependence of the projected distance along the pore axis between K_4 and the average position of oxygens from Thr75. For the (S_1, S_3), the S_4 site is occupied by a water molecule. The distance between oxygen of water and the average position of oxygens from Thr75 is also plotted. As expected, the K_4 ion is mainly located above the Thr75 oxygens (see inset a) since the projected distance is mostly positive. Only between 0.02 and 0.6 ns, the metastable site below Thr75 is observed. For the (S_1, S_3) sequence, the distance between oxygen of water molecule and Thr75 oxygens is always negative (the water molecule lying inside S_4 site, see inset c) except in sudden and particular situations (inset b) where the water molecule leaves the binding site S_4 and strongly interacts with K_3. As a result, this leads to strong contractions of the (S_1, S_3) sequence. Three distinct events can be observed on the time scale investigated here at 3.73, 4.02 and 4.97 ns. Two of them correspond to the strongest contractions already observed in Fig. 3 when one considers the lower limit $R < 4.42$ Å for the occurrence of knock-on. As a conclusion, water molecule in the S_4 site can also lead to the knock-on diffusion by inducing strong changes in the ionic distances, especially in the (S_1, S_3) sequence.

Polarization effects are more and more suspected to play a significant role in the mechanism regulating K^+ binding[35] and permeation[36] in the KcsA filter. We have recently shown that the pore selectivity[32] for K^+ over Na^+ ions can also be investigated on the basis of the same arguments. Until now, it was generally thought that entropic effects or dehydration of ions (Na^+ and K^+, mostly) can lead to substantial changes at the entrance of the extra-cellular mouth of the channel. More specifically, the difference in activation free energy was found equal to 3.1 kcal mol^{-1} [23] at the entry of the selectivity filter was found different for the two types of ions. We have also postulated that the binding inside the filter can be very different for the two species when polarization is introduced. These calculations were done only on the (S_2, S_4) sequence on a restricted part of the filter. A simple view of this phenomenon can be drawn by calculating the effective or partial charges which act on the ions confined in this narrow area constituted mostly by carbonyl groups. As a result, Na^+ ions are shown to be not much polarized (charges remain +1) while K^+ charge undergoes large deviations (charges can decrease even up to +0.8). In this work, we have recalculated both the two sequences and enlarge a little bit our modeled system in order to rule out finite size artefacts. Fig. 5 represents the charges on K^+ ions obtained in two specific sequences corresponding to knock-on phenomena (see insets (a) and (b) in Fig. 4). We retrieve the tendency already observed in our previous study, namely, a decrease of partial charges inside the filter. The charges on the S_2, S_3 and S_4 site are 0.87. To validate

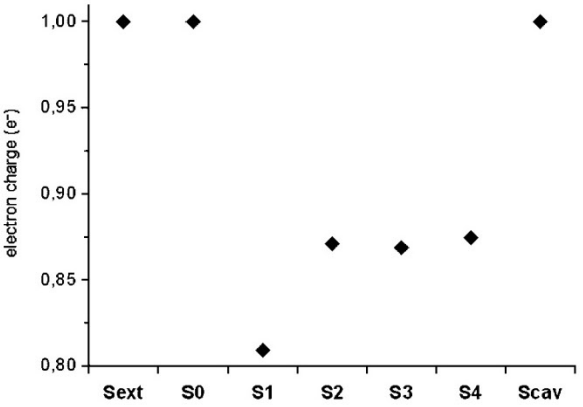

Fig. 5 Partial charges of ions calculated in two different sequences (S_2, S_4) and (S_1, S_3) corresponding to specific configurations, namely (a) and (b) from Fig. 4. Some charges of ions inside external positions from the filter S_{EXT}, S_0, S_{CAV} are also determined. A decrease of the charges is obtained inside the filter (0.87 on average). Note that the stronger change is obtained for S_1 (0.81).

these Merz–Kollman charges, we have also calculated both charges on water molecules and on ions located at the internal (S_{CAV}) and external (S_0 and S_{EXT}) mouths of the filter. The results are very convincing since for water we retrieve the TIP3P charges[31] used to model water in MD force fields. In addition, the charges for those external and internal K^+ ions remain clearly 1. A surprising feature occurs for the ion located in S_1 site, presented there in the (S_1, S_3) sequence. Indeed, a strong charge decrease is obtained (0.81). From a mechanical point of view, the global decrease of the charges could have an impact on the passage from the $N = 2$ configuration toward the $N = 3$ one. Indeed, the previous analysis shows that this alternation should proceed by a decrease of the distances in the ionic file in order to let some free space for the 3rd next ion to enter the filter (see graphical abstract image). Here, the effect of polarization in the knock-on situation is to promote a decrease of the repulsive interactions between ions especially at the external mouths. As a consequence, distances between ions should reduce and favor the entry of another ion, especially in the external mouth of the channel, namely in the S_1 site. Equivalently, the repulsive forces necessary to induce such contraction of the K^+ file could be reduced by the introduction of such polarization effects and hence the lower efficiency (in terms of frequency of events) for the (S_1, S_3) sequence toward the (S_2, S_4) one will certainly increase.

4. Conclusion

In this paper, we have investigated the physical origins of the barrier-less knock-on diffusion. The MD simulations conducted on the (S_1, S_3) and (S_2, S_4) containing 2 and 3 ions, respectively, show that contractions and dilations of the ionic files can be obtained in order to promote the passage from one configuration to the other. We found a criteria for discriminating which events can be treated as effective for the knock-on process. As a result, a decrease (an increase) of 11% of the equilibrium distance between ions in the (S_1, S_3) sequence (in the (S_2, S_4) sequence) allows another ion to come inside (to escape from) the selectivity filter of KcsA, though the alternation of the two sequences is mainly governed by the repulsive interactions between ions. We found sometimes that another reason can induce strong distance changes with respect to equilibrium configurations. Indeed, we have elucidated the role of Thr75 residues which exhibit a kind of double-well in their vicinity. As a result, water molecule can sometimes escape from the S_4 site and induce huge contraction of the (S_1, S_3) file. The frequencies of such events, namely contractions and dilations, due to repulsive interactions and Thr75 residues are rather high (more than 10 per ns) with respect to the efficient measured diffusion (1 ion per 10 ns). This efficiency is reinforced by the polarization effects which can be taken into account through the calculation of partial charges. Indeed, the ion's charge decreases from 1 (outside the filter) to 0.87 (inside the filter). This leads to the decrease of the repulsive interactions and thus allows a better contraction of the (S_1, S_3) sequence. This analysis is fully consistent with the barrier-less knock-on assumptions made by S. Yesylevskyy and V. Kharkyanen.[26]

Acknowledgements

We would like to express our thanks to S. Yesylevskyy and V. Kharkyanen for the fruitful discussions concerning the barrier-less knock-on model.

References

1 F. M. Ashcroft, *Ion channels and disease*, Academic Press, San Diego, 2000.
2 B. Hille, *Ionic channels of excitable membranes*, Sinauer Associates, Sunderland, MA, 2001.
3 H. Schrempf, O. Schmidt, R. Kummerlen, S. Hinnah, D. Muller, M. Betzler, T. Steinkamp and R. Wagner, *EMBO J.*, 1995, **14**, 5170–5178.
4 D. A. Doyle, J. M. Cabral, A. Pfuetzner, A. Kuo, J. M. Gulbis, S. L. Cohen, B. T. Chait and R. MacKinnon, *Science*, 1998, **280**, 69–77.
5 J. H. Morais-Cabral, Y. Zhou and R. MacKinnon, *Nature*, 2001, **414**, 37–42.
6 Y. Zhou, J. H. Morais-Cabral, A. Kaufman and R. MacKinnon, *Nature*, 2001, **414**, 43–48.
7 S. Bernèche and B. Roux, *Nature*, 2001, **414**, 73.
8 R. J. Mashl, Y. Tang, J. Schnitzer and E. Jakobsson, *Biophys. J.*, 2001, **81**, 2473.
9 M. L. Chapman, H. S. Krovetz and A. M. J. VanDongen, *J. Gen. Physiol.*, 2001, **530**, 21.
10 P. Proks, C. E. Capener, P. Jones and F. M. Ashcroft, *J. Gen. Physiol.*, 2001, **118**, 341.
11 H. Choe, H. Sackin and L. G. Palmer, *J. Gen. Physiol.*, 1998, **112**, 433.
12 J. F. Cordero-Morales, L. G. Cuello, Y. Zhao, V. Jogini, D. M. Cortes, B. Roux and E. Perozo, *Nat. Struct. Mol. Biol.*, 2006, **13**, 311.
13 J. F. Cordero-Morales, L. G. Cuello and E. Perozo, *Nat. Struct. Mol. Biol.*, 2006, **13**, 319.
14 S. Bernèche and B. Roux, *Structure*, 2005, **13**, 591.
15 A. M. J. VanDongen, *Proc. Natl. Adad. Sci. U. S. A.*, 2004, **101**, 3248.
16 S. Bernèche and B. Roux, *Proc. Natl. Adad. Sci. U. S. A.*, 2003, **100**, 8644–8648.
17 B. Roux, S. Bernèche and W. Im, *Biochemistry*, 2000, **39**, 13295–13306.
18 S. Bernèche and B. Roux, *Biophys. J.*, 2000, **78**, 2900–2917.
19 C. Capener and M. P. Samson, *J. Phys. Chem.*, 2002, **106**, 4543–4551.
20 I. H. Shrivastava, D. P. Tieelman, P. C. Biggin and M. P. Samson, *Biophys. J.*, 2002, **83**, 633–645.
21 P. C. Biggin and M. P. Samson, *Biophys. J.*, 2002, **83**, 1867–1876.
22 T. W. Allen, A. Bliznyuk, A. P. Rendell, S. Kuyucak and S. H. Chung, *J. Chem. Phys.*, 2000, **112**, 8191–8204.
23 V. Luzhkov and J. Åqvist, *Biochim. Biophys. Acta*, 2001, **1548**, 194–202.
24 M. Compoint, P. Carloni, C. Ramseyer and C. Girardet, *Biochim. Biophys. Acta*, 2004, **1661**, 26–39.
25 M. Compoint, F. Picaud, C. Ramseyer and C. Girardet, *J. Chem. Phys.*, 2005, **122**, 045427.
26 S. Yesylevskyy and V. Kharkyanen, *Chem. Phys.*, 2005, **312**, 127–133.
27 A. Gross, L. Columbus, C. Altenbach and W. L. Hubbell, *Biochemistry*, 1999, **38**, 10324–10335.
28 M. L. Connolly, *Science*, 1983, **221**, 709–713.
29 D. A. Case, T. A. Darden, T. E. Cheatham III, C. L. Simmerling, J. Wang, R. E. Duke, R. Luo, K. M. Merz, B. Wang, D. A. Pearlman, M. Crowley, S. Brozell, V. Tsui, H. Gohlke, J. Mongan, V. Hornak, G. Cui, P. Beroza, C. Schafmeister, J. W. Caldwell, W. S. Ross and P. A. Kollman, AMBER 8, University of California, San Francisco, 2004.
30 U. Essmann, L. Perera, M. L. Berkowitz, T. Darden, H. Lee and L. G. Pedersen, *J. Chem. Phys.*, 1995, **103**, 8577–8593.

This journal is © the Owner Societies 2007

31 W. L. Jorgensen, J. Chandrasekhar and J. D. Madura, *J. Chem. Phys.*, 1983, **79**, 926–935.
32 P. Huetz, C. Boiteux, M. Compoint, C. Ramseyer and C. Girardet, *J. Chem. Phys.*, 2006, **124**, 044703.
33 M. J. Frisch *et al.*, *GAUSSIAN 03 (Revision B.03)*, Gaussian Inc., Pittsburgh PA, 2003, p. 41.
34 B. H. Besler, K. M. Merz, Jr and P. A. Kollman, *J. Comput. Chem.*, 1990, **11**, 431–439.
35 M. Compoint, C. Ramseyer and P. Huetz, *Chem. Phys. Lett.*, 2004, **395**, 510–515.
36 L. Guidoni and P. Carloni, *Biochim. Biophys. Acta*, 2002, **1563**, 1–6.

3.1.2 *L'aspect dynamique du filtre est-il important ?*

Nous avons également effectué une analyse approfondie des forces qui agissent sur les ions K^+ dans le filtre de sélectivité du canal KcsA afin d'estimer l'importance relative de l'influence statique et dynamique de la paroi du filtre et des molécules d'eau sur la perméabilité et la sélectivité ionique du KcsA. Dans l'article suivant *« Is the mobility of the pore walls and water molecules in the selectivity filter of KcsA channel functionally important? »*, nous avons montré que la dynamique du filtre de sélectivité contribue faiblement dans la force nette agissant sur les ions et peut être négligée dans les études axées sur les propriétés macroscopiques du canal, comme le courant. Contrairement au modèle de libre fluctuation des ligands de ROUX *et coll.* [123] nous démontrons que le squelette du filtre de sélectivité ainsi que le reste de la protéine peuvent être considérés comme statiques pour la majorité des applications. Nos données suggèrent que seuls les groupes carbonyles du filtre devraient être considérés comme flexibles. L'influence dynamique de ces groupements ne dépasse pas 3% de la force nette agissant sur les ions, tandis que l'influence dynamique de tous les autres atomes est négligeable (*voir Figure IV.8*). En revanche, nous avons constaté que les effets dynamiques des molécules d'eau sont un ordre de grandeur plus grand que la dynamique des atomes du filtre. Les forces instantanées provenant des molécules d'eau peuvent être si fortes qu'elles contrebalancent efficacement la force nette de la paroi du filtre agissant sur l'ion. Malgré la rareté de tels événements, ceux-ci peuvent néanmoins jouer un rôle crucial dans le passage des ions dans le filtre. Nos données suggèrent en effet que les fluctuations des molécules d'eau dans le filtre, ainsi que la répulsion entre les ions K^+, peuvent ainsi conduire au processus de « knock-on ». Ceci montre également que les modèles implicites du solvant ne doivent pas être utilisés pour les simulations à l'échelle nanométrique et notamment dans le filtre de sélectivité.

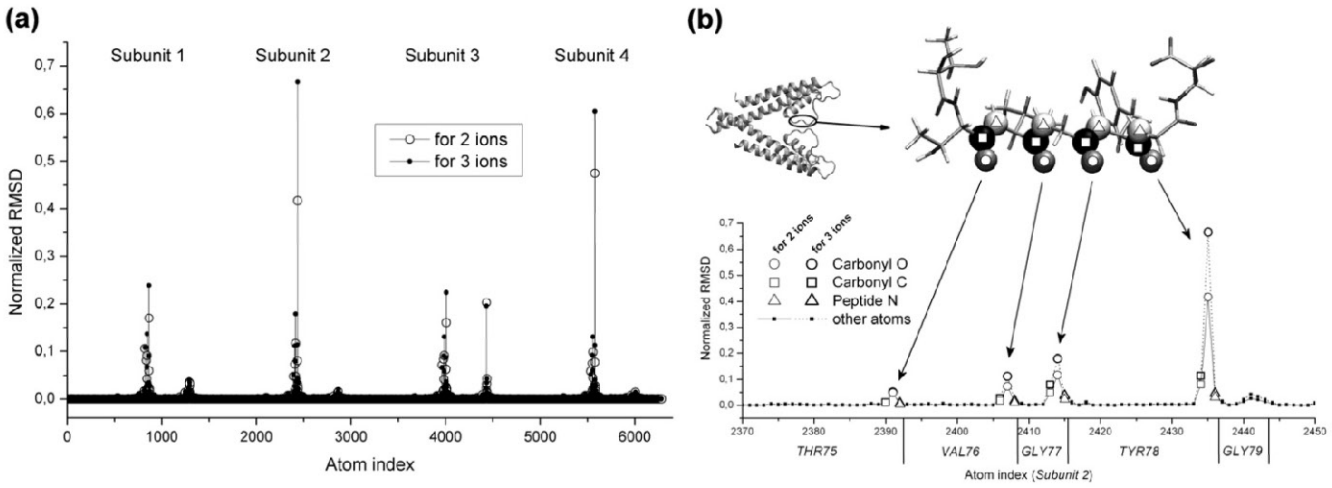

Figure IV.8 (a) Fluctuations maximales (RMSD) de la force agissant sur l'ion provenant de tous les atomes de la protéine. Les forces sont normalisées par rapport à la force nette agissant sur l'ion. Chaque pic correspond aux résidus du filtre de sélectivité. (b) Le zoom sur le pic du deuxième monomère indique que seule les forces des carbonyles agissant sur l'ion sont significatives.

Is the mobility of the pore walls and water molecules in the selectivity filter of KcsA channel functionally important?

Sebastian Kraszewski,[a] Semen O. Yesylevskyy,*[b] Céline Boiteux,[a] Christophe Ramseyer[a] and Valery N. Kharkyanen[b]

Received 18th December 2007, Accepted 1st February 2008
First published as an Advance Article on the web 28th February 2008
DOI: 10.1039/b719512e

We performed in-depth analysis of the forces which act on the K^+ ions in the selectivity filter of the KcsA channel in order to estimate the relative importance of static and dynamic influence of the filter wall and water molecules on ion permeation and selectivity. The forces were computed using the trajectories of all-atom molecular dynamics simulations. It is shown that the dynamics of the selectivity filter contributes about 3% to the net force acting on the ions and can be neglected in the studies focused on the macroscopic properties of the channel, such as the current. Among the filter atoms, only the pore-forming carbonyl groups can be considered as dynamic in the studies of microscopic events of conduction, while the dynamic effects from all other atoms are negligible. We also show that the dynamics of the water molecules in the filter can not be neglected. The fluctuating forces from the water molecules can be as strong as net forces from the pore walls and can effectively drive the ions through the local energy barriers in the filter.

Introduction

Ion channels are transmembrane proteins that form highly selective aqueous pores in the lipid bilayer. They allow the ions crossing the hydrophobic core of the membrane, facilitating the control of ionic concentrations in the cell.[1,2] Ion channels differ in functional, gating and selectivity properties.[3–7] All the K^+ channels (including voltage-gated K^+ channels[8,9]) share the same core structure. Tetrameric K^+ channels, like KcsA, are probably the most widely studied class of the ion channels because of their functional importance and the availability of several high-resolution crystal structures.[10–14] The structure of the KcsA K^+ channel is shown in Fig. 1. Each subunit contains two transmembrane helices (M1 and M2) with an intervening P-loop. The central structural element of the KcsA, conserved in all K^+ channels, is the selectivity filter. It is located close to the outer mouth of the channel and forms the narrowest part of the pore. The filter extends over about 12 Å with a mean radius of about 1.4 Å. It exhibits highly conserved TVGYG sequence and is responsible for the selective permeation of potassium ions.[12] The backbone carbonyl groups of the filter residues form five binding sites (S0–S4) that can be occupied by either K^+ ions or water molecules. Two additional sites (S_{EXT} and S_{CAV}) were elucidated experimentally at the extra and intracellular mouths of the filter, respectively. Under physiological conditions two or three K^+ ions occupy the filter. They reside in non-adjacent binding sites with the water molecules intercalated between them.

Computational studies, such as Molecular Dynamics (MD), Brownian dynamics and the quantum chemical calculations, are currently the only techniques which allow study of the mechanism of conduction and selectivity in the potassium channels in atomic detail.[15–26] The role of the selectivity filter mobility in permeation is argued since the first attempts of modeling the potassium KcsA channel. There is a hypothesis, widely accepted by the community, that the filter wall plays an important role in the selectivity and conductance of the channel.[27] This hypothesis is supported by the observation of concerted motion of the ions and the carbonyl groups, which form the filter wall.[28] It was also shown that the conformation of the filter wall depends on the positions of K^+ ions in the filter.[27] Recently, an induced-fit mechanism was proposed as explanation of selectivity.[28] This concept takes into account the dynamics of the hydration processes in the filter. The model of freely fluctuating carbonyls, which was proposed recently, shows significant correlation between

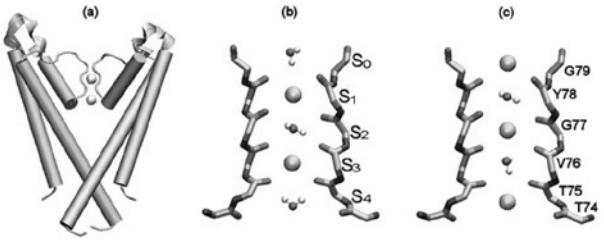

Fig. 1 Schematic representation of the KcsA channel structure. Only two of the four subunits are shown for clarity. (a) The whole channel as it appears in the crystal structure. (b) The selectivity filter with the double occupancy (S1,S3) configuration. Positions of the (S0–S4) binding sites are indicated. (c) Selectivity filter with the triple occupancy (S0,S2,S4) configuration. The residues forming the TVGYG sequence are also indicated.

[a] *Institut UTINAM, Laboratoire de Physique Moléculaire, UMR CNRS 6213, Faculté des Sciences et Techniques, Université de Franche-Comté, 16 route de Gray, 25030 Besançon Cedex La Bouloie, France*
[b] *Department of Physics of Biological Systems, Institute of Physics of National Academy of Science of Ukraine, Prospect Nauky 46, 03680 Kiev-28, Ukraine. E-mail: yesint3@yahoo.com*

This journal is © the Owner Societies 2008

the mobility of the structure and some microscopic events at the filter. However, all these data are obtained in rather short MD simulations (nanosecond time scale), which do not allow to estimate the current through the channel (microsecond time scale). As a result it is not known if the filter dynamics influences the macroscopic characteristics of the channel, such as the current or permeability ratio for different ions.

In this work we performed detailed analysis of the electrostatic and the van der Waals (VDW) forces, which act on the ions located in the selectivity filter of KcsA channel using the results of all-atom MD simulations. The static and dynamic influences of the filter wall and water molecules, located in the filter, on the permeating K^+ ions were studied. Our results allows to clarify the role of the flexibility of the filter wall in permeation and shows an important role of water molecules in driving the ions through the binding sites in selectivity filter.

Methods

The molecular dynamics simulations

The model of the KcsA channel was built using the experimental X-ray structure with 2.0 Å resolution (PDB code 1K4C[12]). The lipid bilayer was modelled by an octane slab, which mimics the hydrophobic core of the membrane.[30] Two slabs of water molecules were added from both sides to solvate the hydrophilic parts of the protein. The thickness of the octane slab is approximately 29 Å. The protein is positioned in such a way, that the residues Trp66 and Trp92 of each subunit are located close to two octane–water interfaces. The protein's cavity was hydrated with approximately 40 water molecules, which corresponds to the density determined by evaluating the Connolly surface.[31] The cases of double and triple ionic occupancies were studied. In agreement with Zhou *et al.*[12] the binding sites were filled by two distinct alternate sequences of K^+ ions and water molecules, namely WKWKW and KWKWK as shown in Fig. 1b and c. Our sequences of K^+ ions and water molecules in the filter will be referred according to the positions of the ions as (S1,S3) and (S0,S2,S4) sequences, respectively.

All MD calculations were carried out using the AMBER suite of programs with the AMBER8 force fields.[32] The Coulomb interactions were treated using the particle mesh Ewald (PME) method.[33] Water molecules were treated using the TIP3P model.[34] In order to be consistent with our previous simulations, the polarization interactions were switched off.[29] The integration step of 1 fs was used in order to account for all motions including the fastest water rotations. The protein was first equilibrated with two ions in the binding sites 1 and 3 ((S1,S3) sequence) during 3 ns. Then the simulation was stopped, three ions were placed into binding sites 0, 2 and 4 ((S0,S2,S4) sequence) and the whole system was equilibrated again for 3 ns. Production runs of 3 ns were performed for the systems with double and triple occupancies in NPT conditions. The trajectories were recorded with 1 ps intervals. The constant temperature was maintained with the Berendsen weak coupling algorithm.[36] The details of the simulation protocol are described in our previous papers.[29,35]

Force calculations

In order to estimate the influence of the dynamics of the filter walls on the permeating ions we evaluated the electrostatic and the VDW forces, which would act on the ion located in different positions of the channel axis. The force component, directed along the channel axis, was evaluated with small (0.1 Å) discrete steps and averaged over all trajectory frames. Several major assumptions were introduced:

(1) Possible radial motions of the ions are excluded from consideration. It is assumed that these motions are fast and can be averaged for each axial position of the ion.[37]

(2) No explicit interaction with water molecules is considered at this stage (the influence of water is analyzed separately below).

(3) The coordinates of the filter atoms are obtained in the conditions where the ions occupy one of the two stable configurations, namely (S1,S3) and (S0,S2,S4), while the forces are evaluated in all possible positions along the channel axis. As a results alternative configurations of the filter wall, which correspond to other placement of ions in the translocation process are not sampled. This is an inevitable consequence of restricted simulation time and the limited sampling.

The total non-bonded force F, which acts on the ion from particular atom i at particular trajectory frame k is

$$F_{ik}(z) = \left[a\left(\frac{6c_{i6}}{r_{ik}(z)^7} - \frac{12c_{i12}}{r_{ik}(z)^{13}} \right) + b\frac{q_{\text{ion}}q_i}{r_{ik}(z)^3} \right](z_{ik} - z)$$

where z is the position of the ion along the pore axis; c_{i6} and c_{i12} are the coefficients of the VDW interaction between K^+ and the ith atom defined in the force field; q_{ion} is the ion charge, q_i is the partial charge of the ith atom; $r_{ik}(z)$ is the distance between the ion and the ith atom for given frame; z_{ik} is the z coordinate of the ith atom for a given frame; a is the coefficient which converts the VDW energy into k_BT units if c_6 and c_{12} coefficients are expressed in kcal mol^{-1} Å^{-6} and kcal mol^{-1} Å^{-12}, respectively and the distance is in angstroms; b is the coefficient, which converts the electrostatic energy into k_BT units if the charge is expressed in elementary charges and the distance is in angstroms. For T = 300 K, a = 1.6788, b = 566.2.

We calculated the mean force acting on the ion in each position on the channel axis as

$$F_{\text{mean}}(z) = \frac{1}{N_{fr}} \sum_{k=1}^{N_{fr}} \sum_{i=1}^{N} F_{ik}(z)$$

where N is the number of atoms in the subset under study, N_{fr} is the number of trajectory frames.

The single-ion energy profile is calculated as:

$$E_{\text{ion}}(z) = -\int_{z_{\min}}^{z_{\max}} F_{\text{mean}}(z)\mathrm{d}z$$

where $z_{\min}$ and $z_{\max}$ are the boundaries of the filter in z direction measured from the center of masses of all heavy atoms in the filter. We assume that $z_{\min} = -20$, $z_{\max} = 20$, which is consistent with the conventions adopted in ref. 38.

This journal is © the Owner Societies 2008

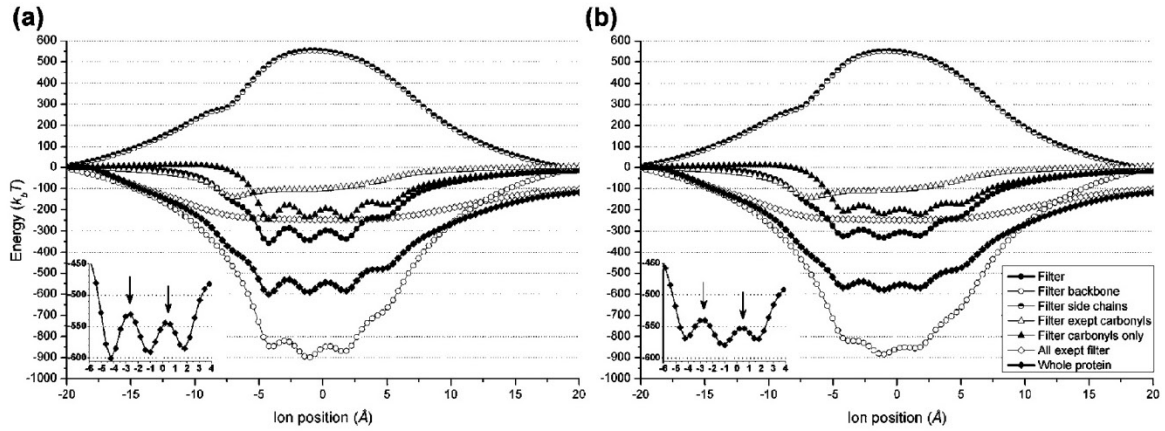

Fig. 2 Single-ion energy profiles in the selectivity filter region of KcsA channel produced by various subsets of atoms in presence of 2 (a) and 3 (b) ions. The insets show the energy barriers between the binding sites, which are indicated by the arrows. On this and all subsequent figures the Z coordinate of the center of masses of all heavy atoms of the filter-forming TVGYG residues is assumed to be zero.

The root means square (RMS) fluctuations of the mean force are computed as:

$$\Delta F_{\mathrm{rms}}(z) = \sqrt{\frac{1}{N_{fr}} \sum_{k=1}^{N_{fr}} \sum_{i=1}^{N} (F_{ik}(z) - F_{\mathrm{mean}}(z))^2}$$

The contribution of particular atom i into the RMS fluctuation of the force is computed as:

$$\Delta F_i(z) = \sqrt{\frac{1}{N_{fr}} \sum_{k=1}^{N_{fr}} (F_{ik}(z) - F_{\mathrm{mean}}(z))^2}$$

All force calculations were performed in VMD 1.8.6[39] using custom TCL scripts.

Results and discussion

Single ion energy profile in the filter region

Single-ion energy profiles play an important role in understanding the behavior of the ion channels. The single-ion energy profile is defined as the free energy of the single ion placed into a given position of the channel axis. Later on we will use the term "energy profile" instead of the "free energy profile" for the sake of simplicity. Single-ion energy profiles in the selectivity filter of KcsA channel were calculated in several studies.[38,40] It was shown that the profile has an inverted bell-like shape with a relatively small local minima at the bottom, which corresponds to experimentally determined binding sites for the K^+ ions and the water molecules. While the shape of the profile can be considered well-established, its depth is still uncertain. The values found in the literature vary from 10 to 200 kBT depending on the calculation technique and the assumptions made.[41] In the present work we calculated the single-ion energy profile of electrostatic and VDW forces between the channel wall and the ion in the pore. We computed the profile created by the whole channel-forming protein and extracted the parts of this profile, created by various functionally important subsets of atoms in the structure, such as the whole filter, filter backbone, filter carbonyls *etc*. The results presented in Fig. 2 correspond to the cases of double and triple occupancies of the selectivity filter.

It is well seen that the fine shape of the energy profile is created mostly by the carbonyl groups of the selectivity filter, while the other atoms of the filter backbone increase the overall depth of the potential. It is interesting to note that the influence of the filter side chains is repulsive, while the influence of the filter backbone is attractive to the ion. The rest of the protein imposes a very strong effect on the single ion energy profile in the filter despite the large distance from the ions. The filter itself produces the energy well of ~300 kBT, while the whole protein make this number twice larger—around 600 kBT. This means that the remote regions of the channel protein have a strong influence on the ions in the filter and their contribution cannot be neglected in the quantitative studies. At the same time the shape of the energy profile is not changed by these long-range interactions. Moreover, different ion sequences in the selectivity filter do not change the shape of the profile significantly. The only detectable difference between the cases of double and triple occupancies is the heights of the energy barriers between the binding sites. These barriers are approximately two times larger in the case of double occupancy (insets in Fig. 2). This observation confirms the well-known fact that the (S0,S2,S4) sequence is more stable than the (S1,S3) one.[25] It is not completely clear, however, what causes this difference. To address this question we computed average structures of the whole channel for the trajectories, which correspond to the double and triple occupancies of the selectivity filter and compared them. The root mean square deviation (RMSD) between these aligned structures is 0.58 Å. The RMSD deviation of the aligned selectivity filter regions of the average structures is even smaller (0.192 Å). This means that the average structure of the channel is almost independent on the sequence of the ions in the selectivity filter in our simulations. We did not study in details how observed minor structural differences can cause quite significant changes of the barrier heights, which are visible in Fig. 2. The most probable reason is the very small distance between the filter carbonyl groups and the ions in the binding sites, which leads

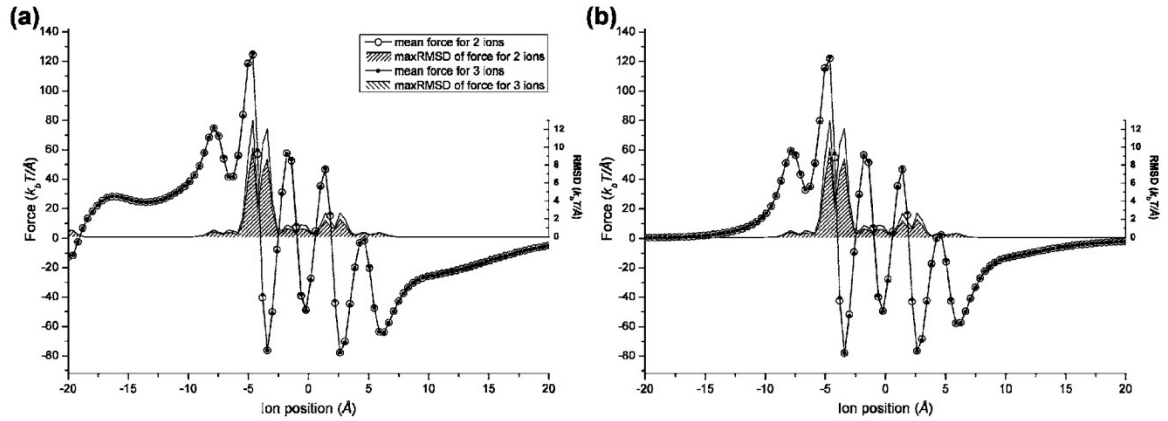

Fig. 3 Mean force and its associated RMSD fluctuations acting on the ion from all protein atoms (a) and from the selectivity filter only (b) in the presence of two or three ions in the filter as a function of ion position along the pore axis. Note the different scales used for forces and their RMSDs.

to extremely steep dependence of the energy profile in this region on the positions of the carbonyls.

We also computed the fluctuations of the filter structure during the simulations with particular occupancy. These fluctuations are much larger than the RMSD between the average structures for different occupancies (~0.5 Å and 0.192 Å, respectively). It is possible to speculate that during the simulations the instantaneous structure of the filter samples approximately the same conformational space for both occupancies, but the probabilities of different configurations depend on the occupancy, which results in slightly different average structures. This assumption should be verified by additional simulations, however.

In general the single-ion energy profile and the average structure of the channel are surprisingly insensitive to the occupancy of the selectivity filter in our simulations. We are aware that the simulation time is quite small and thus only small part of accessible conformational space is sampled. However, our data allows concluding that the general shape of single-ion energy profile in the filter region is insensitive to the occupancy of the filter, while the heights of the energy barriers between the binding sites can change significantly upon change of occupancy.

It should be emphasized that the electrostatic forces were computed in the present work by summing up the Coulombic terms for the protein atoms, while the MD trajectories were obtained using the PME summation of electrostatic forces over the multiple periodic images of the system.[33] This means that the calculated absolute depth of the single ion energy profile can be somewhat different from the real value observed in MD calculations. This can not, however, change the results and conclusions qualitatively.

The role of dynamics of the filter walls

The single ion energy profile is the time-averaged quantity. It is created by the mean force acting from the fluctuating channel structure to the ion in the filter. This force can be decomposed into the static component created by the static structure, "frozen" in the average conformation, and the fluctuating component, created by the fluctuations of the channel structure around this average conformation. To our knowledge the magnitude of this fluctuating force component was not studied in details. To estimate the magnitude of the force fluctuations, we calculated the RMSD of the force acting to the ion in each point on the filter axis. The results are shown in Fig. 3.

It is clearly seen that the magnitude of force fluctuations is rather small in comparison to the average force itself (note different scales in Fig. 3). RMSD of the force changes in accord with the force itself and reaches the maximum at the maxima of the force (the absolute value of the force is considered). The RMSD constitutes generally only 3% of the average force. This allows concluding that the dynamics of the filter does not change the force acting on the ion significantly and, as a consequence, does not influence the motion of the ions to the extent, which can be detected in most simulations. It is remarkable that the fluctuations of the force are identical for double and triple occupancy. This means that the sequence of the ions and water molecules in the selectivity filter does not influence the dynamic contribution of the selectivity filter walls to the force, which is acting on the ions.

Our data shows that the fluctuations of the filter atoms can be neglected and the filter can be considered essentially static for the majority of purposes, which imply the calculation of the macroscopic characteristics of the channel, such as current. In contrast, in order to study short time events, which are important for understanding channel selectivity, the filter has to be considered highly flexible and the carbonyl groups should be treated explicitly. This approach was also proposed by S. Yu. Noskov and B. Roux in their "toy model" to explain the selectivity of KcsA and NaK channels.[28]

Dynamics of individual atoms in the filter wall

Despite the fact that the dynamics of the filter can change the average force acting on the ions by only 3% in average, it is still possible that the motions of particular atoms in the filter wall influence the selectivity in the filter or other microscopic events of conduction. In order to study such events one can run sufficiently long MD simulations of the whole channel, but this seems to be excessively detailed, since it is obvious that only the atoms in the close proximity to the ion can change its

 This journal is © the Owner Societies 2008

motion significantly. In principle, it is enough to study the dynamics of only few atoms, which influence the ion directly on the short distance and keep the rest of the structure fixed, since the dynamic effects from the distant atoms are obviously negligible. Despite numerous technical problems, such partitioning was recently used in the molecular dynamics[28] and the Brownian dynamics[42] studies of KcsA channel. However, the subset of atoms, which were considered dynamic in these studies, was chosen rather arbitrarily. In order not to include excessive number of moving atoms into simulation, one has to know which atoms constitute the dynamic subsystem.

In order to clarify this question we computed the RMSD of the force acting on the ion created by each atom of the channel separately. This quantity was then normalized with respect to the net force acting on the ion from the whole filter and finally the maximal values of RMSD along the pore axis were recorded. To our knowledge this is the first attempt analyzing the dynamic influences of each individual atom in the channel structure on the motion of the ions. Fig. 4 shows the results of these calculations. There are eight pronounced peaks of RMSD, each pair of which corresponds to the single subunit of the KcsA channel. The larger peaks correspond to the filter-forming residues. The smaller peaks (with lower RMSD values) correspond to the gate region and more precisely the interaction with the Thr107 residue located in this narrow part of the protein. The fine structure of each large peak is shown in Fig. 4b. Each subunit produces four close peaks, which correspond to four filter-forming residues, namely Thr75, Val76, Gly77 and Tyr78. The last Gly79 of the well-known filter forming sequence TVGYG only produces a small contribution to the net force. There are only two atoms in each residue, which exhibit significant value of RMSD, namely the backbone carbonyl oxygen and the backbone carbonyl carbon, which are located very close to the ion. The fluctuations of the force produced by the motion of these atoms constitute around 3% of the net force acting on the ion. So, it is evident that the overall dynamic contribution of the filter is effectively reduced to the dynamic contribution of only 32 atoms (two atoms in each of four filter residues in each of four subunits) from the pore-forming carbonyl groups, while the dynamic contribution of all other atoms is insignificant. In principle this opens the possibility to construct very simple and time efficient simulation protocol for studying the microscopic events in the filter, which has only about 100 moving particles (filter carbonyls, ions and water molecules). The "toy model"[28] mentioned above can be used as a basis for such simulation protocols, which are, however, out of the scope of the present study.

The role of water

The role of water molecules in the functioning of the selectivity filter can hardly be overestimated. It is well known that the selectivity itself originates in a difference in dehydration costs for different ions.[12] However, the role of the water molecules in the narrow part of the filter is still a subject of discussion. In the context of the current work it was interesting to evaluate the force which acts on the ion in the filter from the water molecules. Unfortunately, it is not possible to include this force into the single-ion energy profile since the ions are confined by their initial binding sites during the MD simulations and the lengths of available trajectories are too small to sample other positions of K^+ ions. That is why we were only able to calculate the force, which acts on the ions fluctuating around their local equilibrium positions. This samples only the close proximity of the initial binding sites, but still provides some insight into the role of water molecules in permeation. We summed up the electrostatic and VDW forces from all water molecules located within the 25 Å from the ion of interest for each frame of the trajectory and plotted them as a function of the ion position. The computations were performed for the two trajectories, namely for the (S_1,S_3) and (S_0,S_2,S_4) configurations (Fig. 5).

In the case of double occupancy (Fig. 5a), the force from the water molecules is significantly different for the inner and outer ion (see average bar). The average force acting on the outer ion, located in the binding site S_1, is almost zero. By contrast, the average force acting on the inner ion, located in the site S_3, is about 12 k_BT/Å. The fluctuations of the force are

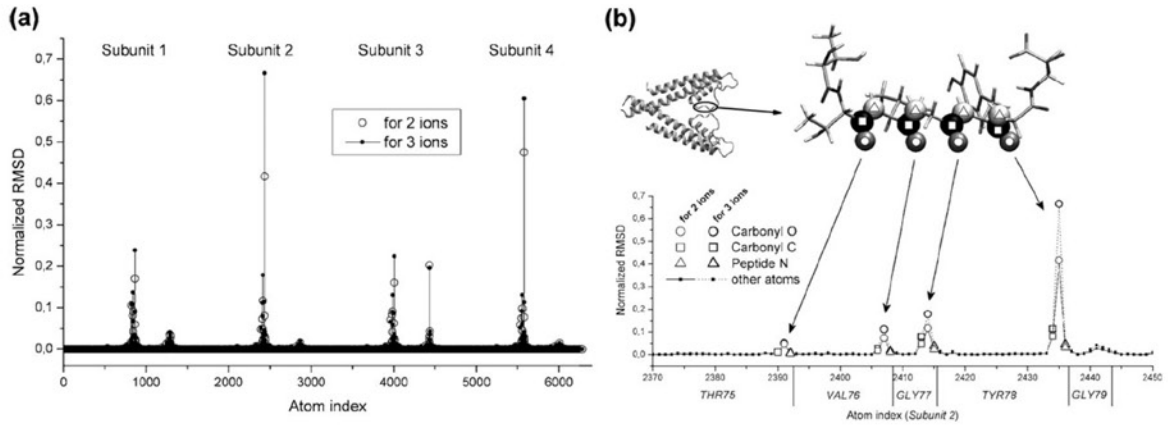

Fig. 4 (a) The maximal RMSD fluctuations of the force acting on the ion at every Z position from individual atoms normalized by the net force acting on the ion. Data collected for all atoms in the channel-forming protein in the presence of 2 and 3 ions in the filter. Each peak corresponds to TVGYG residues in one monomer. (b) Data zoomed on the filter residues (Thr75, Val76, Gly77, Tyr78 and Gly79) of the second monomer corresponding to structure with 2 and 3 ions.

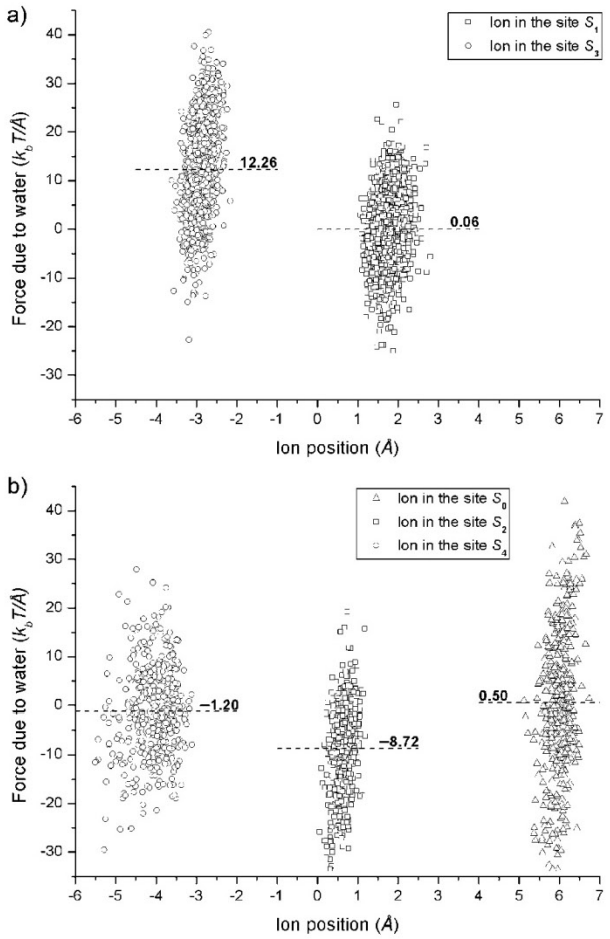

Fig. 5 The force acting on each ion from the water molecules located within 25 Å from the ion: (a) Two ions are located in the binding sites S_1 and S_3. (b) Three ions are located in the binding sites S_0, S_2 and S_4. For clarity, the values of average forces are given and indicated by the dashed lines.

also much larger for the inner ion. In the case of triple occupancy (Fig. 5b), the average forces for the ions in the sites S_0 and S_4 are essentially zero, while the ion in the binding site S_2 exhibits an average force of about $-9\ k_BT$/Å. However, the magnitude of force fluctuations can reach 40 k_BT/Å for the outer ion and 30 k_BT/Å for the inner ion. By contrast, the force fluctuations for the S_2 ion are smaller and reach only 20 k_BT/Å, which reflect the stronger confinement of this ion between the carbonyl rings.

In general, the maximal force acting on the ions from the water molecules constitutes as much as 50–150% of the net force, which acts on the ion at the same positions from the filter walls (as is evident from comparison with Fig. 3). This maximal force is observed only rarely during large fluctuations of the positions and orientations of the water molecules. However, such events can be crucial for conductance since they can allow jumps between the binding sites inside the filter, which are otherwise separated by prohibitively high energy barriers. This allows us to conclude that the dynamics of the water molecules is much more significant then the dynamics of the filter wall. This also strongly discourages from the usage of implicit solvent models in the modeling of the events in the selectivity filter, since it is clear that continuous models can not mimic the fluctuating forces imposed by the water molecules.

Conclusions

The ultimate goal of the majority of simulations of the ion channels is the prediction of their conductance. In this sense it is very important to know the amount of details, which should be included into the model in order not to lose the accuracy. Our work provides the evidence that the structure of the selectivity filter can be considered static in the simulations focused on obtaining the macroscopic properties of the channel. Although the selectivity filter displays considerable flexibility in our simulations (RMSD of ~0.5 Å) the force fluctuations, which originate from the structure fluctuations, remain very small. It is shown that the dynamics of the filter during the MD simulations can change the forces, which act on the permeating ions, by only 3% in comparison to the static average structure. Since the accuracy of the conductance calculations is usually smaller than this, accounting for dynamic effects is not justified.

It is shown that the dynamic contribution of the filter is independent on the filter occupancy, while its static contribution can be sensitive to small changes of the filter structure caused by different number of ions in the filter. The RMSD between the average structures of the selectivity filter in the cases of double and triple occupancies is only 0.19 Å in our simulations, however this leads to significant change of the heights of the energy barriers between the binding sites in the filter. Despite this differences the general shape of the single-ion energy profile is insensitive to the occupancy.

Our data suggest that only the carbonyl atoms of the filter forming residues can be considered as moving, while all the other structure of the filter can be modeled as static for the majority of applications. The dynamic influence of the carbonyl atoms can be as large as 3% of the net force acting on the ions, while the dynamic influence of all other atoms is negligible.

Finally, we have found that the dynamic effects of the water molecules are an order of magnitude larger than the dynamic effects of the filter atoms. Instantaneous forces from the water molecules can be so strong, that they effectively counterbalance the net force acting on the ion from the filter wall. Despite the fact that such events are rare, they can play a crucial role in hoping over the energy barriers between the binding sites. Our data suggest that fluctuations of the water molecules in the filter as well as the repulsion between the K^+ ions can lead to the knock-on translocation process. Our data also suggest that implicit solvent models should not be used for simulations of the selectivity filter.

Acknowledgements

V. Kharkyanen thanks the Université de Franche-Comté for providing the Visiting Professor grant, which stimulated this collaboration.

 This journal is © the Owner Societies 2008

References

1 B. Hille, in *Ionic channels of excitable membranes*, Sinauer Associates, Sunderland, 1992.
2 F. M. Ashcroft, in *Ion channels and diseases*, Academic Press, San Diego, 2000.
3 R. MacKinnon, *FEBS Lett.*, 2003, **555**, 62–65.
4 R. MacKinnon, *Biosci. Rep.*, 2004, **24**, 75–100.
5 E. Perozo, *Structure*, 2002, **10**, 1027–1029.
6 S. H. Chung and S. Kuyucak, *Eur. Phys. J.*, 2002, **31**, 283–293.
7 C. Miller, *Nature*, 2001, **414**, 23–24.
8 Y. Jiang, A. Lee, J. Chen, V. Ruta, M. Cadene, B. T. Chait and R. MacKinnon, *Nature*, 2003, **423**, 33–41.
9 B. S. Long, E. B. Campbell and R. MacKinnon, *Science*, 2005, **309**, 897–903.
10 H. Schrempf, O. Schmidt, R. Kummerlen, S. Hinnah, D. Muller, M. Betzler, T. Steinkamp and R. Wagner, *EMBO J.*, 1995, **14**, 5170–5178.
11 D. A. Doyle, J. M. Cabral, A. Pfuetzner, A. Kuo, J. M. Gulbis, S. L. Cohen, B. T. Chait and R. MacKinnon, *Science*, 1998, **280**, 69–77.
12 Y. Zhou, J. H. Morais-Cabral, A. Kaufman and R. MacKinnon, *Nature*, 2001, **414**, 43–48.
13 A. Gross, L. Columbus, C. Altenbach and W. L. Hubbell, *Biochemistry*, 1999, **38**, 10324–10335.
14 E. Perozo, D. M. Cortes and L. G. Cuello, *Science*, 1999, **285**, 73–78.
15 S. Bernèche and B. Roux, *Biophys. J.*, 2001, **78**, 2900–2917.
16 B. Roux, S. Bernèche and W. Im, *Biochemistry*, 2000, **39**, 13295–13306.
17 S. Bernèche and B. Roux, *Nature*, 2001, **414**, 73–77.
18 I. H. Shrivastava and M. P. Sansom, *Biophys. J.*, 2000, **78**, 557–570.
19 M. S. P. Sansom, I. H. Shrivastava, J. N. Bright, J. Tate, C. Capener and P. Biggin, *Biochim. Biophys. Acta*, 2002, **1565**, 294–307.
20 T. W. Allen, A. Bliznyuk, A. P. Rendell, S. Kuyucak and S. H. Chung, *J. Chem. Phys.*, 2000, **112**, 8191–8204.
21 T. W. Allen, S. Kuyucak and S. Chung, *Biophys. Chem.*, 2000, **86**, 1–14.
22 L. Guidoni, V. Torre and P. Carloni, *Biochemistry*, 1999, **38**, 8599–8604.
23 L. Guidoni and P. Carloni, *Biochim. Biophys. Acta*, 2002, **1563**, 1–6.
24 V. Luzhkov and J. Aqvist, *Biochim. Biophys. Acta*, 2001, **1548**, 194–202.
25 W. Treptow and M. Tarek, *Biophys. Lett.*, 2006, DOI: 10.1529/biophysj.106.095992.
26 W. Treptow and M. Tarek, *Biophys. Lett.*, 2006, DOI: 10.1529/biophysj.106.087437.
27 S. Y. Noskov, S. Bernèche and B. Roux, *Nature*, 2004, **431**, 830–834.
28 S. Y. Noskov and B. Roux, *J. Gen. Physiol.*, 2007, **129**, 135–143.
29 M. Compoint, P. Carloni, C. Ramseyer and C. Girardet, *Biochim. Biophys. Acta*, 2004, **1661**, 26–39.
30 C. Capener and M. P. Sansom, *J. Phys. Chem.*, 2002, **106**, 4543–4551.
31 M. L. Connolly, *Science*, 1983, **221**, 709–713.
32 D. A. Case, T. A. Darden, T. E. Cheatham III, C. L. Simmerling, J. Wang, R. E. Duke, R. Luo, K. M. Merz, B. Wang, D. A. Pearlman, M. Crowley, S. Brozell, V. Tsui, H. Gohlke, J. Mongan, V. Hornak, G. Cui, P. Beroza, C. Schafmeister, J. W. Caldwell, W. S. Ross and P. A. Kollman, *AMBER 8*, University of California, San Francisco, 2004.
33 U. Essmann, L. Perera, M. L. Berkowitz, T. Darden, H. Lee and L. G. Pedersen, *J. Chem. Phys.*, 1995, **103**, 8577–8593.
34 W. L. Jorgensen, J. Chandrasekhar and J. D. Madura, *J. Chem. Phys.*, 1983, **79**, 926–935.
35 S. Kraszewski, C. Boiteux, M. Langner and C. Ramseyer, *Phys. Chem. Chem. Phys.*, 2007, **9**, 1219–1225.
36 H. J. C. Berendsen, *Science*, 1996, **271**, 954–955.
37 S. Bernèche and B. Roux, *Biophys. J.*, 2000, **78**, 17A.
38 R. J. Mashl, Y. Tang, J. Schnitzer and E. Jakobsson, *Biophys. J.*, 2001, **81**, 2473–2483.
39 W. Humphrey, A. Dalke and K. Schulten, *J. Mol. Graphics*, 1996, **14**, 33–38.
40 S. Chung, T. W. Allen, M. Hoyles and S. Kuyucak, *Biophys. J.*, 1999, **77**, 2517–2533.
41 S. O. Yesylevskyy and V. N. Kharkyanen, *Phys. Chem. Chem. Phys.*, 2004, **6**, 3111–3122.
42 S. H. Chung and B. Corry, *Biophys. J.*, 2007, DOI: 10.1529/biophysj.106.098954.

3.2 Origine de la sélectivité dans le KcsA

Si les canaux ioniques comme le KcsA sont très efficaces (1 ion/10 ns) ils sont aussi très sélectifs. La probabilité de passage des ions Na^+ est réduite énormément par rapport à K^+ (on compte 1 Na^+ par 10^4 à 10^6 K^+).

3.2.1 Rôle des effets de polarisation

Différentes hypothèses ont été déjà proposées pour expliquer la dualité entre la forte sélectivité et la perméation efficace des canaux ioniques. En particulier, pour le KcsA, il a été proposé que la sélectivité pouvait provenir :

a) d'**un effet stérique** (ang. *snug-fit*) – une conformation précise, adaptative, constituée par le filtre de sélectivité enveloppe parfaitement les ions K^+ et pas les ions Na^+ [114, 124] ;

b) d'**un effet électrostatique** (ang. *field-strength*) – un comportement intrinsèque et dynamique des groupes carbonyles du filtre jouent un rôle déterminant en faisant fluctuer les interactions attractives ions-ligand et répulsives ligand-ligand [125-126] ;

c) **des propriétés de solvatation des ions** (ang. *over-coordination*) – pour entrer dans le canal, il est nécessaire que les ions à l'entrée du canal se déshydratent et se réhydratent à la sortie. La perte énergétique est compensée par la réassociation avec les carbonyles du filtre. Ce mécanisme de déshydratation/dissociation est meilleur dans le cas des ions plus gros [127-130].

La polarisation et les effets de transfert de charge sur la dynamique des ions, de la perméabilité et de la sélectivité du filtre de canal sont aussi des aspects très importants mais souvent négligés dans les simulations de dynamique moléculaire des canaux ioniques tels que le KcsA. Dans l'article suivant *« Determination of the charge profile in the KcsA selectivity filter using* ab initio *calculations and molecular dynamics simulations »* nous discutons cette influence en termes de modèle à charge partielles. Nous avons analysé les trois hypothèses à l'aide de la DM et nous avons également mené une analyse du **mécanisme de transfert de charge** entre les cations et le filtre en combinant des simulations de DM et de calculs *ab initio*. Cette quatrième hypothèse nous a permis en quelque sorte de démontrer que le transfert est particulièrement efficace pour les ions K^+, alors qu'il reste très faible pour les ions Na^+. En moyenne, la charge de K^+ est proche de 0.85e alors que celle de Na^+ reste voisine de 1e. Le profil des charges obtenu (*voir Figure IV.9*) nous a conduit à penser que le transfert de charge doit être un facteur clé pour l'interprétation de la sélectivité. L'analyse des trajectoires de DM montre également que les hypothèses *a)* et *b)* demeurent légitimes et que les effets structuraux et dynamiques sont importants. Le processus *c)* est quant à lui aussi déterminant à l'entrée du filtre. Pour savoir lequel de ces quatre phénomènes est le plus important, il faudrait recalculer le courant d'ions dans le filtre. Si cela a déjà été fait dans le cadre des hypothèses *a)*, *b)* et *c)* il serait souhaitable

de le faire à partir de nos résultats sur le transfert de charge. Par conséquent, l'inclusion d'un tel profil dans les modèles cinétiques devrait certainement améliorer ce point de vue du fonctionnement du canal.

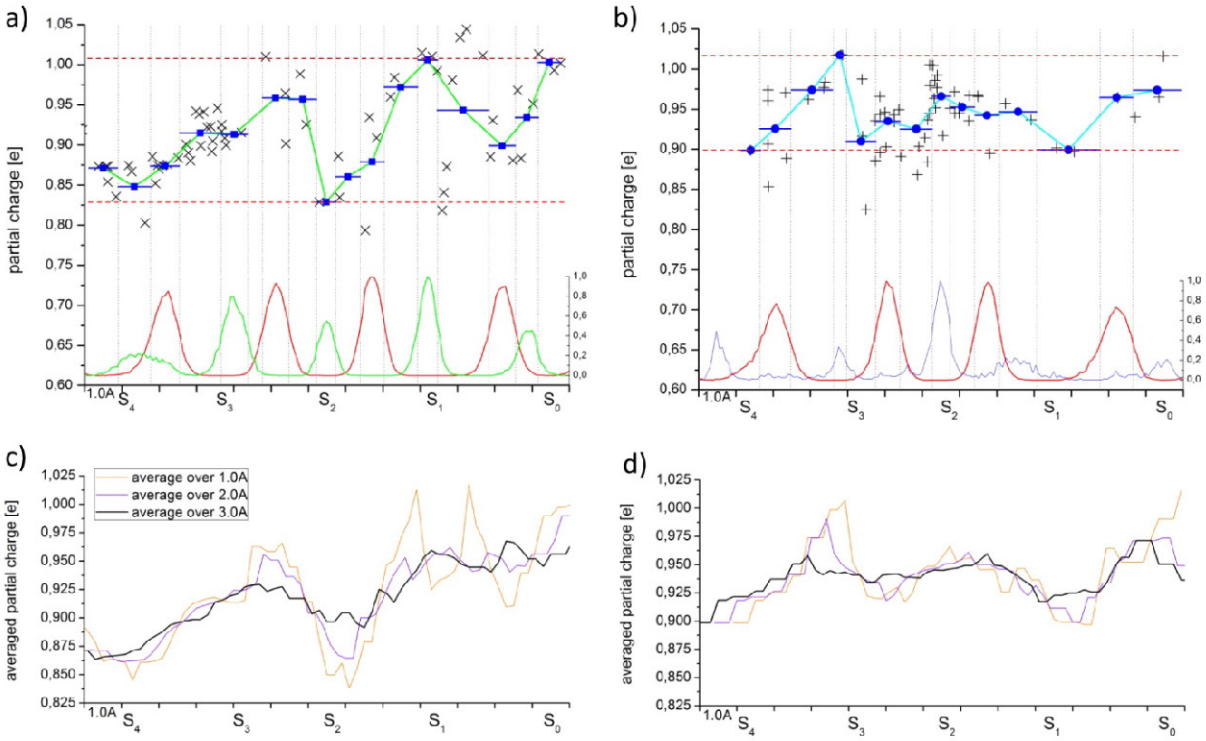

Figure IV.9 Profils des charges partielles des ions K^+ (à gauche) et Na^+ (à droite) en fonction de leur position à l'intérieur du filtre. Les données originales obtenues à partir des calculs *ab initio* correspondant aux ions K^+ (a) et Na^+ (b) sont indiquées par des petites croix. En (a) et (b) nous présentons le profil de charges pondérées par la probabilité de présence d'un cation et des oxygènes des carbonyles. En (c) et (d) nous proposons des profils moyennés incluant l'impact de l'environnement à distance de 1, 2 ou 3 Å.

Determination of the charge profile in the KcsA selectivity filter using *ab initio* calculations and molecular dynamics simulations

Sebastian Kraszewski,* Céline Boiteux, Christophe Ramseyer and Claude Girardet

Received 25th March 2009, Accepted 12th June 2009
First published as an Advance Article on the web 24th July 2009
DOI: 10.1039/b905991a

The charge profile of K^+ and Na^+ ions moving in a single file across the filter of the KcsA channel is determined using both molecular dynamics simulations and *ab initio* calculations. We show a strong correlation between the charge variation and the ion location resulting in a saw-tooth profile, which provides additional information on the influence of charge transfer on the permeation and selectivity of the channel.

Introduction

The fundamental catalytic role of all K^+ channels is to conduct K^+ ions across the cell membrane.[1] The discovery, cloning, and electrophysiological observations of the *Streptomyces lividans* potassium channel KcsA, by Schrempf *et al.*,[2] have stimulated numerous studies to understand the structure of this channel. X-Ray crystallographic analysis of residues 23–119 by Doyle *et al.*[3] and residues 1–125 by Zhou *et al.*[4,5] has depicted the tetrameric structure of the transmembrane helices, the narrow selectivity filter, and the wide channel vestibule formed by the membrane portion of KcsA. Despite these advances, the atomic interpretation of the basic functional properties of KcsA (permeation, selectivity, gating and blocking) still remains controversial.[6–10] The comparison between the atomic radii of potassium and sodium ions (1.33 and 0.95 Å, respectively) leads to an apparent conundrum: with only this small difference in ionic radii and with the same charge, how can K^+ channels select K^+ ions over Na^+ ions by a factor of more than 10^3 without compromising the rates of conduction (10^8 ions per s, leading to currents of a few pA)?

Based on previous studies several decades ago, which introduced the key concepts in ion permeation, especially the "snug-fit" mechanism by Bezanilla and Armstrong[11] and the "field-strength" model by Eisenman and Krasne,[12] different hypotheses have been proposed to explain this duality of strong selectivity and efficient permeation in light of recently determined atomic structures.

(i) The precise conformationally adaptive surroundings constituted by the selectivity filter which snugly wraps K^+ ions has been postulated,[9,10] although this condition requires a sub-Ångström arrangement to discriminate the two cations of such close sizes.

(ii) The intrinsic electrostatic and dynamic behavior of the carbonyl groups lining the selectivity filter has been shown to play a determinant role due to the interplay between attractive ion–ligand and repulsive ligand–ligand interactions, although the local adjustment of dipoles can be perturbed by the 3D structure of the protein.[13,14]

(iii) Ion permeation at the mouths of the channel could be facilitated for the heavier ion, since the dehydration of K^+ ions is better compensated for, compared to Na^+ (oxygen coordination numbers are 8 and 6, respectively), by reassociation with the protein carbonyls.[15–19] The over-coordination hypothesis, which asserts that the cation in the filter is coordinated by more ligands than it would experience in bulk water, has been recently proposed[20–23] as a plausible explanation of selectivity in K^+ channels.

These three hypotheses have been tested very recently[24] by comparing the predictions to calculations of classical molecular dynamics (MD) simulations performed on the KcsA channel and on the less selective NaK one. It was shown that selectivity was a subtle phenomenon, which cannot be explained using the snug-fit hypothesis [item (i)]. These calculations neither confirmed nor refuted the field-strength hypothesis [item (ii)] but they were consistent with the over-coordination hypothesis [item (iii)]. However, as mentioned in ref. 24, classical MD simulations are unable to account for chemical effects which could have a significant role in the explanation of the channel selectivity. Indeed, large polarization effects and charge transfers in the K^+ and the oxygen ligands have been recently reported using either density-functional theory (DFT) or *ab initio* methods.[18,25–28] These latter effects are twofold: they influence the barriers at the filter mouths and modify the binding of the ions inside the filter. A detailed discussion of the polarization of the channel backbone carbonyl groups has been made,[27] but the analysis of the charge transfer between the cations and the backbone has only been studied in specific sites.

Unfortunately, experiments cannot provide fine enough details to corroborate or invalidate these hypotheses. They only give macroscopic features in more or less direct connection to the microscopic processes occurring inside the cell membrane. In that sense, molecular modeling has been, and is still, of great help.[29–31] MD simulations of the ion channels in the membrane-water environment allow investigation of the molecular mechanisms of the functioning of the channel, and in particular the influence of the channel environment (by mutations of residues) on the permeation and selectivity.

Laboratoire de Physique Moléculaire-UMR CNRS 6624, Faculté des Sciences Université de Franche-Comté, 16, Route de Gray, 25030, Besançon Cedex, France.
E-mail: sebastian.kraszewski@univ-fcomte.fr

 This journal is © the Owner Societies 2009

A collective mechanism description of the ion motions has been obtained using this method.[16,32] However, MD calculations generally cover the time scale of only a few tens of nanoseconds. This is obviously not sufficient to investigate the conduction through the channel with characteristic times of microseconds, or gating events with times of milliseconds. No macroscopic information on the current or opening probability can be extracted from MD due to this difference in time scales. In that sense, Brownian dynamics[33] can help substantially, but it involves the necessary loss of some atomic details. Water molecules are treated like a continuum with high permittivity, while it was recently proved[34,35] that, inside the selectivity filter, water molecules behave differently from those located in the bulk intra- and extracellular media.

Additionally, kinetic models have been studied to help interpret the concentration-dependent ion permeation in single file multi-ion channels. A single-vacancy model has been developed to account for multiple-ion effects, including possible inhibition of conductance at high levels of external ion concentration.[36] Similarly, a two-state occupancy model (n and $n-1$ ions in the selectivity filter) has been proposed[37] to describe the multi-ion permeation kinetics in KcsA. This phenomenological theory, which operates with a few empirical kinetic parameters to describe transitions between different occupancy states of the channel, is able to accurately fit the macroscopic characteristics of the channel. However, there is still a gap between the microscopic information gained by MD simulations at the nanosecond time scale and the permeation models based on tunable parameters. A simple theoretical approach which correctly describes the permeation through the channel and includes necessary small-scale details would be required. A recent attempt incorporates the basic physical principles (namely the equations of motion for individual ions), and accounts for the collective motion of multiple ions located in the selectivity filter.[38,39] The motion of the ions can be reduced to the motion of a single quasi-particle. This theoretical framework, based on empirical quantities (ion exchange probabilities, single-ion energy profiles, effective diffusion coefficients in the channel pore, *etc.*), provides a quite robust and physically consistent background for understanding the functioning of the ion channels.

These efforts to link continuum models with the salient features extracted from MD will certainly give, in the near future, a deep understanding of the large permeation of K^+ ions observed in KcsA and other high-conductance channels, and of their selectivity. The incidence and the role of the proposed mechanisms already mentioned will certainly be clarified since they are actually included in the most recent permeation models. However, charge transfer effects inside the filter remain to be explicitly taken into account. Since all the models are charge dependent and since polarization effects can be expressed in terms of partial charges, we have come to the conclusion that charge profiles should be of great help for future models, even if it is a hard task (in terms of computational time) to get them. We have therefore conducted MD simulations corresponding to different ion occupations. From selected snapshots, we have derived partial charges using quantum calculations of the potential experienced by the ion in its various occupations. MD set-up and quantum calculations are briefly presented. Then the results on the continuous charge profile of the K^+ and Na^+ cations moving inside the filter are reported, while the last section is devoted to the discussion of the application of these results with a continuum model of permeation.

Method

MD setup

The model structure of the KcsA channel based on the 2 Å resolution X-ray data (Protein Data Bank: 1K4C)[5] which is used in MD simulations is presented in Fig. 1a. Each subunit contains two transmembrane helices (M1 and M2) with an intervening loop formed by a short helix (P-loop). The central structural element of the K^+ channel is the selectivity filter located close to the outer mouth of the channel. This narrowest part of the pore has a length of about 12 Å and a mean radius of 1.4 Å. At the membrane center, the size of the pore increases to form a 5 Å radius hydrophobic cavity. Fig. 1b and c exhibit the highly conserved TVGYG sequence, which is responsible for the high selective permeation of potassium ions.[9] It is paved with carbonyl groups that provide five binding sites (S_0–S_4) which can be occupied by monovalent cations or water molecules. Experimentally, two additional sites were elucidated at the mouths of the filter, namely S_{EXT} in the extracellular medium and S_{CAV} in the cavity, with this latter site appearing in the closed channel structure, not in the open one. Under physiological conditions,

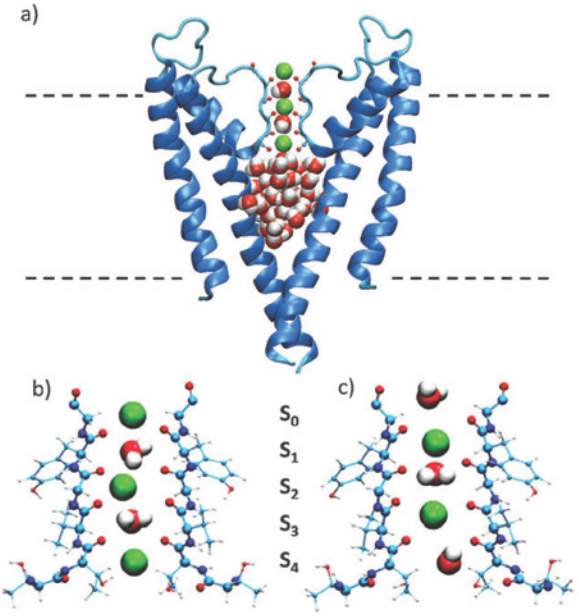

Fig. 1 (a) Schematic view of the system containing the KscA protein. The dashed lines delineate the membrane position. For clarity, only two monomers out of four in the channel are displayed, with the ions and water molecules filling the protein. Close-up of the selectivity filter with S_0, S_2, S_4 (even) sequence (b) and S_1, S_3 (odd) sequence (c) of K^+ ions. Sites are indicated as follows: green, red, white, blue and blue dark balls correspond to K^+, oxygen, hydrogen, carbon and nitrogen atoms, respectively.

approximately two K^+ ions occupy the filter. They reside in specific configurations (S_1, S_3) or (S_2, S_4) (in this latter case, one more ion is located in the S_0 site), with a water molecule intercalated between them in the residual sites.

The lipid bilayer of the cellular membrane was modeled by an octane slab, which has proved efficient at mimicking the hydrophobic behavior of the membrane.[31] In a cubic box of $(73\ Å)^3$, we immersed the portion of protein ranging from Trp66 to Trp92 inside the hydrophobic slab of 29 Å thickness. On each part of the membrane, the extracellular and intracellular sides were mimicked by two water slabs of 22 Å thickness containing 4 K^+ ions, 4 Na^+ ions and 20 Cl^- counterions to counterbalance the 12 positive charges of the protein,[32] and thus to keep the whole system electrically neutral. Water also hydrates the cavity, as proved by EPR experiments.[40] This cavity can contain up to 40 water molecules, which corresponds to saturation[32] in the closed structure, in order to avoid large fluctuations in the position of the channel. In the extra- and intracellular sides, the density of the bulk water has been chosen, while the density of water molecules in the cavity was determined by evaluating the Connolly surface.[41] Along the pore axis, at the filter level, the cases of double and triple occupancies were both studied. In agreement with Zhou *et al.*,[5] six of the seven ionic sites experimentally elucidated, namely, sites S_0, S_1, to S_{CAV} inside the channel were filled by alternate sequences of K^+ ions and water molecules. Two distinct sequences, namely KWKWK and WKWKW, shown in Fig. 1b and c correspond to the occupancies of interest, namely 3 and 2 ions, respectively. For clarity and consistency with the literature, these occupancies will be called even (S_0, S_2, S_4) and odd (S_1, S_3).

All MD simulations were performed with the AMBER8[42] suite of programs using the ff99 force field. Periodic boundary conditions were applied in all directions. Electrostatic interactions were calculated using the particle mesh Ewald (PME) algorithm[43] and all the non-bonded interactions were truncated, using a cut-off of 12 Å. The bonds involving hydrogen atoms were constrained using the SHAKE algorithm. The TIP3P model[44] was used to describe the interaction between water molecules. The temperature was maintained at a constant value using Berendsen thermal coupling[45] and constant pressure was applied. The equations of motion were integrated with a 1 fs time-step, and coordinates were saved every 0.1 ps.

The protein was first relaxed with the (S_0, S_2, S_4) or, equivalently, the KWKWK sequence, for 3 ns. It was then replaced by the (S_1, S_3) or WKWKW configuration, and the whole system was equilibrated again for 3 ns. We refer the reader to previous work if modeling and equilibration protocols of the channel details are required.[32] Then, in the second stage, an intermediate structure extracted from the KWKWK simulation was used to simulate the Na^+ occupation. The K^+ ion in site S_2 was substituted by one Na^+ ion previously located in the intra- or extracellular media. This KWNaWK sequence was then studied for 2 ns (Fig. 2a). An exploration of the whole filter by the Na^+ ion was achieved by forcing it to move toward either the intra- or the extracellular mouths of the filter. Two trajectories were then generated for Na^+, one from sites S_2 to S_0 (Fig. 2b), and one from S_2 to S_4

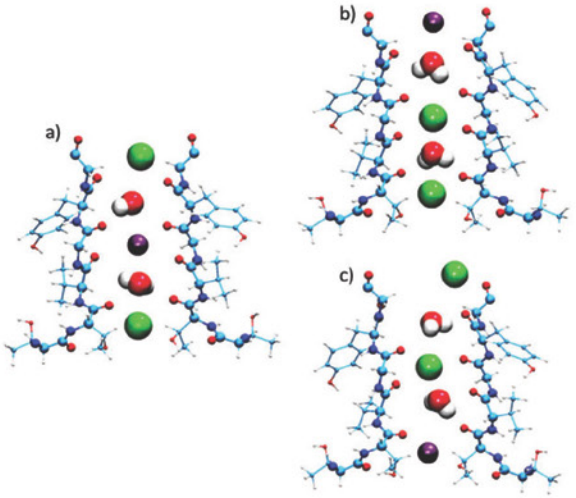

Fig. 2 (a) Initial configuration for the simulation with the Na^+ ion in the S_2 site of the selectivity filter. Final configurations of the molecular dynamics permitting exploration of sites S_2–S_0 (b) and sites S_2–S_4 (c), respectively. See Fig. 1 for the definition of atoms; dark (purple) ball represents the Na^+ ion.

(Fig. 2c). The applied constraint on the Na^+ ion was chosen to be equal to 20 kcal mol^{-1} $Å^{-2}$ for 100 ps, and then the ion was allowed to relax in each arrival site for the next 100 ps, which is enough to minimize force fluctuations. All the K^+ ions and water molecules in the sequence were forced to move with the Na^+ ion.

For the analysis of the coordinating ligands, we performed additional unconstrained MD simulations for 300 ps, preceded by 200 ps of equilibration with a selectivity filter filled by the two sequences, WWKWK or WWNaWK. Two sets of simulations, with and without modified charges, were carried out for each sequence. The charges on K^+ and Na^+ ions in S_2 and S_4 sites and those on the filter backbone and carbonyls were applied accordingly to mean values calculated from *ab initio* simulations.

Ab initio calculations

To determine the partial charges along the whole filter, *ab initio* calculations were performed on particular sets of coordinates extracted from MD simulations. These specific structures were selected with the aim of obtaining at least one point of calculations every 0.5 Å from the bottom to the top of the filter, for the two ionic species. For each calculation, the KcsA channel was truncated so as to keep the studied ion and the nearest surrounding environment only, *i.e.* the 4–5 nearest amino acids within the characteristic Thr-Val-Gly-Tyr-Gly sequence of the filter, and the ions and water molecules in a radius of 7 Å around the ion. As they were cut to truncate the filter, the peptide (at the top) and amide bonds (at the bottom) were passivated with hydrogen atoms.

Amongst the numerous methods proposed for the evaluation of relevant atomic charges needed to describe electrostatic interactions, we have chosen the electrostatic potential surface (ESP) derived charges. In this method, atomic charges are calculated at various points, so that their

 This journal is © the Owner Societies 2009

resulting ESP accurately fits the one determined by quantum mechanics,[46] with the constraint that the total charge of the molecule should be respected. In the MKS (Merz–Kollman–Singh) scheme,[47,48] points are selected on embedded Connolly surfaces, with a density of one point each Ångström. In the following, we calculated the Merz–Kollman–Singh partial charges, using GAUSSIAN03[49] at the Hartree–Fock 6-31G(d) level of theory. This approach was validated in a previous study[28] for specific sites (like S_2). The charge, q, was calculated by considering an average configuration of the filter environment, $\langle r \rangle$, *i.e.* $q(\langle r \rangle)$. Here, we have taken a more accurate approach by determining $\langle q(r) \rangle$, *i.e.* an average charge over several random configurations around a given z (z is the coordinate on the pore axis).

Results

Fig. 3 displays the probability density of finding the K^+ or Na^+ ion along the filter. To approximately define the boundaries of the various sites $S_0,\ldots,S_4$, appearing in Fig. 1 and 2, the location probability of the oxygen atoms belonging to the carbonyls of the four tetramers is also shown. These probabilities illustrate two items already mentioned. The overlap between the ion and carbonyl probabilities is related to the conformational adaptive structure of the filter [item (i)], while the widths of the oxygen peaks represent the dynamics of the CO groups [item (ii)]. The peaks corresponding to this latter probability are, in general, narrower by about 7% on average for K^+ than for Na^+ (Table 1), indicating a better consistency of the heavier ion with its surroundings. Indeed, the oxygen positions are more perturbed by the presence of the Na^+ ion, which can explore finer details of the channel wall. As a result, the peaks broaden. This feature is consistent with a better adaptive structure of the channel for K^+ [item (i)]. Moreover, the positions of the probability maxima of the carbonyl oxygens in the filter are different for K^+ and Na^+, as shown in Table 1. Indeed, the carbonyl oxygens tend to move consistently with the K^+ ion to adapt the site, but they are less sensitive to the Na^+ motion. In particular, the oxygen peak-to-peak distance delineating the S_2 site appears to be smaller for K^+ when compared to Na^+. These differences can be interpreted as resulting from a dynamical influence of the ion motion on the filter walls [item (ii)].

Examination of the values of Δ_{HM}, which characterize the effective size of the various sites (Table 1), shows very small differences between K^+ and Na^+ which do not exceed 0.1 Å, while the ionic radii of the two cations differ by 0.4 Å. This could mean that the filter walls remain quite insensitive to the ion species.

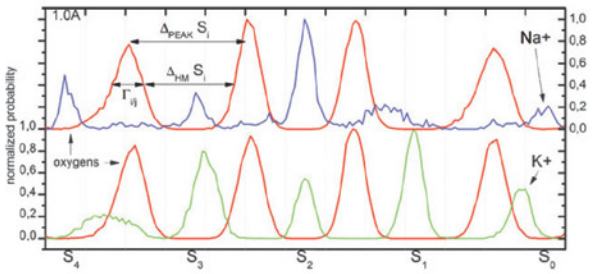

Fig. 3 Normalized location probability of the cation and the carbonyl oxygens in the presence of Na^+ (top) and K^+ (bottom) in the selectivity filter.

Sites S_1, S_2 and S_3 are well defined for K^+ as shown by the location probability inside them, while the peak probability in the S_4 site is much wider. This can be interpreted as the existence of two adjacent states in this S_4 site, in agreement with previous results.[32] In site S_0, the superimposition of the probabilities for K^+ and oxygen atoms indicates a less adapted site geometry. For Na^+, the sites S_0 and S_1 are less defined, showing that the cation generally prefers to bind to the filter wall in specific conformations.

We show in Fig. 4a and b the partial charges obtained for K^+ moving in the sequence KWKWK and for Na^+ moving in the sequence KWNaWK across the selectivity filter (crosses in the top part of the figure). We see larger fluctuations of the K^+ charges, from 0.825 *e* to 1.025 *e*, than those of Na^+, from 0.90 *e* to 1.03 *e*. These charges strongly depend on the ion location, with a minimum value when K^+ lies in even sites and maximum value in the odd sites. In particular, site S_2 corresponds to the smallest charge of 0.825 *e*. In contrast, site S_2 does not have a specific role in the charge transfer for Na^+ and it corresponds rather to a maximum charge. Note moreover that the Na^+ charge tends to reach a minimum in the odd sites and have a maximum value in the even sites.

To correlate the charge fluctuations with the cation location, we give at the bottom of the figure the location probability of the cations and the oxygens along the filter. The charges obtained after weighting the instantaneous charges by this probability display a saw-shape for both cations, indicating significant charge transfers. However, there are two main differences depending on whether Na^+ is present or not. Indeed, this shape appears to be more regular with K^+ than Na^+, the teeth being more acute and the slopes more regular. This approach, which corresponds to the assumption of a slow translocation motion of the cation throughout the filter, shows that the heavier ion tends to adapt more easily to the surroundings, accepting electrons from the ligands of the filter wall.

In order to mimic the reverse situation, in which the cation quickly moves through the channel, we plot in Fig. 4c and d the average charges for the ion, as it continuously experiences the surrounding channel during its motion. We propose here three different average distances (1, 2 or 3 Å) which could correspond to various ion translocation velocities, if we assume that the faster ion experiences the larger surroundings. At low velocity (average of 1 Å), we nearly recover the same shape as in Fig. 4a and b. At faster velocities, the charge oscillations remain visible for K^+, while for Na^+, they disappear, with the resulting profile being much flatter.

To evaluate the charge transfer on the filter wall, which are responsible for the fluctuations of the cation charge, we have also studied the behavior of the charge of the C and O carbonyl atoms and of the N atoms of the peptide bonds (Fig. 5a and b). Due to their relative angular mobility, the oxygen charges are less modified than the charges of the less mobile carbon and nitrogen atoms. Note, however, that the N charges follow the same behavior in the presence of each

Table 1 Site geometry determined using the oxygen location probability

	Distance in presence of Na^+ ion/Å	Distance in presence of K^+ ion/Å
$\Gamma_{0/1}$ [a]	0.88	0.72
$\Gamma_{1/2}$	0.68	0.65
$\Gamma_{2/3}$	0.65	0.71
$\Gamma_{3/4}$	0.82	0.77
Δ_{PEAK} S_0 [b]	2.64	2.64
Δ_{PEAK} S_1	3.44	3.60
Δ_{PEAK} S_2	2.72	2.56
Δ_{PEAK} S_3	2.96	2.88
Δ_{PEAK} S_4	2.96	3.28
Δ_{HM} S_0 [c]	1.83	1.81
Δ_{HM} S_1	2.69	2.80
Δ_{HM} S_2	1.99	1.91
Δ_{HM} S_3	2.29	2.23
Δ_{HM} S_4	2.22	2.31

[a] $\Gamma_{i/j}$ is the full width at half maximum of the carbonyl oxygen location probability peak between sites i and j. [b] Δ_{PEAK} S_i describes the distance between consecutive oxygen peak maxima delimiting the site i. [c] Δ_{HM} S_i characterizes the effective size of site i (see Fig. 3).

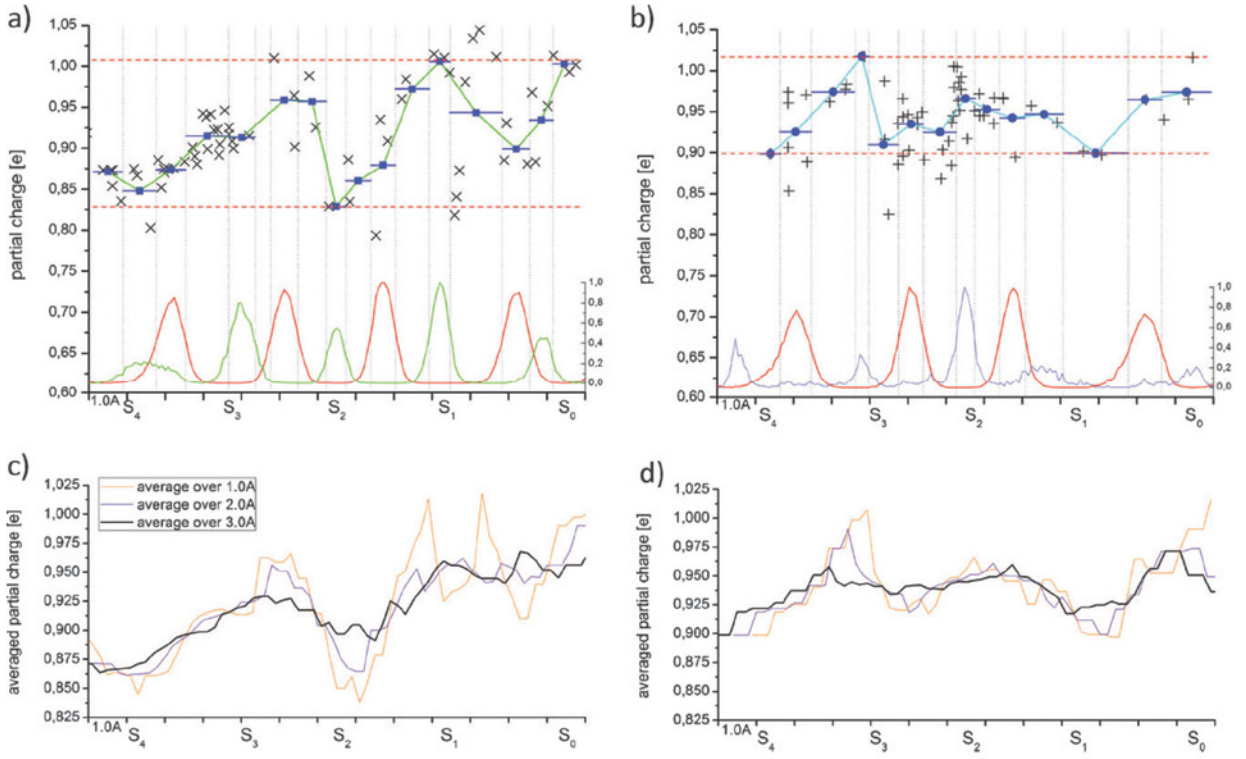

Fig. 4 Partial charge profiles of the K^+ (left) and Na^+ (right) ions as a function of the position inside the filter. Original data from *ab initio* calculations corresponding to the K^+ (a) and Na^+ (b) ions are reported as small crosses. In (a) and (b), we report the charge profile weighted by the location probability of the corresponding cation and the carbonyl oxygens. Note the different scale for the location probabilities (right ordinate scale). In (c) and (d), we propose averaged profiles for different ion-surrounding sensitivities, namely the 1, 2 and 3 Å range.

cation. The charges on the oxygens and carbons of the carbonyls exhibit larger fluctuations for Na^+ and are hence more perturbed for Na^+ than for K^+.

Fig. 6 displays the coordination number of K^+ and Na^+ in the S_2 site as a function of the distance between cations and oxygen atoms belonging to carbonyls or water molecules. We see that the charge transfer has a small influence on the ion hydration in this site. For Na^+, the coordination sphere with 6 oxygen neighbors appears slightly reinforced with polarization, as shown by the plateau from 2.3 to 4.1 Å. Examination of the ion trajectory indicates a main location between sites S_2 and S_1 that allows coordination with 4 carbonyls and 2 water molecules. In contrast, the plateau for K^+ occurs between 3.7 and 5.5 Å, indicating an over-coordination of 10 oxygens, with respect to 8 in bulk water. In that case, the cation lies in the well-adapted S_2 site and the charge transfer improves the symmetry of the first coordination sphere by locating all the closest oxygens at the same distance from the bound ion.

This journal is © the Owner Societies 2009

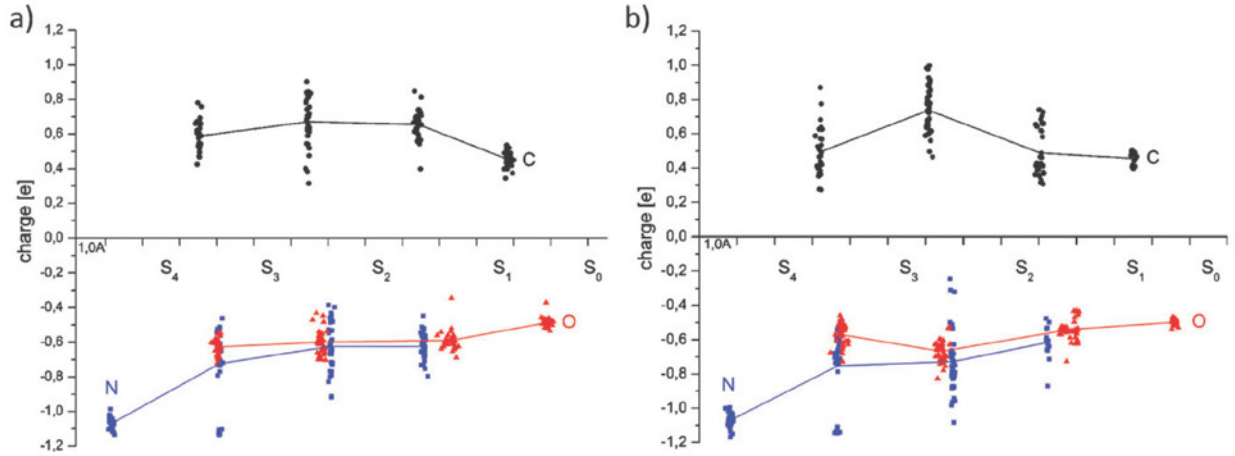

Fig. 5 Partial charges occurring in the carbonyl carbon, C, carbonyl oxygen, O, and peptide nitrogen, N, in the presence of K^+ (a) and Na^+ (b) ions in the selectivity filter. Lines correspond to average values.

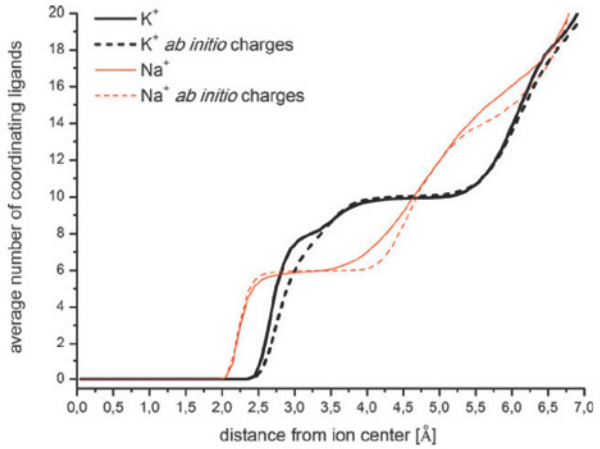

Fig. 6 Average numbers of oxygen atoms bound to K^+ and Na^+ ions *vs.* the distance from the cation in the S_2 site. Solid curves correspond to the simulations performed with standard charges while dashed curves correspond to those with charges modified according to Fig. 4 and 5.

Discussion

Our results on the charge profile of K^+ and Na^+ ions in the single file motion across the filter and of the neighboring oxygen, carbon and nitrogen atoms forming the filter wall of the KcsA channel show a strong correlation between the charge fluctuations and the location probability of the moving cations. The saw-tooth shape of the charge behavior obtained for the two ions demonstrate that charge transfer is a significant mechanism, which should be taken into account for interpreting selectivity and permeation in KcsA channels. Indeed, while the charge profile in the pore displays common features for both cations, some differences discriminate the behaviors of K^+ and Na^+. Amongst the common features, let us mention that, at the outer mouth of the filter, the two cations recover a charge close to 1.0 *e*, as expected from near-total hydration in the extracellular medium, while at the inner mouth, their charge is at a minimum, indicating only partial rehydration at the entry of the cavity. Another common feature is the occurrence of well-defined maxima and minima in the charge profile within the sites.

However, the charge variations are clearly larger for K^+ than for Na^+ and the saw-tooth shape appears more acute (deeper teeth) for K^+, which displays large charge transfer in the even sites and small transfer in the odd sites. Another important difference comes from the reverse behavior of the maxima and minima in the charge profile. Sites displaying maximum charges for K^+ become sites with minimum charges for Na^+, and *vice versa*. The last main difference is the more perturbed charge profiles for Na^+ of the carbonyls and nitrogen atoms belonging to the filter wall.

It is interesting to analyze how these features can influence the translocation of the cations across the filter. In previous calculations[28] devoted to the determination of the potential experienced by a cation moving in the pore, the charges of K^+ and Na^+ were modified to account for charge transfer throughout the filter. These partial charges were taken as a constant equal to $q^* = \delta q$ where $q = +e$ is the usual ionic charge (e being the electron charge) and δ characterizes the fraction of charge, which is lost or gained by the electronic cloud of the ion under the influence of its surroundings. Using a single file motion of ions to describe permeation in the channel,[37] it was shown[28] that the Na^+ ions were more strongly trapped when inside the filter due to a q^* value closer to 1.0 *e*. However, the trapping energy difference, $\Delta\Delta E$, determined by this approach, was found to be unrealistically large. In the present calculations, the evolution of q^* with the cation location, z, gives a new insight into the permeation process by providing indirect information on the coupled dynamics of the ions with the filter wall atoms. The very small fluctuations of the charges in the carbonyl oxygen atoms, which nearly keep their initial value of around -0.6 *e* indicate that their high mobility compensates the charge change, whereas the charges on the much less mobile carbon and nitrogen atoms are more strongly modified. Moreover, the larger fluctuations of the filter wall charges in the presence of

the Na^+ ion demonstrate an increased perturbation of the filter wall associated with specific interactions in a less symmetric surrounding, as shown by the Na^+ location probability.

The variation of the charges on the cations (as well as on the filter wall atoms) with z leads to the modification of the interaction potential experienced by the moving cation. The electrostatic interaction energy on the cation can be written as:

$$V(z) = q(z)\left[\varphi_P + \Delta\varphi_F(z) + \int \frac{dz'q(z')}{|z-z'|}\right], \qquad (1)$$

where φ_P defines the potential created by the protein without including the charge transfer of the atoms of the filter wall. $\Delta\varphi_F$ takes into account the change of the partial charges on the filter wall (carbon, oxygen and nitrogen atoms) with the cation position, z. The third contribution describes the potential due to the presence of the other cations in the filter.

The saw-tooth profile of the cation charge, $q(z)$, is responsible for the oscillations of the interaction potential, $V(z)$, as shown in eqn (1). For K^+, the charge behavior can be approximately written as $q(z) = (0.91 \pm 0.09)\ e$, while the charge is larger and the fluctuations smaller for Na^+, with $q(z) = (0.96 \pm 0.05)\ e$. Since φ_P can be assumed to be z independent in a first approximation, the first contribution in eqn (1) is linear with q, and it is more attractive on average for Na^+ than for K^+. The second contribution can be analyzed in terms of the interaction between the cation charge, $q(z)$, and the carbonyl dipole, $\mu(z)$, by using the average charge values given in Fig. 5. For K^+, the carbonyl dipoles, equal to 3.5 D, are nearly insensitive to the cation position and $\Delta\varphi_F$ can then be considered to be z independent. This is not the case for Na^+ since the value of the carbonyl dipoles increases from 2.9 D at the filter sides to 4.1 D at the boundary of the S_2 and S_3 sites. Since $q(z)$ is at a maximum in the S_2 site, this potential contribution is much more attractive for Na^+ than for K^+. The third contribution varies as the square of the cation charge. It oscillates between maximum and minimum repulsion, depending on whether the K^+ ions are in the odd or even configurations, respectively, while the reverse situation occurs for the Na^+ cation, which exhibits a smaller magnitude of oscillation.

The resulting behavior of $V(z)$ is a linear dependence of the K^+ charge, weighted by near-constant attractive contributions from φ_P and $\Delta\varphi_F$, and by a repulsive contribution, which is minimum in the even sites and maximum in the odd sites. The interaction energy experienced by K^+ in its motion across the filter shows that the odd configuration is less stable than the even one, in agreement with the most probable observation of the KWKWK (even) sequence.[5,16] For Na^+, the increase of both repulsive and attractive potentials in the even sites leads to a competition between these two contributions. However, since the charge variations with z in the odd and even sites are smaller than for K^+, the Na^+ ion experiences, on average, a more attractive potential which tends to trap it more strongly in any given configuration (odd or even) inside the filter and, therefore, reduces the permeation of the lighter ion in the pore. Application of the Nelson approach[37] to the S_2 site shows that the $\Delta\Delta E$ trapping energy difference between K^+ and Na^+ in the filter becomes equal to 31 kcal mol^{-1}. Subtracting the hydration energy of -18 kcal mol^{-1} leads to an effective value of $\Delta\Delta E = 13$ kcal mol^{-1} which is only slightly larger than the expected value of 10 kcal mol^{-1} required to interpret the experimental K^+/Na^+ selectivity value of around 10^3.

This interpretation based on charge transfer can be compared to the one proposed by Roux *et al.*[14] which is based on the interplay between attractive ion–carbonyl and repulsive carbonyl–carbonyl interactions. In the S_2 site, the K^+ charge is at its minimum and the carbonyl dipoles belonging to the filter backbone have a near-constant value. On the contrary, the Na^+ charge and carbonyl dipoles have maximum values in the S_2 site, thus favoring attractive interactions between the lighter cation and the carbonyl groups, and repulsive interactions between carbonyls. The resulting effect is a more rigid conformational structure around the Na^+ cation, favoring its trapping in the filter.

The very similar size of the sites of the two cations, with, nevertheless, a slightly larger width of the carbonyl distribution for Na^+ proves that the filter geometry remains relatively stiff, although the carbonyl dynamics appear to be important. The comparison of the hydration spheres of the two cations in the S_2 site, correlated with the analysis of the ion location, demonstrates a highly adaptive configuration for K^+ which is over-coordinated in a very symmetric position in its site, whereas Na^+ prefers to move in a more asymmetric position and coordinates with only 6 oxygens. This feature can be compared to the results obtained by Sansom *et al.*[24] who use two different classical force fields to calculate the average number of ligands (any oxygen atoms within 3.5 or 4.0 Å of the bound ion). At 3.5 Å, they find an over-coordination for both Na^+ and K^+ (coordination number around 9) using CHARMM, while GROMOS leads to the usual coordination (around 6 and 8, respectively). For this distance of 3.5 Å, the coordination numbers of 9 for K^+ and 6 for Na^+ (Fig. 6) is only in partial agreement with classical simulations. However, it may be noted, as discussed in ref. 24, that all these results are very sensitive to the force field used in the simulations.

Our results can also be compared to a recent study of the polarization and charge transfer effects in the KcsA channel.[27] The electronic structure of the protein backbone during the hopping process of a cation from S_3 to S_2 sites was analyzed in terms of Wannier functions extracted from QM/MM simulations and Bader's atoms in a molecular approach. The influence of polarization and charge transfer was then discussed in a different way. It was shown that the carbonyl groups were strongly polarized by the presence of the cations, with a more significant difference for Na^+ ($\Delta\mu \approx 1.5$ D) than for K^+ ($\Delta\mu \approx 0.2$ D), in agreement with our results. Moreover, a large charge transfer from the filter backbone to the cations was calculated, since net charges of 0.87 e and 0.90 e were found for the two cations in the S_3 and S_1 sites, respectively. Our results show that the charge transfer is different for K^+ and Na^+ ions located in the odd sites, with charge values around 0.9 e for Na^+, consistent with those of ref. 27, but closer to 1.0 e for K^+. Although our calculations do not allow the separating of polarization and charge transfer mechanisms, they offer a more extended view of the charge transfer throughout the whole filter and a new picture of the cation charge profile for K^+ and Na^+ during their motion across the pore.

This journal is © the Owner Societies 2009

Conclusions

To conclude, a combined analysis of molecular dynamics simulations and *ab initio* calculations of the charge transfer mechanism between the cations and the filter backbone shows that this transfer is particularly efficient for the K^+ ion, while it appears to be more attenuated for Na^+. The resulting profile of the cation charge has a saw-tooth behavior when the cations move in a single file sequence throughout the filter. Noticeable differences obtained between K^+ and Na^+ charges led us to think that charge transfer should be a key factor for interpreting the channel selectivity, when associated with the other structural and dynamical effects discussed in the four items (see Introduction). Therefore, inclusion of such a profile in kinetic models should certainly improve our view of the functioning of the channel.

Notes and references

1 B. Hille, *Ionic Channels of Excitable Membranes*, Sinauer, Sunderland, MA, 2nd edn, 1992.
2 H. Schrempf, O. Schmidt, R. Kummerlen, S. Hinnah, D. Muller, M. Betzler, T. Steinkamp and R. Wagner, *EMBO J.*, 1995, **14**, 5170.
3 D. A. Doyle, J. M. Cabral, R. A. Pfuetzner, A. Kuo, J. M. Gulbis, S. L. Cohen, B. T. Chait and R. MacKinnon, *Science*, 1998, **280**, 69–77.
4 J. H. Morais-Cabral, Y. Zhou and R. MacKinnon, *Nature*, 2001, **414**, 37–42.
5 Y. Zhou, J. H. Morais-Cabral, A. Kaufman and R. MacKinnon, *Nature*, 2001, **414**, 43–48.
6 C. Miller, *Nature*, 2001, **414**, 23–24.
7 S. H. Chung and S. Kuyucak, *Eur. Biophys. J.*, 2002, **31**, 283–293.
8 E. Perozo, *Structure*, 2002, **10**, 1027–1029.
9 R. MacKinnon, *FEBS Lett.*, 2003, **555**, 62–65.
10 R. MacKinnon, *Biosci. Rep.*, 2004, **24**, 75–100.
11 F. Bezanilla and C. M. Armstrong, *J. Gen. Physiol.*, 1972, **60**, 588–608.
12 G. Eisenman and S. Krasne, in *IV International Biophysics Congress Symposium on Membrane Structure and Function*, Moscow, 1973.
13 S. Y. Noskov, S. Berneche and B. Roux, *Nature*, 2004, **431**, 830–834.
14 S. Y. Noskov and B. Roux, *Biophys. Chem.*, 2006, **124**, 279–291.
15 L. Guidoni, V. Torre and P. Carloni, *Biochemistry*, 1999, **38**, 8599–8604.
16 S. Berneche and B. Roux, *Nature*, 2001, **414**, 73–77.
17 A. Warshel and W. W. Parson, *Q. Rev. Biophys.*, 2001, **34**, 563.
18 L. Guidoni and P. Carloni, *Biochim. Biophys. Acta, Biomembr.*, 2002, **1563**, 1–6.
19 A. Burykin, M. Kato and A. Warshel, *Proteins: Struct., Funct., Genet.*, 2003, **52**, 412–426.
20 D. L. Bostick and C. L. Brooks, *Proc. Natl. Acad. Sci. U. S. A.*, 2007, **104**, 9260–9265.
21 S. Varma and S. B. Rempe, *Biophys. J.*, 2007, **93**, 1093–1099.
22 M. Thomas, D. Jayatilaka and B. Corry, *Biophys. J.*, 2007, **93**, 2635–2643.
23 S. Varma, D. Sabo and S. B. Rempe, *J. Mol. Biol.*, 2008, **376**, 13–22.
24 P. W. Fowler, K. H. Tai and M. S. P. Sansom, *Biophys. J.*, 2008, **95**, 5062–5072.
25 A. A. Bliznyuk and A. P. Rendell, *J. Phys. Chem. B*, 2004, **108**, 13866–13873.
26 M. Compoint, C. Ramseyer and P. Huetz, *Chem. Phys. Lett.*, 2004, **397**, 510–515.
27 D. Bucher, S. Raugei, L. Guidoni, M. Dal Peraro, U. Rothlisberger, P. Carloni and M. L. Klein, *Biophys. Chem.*, 2006, **124**, 292–301.
28 P. Huetz, C. Boiteux, M. Compoint, C. Ramseyer and C. Girardet, *J. Chem. Phys.*, 2006, **124**, 044703.
29 S. Berneche and B. Roux, *Biophys. J.*, 2000, **78**, 2900–2917.
30 V. B. Luzhkov and J. Aqvist, *Biochim. Biophys. Acta*, 2000, **1481**, 360.
31 C. E. Capener and M. S. P. Sansom, *J. Phys. Chem.*, 2002, **106**, 4543.
32 M. Compoint, P. Carloni, C. Ramseyer and C. Girardet, *Biochim. Biophys. Acta, Biomembr.*, 2004, **1661**, 26–39.
33 S. H. Chung, T. W. Allen and S. Kuyucak, *Biophys. J.*, 2002, **83**, 263–277.
34 M. Compoint, C. Boiteux, P. Huetz, C. Ramseyer and C. Girardet, *Phys. Chem. Chem. Phys.*, 2005, **7**, 4138–4145.
35 M. Aguilella-Arzo, A. Andrio, V. M. Aguilella and A. Alcaraz, *Phys. Chem. Chem. Phys.*, 2009, **11**, 358–365.
36 P. H. Nelson and S. M. Auerbach, *J. Chem. Phys.*, 1999, **110**, 9235–9243.
37 P. H. Nelson, *J. Chem. Phys.*, 2002, **117**, 11396–11403.
38 S. O. Yesylevskyy and V. N. Kharkyanen, *J. Biol. Phys.*, 2004, **30**, 187–201.
39 S. O. Yesylevskyy and V. N. Kharkyanen, *Phys. Chem. Chem. Phys.*, 2004, **6**, 3111–3122.
40 E. Perozo, D. M. Cortes and L. G. Cuello, *Science*, 1999, **285**, 73–78.
41 M. L. Connolly, *Science*, 1983, **221**, 709–713.
42 D. A. Case, T. A. Darden, T. E. Cheatham III, C. L. Simmerling, J. Wang, R. E. Duke, R. Luo, K. M. Merz, B. Wang, D. A. Pearlman, M. Crowley, S. Brozell, V. Tsui, H. Gohlke, J. Mongan, V. Hornak, G. Cui, P. Beroza, C. Schafmeister, J. W. Caldwell, W. S. Ross and P. A. Kollman, *AMBER 8*, University of California, San Francisco, 2004.
43 T. Darden, D. York and L. Pedersen, *J. Chem. Phys.*, 1993, **98**, 10089–10092.
44 W. L. Jorgensen, J. Chandrasekhar, J. D. Madura, R. W. Impey and M. L. Klein, *J. Chem. Phys.*, 1983, **79**, 926–935.
45 H. J. C. Berendsen, J. P. M. Postma, W. F. van Gunsteren, A. DiNola and J. R. Haak, *J. Chem. Phys.*, 1984, **81**, 3684–3690.
46 E. Sigfridsson and U. Ryde, *J. Comput. Chem.*, 1998, **19**, 377–395.
47 U. C. Singh and P. A. Kollman, *J. Comput. Chem.*, 1984, **5**, 129–145.
48 B. H. Besler, K. M. Merz and P. A. Kollman, *J. Comput. Chem.*, 1990, **11**, 431–439.
49 M. J. Frisch, G. W. Trucks, H. B. Schlegel, G. E. Scuseria, M. A. Robb, J. R. Cheeseman, J. A. Montgomery, Jr., T. Vreven, K. N. Kudin, J. C. Burant, J. M. Millam, S. S. Iyengar, J. Tomasi, V. Barone, B. Mennucci, M. Cossi, G. Scalmani, N. Rega, G. A. Petersson, H. Nakatsuji, M. Hada, M. Ehara, K. Toyota, R. Fukuda, J. Hasegawa, M. Ishida, T. Nakajima, Y. Honda, O. Kitao, H. Nakai, M. Klene, X. Li, J. E. Knox, H. P. Hratchian, J. B. Cross, V. Bakken, C. Adamo, J. Jaramillo, R. Gomperts, R. E. Stratmann, O. Yazyev, A. J. Austin, R. Cammi, C. Pomelli, J. Ochterski, P. Y. Ayala, K. Morokuma, G. A. Voth, P. Salvador, J. J. Dannenberg, V. G. Zakrzewski, S. Dapprich, A. D. Daniels, M. C. Strain, O. Farkas, D. K. Malick, A. D. Rabuck, K. Raghavachari, J. B. Foresman, J. V. Ortiz, Q. Cui, A. G. Baboul, S. Clifford, J. Cioslowski, B. B. Stefanov, G. Liu, A. Liashenko, P. Piskorz, I. Komaromi, R. L. Martin, D. J. Fox, T. Keith, M. A. Al-Laham, C. Y. Peng, A. Nanayakkara, M. Challacombe, P. M. W. Gill, B. G. Johnson, W. Chen, M. W. Wong, C. Gonzalez and J. A. Pople, *GAUSSIAN 03 (Revision C.02)*, Gaussian, Inc., Wallingford, CT, 2004.

V Interactions des nanostructures de carbone

La connaissance approfondie des cibles et des canaux ioniques en particulier, a demandé beaucoup d'effort. Ce chapitre concerne à présent directement l'objectif que je m'étais fixé au début de ma thèse. Il s'agit de l'interaction des nanostructures de carbone avec les constituants essentiels de la membrane, i.e. les lipides et les canaux ioniques.

1 Interactions des fullerènes avec les protéines membranaires

Comme nous l'avons décrit précédemment, les protéines transmembranaires telles que les canaux ioniques sont des composantes particulièrement importantes du système nerveux et elles sont aussi des cibles favorites des toxines et des médicaments. De multiples études sur les toxines naturelles [58, 131-136] ont éclairé les mécanismes moléculaires à l'origine de l'anesthésie provoquée par ces espèces. Récemment PARK *et coll.* ont proposé les nanotubes de carbone à simple paroi (SWNT) comme une nouvelle classe de bloqueurs des canaux ioniques en présentant des résultats électrophysiologiques intéressants [96]. Ils ont proposé un mécanisme très simple par lequel les CNT bloquent le canal. Ils agissent comme des bouchons dans les bouches du pore. L'inhibition cytotoxique des canaux ioniques par les nanostructures de carbone pourrait donc être utile en anesthésie à condition d'obtenir un phénomène réversible. A notre connaissance, les expériences de Parc *et coll.* sont les seules à ce jour. En ce sens, des simulations numériques à l'échelle atomique nous ont paru très importantes pour approfondir cela.

Dans l'article suivant *« Affinity of C60 Neat Fullerenes with Membrane Proteins: a Computational Study on Potassium Channels »* nous avons considéré les aspects structurels et dynamiques du mécanisme de liaison des C60 aux canaux ioniques à potassium. L'analyse a d'abord été effectuée par du docking et ensuite par dynamique moléculaire. Nous avons fondé notre analyse sur les modèles atomistiques des canaux ioniques déjà étudiés, comme le KcsA, MthK et Kv1.2. Nous nous sommes concentrés uniquement sur l'étude des fullerènes C60 sans aucune fonctionnalisation. Le but était d'explorer une grande variété d'endroits qui semblaient être des sites cibles (*voir Figure V.1*). Contrairement à l'hypothèse de K. H. PARK, les simulations avec des molécules de C60 initialement situées près de l'entrée du canal KcsA ne révèlent aucune affinité à s'y lier (*voir Figure V.1 a*). Nous avons cependant trouvé des sites spécifiques extracellulaires, comparables à ceux de nombreuses toxines. Nous avons aussi mis en évidence des sites intracellulaires se trouvant vers la porte du canal. Un seul fullerène peut bloquer la conduction des ions (*voir Figure V.1 b et d*) en analogie à un

bloqueur reconnu – le tétraéthylammonium (TEA). Nous avons quantifié notre approche en calculant les valeurs d'énergie libre de liaison dans les différents sites (la méthode de l'énergie d'interaction linéaire (LIE) [60]) et en comparant ces valeurs avec celles du TEA. Les résultats obtenus sont présentés dans la Table V.1. Le rôle d'inhibition des C60 est ainsi confirmé.

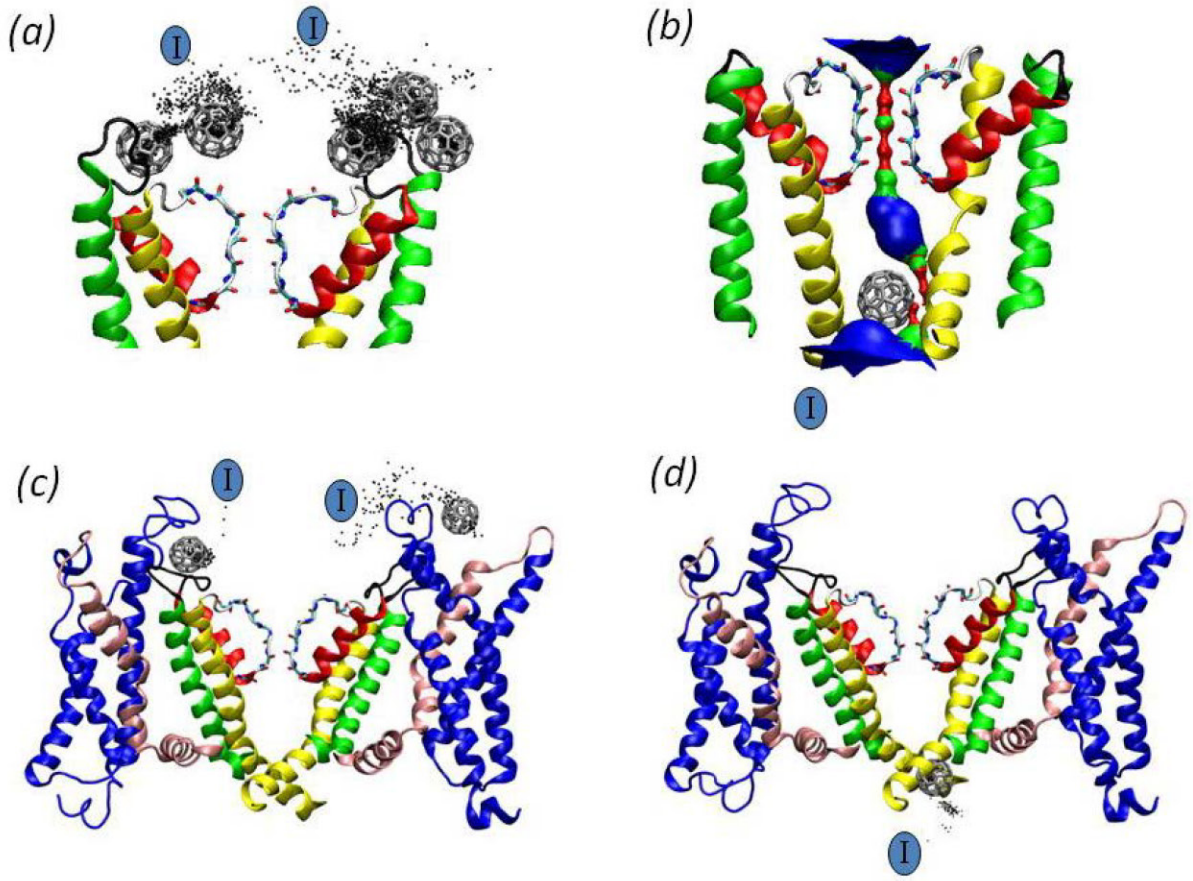

Figure V.1 Sites spécifiques de liaisons des fullerènes sur des canaux ioniques. Les molécules de C60, une fois liées aux sites extracellulaires du KcsA (a) ou du Kv1.2 (c) ou aux sites intracellulaires du MthK (b) ou du Kv1.2 (d), induisent des changements conformationnels importants des protéines.

Les interactions des C60 avec les canaux K^+ semblent dépendre essentiellement de la taille et de l'hydrophobicité du composé. Ces études montrent donc une forte interaction des C60 avec les canaux ioniques. Sans parler de toxicité, une attention toute particulière doit être prêtée quant à leur impact si l'on souhaite les utiliser un jour dans l'administration ciblée de médicaments. Nos résultats suggèrent que, en dépit de leur biocompatibilité suspectée, leur action sur les canaux ioniques doit être beaucoup mieux évaluée.

Table V.1 Energies des liaisons de C60 et de TEA avec les canaux K^+ (± estimation d'erreur).

Protéine	Ligand	Site	ΔG [kcal.mol^{-1}]
KcsA	C_{60} (cluster de deux)	boucle P	-4.1 ± 0.7
	C_{60} (cluster de quatre)	boucle P	-7.4 ± 1.0
	TEA	entré du filtre de sélectivité	-2.4 ± 3.8
MthK	C_{60}	porte intracellulaire	-3.2 ± 0.4
	C_{60}	côté membranaire	-0.7 ± 0.4
	TEA	cavité interne	-7.6 ± 4.0
Kv1.2	C_{60}	entre helices S1-S2/S5-S6	-3.3 ± 0.5
	C_{60}	entre helices S1-S2/S5-S6	-2.5 ± 0.5
	C_{60}	entre helices S3-S4	-3.0 ± 0.5
	C_{60}	porte intracellulaire	-1.9 ± 0.4

ARTICLE

Affinity of C_{60} Neat Fullerenes with Membrane Proteins: A Computational Study on Potassium Channels

Sebastian Kraszewski,[†] Mounir Tarek,[‡,*] Werner Treptow,[§] and Christophe Ramseyer[†]

[†]Institut UTINAM, UMR 6213, CNRS Université de Franche, Comté, Besançon, France, [‡]UMR Structure et Réactivité des Systèmes Moléculaires Complexes, Nancy-University, CNRS, France, and [§]Laboratório de Biologia Teórica e Computacional, Universidade de Brasília, Brasil

ABSTRACT Most studies of the interactions of neat and functionalized fullerenes with cells have focused so far on their ability to cross the cell membrane envelopes. Membranes are, however, also host to a large number of proteins responsible for various cellular functions. Among these, ion channels are prominent components of the nervous system. Recently, it was shown that fullerenes may act as blockers or modulators of a variety of K^+ channels. Here we use computer simulations to investigate the propensity of such nanocompounds to bind to K^+ channels. Our results based on extensive atomistic molecular dynamics simulations reveal a variety of specific binding sites depending on the structure and properties of the channel. The corresponding binding free energies and putative mechanisms suggest that C_{60} may indeed effectively hinder the function of K^+ channels and hence induce toxicity.

KEYWORDS: fullerenes · ionic channels · toxicity · binding · molecular dynamics

The years to come will probably see a dramatic increase in the industrial generation and use of nanomaterials. Preliminary studies suggest that some types of nanoparticles might pose a health hazard, which could throw a shadow over the nanotech revolution. The impact of this development on worker safety, consumer protection, public health, and the environment has to be considered carefully, especially as the toxicity of nanomaterials is *a priori* not predictable from that of bulk material.[1,2] Bulk carbon-based biomaterials have demonstrated excellent long-term biocompatibility and biological performances in medical device applications. This has thus led to many proposed applications for carbon-based nanostructures in the biomedical field, including biosensors and drug and vaccine delivery using carbon nanotubes (CNTs)[3,4] and fullerenes (C_{60}).[5] A lot of studies at the cellular level clearly suggest that fullerenes and, to a lesser extent, CNTs can cross the lipid membranes of cells.[6−10] In addition, it was shown that functionalized CNTs are biocompatible with cells of the immune system (B and T lymphocytes as well as macrophages), indicating no apparent toxicity.[11] However, the cell membrane is not made of lipids only but also hosts a large amount of proteins that are responsible for the cell functions and activities.

Among them, K^+ channels are responsible for nerve impulse by mediating conduction across synapses and, as such, are involved in a variety of biological processes, including cardiac, skeletal, and smooth muscle contraction, epithelial transport of nutrients and ions,[12] *etc.* K^+ channels are complex quaternary structures in which the central hydrophilic pore results from an arrangement of four transmembrane (TM) domains. This pore domain is homologous to all K^+ channels, and its structure has been first resolved for bacterial channels in the closed (KcsA)[13] and open (MthK)[14] states. The ionic pathway is delimited by the so-called selectivity filter (SF), a highly conserved sequence that allows these channels to discriminate K^+ from other cations (see Supporting Information, Figure S1). K^+ channels are a favorite target of several blockers and modulators such as toxins that inhibit, by a variety of mechanisms, their function.[15−18] The so-called pore-blocking toxins[19,20] and other small organic molecules, such as quaternary ammonium (QA) compounds, bind to the extracellular pore entryway of K^+ channels and prevent ion conduction. Others permeate the channel from the intracellular side to reach binding sites inside the pore.[21,22] In contrast, gating modifier peptides such as Hanatoxin and VSTX1 spider toxins[16,23,24] are known to bind to voltage-gated potassium (Kv) channels. In these channels, the TM voltage sensing is ensured by a supplementary domain surrounding the pore, the so-called voltage sensor domain (VSD) that undergoes the

*Address correspondence to mtarek@edam.uhp-nancy.fr.

Received for review April 8, 2010 and accepted June 17, 2010.

Published online June 22, 2010.
10.1021/nn100723r

© 2010 American Chemical Society

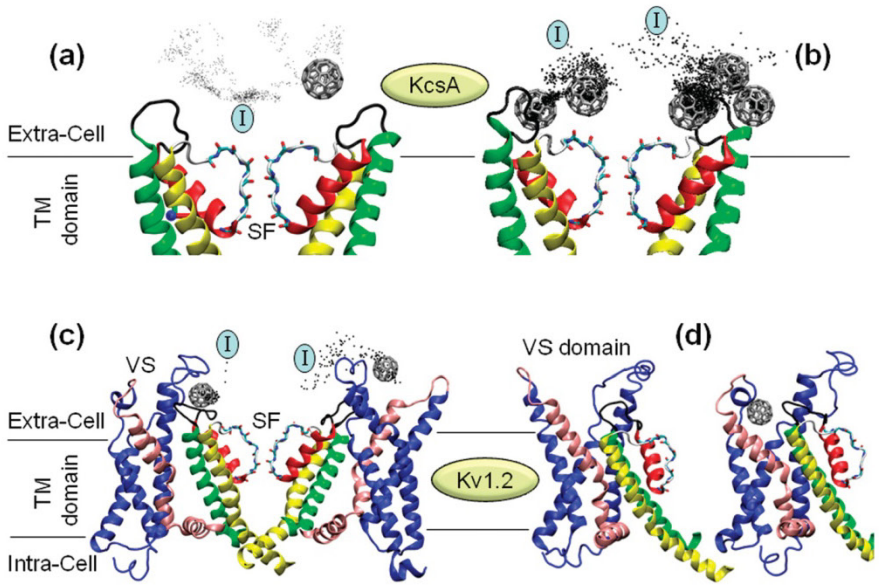

Figure 1. Binding of C_{60} to the extracellular domains of KcsA (top) and Kv1.2 (bottom). The dots represent the position of C_{60} along the MD trajectory sampled every 0.1 ns starting at position I and ending at the displayed C_{60}. Binding of (a) monomeric and (b) aggregates of C_{60} to the extracellular part of KcsA. (c) Binding of C_{60} to the voltage sensor domain (VSD) of Kv1.2. (d) Structure of the Kv1.2 VSD (d,left) before and (d,right) after binding of C_{60}. For clarity, the membrane lipids and the water molecules are not shown and only two monomers of each channel are displayed. KcsA channel is shown truncated in order to focus only on its extracellular side.

conformational changes necessary for opening of the intracellular gate.[25] The gating modifier toxins bind to this domain and alter the gating process by hindering its motion.

Owing to the complexity and diversity of K^+ channels, we investigate in this study the structural and energetic aspects of C_{60} binding mechanism to several channels, namely, KcsA, MthK, and Kv1.2. A preliminary study involving the use of *docking*-type calculations of C_{60} to KcsA and MthK channel revealed few binding sites and no affinity of fullerene to the ion channels' selectivity filter (see Supporting Information, Figure S2). These results clearly contrast with those of Park *et al.*,[26] who showed recently that C_{60} and single-walled carbon nanotubes (SWNTs) may act as blockers or modulators of K^+ channels expressed in mammalian CHO cells, while they have no effect on endogenous CHO cell ClC chloride channels.

As *docking* studies are of limited insight and are applied only to channel structures in vacuum, we have undertaken extensive MD simulations of the K^+ channels embedded in model membranes (see Methods section for more details) and interaction with mono- and oligomeric C_{60} molecules in order to shed light on the actions the latter may have on the channel's function.

RESULTS AND DISCUSSION

In contrast to the hypothesis put forward by Park *et al.*,[26] MD simulations of individual C_{60} molecules initially located near the extracellular mouth of the bacterial KcsA channel reveal no propensity of fullerenes to bind to the SF (Figure 1a). However, monomeric C_{60} shows (within the 15 ns MD run) an affinity toward the hydrophobic residues of the extracellular loops linking segments S6 and the P helices. Control simulations considering six C_{60} placed near the SF evolved toward the same final conformation (Figure 1b) in which one C_{60} binds to the loops before aggregation of other C_{60} around the S6/P helix linker.

Hence, MD simulations indicate clearly that neither monomeric nor oligomeric C_{60} anchor to or block the SF of K^+ channels. The topology of the extracellular domain of voltage-gated K^+ (Kv) channels is far more complex than that of KcsA[27] (see Supporting Information, Figure S1) and provides for other binding sites. MD simulations of the mammalian Kv1.2 channel embedded in its membrane environment reveal indeed that C_{60} binds to the extracellular loops of the channel. All binding sites involve residues of the so-called voltage sensor domain (VSD). In some instances, C_{60} binds both to the VSD (in particular, the S1−S2 helices) and to S5−S6 (Figure 1c). In others, C_{60} binds specifically to the top of S3−S4 segments. Interestingly, in such a case, the VSD of the channel undergoes a large conformational movement "triggered" by the binding of C_{60} (Figure 1d).

In order to investigate the propensity of C_{60} molecules to bind to K^+ channels when approaching from the intracellular side, we have considered two scenarios. First, the MthK channel was used as a paradigm for open channel structures, and a fullerene molecule was placed in the intracellular membrane side, near the pore

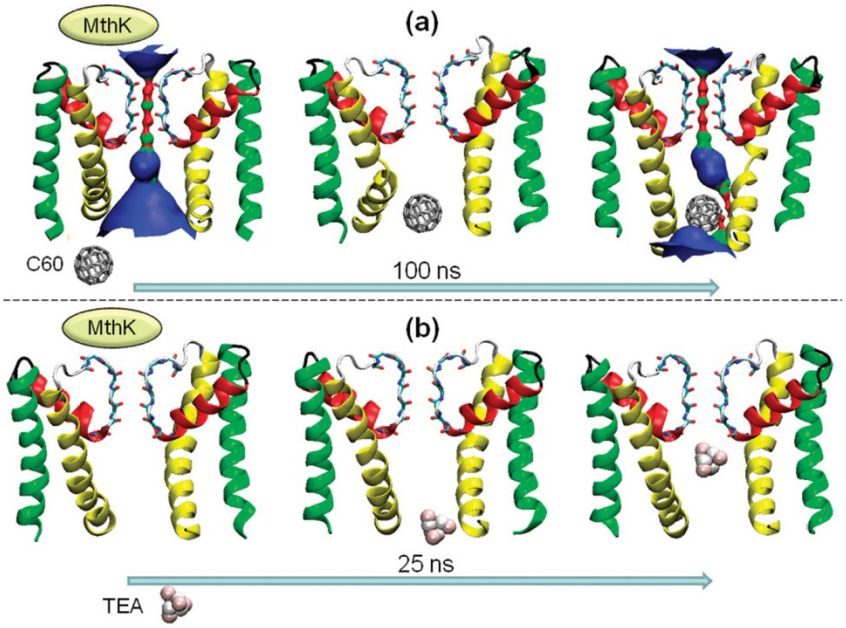

Figure 2. (a) Binding of C_{60} from the intracellular domain of MthK. From left to right: consecutive snapshots from MD simulations. The compound binds to the channel's gate and induces a blockage of the K^+ conduction pathway represented here (point density in color codes) by its hydrophilic pore volume.[28] (b) Snapshots from MD simulations of a tetraethylammonium (TEA) ion approaching the channel from the intracellular domain. Note that here TEA migrates through the channel gate toward its binding site inside the internal cavity.

entrance. During the simulation run (over 100 ns), the C_{60} migrates toward the internal cavity entrance (within 25 ns). Subsequently, a large conformational change of the M2 (S6) helices stabilizes the fullerene in its binding site (Figure 2a). This conformational change involves mainly a bending of the helix around the conserved glycine motif,[14] favoring therefore interactions of the channel hydrophobic residues with the inclusion compound. Such a process bears a large resemblance to the concept of "hydrophobic seals" previously described for the KcsA channel[29] and causes a drastic alteration of the ion conduction pathway. To check whether the channel closing is correlated with the presence of C_{60} near the pore entrance, we performed a control simulation in which we considered tetraethylammonium (TEA), a widely used nonhydrophobic K^+ channel blocker.[21,22] In agreement with experiments, when placed near the intracellular gate of MthK, TEA migrates through the gate to the central cavity toward its putative binding site[30] (Figure 2b). In contrast to the previous simulation, partial closing of the gate occurred only after TEA diffused toward the internal cavity.

Second, we investigated also the affinity of C_{60} to bind to the intracellular domain of Kv1.2. As in the MthK case, C_{60} molecules adequately placed near the gate bind quickly to the latter and "plug" the entrance of the channel (see Supporting Information, Figure S3).

Due to the hydrophobic character, C_{60} partitions in the membrane core[7−9] and can therefore migrate laterally toward membrane proteins. MD simulations of C_{60} aggregates placed in the vicinity of a model membrane show indeed, in agreement with previous experiments[6] and simulations,[7−9] that neat fullerenes partition toward the interior of the membrane (see Supporting Information, Figure S4). We have investigated using MD simulations the behavior of C_{60} placed in the lipid bilayer core and free to diffuse laterally toward MthK. While the approach to the channel, as expected, was diffusion driven, we sampled a trajectory in which a C_{60} reaches the channel and binds to a hydrophobic surface formed by an interhelical domain (Figure 3).

In summary, MD simulations of C_{60} show its propensity to interact with K^+ channels. The results point to a wide variety of locations that appear to be target sites of binding. In order to estimate the free energy of binding (BFE) associated with these sites, we have performed further calculations using the linear interaction energy (LIE) method.[31] This approach allows a simple and efficient way[32] of estimating the BFE from MD simulations of the ligand (here C_{60}) in associated and dissociated states (see Methods section and Supporting Information). Free energies of binding estimated with the LIE method may be not, for the present systems, as quantitatively reliable as those evaluated by other methods.

The BFE of C_{60} monomers and oligomers to the sites obtained from unconstrained simulations is reported in Table 1. For comparison, we report also results from simulations of TEA, the efficient K^+ channels blocker. Note that the latter binds strongly to the SF if approaching from the extracellular domain and to the

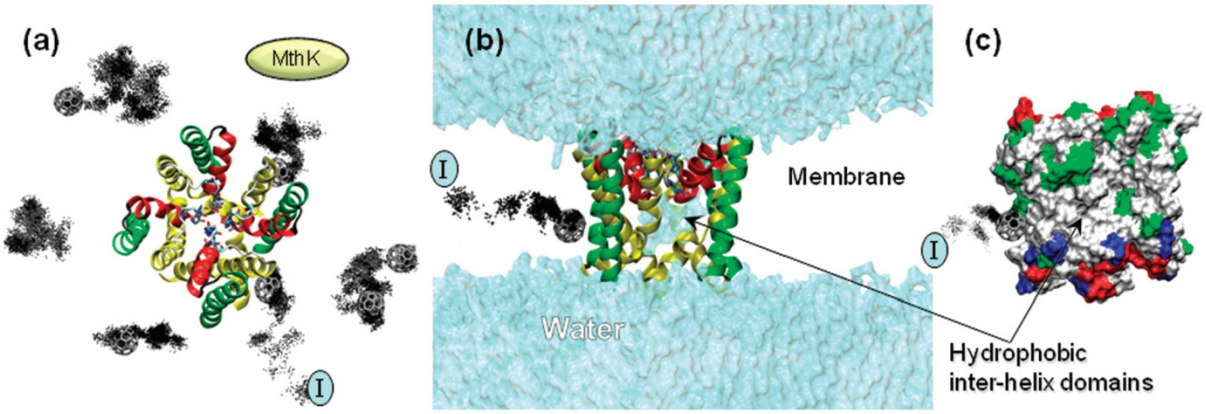

Figure 3. Binding of C_{60} to the transmembrane domain of MthK. (a) Top view. (b) Side view with a highlight of the solvent (blue) and the interhelices' binding domain; membrane not shown for clarity. (c) Same side view with a protein representation highlighting (white) the transmembrane hydrophobic protein domain. The dots represent the position of C_{60} along the MD trajectory sampled every 0.1 ns starting at position I and ending at the displayed C_{60}.

internal cavity when approaching from the intracellular domain. For all putative sites, the estimated BFEs of monomeric C_{60} are larger than ~2.4 kcal mol^{-1} (*i.e.*, similar to the BFE of TEA to the SF of K^+ channels). The energies corresponding to the binding of fullerene to the MthK gate are somewhat larger probably due to its specific interaction with the M2 helices. The BFE of C_{60} to the extracellular domains of the voltage sensor of the Kv1.2 voltage-gated channel is also significant. This binding involves several channel amino acids that probably stabilize the protein−C_{60} complex. Finally, despite the affinity of C_{60} for the transmembrane domain of MthK, the free energy of partitioning between the hydrophobic membrane core and the channel is less than 1 kcal mol^{-1}. While the values of the estimated of C_{60} BFE from the present analysis ought to be taken with care, the comparison, under similar conditions with binding of TEA, indicates that most of the putative target sites revealed by MD simulations involve a rather strong binding. In contrast to what has been suggested by Park *et al.*,[26] none of these sites corresponds to the mouth of the SF.

TABLE 1. Free Energies of C_{60} and TEA Binding to K^+ Channels (± Error Estimate)

protein	ligand	site	ΔG (kcal/mol)
KcsA	C_{60} (cluster of 2)	S6−P loop	−4.1 ± 0.7
	C_{60} (cluster of 4)	S6−P loop	−7.4 ± 1.0
	TEA	selectivity filter[a]	−2.4 ± 3.8[c]
MthK	C_{60}	intracellular gate	−3.2 ± 0.4
	C_{60}	membrane side	−0.7 ± 0.4
	TEA	internal cavity[b]	−7.6 ± 4.0[d]
Kv1.2	C_{60}	S1−S2/S5−S6	−3.3 ± 0.5
	C_{60}	S1−S2/S5−S6	−2.5 ± 0.5
	C_{60}	S3−S4	−3.0 ± 0.5
	C_{60}	intracellular gate	−1.9 ± 0.4

[a]TEA bound in the conformation (TEA_0,W_1,K_2,W_3,K_4) of the SF, where W and K denotes a water molecule and potassium ion, respectively, and the subscripts relate to the specific sites of the SF; value averaged over 4 ns of simulation. [b]TEA bound in the conformation (K_1,W_2,K_3,W_4, TEA_{cav}) of the SF; value averaged over last 5 ns of simulation. [c](−4.0 ± 0.2) averaged over 200 ps of simulation from Luzhkov and Aqvist.[35] [d](−4.2 ± 0.6) averaged over 200 ps of simulation from Luzhkov and Aqvist.[35]

Despite the fact that C_{60} modulates ionic currents[26] and therefore the function of K^+ channels, the molecular mechanisms involved can only be inferred from comparison to the action of other blockers. When C_{60} binds to the intracellular pore domain, it is clear that it *plugs* the ionic conduction pathway. As for TEA,[33] we expect that such a block may be relieved by inward K^+ currents. The effect of binding to the VSD of Kv1.2 is less obvious. There is, however, a strong similarity to the binding of the gating modifier toxins. Such toxins bind to the top of S3 and S4 and shift the channel opening to more depolarized voltages.[21,34] Compounds alike are believed to perturb the conformational freedom of the VSD, inhibiting directly the channel's activation. Given the large BFEs of C_{60} estimated from simulations and the structural effect it has on the VSD, our data suggest a similar scenario. Finally, partitioning of C_{60} in the membrane core allows accessibility to and binding to interhelical domains. This could hinder these helices' motion for several channels, altering therefore their function.

In summary, the results presented here provide an insight into the possible mechanisms governing the interaction of C_{60} with K^+ channels and a molecular view on their blockage capability. Further studies are needed in order to fully understand why C_{60} has no measurable effect on endogenous CHO cell ClC channels.[26] Two properties of the latter may be at the origin of the discrepancy. The ClC crystal structure[36] indicates indeed that (i) the mouth of the channel is lined with hydrophilic residues, which does not favor binding of C_{60}, and (ii) that the size of the hydrophilic ionic pathway is not large enough to allow

for diffusion of C_{60} inside the structure. Finally, binding of C_{60} to K^+ channels appears to depend mainly on the size and hydrophobicity of the compound, which holds for functionalized fullerenes. As the latter are potential candidates for drug delivery,[37] our results suggest that, despite their suspected biocompatibility and low toxicity, their action on ion channels needs much further evaluation.

METHODS

Unconstrained full atomistic MD simulations were performed on three models of ionic channels belonging to potassium channel family. Considered channels were studied in a lipid environment composed of a hydrated palmitoyloleylphosphatidylcholine (POPC) lipid bilayer for MthK and Kv1.2 and a hydrated dioleylphosphatidylcholine (DOPC) lipid bilayer for KcsA. The binding sites of fullerene to different protein regions were first determined using docking and MD simulations and then confirmed by evaluation of the corresponding binding free energies (BFE) using the linear interaction energy (LIE) method.

Docking Method: In order to determine the channels' energetically favorable binding sites, the GRAMM (Global RAnge Molecular Matching) program[38] was used to dock C_{60} to KcsA and MthK channels structures (considered in vacuum). GRAMM is a fast-automated docking program that performs an exhaustive six-dimensional search through the relative intermolecular translations and rotations using a very efficient fast Fourier transform (FFT) correlation technique and a simple scoring function that measures shape complementarities and penalizes overlaps.

Two thousand docking solutions (poses) were computed and scored on a few different configurations for KcsA and MthK channels (see Supporting Information, Figure S2). Matching was performed in vacuum with minimal grid step of 1.4 Å for fullerenes. All interactions taken into account were based on included force field in generic mode, and the repulsion factor was equal to 30. The best complexes were chosen considering the best score of the docking results in which at least a ligand (C_{60}) molecule interacts with the internal or external part of the ion channel.

Fullerenes were found to bind preferentially at few extracellular sites and at few intracellular sites and showed no affinity for the selectivity filter. We have performed statistical analyses on the docking results. We have defined the binding constant as

$$K_{\mathrm{P}}^{C_{60}}(i) = \frac{n_i \times E_{\mathrm{score}}^{C_{60}}(i)}{\sum_{i=\mathrm{E,I}} n_i \times E_{\mathrm{score}}^{C_{60}}(i)}$$

which represents the statistical average of the score energy $E_{\mathrm{score}}^{C_{60}}$ of the fullerene C_{60} over the docking simulations on the protein P. Here i denotes the two different potential locations of the C_{60}, namely, at the extracellular E or intracellular I side of the membrane.

For C_{60}, the two sites are statistically nearly equivalent for MthK since $K_{\mathrm{MthK}}^{C_{60}}(E) = 0.48$ and $K_{\mathrm{MthK}}^{C_{60}}(I) = 0.52$. For KcsA $K_{\mathrm{KscA}}^{C_{60}}(E) = 0.63$ and $K_{\mathrm{KscA}}^{C_{60}}(I) = 0.37$.

Molecular Dynamics Method: The MD simulations were performed using NAMD software.[39] They were conducted at a constant temperature of 300 K (Langevin dynamics) and a constant pressure of 1 atm using the Langevin piston Nosé−Hoover method.[40] Short- and long-range forces were calculated every 1 and 2 time steps, respectively, with a time step of 2.0 fs. Chemical bonds between hydrogen and heavy atoms were constrained to their equilibrium value. Long-range electrostatic forces were evaluated using the particle mesh Ewald (PME) method.[41]

The following molecular systems were studied. A summary of the MD simulation runs carried out is reported in Table 2 (total of 646 ns).

(i) KcsA: A three-dimensional model of KcsA (PDB code: 1bl8) was inserted at the center of a pre-equilibrated and fully hydrated DOPC lipid bilayer. The complete system (a total of *ca.* 90 300 atoms, 110 × 106 × 105 Å^3) contains channel, 325 lipid molecules, 19 765 water molecules, and 10 chloride ions to ensure electroneutrality of the system. For more details see ref 27.

TABLE 2. MD runs carried out

molecular system	system description	total simulation time (ns)
(i)	KcsA in presence of monomeric C_{60}	15
(i)	KcsA in presence of six C_{60}	29
(ii)	MthK in presence of six C_{60} in the membrane and one C_{60} at the gate	119
(iii)	Kv1.2 in presence of four C_{60} in the solvent and one C_{60} at the gate	213
(iv)	four C_{60} in the vicinity of lipid membrane	101
(iv)	six C_{60} in a water box	60
(v)	KcsA in presence of TEA	10
(v)	MthK in presence of TEA	25

(ii) MthK: The open state K^+ MthK (PDB code: 1lnq) was embedded in a pre-equilibrated POPC bilayer. The total system contains the channel, 357 lipid molecules, 23 863 water molecules, and 10 sodium ions, that is, a total of *ca.* 103 500 atoms (110 × 109 × 100 Å^3).

(iii) Kv1.2: In this study, we considered only the TM domain (residues 122 to 390) of the voltage-gated channel Kv1.2[42] (PDB code: 2a79) inserted at the center of a POPC membrane patch. The system contains 426 lipid molecules, 41 464 water molecules, and the 22 cations distributed in the solvent to ensure the electroneutrality of the system (a total of *ca.* 173 000 atoms, 130 × 134 × 110 Å^3). More detailed information concerning equilibration process was described elsewhere,[43] and a general view on this system is provided in Supporting Information in Figure S5.

(iv) C_{60} Fullerene: The neat C_{60} carbon fullerene molecules were successively modeled with all systems containing ionic channels, in a water box or with fully hydrated POPC membrane patches. We investigated binding to the extracellular regions of K^+ channels using the KcsA channel model, binding to the intracellular open gate region and laterally through the hydrophobic transmembrane region using the opened MthK channel model, and binding to the voltage-gated channels using the Kv1.2 channel model.

(v) Tetraethylammonium Ion (TEA): A pyramidal configuration of one TEA ion was used to study binding to the extracellular side of the KcsA channel and binding to the intracellular open gate and internal cavity regions of the MthK channel.

(vi) LIE Reference Systems: The LIE method required supplementary simulations for each ligand (C_{60} or TEA) in a reference environment. Accordingly, the following molecular systems were also used: (a) one C_{60} molecule in a (48.5 Å)^3 water box; (b) aggregates of two and four C_{60} molecules in a water box; (c) one C_{60} molecule positioned in the hydrophobic region of a fully hydrated POPC lipid bilayer; (d) TEA in a water box. The simulations of the reference systems lasted 5 ns for each of the C_{60} systems and 54 ns for the TEA.

Linear Interaction Energy (LIE) Method: All systems were modeled using the CHARMM27[44] force field with a united atoms representation for the acyl chains of the lipid molecules. No charges were attributed to the C_{60} carbon atoms and for fullerene C−C or fullerene C−water oxygen interactions we used the Bedrov *et al.*[9,45] Lennard-Jones potential parameters (CHARMM27 functional: $\sigma_{CC} = 3.895$ Å, $\varepsilon_{CC} = 0.066$ kcal mol^{-1}, and $\sigma_{CO} = 3.58$ Å, $\varepsilon_{CO} = 0.0936$ kcal mol^{-1}). The potential parameters for TEA ion were taken from Crouzy *et al.*[46]

For energetic properties analysis, we used the LIE method proposed by Aqvist *et al.* to study ionic channel blockage by qua-

ternary ammonium (QA) compounds such as TEA or by local anesthetics.[32,35] The approach is based on the estimates of scaled differences between two MD simulations, one with the free ligand in its reference environment and one where the ligand bound to the protein. For all systems, the time evolutions of the binding energies are reported in Supporting Information.

The average free binding energies were computed as

$$\Delta G = \alpha\left(\langle V_{l-s}^{vdW}\rangle_{bind} - \langle V_{l-s}^{vdW}\rangle_{free}\right) + \beta\left(\langle V_{l-s}^{el}\rangle_{bind} - \langle V_{l-s}^{el}\rangle_{free}\right)$$

where ΔG is the Gibbs free energy of binding, V^{vdW} and V^{el} are the Lennard-Jones and the Coulomb ligand-surroundings potential interaction, respectively, the subscripts "free" and "bind" describe the ligand-free or the bound state, and α and β are empirical scaling factors. Following Luzhkov *et al.*, we used the scaling coefficients $\alpha = 0.18$ and $\beta = 0.52$.[31,47] No electrostatic contribution was taken into account for fullerenes since their carbon atoms bear no partial charge.

Acknowledgment. This work was granted access to the HPC resources of the Centre Informatique National de l'Enseignement Supérieur (CINES) under the allocation 2009-075137 made by GENCI (Grand Equipement National de Calcul Intensif).

Supporting Information Available: Results of docking and MD calculations and details on the LIE method corresponding results. This material is available free of charge *via* the Internet at http://pubs.acs.org.

REFERENCES AND NOTES

1. Panessa-Warren, B. J.; Warren, J. B.; Wong, S. S.; Misewich, J. A. Biological Cellular Response to Carbon Nanoparticle Toxicity. *J. Phys.: Condens. Mater.* **2006**, *18*, S2185–S2201.
2. Smart, S. K.; Cassady, A. I.; Lu, G. Q.; Martin, D. J. The Biocompatibility of Carbon Nanotubes. *Carbon* **2006**, *44*, 1034–1047.
3. Ajayan, P. M. Nanotubes from Carbon. *Chem. Rev.* **1999**, *99*, 1787–1799.
4. Baughman, R. H.; Zakhidov, A. A.; de Heer, W. A. Carbon Nanotubes—The Route toward Applications. *Science* **2002**, *297*, 787–792.
5. Da Ros, T.; Prato, M. Medicinal Chemistry with Fullerenes and Fullerene Derivatives. *Chem. Commun.* **1999**, 663–669.
6. Sayes, C. M.; Fortner, J. D.; Guo, W.; Lyon, D.; Boyd, A. M.; Ausman, K. D.; Tao, Y. J.; Sitharaman, B.; Wilson, L. J.; Hughes, J. B.; *et al.* The Differential Cytotoxicity of Water-Soluble Fullerenes. *Nano Lett.* **2004**, *4*, 1881–1887.
7. Qiao, R.; Roberts, A. P.; Mount, A. S.; Klaine, S. J.; Ke, P. C. Translocation of C-60 and Its Derivatives across a Lipid Bilayer. *Nano Lett.* **2007**, *7*, 614–619.
8. Wong-Ekkabut, J.; Baoukina, S.; Triampo, W.; Tang, I. M.; Tieleman, D. P.; Monticelli, L. Computer Simulation Study of Fullerene Translocation through Lipid Membranes. *Nat. Nanotechnol.* **2008**, *3*, 363–368.
9. Bedrov, D.; Smith, G. D.; Davande, H.; Li, L. W. Passive Transport of C-60 Fullerenes through a Lipid Membrane: A Molecular Dynamics Simulation Study. *J. Phys. Chem. B* **2008**, *112*, 2078–2084.
10. Andreev, I.; Petrukhina, A.; Garmanova, A.; Babakhin, A.; Andreev, S.; Romanova, V.; Troshin, P.; Troshina, O.; DuBuske, L. Penetration of Fullerene C60 Derivatives through Biological Membranes. *Fullerenes, Nanotubes, Carbon Nanostruct.* **2008**, *16*, 89–102.
11. Bianco, A.; Prato, M. Can Carbon Nanotubes Be Considered Useful Tools for Biological Applications? *Adv. Mater.* **2003**, *15*, 1765–1768.
12. Hille, B. *Ionic Channels of Excitable Membranes*, 2nd ed.; Sinauer: Sunderland, MA, 1992.
13. Doyle, D. A.; Cabral, J. M.; Pfuetzner, R. A.; Kuo, A.; Gulbis, J. M.; Cohen, S. L.; Chait, B. T.; MacKinnon, R. The Structure of the Potassium Channel: Molecular Basis of K^+ Conduction and Selectivity. *Science* **1998**, *280*, 69–77.
14. Jiang, Y.; Lee, A.; Chen, J.; Cadene, M.; Chalt, B. T.; Mackinnon, R. The Open Pore Conformation of Potassium Channels. *Nature* **2002**, *417*, 523–526.
15. Oseguera, A. J.; Islas, L. D.; Garcia-Villegas, R.; Rosenbaum, T. On the Mechanism of Tba Block of the Trpv1 Channel. *Biophys. J.* **2007**, *92*, 3901–3914.
16. Huang, P. T.; Shiau, Y. S.; Lou, K. L. The Interaction of Spider Gating Modifier Peptides with Voltage-Gated Potassium Channels. *Toxicon* **2007**, *49*, 285–292.
17. Yu, K. Q.; Fu, W.; Liu, H.; Luo, X. M.; Chen, K. X.; Ding, J. P.; Shen, J. H. Computational Simulations of Interactions of Scorpion Toxins with the Voltage-Gated Potassium Ion Channel. *Biophys. J.* **2004**, *86*, 3542–3555.
18. Holmgren, M.; Smith, P. L.; Yellen, G. Trapping of Organic Blockers by Closing of Voltage-Dependent K+ Channels—Evidence for a Trap Door Mechanism of Activation Gating. *J. Gen. Physiol.* **1997**, *109*, 527–535.
19. Ruta, V.; Jiang, Y. X.; Lee, A.; Chen, J. Y.; MacKinnon, R. Functional Analysis of an Archaebacterial Voltage-Dependent K+ Channel. *Nature* **2003**, *422*, 180–185.
20. Eriksson, M. A. L.; Roux, B. Modeling the Structure of Agitoxin in Complex with the *Shaker* K^+ Channel: A Computational Approach Based on Experimental Distance Restraints Extracted from Thermodynamic Mutant Cycles. *Biophys. J.* **2002**, *83*, 2595–2609.
21. Armstrong, C. M. Interaction of Tetraethylammonium Ion Derivatives with Potassium Channels of Giant Axons. *J. Gen. Physiol.* **1971**, *58*, 41.
22. French, R. J.; Shoukimas, J. J. Blockage of Squid Axon Potassium Conductance by Internal Tetra-*N*-alkylammonium Ions of Various Sizes. *Biophys. J.* **1981**, *34*, 271–291.
23. Lee, H. C.; Wang, J. M.; Swartz, K. J. Interaction between Extracellular Hanatoxin and the Resting Conformation of the Voltage-Sensor Paddle in Kv Channels. *Neuron* **2003**, *40*, 527–536.
24. Lee, S. Y.; MacKinnon, R. A Membrane-Access Mechanism of Ion Channel Inhibition by Voltage Sensor Toxins from Spider Venom. *Nature* **2004**, *430*, 232–235.
25. Yellen, G. The Voltage-Gated Potassium Channels and Their Relatives. *Nature* **2002**, *419*, 35–42.
26. Park, K. H.; Chhowalla, M.; Iqbal, Z.; Sesti, F. Single-Walled Carbon Nanotubes Are a New Class of Ion Channel Blockers. *J. Biol. Chem.* **2003**, *278*, 50212–50216.
27. Treptow, W.; Tarek, M. K^+ Conduction in the Selectivity Filter of Potassium Channels Is Monitored by the Charge Distribution Along Their Sequence. *Biophys. J.* **2006**, *91*, L81–L83.
28. Smart, O. S.; Goodfellow, J. M.; Wallace, B. A. The Pore Dimensions of Gramicidin A. *Biophys. J.* **1993**, *72*, 1109–1126.
29. Kitaguchi, T.; Sukhareva, M.; Swartz, K. J. Stabilizing the Closed S6 Gate in the *Shaker* Kv Channel through Modification of a Hydrophobic Seal. *J. Gen. Physiol.* **2004**, *124*, 319–332.
30. Kutluay, E.; Roux, B.; Heginbotham, L. Rapid Intracellular Tea Block of the Kcsa Potassium Channel. *Biophys. J.* **2005**, *88*, 1018–1029.
31. Aqvist, J.; Luzhkov, V. B.; Brandsdal, B. O. Ligand Binding Affinities from MD Simulations. *Acc. Chem. Res.* **2002**, *35*, 358–365.
32. Luzhkov, V. B.; Nilsson, J.; Arhem, P.; Aqvist, J. Computational Modelling of the Open-State K(V)1.5 Ion Channel Block by Bupivacaine. *BBA-Proteins Proteom.* **2003**, *1652*, 35–51.
33. Taglialatela, M.; Vandongen, A. M. J.; Drewe, J. A.; Joho, R. H.; Brown, A. M.; Kirsch, G. E. Patterns of Internal and External Tetraethylammonium Block in 4 Homologous K+-Channels. *Mol. Pharmacol.* **1991**, *40*, 299–307.
34. Swartz, K. J.; MacKinnon, R. Mapping the Receptor Site for Hanatoxin, a Gating Modifier of Voltage-Dependent Potassium Channels. *Neuron* **1997**, *18*, 675–682.
35. Luzhkov, V. B.; Aqvist, J. Mechanisms of Tetraethylammonium Ion Block in the Kcsa Potassium Channel. *FEBS Lett.* **2001**, *495*, 191–196.

36. Dutzler, R.; Campbell, E. B.; Cadene, M.; Chait, B. T.; MacKinnon, R. X-ray Structure of a Cic Chloride Channel at 3.0 Angstrom Reveals the Molecular Basis of Anion Selectivity. *Nature* **2002**, *415*, 287–294.
37. Klumpp, C.; Lacerda, L.; Chaloin, O.; Da Ros, T.; Kostarelos, K.; Prato, M.; Bianco, A. Multifunctionalised Cationic Fullerene Adducts for Gene Transfer: Design, Synthesis and DNA Complexation. *Chem. Commun.* **2007**, 3762–3764.
38. Vakser, I. A.; Matar, O. G.; Lam, C. F. A Systematic Study of Low-Resolution Recognition in Protein−Protein Complexes. *Proc. Natl. Acad. Sci. U.S.A.* **1999**, *96*, 8477–8482.
39. Phillips, J. C.; Braun, R.; Wang, W.; Gumbart, J.; Tajkhorshid, E.; Villa, E.; Chipot, C.; Skeel, R. D.; Kale, L.; Schulten, K. Scalable Molecular Dynamics with Namd. *J. Comput. Chem.* **2005**, *26*, 1781–1802.
40. Feller, S. E.; Zhang, Y. H.; Pastor, R. W.; Brooks, B. R. Constant-Pressure Molecular-Dynamics Simulation—The Langevin Piston Method. *J. Chem. Phys.* **1995**, *103*, 4613–4621.
41. Darden, T.; York, D.; Pedersen, L. Particle Mesh Ewald: An $N \cdot \mathrm{Log}(N)$ Method for Ewald Sums in Large Systems. *J. Chem. Phys.* **1993**, *98*, 10089–10092.
42. Long, S. B.; Campbell, E. B.; MacKinnon, R. Crystal Structure of a Mammalian Voltage-Dependent *Shaker* Family K^+ Channel. *Science* **2005**, *309*, 897–903.
43. Treptow, W.; Tarek, M. Environment of the Gating Charges in the Kv1.2 *Shaker* Potassium Channel. *Biophys. J.* **2006**, *90*, L64–L66.
44. MacKerell, A. D.; Bashford, D.; Bellott, M.; Dunbrack, R. L.; Evanseck, J. D.; Field, M. J.; Fischer, S.; Gao, J.; Guo, H.; Ha, S.; *et al.* All-Atom Empirical Potential for Molecular Modeling and Dynamics Studies of Proteins. *J. Phys. Chem. B* **1998**, *102*, 3586–3616.
45. Li, L. W.; Bedrov, D.; Smith, G. D. Water-Induced Interactions between Carbon Nanoparticles. *J. Phys. Chem. B* **2006**, *110*, 10509–10513.
46. Crouzy, S.; Berneche, S.; Roux, B. Extracellular Blockade of K+ Channels by Tea: Results from Molecular Dynamics Simulations of the Kcsa Channel. *J. Gen. Physiol.* **2001**, *118*, 207–217.
47. Hansson, T.; Marelius, J.; Aqvist, J. Ligand Binding Affinity Prediction by Linear Interaction Energy Methods. *J. Comput.-Aided. Mol. Des.* **1998**, *12*, 27–35.

Affinity of C_{60} Neat Fullerenes with Membrane Proteins: a Computational Study on Potassium Channels

Sebastian Kraszewski[1], *Mounir Tarek**[2], *Werner Treptow*[3], *and Christophe Ramseyer*[1]

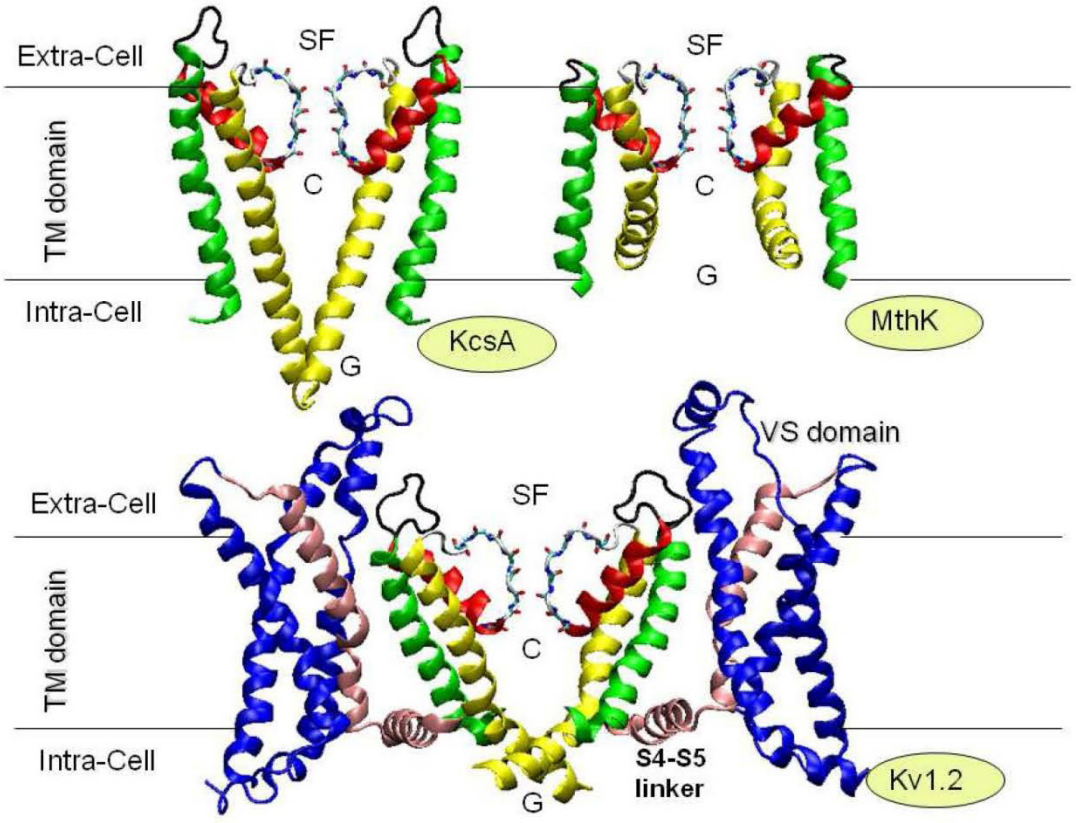

Figure S1. Schematic view on the three ionic channels belonging to the K^+ channels family. **a)** KscA (closed state), **b)** MthK (open state) and **c)** mammalian voltage-gated channel Kv1.2.

[1] Institut UTINAM - UMR 6213, CNRS Université de Franche-Comté, Besançon, France
[2] UMR Structure et Réactivité des Systèmes Moléculaires Complexes, Nancy-University, CNRS, France
[3] Laboratario de Biofisica, Universidade de Brasalia, Brasil
* to whom correspondence should be addressed : mtarek@edam.uhp-nancy.fr

Characteristic regions of the channels are highlighted: the selectivity filter (SF), the internal cavity (C), the intracellular gate (G), the transmembrane (TM) domain and the voltage sensor (VS) domain. For clarity only two out of four subunits for each channel are shown. The approximate limits of the transmembrane region are indicated with solid lines.

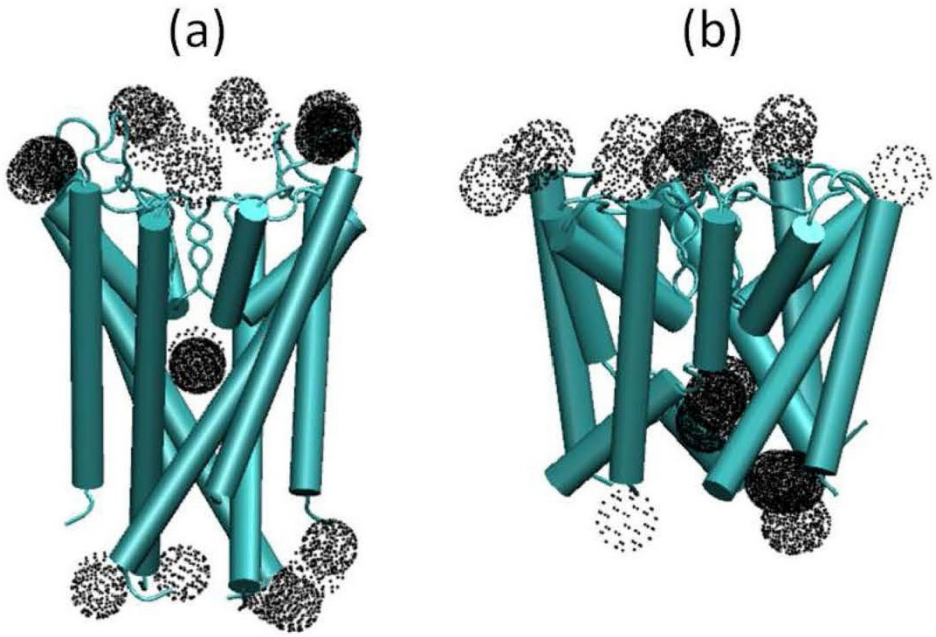

Figure S2. Representation of the docking results on KcsA (a) and MthK (b) channels. C_{60} are found to bind at different extracellular and intracellular sites but show no affinity to the selectivity filter.

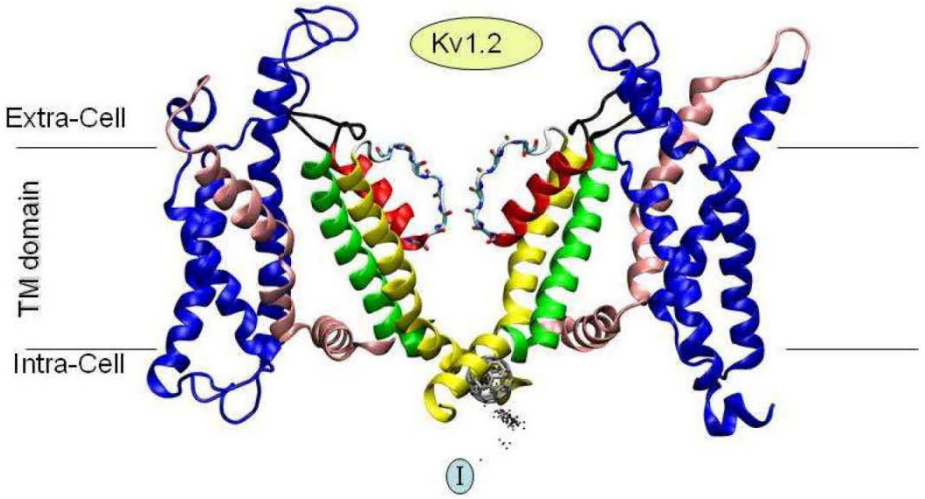

Figure S3. Binding of C_{60} from the intracellular domain of Kv1.2: Intracellular binding site on the mammalian voltage-gated Kv1.2 channel. The dots represent the C_{60} molecules positions sampled every 0.1 ns over the 80 ns MD trajectory starting from the initial position (I) and ending on the position of the displayed molecule.

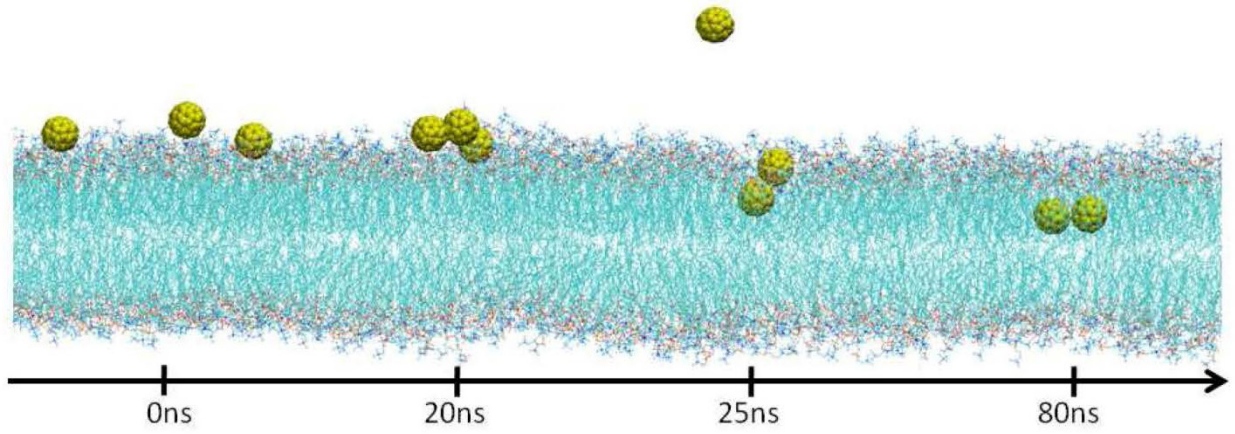

Figure S4. Partitioning of fullerene molecules (yellow balls) between water (not shown for clarity) and POPC lipid membrane (blue lines). Results coming from 100 ns unconstrained MD simulations. Note here that in this run, the three monomers aggregate first at the interface, then a dimer crosses the lipid/water interface. Such a scenario is probably not representative of the permeation mechanism, but instead indicative of its stochastic nature.

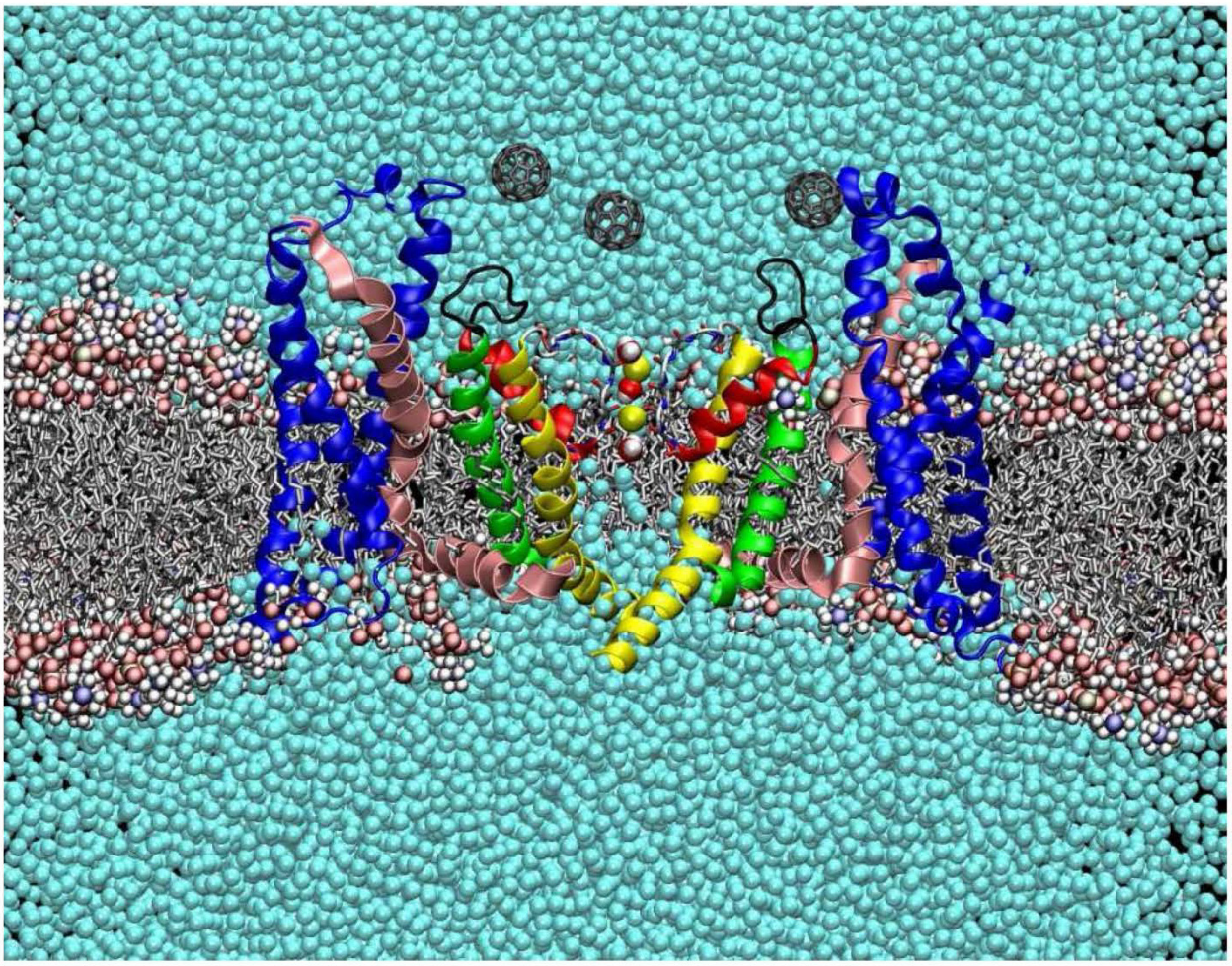

Figure S5. Representation of the Kv1.2 channel embedded in the POPC lipid bilayer and the initial position of C_{60} molecules. Water molecules are represented by their Van der Waals radii (cyan). For clarity, the lipid acyl chains (dark gray) are represented as sticks and the lipid head group atoms are represented in small spheres.

LIE Results

The energies for all reference systems (vi) were evaluated from the corresponding MD simulations and were averaged over the last 4ns of each giving following results:

C_{60} (monomeric) $\left\langle V_{l-s}^{vdW} \right\rangle_{free}$ = -39.50 ± 2.14 kcal.mol^{-1} ; C_{60} (cluster of two) $\left\langle V_{l-s}^{vdW} \right\rangle_{free}$ = -73.36 ± 3.18 kcal.mol^{-1} ; C_{60} (cluster of four) $\left\langle V_{l-s}^{vdW} \right\rangle_{free}$ = -121.76±4.74 kcal.mol^{-1} ; C_{60} (in_POPC) $\left\langle V_{l-s}^{vdW} \right\rangle_{free}$ = -53.00±2.75 kcal.mol^{-1} ; TEA $\left\langle V_{l-s}^{vdW} \right\rangle_{free}$ = -16.76±1.83 kcal.mol^{-1} $\left\langle V_{l-s}^{el} \right\rangle_{free}$ = -59.72±7.25 kcal.mol^{-1}

ΔG estimates averaged over blocks of 10 ps for all systems are represented in the following figures (see next two pages):

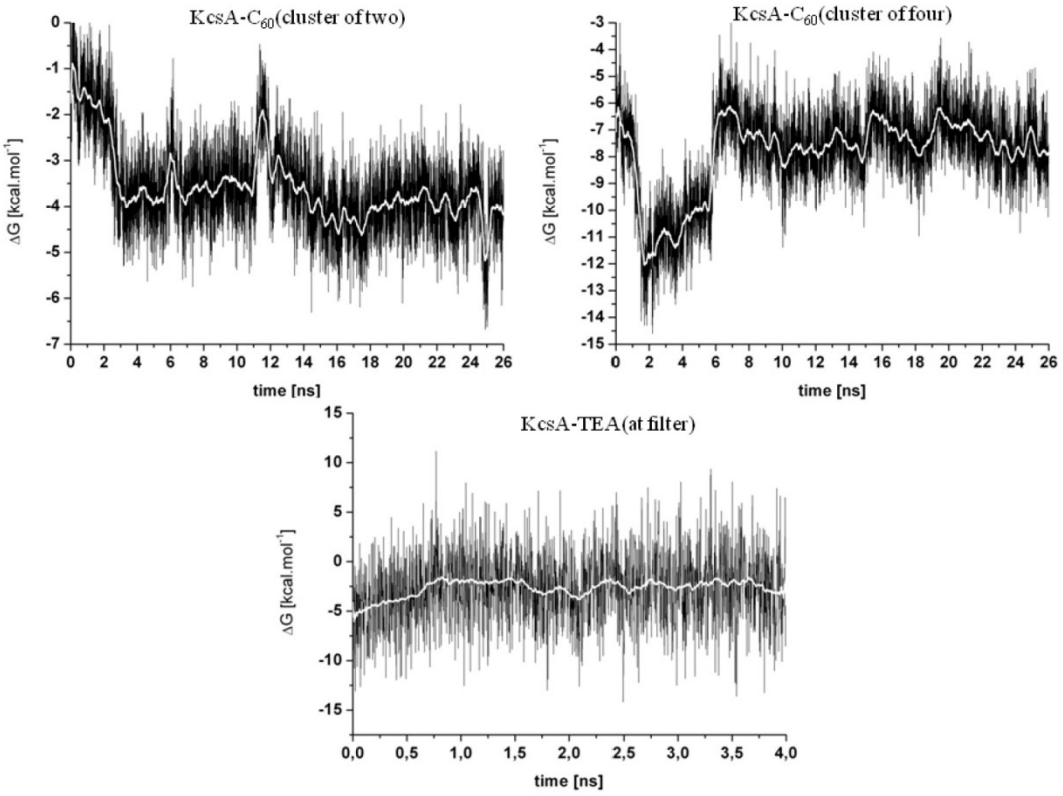

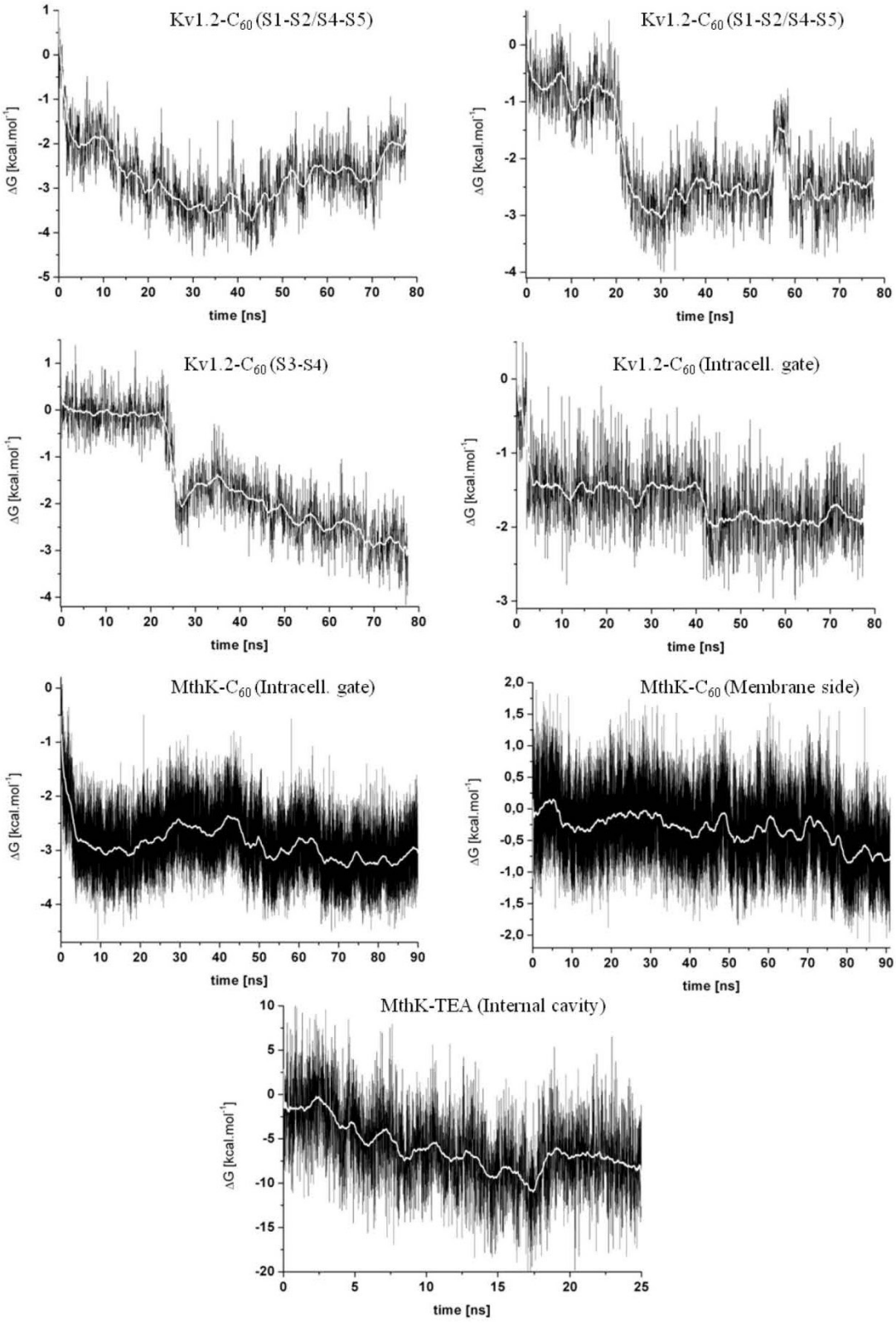
Kv1.2-C60 (S1-S2/S4-S5)
Kv1.2-C60 (S1-S2/S4-S5)
Kv1.2-C60 (S3-S4)
Kv1.2-C60 (Intracell. gate)
MthK-C60 (Intracell. gate)
MthK-C60 (Membrane side)
MthK-TEA (Internal cavity)
ΔG [kcal.mol-1]
time [ns]

2 Interactions des fullerènes avec la membrane cellulaire

La partition des fullerènes entre l'eau et la membrane lipidique a été déjà abandonnement étudiée [51, 92-93, 137-141]. Grâce au paramétrage du potentiel des interactions pour les fullerènes dans le milieu lipidique de BEDROV *et coll.* [141-142] nous avons pu poursuivre les simulations de DM de ces espèces en présence de la membrane du type POPC. Nous avons trouvé que les fullerènes nus sont capables de pénétrer la membrane lipidique à l'échelle d'une centaine de nanosecondes grâce au processus coopératif d'agrégation (*voir Figure V.2*). Au contraire, les fullerènes fonctionnalisés (solubles) peuvent traverser la membrane séparément, même si l'agrégation de ces espèces dans le milieu aqueux est toujours présente (*voir Figure V.3*).

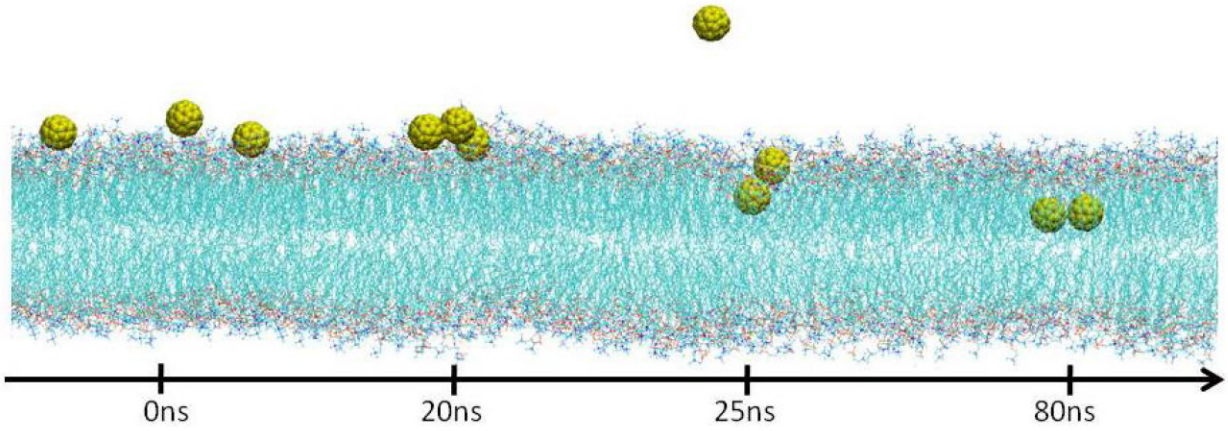

Figure V.2 Résultats des simulations de DM sur une membrane cellulaire (en bleu) en interaction avec des fullerènes (en jaune) en fonction du temps. Au bout de 20 ns de simulation, les fullerènes s'agrègent pour franchir l'interface eau/lipides. Au bout de 25 ns, deux fullerènes pénètrent la membrane alors que le troisième s'éloigne. (Image issue des Informations Supplémentaires (SI) de l'article 5, page 117.)

La barrière énergétique pour franchir l'interface eau/lipides est plus élevée pour un seul fullerène et peut être considérablement abaissée si plusieurs molécules essayent de diffuser au même endroit ou par un nombre précis des fonctionnelles greffés sur la surface du fullerène. Pour confirmer cette hypothèse et évaluer la contribution énergétique de chaque fullerène dans l'agrégat, nous avons calculé les profils d'énergie libre du passage des fullerènes (fonctionnalisés ou non) à travers la membrane (*voir Figure V.4*). Nous avons aussi tenté d'évaluer les énergies d'agrégations dans le cas des fullerènes solubles.

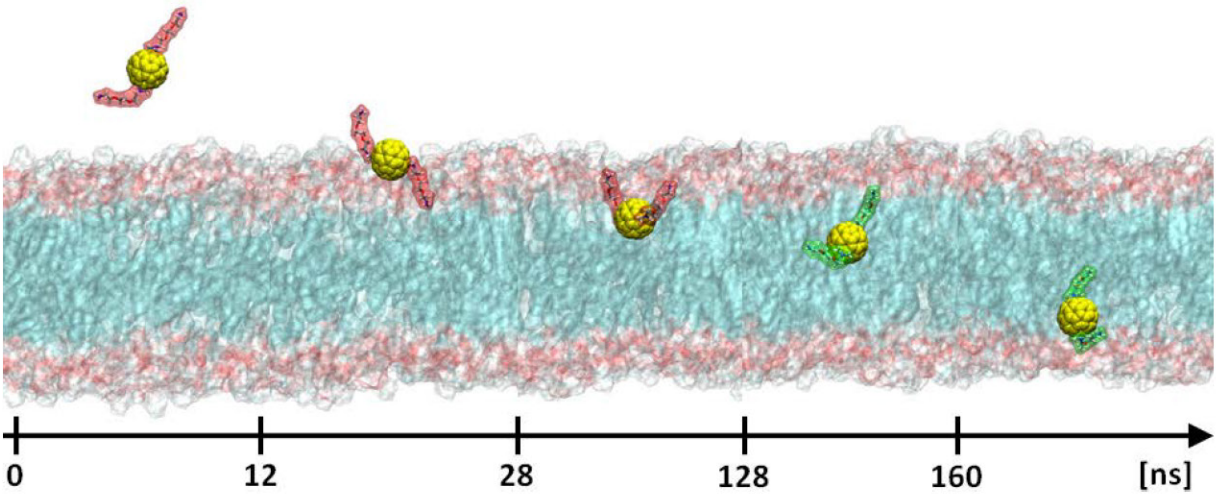

Figure V.3 Résultats des simulations de DM sur une membrane cellulaire (en bleu) en interaction avec un fullerène doublement fonctionnalisé (en jaune) en fonction du temps. Au bout de 28 ns le fullerène pénètre la membrane mais pour passer à travers la membrane les groupements fonctionnels doivent être déprotonés (changement du couleur de rouge vers le vert). À l'échelle de 200 ns, le fullerène soluble arrive sur la deuxième interface eau/lipides.

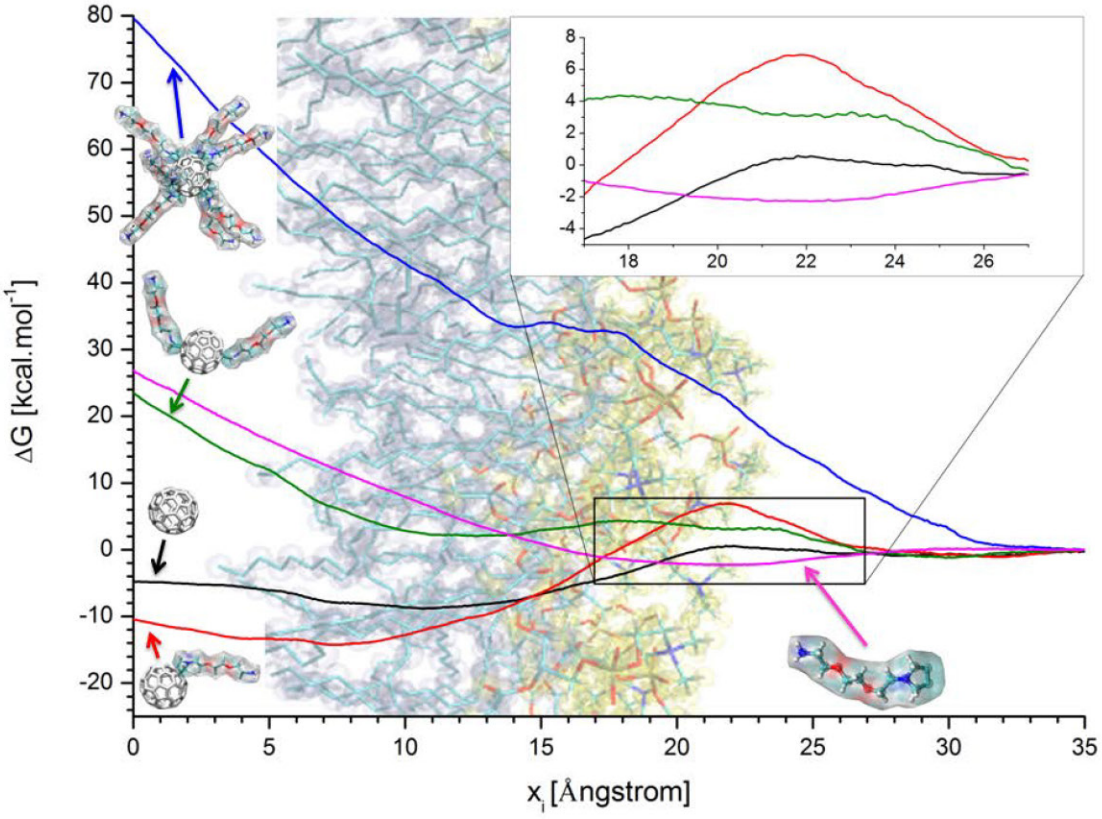

Figure V.4 Les profils d'énergie libre obtenus avec l'approche ABF pour différents types des fullerènes (fonctionnalisés ou non). Un agrandissement montre plus clairement la première barrière à franchir au l'interface eau/lipides.

Uptake and Translocation Mechanisms of Cationic Amino Derivatives Functionalized on Pristine C_{60} by Lipid Membranes: A Molecular Dynamics Simulation Study

Sebastian Kraszewski,[†,*] Mounir Tarek,[‡,*] and Christophe Ramseyer[†]

[†]Laboratoire de Nanomédecine, Imagerie et Thérapeuthique, Université de Franche-Comté, Centre Hospitalier Universitaire de Besançon, 25000 Besançon, France and, [‡]UMR Structure et Réactivité des Systèmes Moléculaires Complexes, CNRS Nancy Université, France

ABSTRACT Bioactive molecules, cationic peptides among them, are nowadays well-recognized in modern pharmacology for their drug potential. However, they usually suffer from poor translocation across cell membranes, and specific drug carriers should be designed to circumvent this problem. In the present study, the uptake mechanism of fullerene bearing cationic ammonium groups by membranes modeled as lipid bilayers is investigated using extensive molecular dynamics simulations and free-energy calculations. Three main results issued from this work can be drawn. First, the fullerene core appears to be a good drug vector since it greatly enhances the uptake of the cationic groups by the membrane. Second, we show that the amino derivatives should be deprotonated at the lipid headgroup level in order to fully translocate the membrane by passive diffusion. Finally, the fullerenes bearing too many cationic groups display mostly a hydrophilic character; thus, the lipophilic fullerene core is not anymore effective as an insertion enhancer. Therefore, the lipid bilayer appears to be very selective with respect to the amount of amino groups conjugated with C_{60}.

KEYWORDS: fullerenes · cationic functionalization · drug vectors · uptake passive diffusion · molecular dynamics · free-energy profiles

Nanomedicine, a combinatorial approach using nanotechnology and medicine, has become an increasingly important field of research for diagnostics and theranostics.[1–3] The field of nanomedicine involves the design and development of novel nanomaterials such as multifunctional liposomal nanoparticles,[4–6] polymeric micelles,[7] iron oxide nanoparticles,[8] nanoshells,[9] and functionalized nanomaterials such as nanotubes[10,11] and fullerenes.[12–15] The latter, and more especially Buckminsterfullerenes (C_{60}), have unique physical and chemical properties.[16] Their nanometer size makes them perfectly suitable for biomedical applications. However, it is important to emphasize that their potential biological benefits can be fully realized only after chemical modifications. Indeed, C_{60}, like all carbon-based nanomaterials, has a poor solubility (less than 0.1 ng·L^{-1}) and displays a tendency for aggregation.[17,18] Accordingly, various functionalizations have been used to increase its hydrophilicity (*e.g.*, −OH, −COOH, $-NH_2$).[16] For instance, a very high level of solubility in water (34 mg·L^{-1}) can be obtained at pH = 7.4 with a dendritic fullerene containing up to 18 carboxylic groups.[12] The fullerene physical and chemical properties play critical roles in many biological processes. Their hydrophobicity and lipophilicity seem to be crucial in optimizing the interaction with the active site of various enzymes,[19,20] especially HIV proteases.[21,22] This specific character allows also C_{60} to directly intercalate into biological membranes, provoking destabilization,[23,24] and has an important role in the antibacterial activity found for several derivatives.[25–27]

Functionalization of fullerenes aimed at drug delivery application is another very active field of research (see recent review by Partha and Conyers).[15] Indeed, bioactive molecules, especially charged ones, belong to a major drugs class used in modern pharmacology, and there is a crucial need to enhance their translocations into cell membranes. For a wide variety of peptides, carbon nanomaterials such as nanotubes and fullerenes appear as effective drug carriers once grafting of peptide to the nanomaterial is achieved. Amphifullerenes, for example, which contain both hydrophobic and hydrophilic moieties, and their associated supramolecular complexes, known as "buckysomes", are very promising nanovectors that can deliver drug to specific sites.[28] Carboxyfullerenes, engineered with three malonic acid molecules, were also shown to be effective radical scavengers and to act *in vitro* and *in vivo* as neuroprotective antioxidants.[29] The relative toxicity of fullerene-based nanoparticles is

* Address correspondence to sebastian.kraszewski@univ-fcomte.fr; mounir.tarek@srsmc.uhp-nancy.fr.

Received for review May 27, 2011 and accepted October 7, 2011.

Published online 10.1021/nn201952c

© XXXX American Chemical Society

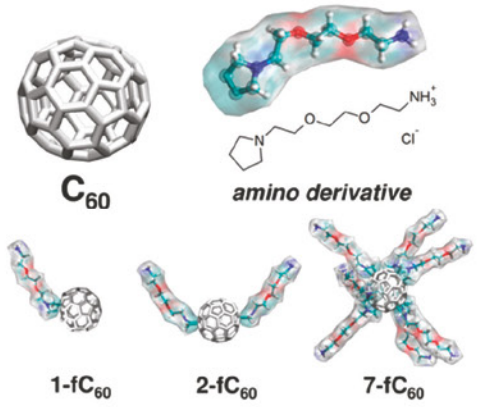

Figure 1. Neat C_{60}- and n-fC_{60}-functionalized fullerenes with n = 1, 2, or 7 amino derivatives investigated in this study.

mostly attributed to the ratio of the amphiphilic/lipophilic character of these derivatives, which can lead to cell membrane disruption and subsequent cellular death, as already observed in water-soluble C_{60} derivatives.[30] Note that, generally, monofunctionalized derivatives show only a moderate toxicity in comparison to more cytotoxic multifunctionalized compounds.[31]

Despite this widespread effective and potential use, only few studies have been devoted to characterize the molecular mechanisms of functionalized C_{60} (fC_{60}) cellular uptake. Almost all of them concerned theoretical investigations using all-atom or coarse-grained molecular dynamics (MD) simulations of neat C_{60} interacting with model membranes. Only one functionalization of the type $(OH)_n$ was the subject of studies addressing the issues of translocation of $C_{60}(OH)_{20}$ from water toward a dipalmitoyl-phosphatidylcholine (DPPC) bilayer hydrophobic core.[32,33] It was shown using unconstrained MD simulations that neat fullerene and its $(OH)_n$ (with $n \leq 10$) derivatives can easily "jump" into the bilayer and translocate into the membrane, while $C_{60}(OH)_{20}$ remains in the aqueous phase. In contrast to these bare compounds uptake, another mode of nanoparticle insertion into lipid bilayers has been recently studied using coarse-grained MD simulations. It involves precoating negatively charged nanocapsules with detergent and lipid molecules and fusion of the resulting liposome-like structure into a lipid membrane.[34]

Expanding on these pioneering studies, we use here extensive MD simulations aimed at characterizing the interaction of C_{60} and associated cationic functionalization groups with a lipid bilayer. We investigate, in particular, the uptake mechanism of a charged amino derivative ($CCNCCOCCOCCNH_3^+$) currently used for carbon nanostructure cell internalization.[35−38] The main goal of this paper is to shed light on the relative role of the fullerene core and functionalization groups

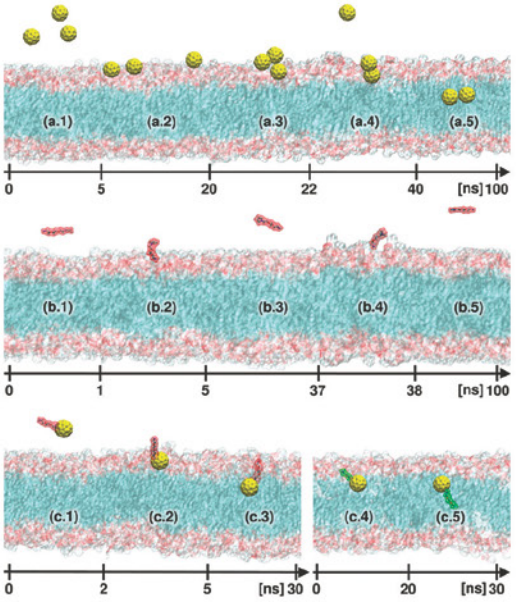

Figure 2. Uptake of a neat C_{60} (a), single cationic molecule (b), and 1-fC_{60} molecule (c) (monomeric cationic group conjugated to fullerene) by a POPC membrane. Results come from unconstrained MD simulations. In the case of C_{60} placed near the membrane (a.1), molecules go first on the membrane surface (a.2) and then start to aggregate (a.3). Aggregation seems to favors penetration (a.4), and the molecules translocate to hydrophobic tails (a.5). The positively charged amino derivative placed near the membrane (b.1) stays most of the time in the solution (b.3, b.5), reaching the membrane surface only during short periods of time (b.2, b.4). The cationic molecule sometimes perturbs the membrane surface (b.4); however, the uptake was not observed. In the case of 1-fC_{60} placed near the membrane (c.1) the molecule easily crosses the lipid headgroup region (c.2). However, due to strong interactions with lipid heads, it remains near the negatively charged phosphorus (c.3) and needs to be deprotonated (c.4) (see details in the text) before further translocation (c.5). The yellow balls indicate the fullerene core. The red transparent and elongated surface corresponds to the ionized cationic group, while the green one is its neutral form. The lipid membrane headgroup and tail sections are shown as red and blue surfaces, respectively. For clarity reasons, water molecules and other fullerenes or monoadducts that are not taken up are not shown.

on the uptake mechanism. Accordingly, we have investigated various systems comprising neat fullerenes and fC_{60} functionalized with one, two, and seven amino groups (see Figure 1). Obtained results show that the hydrophobic fullerene core is able to enhance membrane insertion of a reasonable amount of cationic residues.

RESULTS AND DISCUSSION

C_{60} Favors the Uptake of the Cationic Molecule by the Lipid Bilayer. Unbiased MD simulations show that monomeric neat fullerenes placed in bulk water next to a palmitoyl-oleyl-phosphatidyl-choline (POPC) model lipid membrane spontaneously enter the bilayer within the hundred nanosecond time scale (see Figure 2a). Fullerene crosses the lipid headgroup region (after

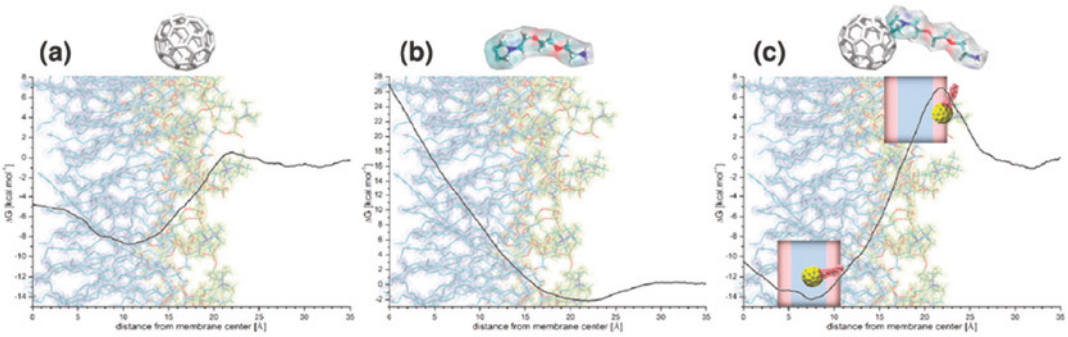

Figure 3. Free-energy profile of translocation through the lipid headgroup region of the neat C_{60} (a), the cationic amino group (b), and the 1-fC_{60} (c), obtained using the adaptive biasing force (ABF) approach. Studied molecules and lipid layer are shown with their real scale. Note different ordinate scale for (b). Insets in (c) show the specific position of 1-fC_{60} corresponding to the barrier at the water/lipid interface and to the energy minimum inside the hydrophobic core of the membrane (see full profile in Figure S2).

about 25 ns) and then proceeds toward the lipid tail region. This shows that monomeric neat C_{60} is able to cross the lipid/water interface, but quite often, fullerenes do aggregate first at the membrane surface. These results confirm previous numerical studies obtained with full atomistic[39] and coarse-grained MD simulations.[33,40] On the other hand, the cationic molecule alone has not shown any propensity to enter the bilayer core (see Figure 2b). Indeed, on the 100 ns time scale, the charged amino derivative stays most of the time in the solvent and, despite occasionally reaching the bilayer headgroup region, does not bind to it strongly (for only 1−4 ns). Hence, the lipid/water interface seems to present a large barrier for translocation of the amino group toward the interior of the membrane. In contrast, when the cationic molecule is conjugated to the fullerene (1-fC_{60} compound), the charged residue penetrates deeper toward the lipid core (see Figure 2c). Several unbiased simulations have indeed shown that 1-fC_{60} crosses the lipid headgroup region. In this process, the amino derivative seems to be dragged toward the middle of the bilayer by the hydrophobic C_{60} moiety.

In order to better quantify the uptake of the three compounds (the C_{60}, the cationic group, and the 1-fC_{60}) by the bilayer, we probed their free-energy profiles as they cross the lipid headgroup interface. The reaction coordinate for fullerene and its derivative was chosen to be the distance between the center of the bilayer and center of mass of the C_{60} sphere and, in the case of the free amino, the distance between its center of the mass and the center of the bilayer. The energy profiles given in Figure 3, estimated using the adaptive biasing force (ABF) method,[41,42] confirm that the hydrophobic nature of the C_{60} favors the uptake of the cationic species by the lipid bilayer. The neat C_{60} displays a large affinity for the lipid tails with an energy well of −8.8 kcal·mol^{-1} (see Figure 3a), and C_{60} uptake is hindered by only a small (~0.5 kcal·mol^{-1}) energetic barrier. This free-energy profile is in excellent agreement with previous studies.[32,43] In contrast, the cationic group alone (Figure 3b) exhibits no affinity for the membrane since only a small well of −2.2 kcal·mol^{-1} occurs at the membrane's surface. Moreover, the translocation of this molecule, toward the center of the lipid core, requires more than +25 kcal·mol^{-1}. The uptake of 1-fC_{60} (Figure 3c) is initially less favored than that of C_{60}, since the compound feels a greater barrier at the entry (+6.9 kcal·mol^{-1}). As this barrier is crossed, however, its translocation toward the lipid hydrophobic core seems to be very much favored (−14.2 kcal·mol^{-1}). It is important to mention that due to the conformational freedom of the 1-fC_{60} molecule, the free-energy profile can hardly be estimated accurately along such a simple reaction coordinate (distance between the center of the compound and the center of the bilayer). The convergence of the herein calculated barrier at the lipid/water interface is probably still questionable. During the constrained uptake of 1-fC_{60}, and specifically when reaching the lipid headgroup area, the compound adopts indeed a wide variety of conformations over which it is sampled. Consequently, seen during the MD run the most representative conformation of the compound at the water/lipid interface (see higher inset of Figure 3c) is thus not the only one, which was taken into account during the evaluation of the free-energy barrier. However, the conformation sampled deep within the bilayer corresponds very well to that of the unconstrained MD simulation (see lower inset of Figure 3c). One can then confidently state from the data at hand that the cationic species conjugated to the fullerene is dragged further toward the membrane interior than the bare cationic residue (see Figure 2c.3).

Translocation across the Lipid Tails: Deprotonation Is Needed. Even if the previous calculations show that fullerene enhances the uptake of the cationic group by the lipid bilayer, so far only the translocation of the 1-fC_{60} compound across the lipid headgroup was witnessed. The unconstrained MD simulations of the 1-fC_{60} compound indicate, in agreement with the results from the free-energy estimates (Figure S2), that the amino group remains strongly bound to the lipid heads once the

fullerene, to which the functionalization is attached, has penetrated the core of the membrane (Figure 2c.3). These results contrast with experiment since *n*-fC$_{60}$ and compounds like it have been shown to cross cell membranes under physiological conditions.[32,44,45] The origin of such discrepancy lies probably in the fact that we have considered translocation of the protonated form of the amino group (stable form in solution under normal pH conditions). Recent theoretical studies based on local pK_a measurements and evaluation of the partitioning of amino acid side chains into lipid bilayers indicate however that it is reasonable to expect that some titrable residues (once in the membrane) may change their protonation state after crossing the charged lipid/water interface.[46,47] Such is the case for instance for the Lys residue, which is shown to have a high probability of changing its state from charged to neutral at ~4 Å from the membrane center. Other charged residues such as acidic Asp and Glu are found to be neutral already in the carbonyl group region! (more than 16 Å from the center of the POPC membrane). Other investigations also considered that a negative shift in local pK_a can occur once the positively charged bases are stabilized in the lipid environment, which importantly increases the probability of losing their charge in favor of a neutral form.[48,49]

In order to check if deprotonation of the amino derivative occurs when the cationic group is located in the headgroup region, one needs to estimate its local pK_a. To our knowledge, there are no experimental pK_a values for *n*-amino-fC$_{60}$ derivatives. As the first approximation, we considered the monoethanolammonium ion (HO(CH$_2$)$_2$-NH$_3^+$) as a good model of the cationic group, which can be treated as independent of the C$_{60}$ core considered in the present study. The pK_a of the monoethanolammonium ion amounts to 9.5 under neutral pH.[50] This corroborates the fact that the protonated state is dominant in the aqueous phase. We then consider dissociation of the proton from the charged amino group taking place in the vicinity of the negatively charged phosphorus of the lipid headgroup, *i.e.*, the location where the amino group is trapped (Figure 2c.3). The lipid headgroups can be modeled in two ways depending on the desired degree of complexity (see Supporting Information for more details). The simplest approach is to consider the dihydrogen phosphate ion ($H_2PO_4^-$) as a model system of the nearest negatively charged phosphorus. Reaction of H_3PO_4 dissociation to $H_2PO_4^-$ has a pK_a value equal to 2.12.[51] A more complicated, yet more realistic, approach is to model the lipid headgroup with a whole phosphocholine molecule ($C_5H_{15}NO_4P$). To our knowledge, there is no experimental pK_a value available for this molecule. A predictive pK_a = 6.18 was found for phosphocholine using the Marvin ChemAxon software. As a consequence, one can evaluate the local pK_a of the ethanolammonium ion in these two models of lipid headgroups (see Supporting Information). When we consider $H_2PO_4^-$, the local pK_a for the ethanolammonium ion decreases to 7.38, being very close to the pH under physiological conditions (from 7.2 for cytoplasm to 7.45 for blood).[52] If the pK_a is equal to the pH, an equal probability to have the neutral and ionized form is thus found. This result, even extremely simplified, shows that it is reasonable to consider deprotonation during translocation of cationic species. The second model using a phosphocholine molecule leads to a much more pronounced negative shift of the pK_a for the ethanolammonium ion (~3.32). This means that over 99.9% of amino groups could be already in the neutral form near the lipid headgroups. Even if the second model is based only on the predictive pK_a, it strengthens the deprotonation hypothesis during translocation of the cationic molecules.

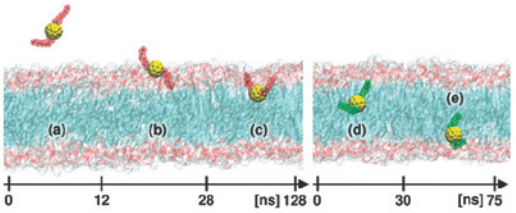

Figure 4. Uptake of a single 2-fC$_{60}$ by POPC membrane (a). Results are from a total of ~200 ns unconstrained MD simulations. This bis-adduct easily crosses the lipid headgroup (b). However, due to strong interactions with lipid heads (c), it needs to be deprotonated in order to fully translocate the membrane (d and e) (see details in the text). Yellow balls indicate the fullerene core with two ionized (red) or neutral (green) amino derivatives. Lipid membrane head and tail sections are shown as red and blue surfaces, respectively. For clarity reasons, water molecules and other mono- and bis-adducts that have not been taken up are not shown.

We have thus taken this into account in the MD simulations of the 1-fC$_{60}$ molecule as shown in Figure 2c. Following the deprotonation of the amino group of the 1-fC$_{60}$ compound (Figure 2c.4), the molecule starts to effectively penetrate the hydrophobic zone of the bilayer, which was unfavorable before. This translocation occurs ~20 ns after the change from the ionized to the neutral form (Figure 2c.5).

Translocation of Multifunctionalized Fullerenes. The number of amino substituents on the C$_{60}$ cage must be chosen carefully in order to ensure the passive diffusion across the lipid headgroups. To quantify the most favorable configuration enabling the relatively easy translocation throughout the lipid bilayer, a MD run of 200 ns of a system containing an equal mixture of 1-fC$_{60}$ and 2-fC$_{60}$ molecules (three mono- and three bis-adducts) was performed. The simulations show that the bis-adduct enters into the membrane core (crosses the lipid headgroup region) within the same time scale as does the monoadduct (see Figure 4). The bis-adduct rapidly passes the lipid headgroup region (within ~28 ns) and remains there for the remainder of the 100 ns simulation; the two amino groups are pinned to the headgroups probably due to favorable electrostatic interactions. Meanwhile, other mono- and bis-adducts aggregate in the bulk water and do not show any specific propensity to go inside the

lipid bilayer (data not shown). As in the previous MD run shown in Figure 2c, when the monomeric species is trapped at the membrane interface, complete translocation is not fully observed. After 128 ns, following the deprotonation hypothesis, we switched the amino groups of the bis-adduct that partially translocated to the membrane core to its neutral form (see Figure 4d). Consequently, within the next 75 ns, it spontaneously migrates toward the other leaflet of the membrane (Figure 4e). To further quantify the influence of the number of cationic residues on the C_{60} cage on passive diffusion, we evaluated the free-energy profiles of three compounds: 1-fC_{60}, 2-fC_{60}, and 7-fC_{60} (see Figures S2, S3, and S4, respectively). The charged species of mono- and bis-adducts show an important energybarrier located deeper in the membrane, which is directly linked to the amino groups that pin to the lipid heads. In the case of their neutral forms, the flat shape of the energy profile confirms their ability to easily cross the hydrophobic part of the membrane, in agreement with the performed unconstrained MD simulation results. In the case of 7-fC_{60}, the uptake is clearly unfavorable since the energy barrier continuously rises from the solvent toward the membrane center up to $+80$ kcal·mol^{-1}. Bearing seven cationic amino derivatives, the 7-fC_{60} is much larger than the mono- and bis-adduct. More importantly, such an amount of the amino derivatives appears to completely screen the lipophilic fullerene core, as the C_{60} can no longer play the role of membrane insertion enhancer. Due to a large number of amino derivatives, the molecule remains in contact with the bulk solvent, and accordingly, it is not appropriate to consider here deprotonation of the cationic groups. This result strongly suggests that if the compounds such as 7-fC_{60} could still penetrate cell membranes, they would probably take another pathway, such as endocytosis. Precise estimation of the cut off, concerning the favorable amount of amino derivatives, still being dragged by C_{60} toward the membrane center, will be the subject of further study.

Insertion and Release Rates. The results presented so far show how and when C_{60} and fC_{60} may insert in the core of the POPC membrane. In order to extract the macroscopic data concerning the permeation of fC_{60} molecules, we have built a simple one-dimensional model inspired by the single-state molecular motor theory.[53] Assuming optimal conditions for protonation/deprotonation of the amino groups exist at the water/lipid interface, we can estimate the insertion and release rates using a stochastic model described in the Methods section, in which the particles diffuse under the action of the MD-derived free-energy profiles. For C_{60} as well as for the charged species 1-fC_{60} and 2-fC_{60}, we found that the molecules are only inserted in the membrane (data not shown). When the deprotonation mechanism is included, we found that 1-fC_{60} and 2-fC_{60} can translocate through the whole bilayer (see Figure S5). The insertion and release rates, namely, $\theta_I(t)$ and $\theta_R(t)$, exhibit an exponential behavior (see Figure S6), and the results of the model show a significant difference in the corresponding characteristic times for insertion τ_I and release τ_R between the two compounds. The estimated rates are respectively $\tau_I = 1.53$ ms and $\tau_R = 1.57$ ms for 1-fC_{60} and $\tau_I = 27.27\ \mu$s and $\tau_R = 28.06\ \mu$s for 2-fC_{60}. For 7-fC_{60}, τ_I and τ_R tend obviously to infinity, which means that this molecule cannot be passively taken up. The net flux of 2-fC_{60} expressed here for the charged species in pA ($I = 6.5$ pA) is about 2 orders of magnitude larger than that obtained for 1-fC_{60} ($I = 0.1$ pA).

CONCLUSIONS

Extensive MD simulations and free-energy calculations have been conducted in order to investigate the interaction of amino derivatives and functionalized fullerenes fC_{60} with model cell membranes. The results show that the fullerene is a good vector that helps the cationic groups (which are not taken up alone) to translocate across the lipid/water interface. Following such translocation, the nature of the charged amino head of the amino derivative favors its strong binding to the lipid headgroups. Meanwhile, the other side of the derivative is dragged toward the bilayer center by the fullerene. Deprotonation of the charged amino head favors full translocation of the fC_{60} compound toward the other bilayer leaflet. Such a deprotonation appears to be in fact necessary for the full permeation of the compound. The lipid bilayer is however very selective with respect to the amount of amino groups conjugated with C_{60}. The ABF profiles show that the uptake mechanism of the n-fC_{60} (n = 1, 2, 7) amino adducts result from a subtle balance involving a repulsive (steric and electrostatic) effect between the fC_{60} and the lipids and the attractive (hydrophobic and lipophilic) character of the C_{60} cage (see Figures S7, S8, and S9). As a result, transferring the 7-fC_{60} fullerene from bulk water into the lipid bilayer is highly unfavorable, while the mono- and bis-adduct are able to passively diffuse toward the hydrophobic part of the membrane. Hence, the fullerene core is shown to enhance intracellular internalization of charged species bearing a reasonable amount of cationic groups.

METHODS

Unconstrained full atomistic MD simulations were performed on neat C_{60} and on amino-C_{60} fullerene derivatives in the vicinity of a fully hydrated palmitoyl-oleyl-phosphatidyl-choline bilayer. The translocation energy profiles of C_{60} fullerene and fC_{60} amino derivatives from bulk water toward to the

membrane center was determined using the adaptive biasing force approach.[41]

We considered the following molecular systems:

(i) Neat C_{60}: Two separate systems were used. The first one was used for the free-energy calculations and contained one C_{60} fullerene interacting with a POPC lipid bilayer composed of 72 molecules. The system was hydrated with 3689 water molecules (total of 16 455 atoms in a volume of $48 \times 40 \times 103$ Å^3). The second system used for MD simulations was composed of four neat C_{60} carbon fullerene molecules, a fully hydrated POPC membrane patch of 180 lipid molecules, and 11 830 water molecules (total system of 49 050 atoms, vol. $68 \times 72 \times 116$ Å^3, total simulation time of 100 ns).

(ii) C_{60} with one amino derivative: Two separate sets were performed. For the free-energy calculation, the system was composed of one C_{60} carbon fullerene molecule to which one charged amino derivative was grafted (monoadduct), a membrane patch of 72 POPC lipid molecules, and 3671 water molecules (total of 16 433 atoms in a volume of $40 \times 51 \times 96$ Å^3). To ensure the electroneutrality of the system, one chloride ion was added. For the unconstrained MD simulations, the system was composed of three monoadducts placed initially near a 180 POPC lipid molecule membrane patch ($70 \times 75 \times 109$ Å^3), hydrated with 11 801 water molecules, and three chloride counterions. Deprotonation (after a 30 ns run) was performed simply by deletion of one hydrogen on the head of the amino derivative (the partial charge was compensated on the nitrogen atom in order to obtain the electroneutrality, which is in very good accordance with the quantum calculations (data not shown)). The counterion was also deleted from the system.

(iii) C_{60} with two amino derivatives: Two independent systems were considered. For the ABF free-energy evaluation, the system was composed of one C_{60} carbon fullerene molecule to which two charged amino derivatives were grafted (bis-adduct), a 72 POPC lipid molecule membrane patch, 3650 water molecules, and two chloride counterions (total of 16 402 atoms in a volume of $46 \times 46 \times 93$ Å^3). For MD simulations, the numerical system contained three bis-adducts and three monoadducts placed initially near the 180 POPC lipid molecule membrane patch (total system of $70 \times 75 \times 109$ Å^3, 11 576 water molecules, nine chloride counterions, total simulation time of 200 ns). The deprotonation of the bis-adduct was ensured in the same way as for the monoadduct, and two corresponding counterions were also deleted from the system.

(iv) C_{60} with seven amino derivatives: Only the ABF free-energy calculation was carried out. The system was composed of one C_{60} carbon fullerene molecule with seven charged amino derivatives attached, a 72 POPC lipid molecule membrane patch, and 3373 water molecules (total of 16 331 atoms in a volume of $47 \times 42 \times 98$ Å^3). To ensure the electroneutrality of the charged system, seven chloride ions were added.

(v) Amino group: An unconstrained MD simulation and ABF free-energy evaluation were performed. For the ABF analysis, one unconjugated amino group was placed in the vicinity of the 72 POPC lipid molecule membrane bilayer hydrated with 3697 water molecules and one chloride counterion (total of 16 457 atoms in a volume of $45 \times 48 \times 89$ Å^3). The MD run was executed during 100 ns on the same system as used for the free-energy evaluation.

Molecular Dynamics Method. The MD simulations were performed using NAMD software.[54] They were conducted at a constant temperature of 300 K (Langevin dynamics) and a constant pressure of 1 atm using the Langevin piston Nosé-Hoover method.[55] Short- and long-range forces were calculated every one and two time steps, respectively, with a time step of 2.0 fs. Chemical bonds between hydrogen and heavy atoms were constrained to their equilibrium values. Long-range electrostatic forces were evaluated using the particle mesh Ewald method.[56]

All systems were modeled using the CHARMM27[57] force field with a united atoms representation for the acyl chains of the lipid molecules. No charges were attributed to the C_{60} carbon (C) atoms, and for fullerene C−C or fullerene C−water oxygen (O) interactions we used the Bedrov *et al.*[58,59] Lennard-Jones potential parameters (CHARMM27 functional: $\sigma_{CC} = 3.895$ Å, $\varepsilon_{CC} = 0.066$ kcal·mol^{-1} and $\sigma_{CO} = 3.58$ Å, $\varepsilon_{CO} = 0.0936$ kcal·mol^{-1}). Water molecules were treated within the TIP3P model.[60] For the potential parameters of the amino group, we followed the general procedure described by Norrby and Brandt,[61] and we performed the *ab initio* quantum calculations using Gaussian 03 package software.[62] The geometrical optimization of a single amino group was performed using the Hartree−Fock approach. The split-valence 6-31+G basis set was employed for all atoms, and obtained Mulliken partial charges were applied to the molecular model.[63]

Adaptive Biasing Force Method. The free-energy profiles were performed using NAMD software[54] with the ABF extensions integrated in the Collective Variables module[64] and under the same conditions as described for MD simulations. The minimal sampling was equal to 100 000 samples for each step along the reaction coordinate, taken as a distance between center of mass (COM) of the fullerene core and the COM of the lipid bilayer along the z axis, with a step of 0.1 Å. In the case of the amino group itself, the reaction coordinate was chosen as a distance along the bilayer normal (z axis) between the COM of the amino group and the COM of the lipid bilayer, with the same step of 0.1 Å.

Stochastic Model. In this model, the individual molecules can diffuse according to the Smoluchowski equation in the effective potential deduced from the MD simulations. Let us assume that the system contains N molecules located initially in the external side of the membrane (say left) and that their motion is restricted to the direction z perpendicular to the membrane surface with imposed boundaries of −40 and 40 Å. Using a discrete description of the position ($z = n\Delta z$ with a Δz step of 1 Å), the probability $p(z, t) \approx p(n, t)$ that a given molecule is located at position z at a given time t obeys the following equation:

$$\begin{aligned} p(n, t+\Delta t) = {} & p(n, t) + k(n+1)W(n+1, n)p(n+1, t)\Delta t \\ & + k(n-1)W(n-1, n)p(n-1, t)\Delta t \\ & - k(n)W(n, n+1)p(n, t)\Delta t \\ & - k(n)W(n, n-1)p(n, t)\Delta t \end{aligned} \quad (1)$$

where $k(i)$ is the attempt frequency, which is closely related to the second derivative of G at site i, and $W(i, j)$ represents the probability for the particle to jump from position i to position j. $W(i, j)$ is related to G and the thermal energy k_bT (k_b is the Boltzmann constant) through a simple Arrhenius law:

$$W(i, j) \propto e^{(-[G(j) - G(i)]/k_bT)} \quad (2)$$

Note that only jumps from adjacent positions are allowed here.

The integration of eq 1 for different sets of time and positions can be easily performed assuming initial conditions of $p(-40,0) = N$. The insertion and release rates, $\theta_I(t)$ and $\theta_R(t)$, respectively, were calculated by considering the number of particles crossing the left and right sides of the membrane. The flux across the membrane was defined as

$$I(t) = \frac{\Delta\theta_R(t)}{\Delta t} q \quad (3)$$

(expressed in pA) where q is the charge carried by n-fC_{60}.

Provided the two energy profiles for each molecule corresponding to the charged and neutral form of cationic residues, the effective potential was constructed as follows: the protonated profile was used for molecules located outside the membrane, while the deprotonated one was considered for the molecules located inside the membrane. The switching distance was fixed for each molecule and was derived directly from MD observations, *i.e.*, ±19, ±11, and ±19 Å for 1-fC_{60}, 2-fC_{60}, and 7-fC_{60}, respectively. Since compound 7-fC_{60} was not

evaluated using unconstrained MD, we adopted the highest value of location where the deprotonation can occur, *i.e.*, those of the 1-fC_{60} molecule.

Acknowledgment. The authors wish to thank F. Obert for the fruitful discussion on the chemical aspects of the pK_a and S. Yasothomsrikul for the critical review of the manuscript. The authors were granted access to the HPC resources of the Mésocentre, a regional computational center at the University of Franche-Comté, and of the Centre Informatique National de l'Enseignement Supérieur (CINES) under the allocations 2009- and 2010-075136 made by GENCI (Grand Equipement National de Calcul Intensif).

Supporting Information Available: Discussion on the local pK_a shift for amino groups in the hydrophilic part of the bilayer is presented. Free-energy profiles, results from the stochastic model, and force profiles acting on charged and neutral forms of studied fC_{60} compounds are also shown. This material is available free of charge *via* the Internet at http://pubs.acs.org.

REFERENCES AND NOTES

1. Riehemann, K.; Schneider, S. W.; Luger, T. A.; Godin, B.; Ferrari, M.; Fuchs, H. Nanomedicine-Challenge and Perspectives. *Angew. Chem., Int. Ed.* **2009**, *48*, 872–897.
2. Caruthers, S. D.; Wickline, S. A.; Lanza, G. M. Nanotechnological Applications in Medicine. *Curr. Opin. Biotechnol.* **2007**, *18*, 26–30.
3. Jain, K. K. Role of Nanobiotechnology in the Development of Personalized Medicine. *Nanomedicine* **2009**, *4*, 249–252.
4. Torchilin, V. P. Multifunctional Nanocarriers. *Adv. Drug Delivery Rev.* **2006**, *58*, 1532–1555.
5. Gregoriadis, G. *Liposomes as Drug Carriers: Recent Trends and Progress*; John Wiley & Sons: New York, 1988.
6. Rolland, A. *Pharmaceutical Particulate Carriers*; Marcel Dekker: New York, 1993.
7. Nishiyama, N.; Kataoka, K. Current State, Achievements, and Future Prospects of Polymeric Micelles as Nanocarriers for Drug and Gene Delivery. *Pharmacol. Ther.* **2006**, *112*, 630–648.
8. Shi, X. Y.; Thomas, T. P.; Myc, L. A.; Kotlyar, A.; Baker, J. R. Synthesis, Characterization, and Intracellular Uptake of Carboxyl-Terminated Poly(Amidoamine) Dendrimer-Stabilized Iron Oxide Nanoparticles. *Phys. Chem. Chem. Phys.* **2007**, *9*, 5712–5720.
9. Lal, S.; Clare, S. E.; Halas, N. J. Nanoshell-Enabled Photothermal Cancer Therapy: Impending Clinical Impact. *Acc. Chem. Res.* **2008**, *41*, 1842–1851.
10. Klumpp, C.; Kostarelos, K.; Prato, M.; Bianco, A. Functionalized Carbon Nanotubes as Emerging Nanovectors for the Delivery of Therapeutics. *Biochim. Biophys. Acta, Biomembr.* **2006**, *1758*, 404–412.
11. Prato, M.; Kostarelos, K.; Bianco, A. Functionalized Carbon Nanotubes in Drug Design and Discovery. *Acc. Chem. Res.* **2008**, *41*, 60–68.
12. Brettreich, M.; Hirsch, A. A Highly Water-Soluble Dendro [60]Fullerene. *Tetrahedron Lett.* **1998**, *39*, 2731–2734.
13. Brettreich, M.; Burghardt, S.; Bottcher, C.; Bayerl, T.; Bayerl, S.; Hirsch, A. Globular Amphiphiles: Membrane-Forming Hexaadducts of C-60. *Angew. Chem., Int. Ed.* **2000**, *39*, 1845–1848.
14. Burghardt, S.; Hirsch, A.; Schade, B.; Ludwig, K.; Bottcher, C. Switchable Supramolecular Organization of Structurally Defined Micelles Based on an Amphiphilic Fullerene. *Angew. Chem., Int. Ed.* **2005**, *44*, 2976–2979.
15. Partha, R.; Conyers, J. L. Biomedical Applications of Functionalized Fullerene-Based Nanomaterials. *Int. J. Nanomed.* **2009**, *4*, 261–275.
16. Da Ros, T.; Prato, M. Medicinal Chemistry with Fullerenes and Fullerene Derivatives. *Chem. Commun.* **1999**, 663–669.
17. Ruoff, R. S.; Tse, D. S.; Malhotra, R.; Lorents, D. C. Solubility of C60 in a Variety of Solvents. *J. Phys. Chem.* **1993**, *97*, 3379–3383.
18. Sivaraman, N.; Dhamodaran, R.; Kaliappan, I.; Srinivasan, T. G.; Rao, P. R. V.; Mathews, C. K. Solubility of C60 in Organic Solvents. *J. Org. Chem.* **1992**, *57*, 6077–6079.
19. Noon, W. H.; Kong, Y. F.; Ma, J. P. Molecular Dynamics Analysis of a Buckyball-Antibody Complex. *Proc. Natl. Acad. Sci. U. S. A.* **2002**, *99*, 6466–6470.
20. Zhao, X. C.; Striolo, A.; Cummings, P. T. C-60 Binds to and Deforms Nucleotides. *Biophys. J.* **2005**, *89*, 3856–3862.
21. Friedman, S. H.; Decamp, D. L.; Sijbesma, R. P.; Srdanov, G.; Wudl, F.; Kenyon, G. L. Inhibition of the Hiv-1 Protease by Fullerene Derivatives—Model-Building Studies and Experimental-Verification. *J. Am. Chem. Soc.* **1993**, *115*, 6506–6509.
22. Sijbesma, R.; Srdanov, G.; Wudl, F.; Castoro, J. A.; Wilkins, C.; Friedman, S. H.; Decamp, D. L.; Kenyon, G. L. Synthesis of a Fullerene Derivative for the Inhibition of HIV Enzymes. *J. Am. Chem. Soc.* **1993**, *115*, 6510–6512.
23. Sayes, C. M.; Fortner, J. D.; Guo, W.; Lyon, D.; Boyd, A. M.; Ausman, K. D.; Tao, Y. J.; Sitharaman, B.; Wilson, L. J.; Hughes, J. B.; *et al.* The Differential Cytotoxicity of Water-Soluble Fullerenes. *Nano Lett.* **2004**, *4*, 1881–1887.
24. Sayes, C. M.; Gobin, A. M.; Ausman, K. D.; Mendez, J.; West, J. L.; Colvin, V. L. Nano-C-60 Cytotoxicity Is Due to Lipid Peroxidation. *Biomaterials* **2005**, *26*, 7587–7595.
25. Mashino, T.; Nishikawa, D.; Takahashi, K.; Usui, N.; Yamori, T.; Seki, M.; Endo, T.; Mochizuki, M. Antibacterial and Antiproliferative Activity of Cationic Fullerene Derivatives. *Bioorg. Med. Chem. Lett.* **2003**, *13*, 4395–4397.
26. Aoshima, H.; Kokubo, K.; Shirakawa, S.; Ito, M.; Yamana, S.; Oshima, T. Antimicrobial Activity of Fullerenes and Their Hydroxylated Derivatives. *Biocontrol Sci.* **2009**, *14*, 69–72.
27. Yacoby, I.; Benhar, I. Antibacterial Nanomedicine. *Nanomedicine* **2008**, *3*, 329–341.
28. Partha, R.; Mitchell, L. R.; Lyon, J. L.; Joshi, P. P.; Conyers, J. L. Buckysomes: Fullerene-Based Nanocarriers for Hydrophobic Molecule Delivery. *ACS Nano* **2008**, *2*, 1950–1958.
29. Dugan, L. L.; Turetsky, D. M.; Du, C.; Lobner, D.; Wheeler, M.; Almli, C. R.; Shen, C. K. F.; Luh, T. Y.; Choi, D. W.; Lin, T. S. Carboxyfullerenes as Neuroprotective Agents. *Proc. Natl. Acad. Sci. U. S. A.* **1997**, *94*, 9434–9439.
30. Cusan, C.; Da Ros, T.; Spalluto, G.; Foley, S.; Janto, J. M.; Seta, P.; Larroque, C.; Tomasini, M. C.; Antonelli, T.; Ferraro, L.; *et al.* A New Multi-Charged C-60 Derivative: Synthesis and Biological Properties. *Eur. J. Org. Chem.* **2002**, 2928–2934.
31. Bosi, S.; Da Ros, T.; Spalluto, G.; Balzarini, J.; Prato, M. Synthesis and Anti-HIV Properties of New Water-Soluble Bis-Functionalized[60]Fullerene Derivatives. *Bioorg. Med. Chem. Lett.* **2003**, *13*, 4437–4440.
32. Qiao, R.; Roberts, A. P.; Mount, A. S.; Klaine, S. J.; Ke, P. C. Translocation of C-60 and Its Derivatives across a Lipid Bilayer. *Nano Lett.* **2007**, *7*, 614–619.
33. D'Rozario, R. S. G.; Wee, C. L.; Wallace, E. J.; Sansom, M. S. P. The Interaction of C-60 and Its Derivatives with a Lipid Bilayer *via* Molecular Dynamics Simulations. *Nanotechnology* **2009**, *20*, 115102.
34. Carr, R.; Weinstock, I. A.; Sivaprasadarao, A.; Muller, A.; Aksimentiev, A. Synthetic Ion Channels *via* Self-Assembly: A Route for Embedding Porous Polyoxometalate Nanocapsules in Lipid Bilayer Membranes. *Nano Lett.* **2008**, *8*, 3916–3921.
35. Kostarelos, K.; Lacerda, L.; Pastorin, G.; Wu, W.; Wieckowski, S.; Luangsivilay, J.; Godefroy, S.; Pantarotto, D.; Briand, J. P.; Muller, S.; *et al.* Cellular Uptake of Functionalized Carbon Nanotubes is Independent of Functional Group and Cell Type. *Nat. Nanotechnol.* **2007**, *2*, 108–113.
36. Pantarotto, D.; Singh, R.; McCarthy, D.; Erhardt, M.; Briand, J. P.; Prato, M.; Kostarelos, K.; Bianco, A. Functionalized Carbon Nanotubes for Plasmid DNA Gene Delivery. *Angew. Chem., Int. Ed.* **2004**, *43*, 5242–5246.
37. Lacerda, L.; Pastorin, G.; Gathercole, D.; Buddle, J.; Prato, M.; Bianco, A.; Kostarelos, K. Intracellular Trafficking of Carbon Nanotubes by Confocal Laser Scanning Microscopy. *Adv. Mater.* **2007**, *19*, 1480–1484.
38. Lacerda, L.; Pastorin, G.; Gathercole, D.; Buddle, J.; Prato, M.; Bianco, A.; Kostarelos, K. Intracellular Trafficking of Carbon Nanotubes by Confocal Laser Scanning Microscopy (Vol 18, Pg 1480, 2007). *Adv. Mater.* **2007**, *19*, 1789–1789.

39. Kraszewski, S.; Tarek, M.; Treptow, W.; Ramseyer, C. Affinity of C-60 Neat Fullerenes with Membrane Proteins: A Computational Study on Potassium Channels. *ACS Nano* **2010**, *4*, 4158–4164.
40. Wong-Ekkabut, J.; Baoukina, S.; Triampo, W.; Tang, I. M.; Tieleman, D. P.; Monticelli, L. Computer Simulation Study of Fullerene Translocation through Lipid Membranes. *Nat. Nanotechnol.* **2008**, *3*, 363–368.
41. Darve, E.; Rodriguez-Gomez, D.; Pohorille, A. Adaptive Biasing Force Method for Scalar and Vector Free Energy Calculations. *J. Chem. Phys.* **2008**, *128*, 144120(13pp).
42. Hénin, J.; Chipot, C. Overcoming Free Energy Barriers Using Unconstrained Molecular Dynamics Simulations. *J. Phys. Chem.* **2004**, *121*, 2904–2914.
43. Li, L. W.; Davande, H.; Bedrov, D.; Smith, G. D. A Molecular Dynamics Simulation Study of C-60 Fullerenes inside a Dimyristoylphosphatidylcholine Lipid Bilayer. *J. Phys. Chem. B* **2007**, *111*, 4067–4072.
44. Andreev, I. M.; Romanova, V. S.; Petrukhina, A. O.; Andreev, S. M. Amino-Acid Derivatives of Fullerene C-60 Behave as Lipophilic Ions Penetrating through Biomembranes. *Phys. Solid State* **2002**, *44*, 683–685.
45. Foley, S.; Crowley, C.; Smaihi, M.; Bonfils, C.; Erlanger, B. F.; Seta, P.; Larroque, C. Cellular Localisation of a Water-Soluble Fullerene Derivative. *Biochem. Biophys. Res. Commun.* **2002**, *294*, 116–119.
46. MacCallum, J. L.; Bennett, W. F. D.; Tieleman, D. P. Partitioning of Amino Acid Side Chains into Lipid Bilayers: Results from Computer Simulations and Comparison to Experiment. *J. Gen. Physiol.* **2007**, *129*, 371–377.
47. Yoo, J.; Cui, Q. Does Arginine Remain Protonated in the Lipid Membrane? Insights from Microscopic pK(a) Calculations. *Biophys. J.* **2008**, *94*, L61–L63.
48. Fernandez, M. S.; Fromherz, P. Lipoid pH Indicators as Probes of Electrical Potential and Polarity in Micelles. *J. Phys. Chem.* **1977**, *81*, 1755–1761.
49. Beschiaschvili, G.; Seelig, J. Peptide Binding to Lipid Bilayers. Nonclassical Hydrophobic Effect and Membrane-Induced pK Shifts. *Biochemistry* **1992**, *31*, 10044–10053.
50. Hall, H. K. Correlation of the Base Strengths of Amines. *J. Am. Chem. Soc.* **1957**, *79*, 5441–5444.
51. McMurry, J. E.; Fay, R. C. *Chemistry*, 4th ed.; Prentice-Hall, Inc.: NJ, 2004.
52. Boron, W.; Boulpaep, E. *Medical Physiology: A Cellular and Molecular Approach*, 2d ed.; Elsevier Saunders: Portland, OR, 2009; p 1337.
53. Aksimentiev, A.; Balabin, I. A.; Fillingame, R. H.; Schulten, K. Insights into the Molecular Mechanism of Rotation in the F_o Sector of ATP Synthase. *Biophys. J.* **2004**, *86*, 1332–1344.
54. Phillips, J. C.; Braun, R.; Wang, W.; Gumbart, J.; Tajkhorshid, E.; Villa, E.; Chipot, C.; Skeel, R. D.; Kale, L.; Schulten, K. Scalable Molecular Dynamics with Namd. *J. Comput. Chem.* **2005**, *26*, 1781–1802.
55. Feller, S. E.; Zhang, Y. H.; Pastor, R. W.; Brooks, B. R. Constant-Pressure Molecular-Dynamics Simulation—the Langevin Piston Method. *J. Chem. Phys.* **1995**, *103*, 4613–4621.
56. Darden, T.; York, D.; Pedersen, L. Particle Mesh Ewald: An N. Log(N) Method for Ewald Sums in Large Systems. *J. Chem. Phys.* **1993**, *98*, 10089–10092.
57. MacKerell, A. D.; Bashford, D.; Bellott, M.; Dunbrack, R. L.; Evanseck, J. D.; Field, M. J.; Fischer, S.; Gao, J.; Guo, H.; Ha, S.; *et al.* All-Atom Empirical Potential for Molecular Modeling and Dynamics Studies of Proteins. *J. Phys. Chem. B* **1998**, *102*, 3586–3616.
58. Bedrov, D.; Smith, G. D.; Davande, H.; Li, L. W. Passive Transport of C-60 Fullerenes through a Lipid Membrane: A Molecular Dynamics Simulation Study. *J. Phys. Chem. B* **2008**, *112*, 2078–2084.
59. Li, L. W.; Bedrov, D.; Smith, G. D. Water-Induced Interactions between Carbon Nanoparticles. *J. Phys. Chem. B* **2006**, *110*, 10509–10513.
60. Jorgensen, W. L.; Chandrasekhar, J.; Madura, J. D.; Impey, R. W.; Klein, M. L. Comparison of Simple Potential Functions for Simulating Liquid Water. *J. Chem. Phys.* **1983**, *79*, 926–935.
61. Norby, P. O.; Brandt, P. Deriving Force Field Parameters for Coordination Complexes. *Coord. Chem. Rev.* **2001**, *212*, 79–109.
62. Frisch, M. J.; Trucks, G. W.; Schlegel, H. B.; Scuseria, G. E.; Robb, M. A.; Cheeseman, J. R.; Montgomery, J. A.; Vreven, J., T. ; Kudin, K. N.; Burant, J. C.; *et al. Gaussian 03*, Rev. C.02; Gaussian, Inc.: Wallingford, CT, 2004.
63. Mulliken, R. S. Electronic Population Analysis on LCAO-MO Molecular Wave Functions 1. *J. Chem. Phys.* **1955**, *23*, 1833–1840.
64. Henin, J.; Fiorin, G.; Chipot, C.; Klein, M. L. Exploring Multidimensional Free Energy Landscapes Using Time-Dependent Biases on Collective Variables. *J. Chem. Theory Comput.* **2010**, *6*, 35–47.

Uptake and Translocation Mechanisms of Cationic Amino Derivatives Functionalized on Pristine C_{60} by Lipid Membranes: A Molecular Dynamics simulation study

Sebastian Kraszewski[1], Mounir Tarek[2] and Christophe Ramseyer[1]

In chemistry, pH is a measure of the acidity or basicity of an aqueous solution. Pure water is said to be neutral, with a pH close to 7.0 at 25°C. Once in water, an acid AH will have the tendency to be deprotonated and forms its associated base A^- following the dissociation reaction :

$$AH + H_2O \rightleftharpoons A^- + H_3O^+ \quad (1)$$

The acid dissociation constant K_a is usually written as the ratio of the equilibrium concentrations:

$$K_a = \frac{[A^-][H_3O^+]}{[AH][H_2O]} \quad (2)$$

and pK_a is given by :

$$pK_a = -\log_{10} K_a \quad (3)$$

The dissociation constant K_a, defined by (2), appears to be solvent dependent. Hence, a change of the environment of a given chemical group can induce a modification of the equilibrium concentrations $[AH]$ and $[A^-]$ in favor to the ionized or contrarily to the neutral form. If the changes in the environment induce a negative shift in pK_a , the A^- compound will predominate, and deprotonation will be favored.

[1] Laboratoire de Nanomédecine, Imagerie et Thérapeuthique, Université de Franche-Comté, Centre Hospitalier Universitaire de Besançon, 25000 Besançon, France
[2] UMR Structure et Réactivité des Systèmes Moléculaires Complexes, CNRS Nancy Université, 54506 Vandoeuvre-lès-Nancy, France

Deprotonation of amino group, Model A: pK_a of fC_{60} or even fCNT bearing amino derivatives is not known experimentally. However, for chemical reasons, it appears to be a good approximation to consider the monoethanolammmonium ion ($HO(CH_2)_2NH_3^+$) as a model for this cationic group, which can be treated as independent of C_{60} core considered in the present study (see Figure S1). Based on (1), the monoethanolammmonium ion dissociation reaction in water can be written as follows:

$$HO(CH_2)_2NH_3^+ + H_2O \rightleftharpoons HO(CH_2)_2NH_2 + H_3O^+ \quad (4)$$

and has a defined experimentally pK_a value of 9.50.[1] This pK_a value is large when compared to pH=7 and explains why only the ionized $HO(CH_2)_2NH_3^+$ form should be considered in the extracellular media, namely outside the membrane.

When the fC_{60} compound is up-taken by the lipid bilayer, the $HO(CH_2)_2NH_3^+$ surrounding changes from pure water to lipid head groups. Since $HO(CH_2)_2NH_3^+$ were observed to be stuck near to the phosphorous atoms, we investigate the possibility of deprotonation at this specific location. As a first approximation, we consider the dihydrogen phosphate ion ($H_2PO_4^-$) as a simple representation of the negatively charged part of the lipid head (see Figure S1a). Its dissociation reaction is characterized by a pK_a value of 2.12,[2] and takes the form :

$$H_3PO_4 + H_2O \rightleftharpoons H_2PO_4^- + H_3O^+ \quad (5)$$

In order to estimate if deprotonation of the amino groups of fC_{60} occurs efficiently, we need to consider the following equation:

$$H_2PO_4^- + HO(CH_2)_2NH_3^+ \rightleftharpoons HO(CH_2)_2NH_2 + H_3PO_4 \quad (6)$$

Reaction (6) is thus equal to (4) – (5), which means that the pK_a of (6) can be written as:

$$pK_a^{(6)} = pK_a^{(4)} - pK_a^{(5)} \quad (7)$$

It gives pK_a value for the monoethanolammmonium ion in the presence of the dihydrogen phosphate ion (see (6)) of ~ 7.38. This is very close to pH under physiological condition (being

from 7.2 for cytoplasm to 7.45 for blood [3]), which means that the concentration of ionized (monoethanolammmonium ion) and neutral (ethanolamine) forms are equally probable at this particular location. It thus validates the hypothesis that deprotonation of amino groups can be considered, and hence that the group can be in its neutral form once the C_{60} cage bearing the cationic groups is up-taken by the lipid bilayer.

Deprotonation of amino group, Model B: Phosphatidylcholines (phospholipids incorporating choline as a headgroup) are much more complicated than in Model A. In particular, the phosphocholine headgroup is charged positively and negatively, carrying thus a dipole moment as it occurs also for molecules of polar solvent. We have also try to extent the previous approach to whole phosphocholine (see Figure S1b) instead of the phosphate group as proposed in Model A. By analogy to (5) we could write:

$$(CH_3)_3N^+(CH_2)_2(OH)_2PO_2 \; + \; H_2O \rightleftharpoons (CH_3)_3N^+(CH_2)_2OHPO_3^- + H_3O^+ \quad (8)$$

To the best of our knowledge, there is no experimental value of pK_a for the phosphocholine molecule. We use here a predictive value of 6.18 issued from the Marvin ChemAxon software.[4] The dissociation reaction of the monoethanolammmonium ion in the presence of the whole phosphocholine molecule can be written as:

$$(CH_3)_3N^+(CH_2)_2OHPO_3^- \; + \; HO(CH_2)_2NH_3^+ \rightleftharpoons \quad (9)$$

$$\rightleftharpoons (CH_3)_3N^+(CH_2)_2(OH)_2PO_2 \; + \; H_3PO_4$$

Finally, the predictive pK_a for (9) is equal to:

$$pK_a^{(9)} = pK_a^{(4)} - pK_a^{(8)} \quad (10)$$

It gives the value of 3.32 which indicates a very important negative shift of the initial pK_a obtained in aqueous solvent. Again, Model B reinforces the hypothesis that the deprotonation of cationic species should be taken into consideration, once they are translocated across lipid head group area.

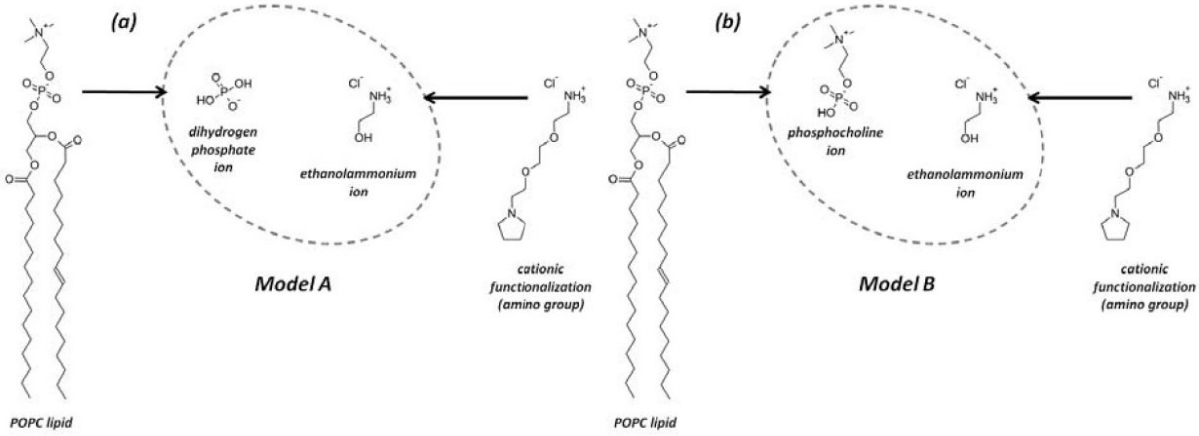

Figure S1 Proposed models of interactions during the deprotonation process of cationic amino group. Model A **(a)**: interaction of ethanolammonium ion with the simplest model of phospholipid head group, namely dihydrogen phosphate ion. Model B **(b)**: interaction of ethanolammonium ion with the whole phosphocholine molecule.

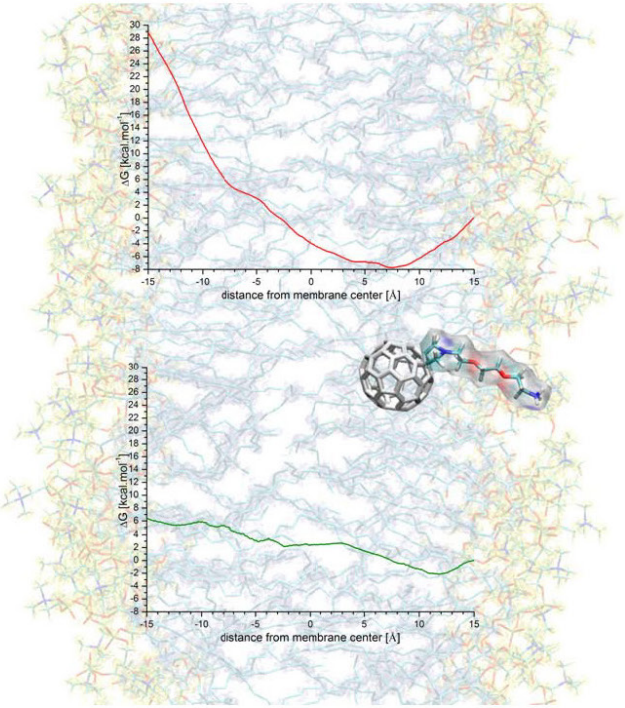

Figure S2 Free energy profiles of translocation of 1-fC_{60} molecule across lipid bilayer. Results obtained using the adaptive biasing force (ABF) approach. The higher inset corresponds to charged amino group (red curve), while the lower one to the neutral form of the amino residue (green curve). Charged form present an important barrier during translocation in contrast to the neutral form able to diffuse passively. Note that relative energy value at +15 Å from membrane center was chose for clarity to be 0 kcal.mol^{-1}. Studied molecule and lipid bilayer are shown with scale corresponding to the abscissa scale.

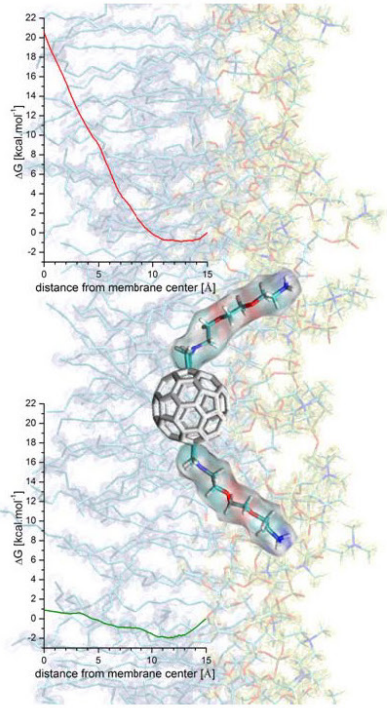

Figure S3 Free energy profiles of translocation of 2-fC_{60} molecule across lipid bilayer. Results obtained using the adaptive biasing force (ABF) approach. The higher inset corresponds to charged amino groups (red curve), while the lower one to the neutral form of the amino residues (green curve). Charged form present an important barrier during translocation in contrast to the neutral form able to diffuse passively. Note that relative energy value at +15 Å from membrane center was chose for clarity to be 0 kcal.mol^{-1}. Studied molecule and lipid layer are shown with scale corresponding to the abscissa scale.

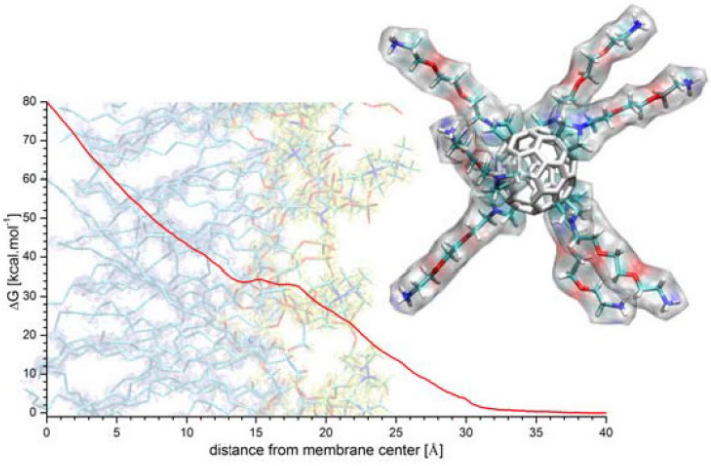

Figure S4 Free energy profile of translocation of 7-fC_{60} molecule across lipid bilayer with charged amino groups. Results obtained using the adaptive biasing force (ABF) approach. There is no energy minimum inside the membrane so the deprotonation cannot occurs due to the lack of deep enough translocaton of cationic groups to the lipid head groups. Studied molecule and lipid layer are shown with scale corresponding to the abscissa scale.

We have used a stochastic model (see Methods section for more detail) in order to get more quantitative assessment for the rates of insertion and release and overall probability of finding fC_{60} molecules in the macroscopic time scale.

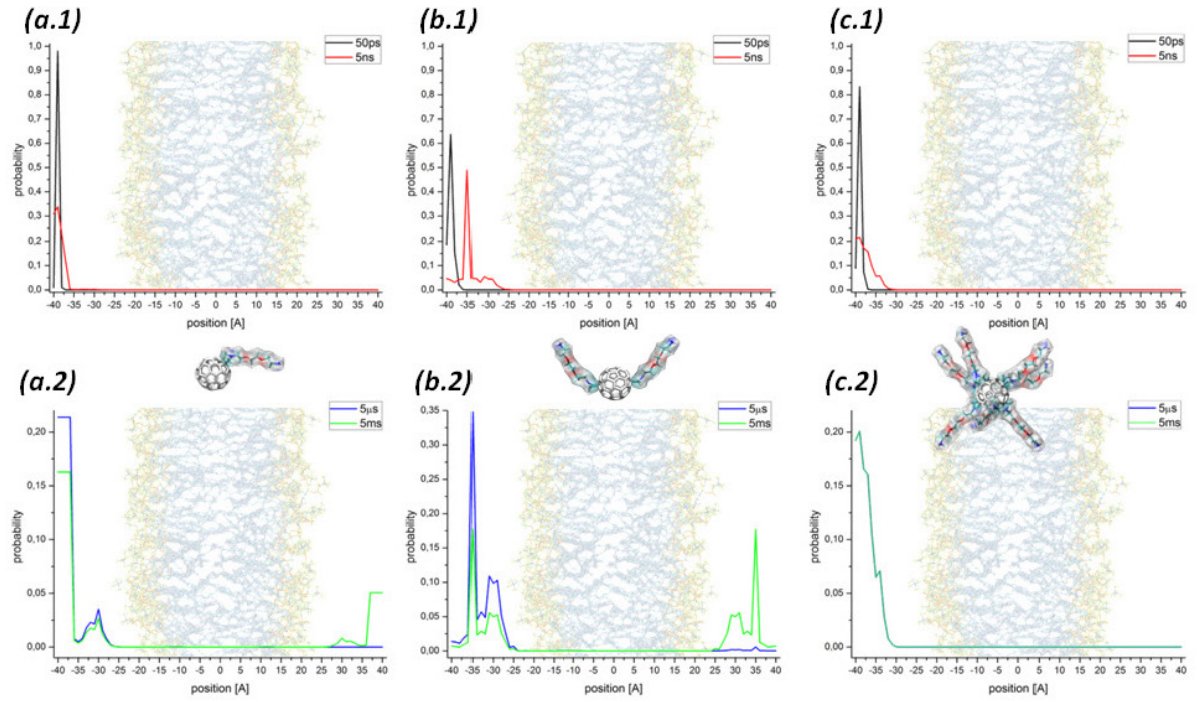

Figure S5 Probabilities of finding 1-fC_{60} (**a.1**) and (**a.2**), 2-fC_{60} (**b.1**) and (**b.2**), and 7-fC_{60} (**c.1**) and (**c.2**), initially located at z = -40 Å after a specific time of propagation, using the effective potential described in Methods section. Insets (**a.1**), (**b.1**) and (**c.1**) corresponds to propagation time of 50 ps and 5 ns, while insets (**a.2**), (**b.2**) and (**c.2**) to propagation times of 5 μs and 5 ms, respectively. Note the different ordinate scales for insets (**a.2**), (**b.2**) and (**c.2**). 1-fC_{60} and 2-fC_{60} are able to cross the membrane in a millisecond time scale, while 7-fC_{60} does not cross the membrane. The high probability of finding the compounds at about -30 and +30 Å is due to a slightly attractive potential near the water/lipids interface (see for example Figure 3).

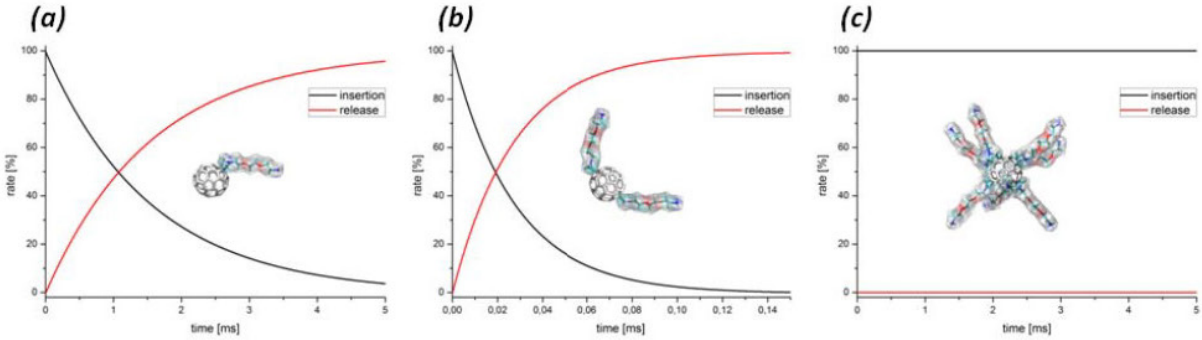

Figure S6 Insertion and release rates of 1-fC_{60} (**a**), 2-fC_{60} (**b**) and 7-fC_{60} (**c**) under the effective potential. Note different time scale (on the x axis) for 1-fC_{60} and of 2-fC_{60} (**b**). The characteristic times are: τ_I = 1,534 ms and τ_R = 1,569 ms for 1-fC_{60}, τ_I = 27,273 μs and τ_R = 28,059 μs for 2-fC_{60}, and for 7-fC_{60} τ_I and τ_R tend to infinity.

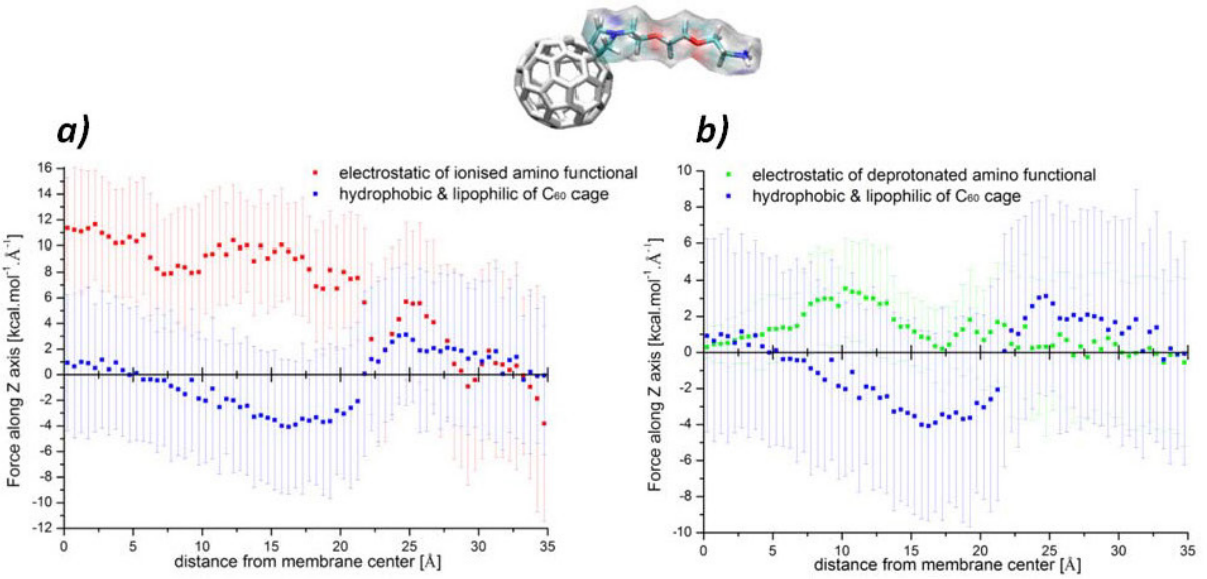

Figure S7 Profiles of forces acting on protonated 1-fC_{60} (**a**) and deprotonated 1-fC_{60} (**b**) during their insertion into the lipid bilayer. Negative forces are attractive (toward the membrane center), while the positive ones are repulsive (toward bulk water). In the case of the deprotonated 1-fC_{60}, the predominant is force is due to the hydrophobic and lipophilic character of the fullerene core.

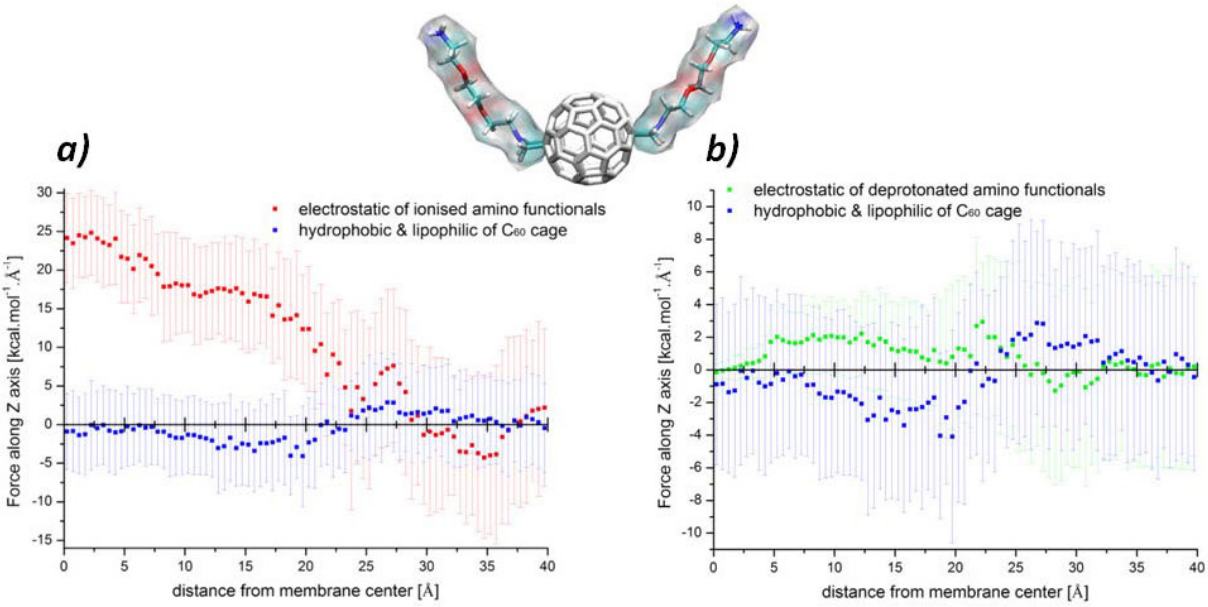

Figure S8 Profiles of forces acting on protonated 2-fC_{60} (**a**) and deprotonated 2-fC_{60} (**b**) during their insertion into lipid bilayer. In case of deprotonated 2-fC_{60} molecule the hydrophobic and lipophilic character of fullerene core is slightly dominant, permitting thus the insertion of molecule in the membrane.

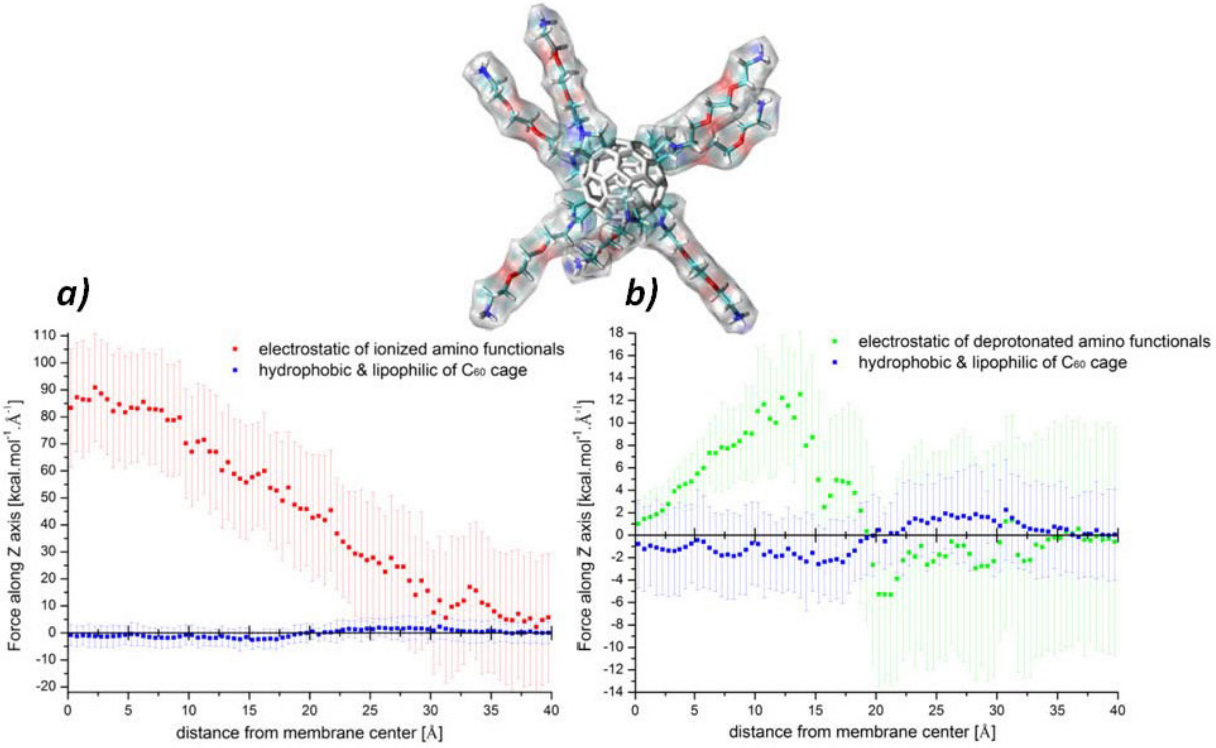

Figure S9 Profiles of forces acting on protonated 7-fC_{60} (**a**) and deprotonated 7-fC_{60} (**b**) during their insertion into lipid bilayer. Note that for the deprotonated 7-fC_{60}, the predominant component is the repulsive force resulting from the electrostatic interactions of the amino functionals. Accordingly the 7-fC_{60} is likely not to penetrate the membrane core.

REFERENCES

1. Hall, H. K., Correlation of the base strengths of amines. *J. Am. Chem. Soc.* **1957,** *79* (20), 5441-5444.
2. McMurry, J. E.; Fay, R. C., *Chemistry*. 4th ed.; Prentice-Hall, Inc.: 2004.
3. Boron, W.; Boulpaep, E., *Medical physiology: a cellular and molecular approach*. 2d ed.; Elsevier Saunders: Portland, 2009.
4. *MarvinView 5.4.1.1 www.chemaxon.com*, ChemAxon Ltd.: 1998-2011.

3 Interactions des CNT avec la membrane cellulaire

Depuis cinq ans, les études expérimentales sur l'interaction entre les nanotubes et les membranes cellulaires se multiplient et plus particulièrement celles qui sont vouées à la délivrance d'agents thérapeutiques fonctionnalisés à la surface de ceux-ci [143-147]. Le mécanisme d'inclusion (ang. *uptake*) n'est pas totalement compris alors qu'il est d'une importance capitale pour la mise en place de nouvelles thérapeutiques à l'échelle cellulaire. Par exemple, dans des cellules de mammifères, deux hypothèses ont été émises [73, 143-144, 146, 148-151] et restent encore matière à débat. La première est de type endocytose alors que la seconde consiste en une diffusion passive simple. Dans cette dernière, le nanotube pénètrerait comme une aiguille dans la membrane sans aucun apport d'énergie extérieure. Néanmoins, depuis les travaux récents de A. BIANCO *et coll.* [72, 146, 152], les conclusions semblent pencher en faveur de la seconde hypothèse. En effet, en utilisant des bloqueurs reconnus pour l'endocytose (DNP ou NaN_3) ou bien en incubant les cellules à basse température (4°C), le groupe de Strasbourg a tout de même observé l'inclusion des tubes dans des macrophages, des lymphocytes B et T. Dans le même ordre d'idée, C. CHENG *et coll.* [153] ont suggéré que les MWNT entrent aussi par diffusion passive dans les macrophages. D'autres études en revanche restent sur la première hypothèse [143-144, 151]. L'origine de ce désaccord peut être due aux techniques expérimentales d'observation (fluorescence [154], microscopie électronique [155], champ proche [156]) mais surtout aux systèmes utilisés (cellules, types et tailles des CNT, fonctionnalisations différentes, ...). Une chose est néanmoins certaine. C'est le caractère hydrophobe des tubes qui leur confère cette propension à passer au travers des membranes cellulaires. Concernant l'aspect chimique, il semblerait que les fonctionnalisations permettant de disperser les tubes dans l'eau n'influent pas sur le mécanisme « uptake » [157]. L'influence des propriétés physiques des tubes est quant à elle peu étudiée jusqu'ici [154, 158]. Il semblerait que la longueur et le diamètre des tubes soient prépondérants pour l'efficacité du transport des tubes à l'intérieur des cellules. Une dernière observation intéressante a été faite récemment par A. BIANCO *et coll.* [146]. Il semblerait que les CNT natifs ne puissent pas traverser la membrane nucléaire (ils percent tout de même les membranes cytoplasmiques) alors que les nanotubes conjugués avec la protéine G_s (la séquence α_s384-394) peuvent entrer dans le noyau de la cellule.

On voit donc, à la lumière de cette analyse bibliographique, qu'il était nécessaire d'analyser le mécanisme d'inclusion à l'aide des simulations numériques sur la base des interactions moléculaires. Nous avons essayé pour cela de répondre aux quatre questions suivantes :

a) S'agit-il d'un mécanisme type endocytose ou bien plutôt de diffusion passive ?

b) La fonctionnalisation « ammonium » de base utilisée par A. BIANCO *et coll.* influence-t-elle l'« uptake » ?

c) Comment expliquer la différence entre membrane nucléaire et membrane cytoplasmique ?

d) Quel est l'effet de la longueur des tubes sur l'inclusion ?

Dans cette étude, nous avons utilisé la dynamique moléculaire sur différents systèmes pour élucider cela. Nous avons aussi conduit des calculs d'énergie libre pour quantifier ces phénomènes. Pour donner une idée de la durée des simulations de la DM effectuées pendant cette thèse, le temps total simulé s'élève à 4.25 µs ; ce qui correspond à 233 ans de calcul monoprocesseur en admettant en moyenne 20 jours pour effectuer une nanoseconde de calul.

3.1 Endocytose ou diffusion passive ?

Comme pour les fullerènes, nous observons que les nanotubes natifs ouverts ou fermés peuvent rentrés de manière passive dans la membrane de POPC, sans agent extérieur et ce en moins de 200 ns de simulation (*voir Figure V.5*). L'origine de cette pénétration réside essentiellement dans le caractère hydrophobe des nanostructures qui cherchent à fuir la phase aqueuse en se cachant dans la membrane. Ce sont visiblement les interactions locales du carbone avec les parties externes des lipides (têtes polaires) qui déclenchent le processus d'inclusion (*voir Figure V.5 b*). Parmi toutes les diffusions que nous avons observées, il semble que l'on peut dégager un mécanisme d'inclusion relativement général. En partant de la solution, le CNT vient d'abord s'accrocher à la surface membranaire (ang. *landing*) puis glisse sur celle-ci pendant un certain temps (ang. *floating*) pour ensuite pénétrer comme une aiguille (ang. *nanoneedle pricking and sliding*). Dans chaque cas, nous n'avons observé qu'une diffusion passive. Ces résultats confortent les hypothèses expérimentales de BIANCO *et coll.* [149] et apporte un éclairage nouveau sur la façon dont les CNT sont internalisés dans les cellules. Notre analyse conforte également le fait que les CNT puissent être utilisés comme vecteurs de médicament puisqu'ils peuvent diffuser de manière passive à travers des membranes biologiques sans aucun effort de la part de la cellule.

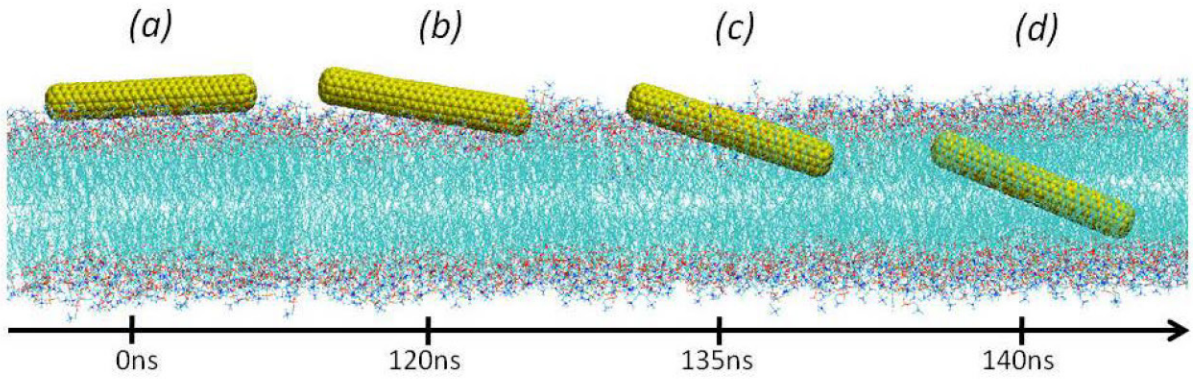

Figure V.5 Résultats des simulations de dynamique moléculaire sur une membrane cellulaire (en bleu) en interaction avec un CNT(6,6) fermé (en jaune) en fonction du temps. (a) *landing*, (b) *floating*, (c) *nanoneedle pricking*, (d) *sliding*.

3.2 La fonctionnalisation joue-t-elle un rôle ?

Sans la déprotonation des groupements fonctionnels ammonium, nous n'avons pas pu observer de pénétration des CNT dans la bicouche de POPC sur des temps raisonnables. Ceux-ci s'accrochent à la surface de la membrane (*landing* + *floating*). Compte tenu de la polarité de la membrane, il est assez légitime de penser que le groupe ammonium puisse se déprotoner facilement. Les simulations montrent alors une inclusion du tube analogue aux tubes non fonctionnalisés. Les temps d'inclusion sont par contre plus longs que pour les tubes nus. La concentration en groupements fonctionnels change l'angle de piqure qui est plus perpendiculaire par rapport à la surface de la membrane pour les CNT fortement fonctionnalisés. En conclusion, la fonctionnalisation ammonium n'empêche aucunement l'« uptake » du CNT mais elle nécessite la déprotonation des groupes fonctionnels à l'interface eau/lipides.

3.3 Quel est l'effet de la longueur des CNT sur l'inclusion ?

Les simulations de dynamique moléculaires effectuées ne permettent pas d'envisager des longueurs de CNT excédant 10 nm. Pour les tubes de 5 nm, nous observons que ceux-ci entrent et s'insèrent complètement dans la membrane sans jamais en ressortir (dans l'échelle de temps envisagée < 400 ns). Cependant, les expériences sont généralement conduites avec des tubes beaucoup plus longs (de l'ordre du micron).

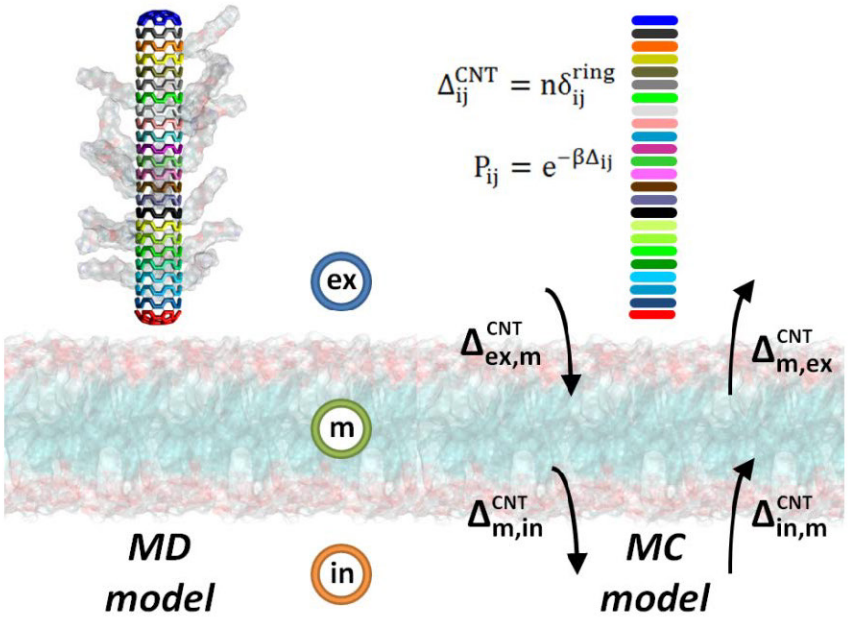

Figure V.6 Modèle statistique Monte-Carlo (MC) fondé directement sur les résultats de simulation de la Dynamique Moléculaire (MD).

Nous avons essayé de modéliser cela en menant une analyse statistique Monte-Carlo (MC). Nous avons décidé de fonder le modèle MC sur les barrières d'énergie extraite à partir des profils d'énergie

libre, obtenu directement à partir de trajectoires de la DM (*voir Figure V.6*). Comme décrit en détails dans l'article suivant, nous avons assimilé le système à trois réservoirs qui se peuplent et se dépeuplent au gré des probabilités de passage de l'un vers l'autre. Les probabilités de passage sont basées sur des barrières énergétiques attribuées par « ring » de carbone exposé aux lipides.

La Figure V.7 montre clairement qu'en dessous d'une longueur de 15 nm, les tubes restent dans la membrane. Au-delà de celle-ci, ils peuvent percer la membrane et rentrer dans le cytoplasme presque complètement. Entre 0.9 et 1.0 µm, le tube se répartit de manière égale de part et d'autre de la membrane. Au delà de 1.3 µm, une grande proportion (70%) du tube reste dans le milieu extracellulaire. Cette dernière observation est clairement une conséquence de l'effet hydrophobe qui est différent de part et d'autre de la membrane cellulaire. Ce modèle Monte-Carlo, bien que très simpliste, est en parfaite concordance avec ce qui est observé expérimentalement. Il montre donc que les barrières d'énergie libre calculées ne sont pas complètement absurdes et que l'hypothèse du rôle important du caractère hydrophobe différencié des CNT peut expliquer la pénétration et la répartition des tubes entre le milieu extérieur et le cytoplasme.

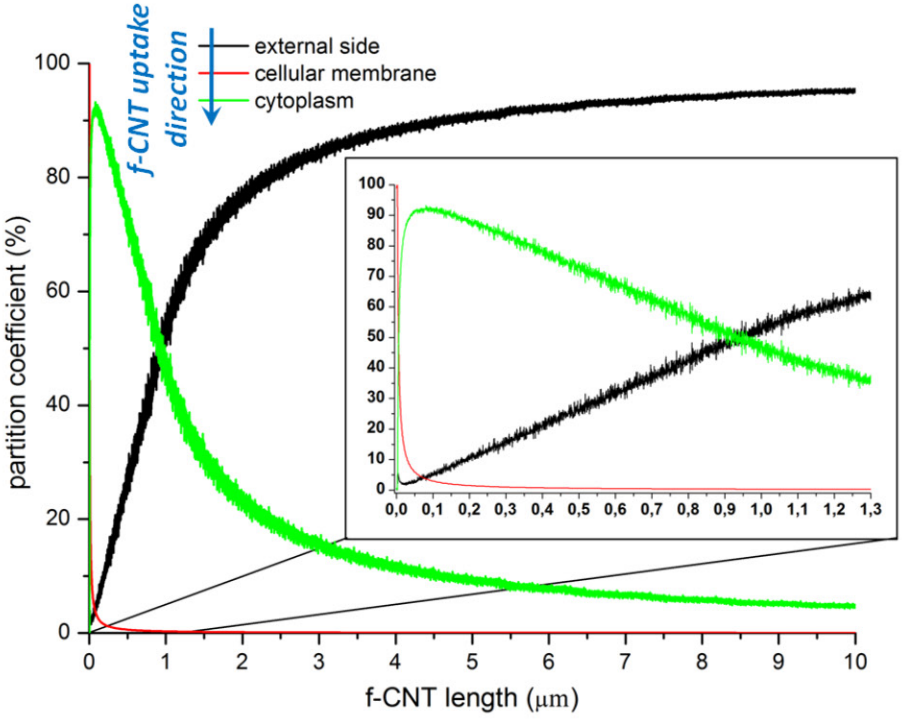

Figure V.7 Coefficient de partition du CNT en fonction de sa longueur dans la membrane cytoplasmique.

3.4 Comment différencier la membrane nucléaire et la membrane cellulaire ?

Jusqu'à présent, aucune explication n'a été donnée sur les observations expérimentales qui montrent que les CNT nus ne peuvent pas pénétrer facilement la membrane nucléaire. Celle-ci est très différente en composition par rapport à une membrane cellulaire. Elle comporte par exemple des agrégats de protéines (ang. *nuclear pore complexes - NPC*) qui peuvent en particulier créer des

pores de 10-20 nm de diamètre [156, 159]. Celles-ci laissent largement la place au CNT pour passer qui bien visiblement n'en profite pas ! Comme précédemment nous avons montré que le solvant jouait un rôle fondamental dans l'inclusion des CNT dans la membrane cellulaire séparant le milieu extracellulaire du cytoplasme, nous avons continué notre analyse sur le même point de vue. La composition du noyau en molécules d'eau fait apparaître également une dissymétrie entre le nombre de molécules d'eau libres et d'eau liées aux macromolécules contenues dans le noyau. Contrairement au cytoplasme, seulement 5% sont visiblement très liées aux macromolécules [160-162]. La Figure V.8 montre le profil d'énergie libre ressentie par un CNT passant une membrane POPC du cytoplasme (50% eau liée) vers le noyau (5% eau liée). Le calcul MC montre des allures de courbes complètement différentes du cas précédent. Les CNT courts, inférieurs à 15 nm, restent enfouis dans la membrane. En revanche, au delà de cette longueur, la proportion restant dans le cytoplasme est très importante (90 % contre 10% dans le noyau). Ce résultat préliminaire est important car il montre que l'effet hydrophobe des tubes de carbone vis à vis de l'eau peut expliquer quasiment les observations expérimentales jusqu'alors restées sans réponse. Il reste néanmoins à faire d'autres analyses et en particulier à fonctionnaliser les tubes avec d'autres fonctionnelles capables de provoquer cette inclusion dans le noyau de la cellule.

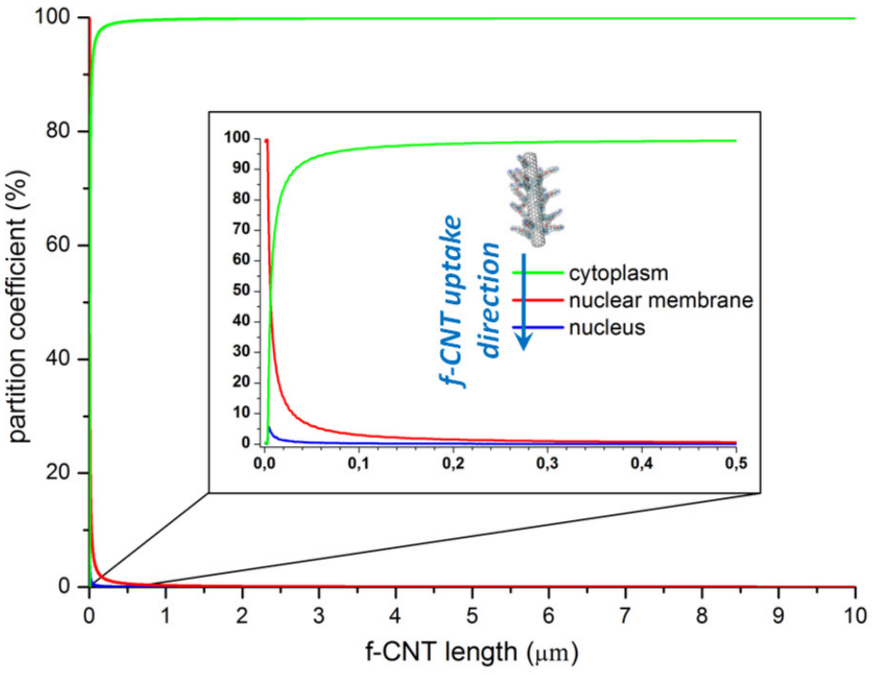

Figure V.8 Coefficient de partition du CNT en fonction de sa longueur dans la membrane nucléaire.

Uptake mechanism of single-walled carbon nanotubes by lipid bilayer. Passive diffusion and role of functionalization derivatives revealed by extensive molecular dynamics simulations.

Sebastian Kraszewski[‡*] *et al.*

[‡]Institut UTINAM - UMR 6213, CNRS Université de Franche-Comté, Besançon, France

sebastian.kraszewski@univ-fcomte.fr

RECEIVED DATE ( )

TITLE RUNNING HEAD: CNT uptake mechanism,

CORRESPONDING AUTHOR:

Sebastian Kraszewski: Institut UTINAM - UMR 6213, CNRS Université de Franche-Comté, Besançon, France

Tel: +33 (0)3 81 66 64 81

DRAFT ONLY

INTRODUCTION

Highly ordered carbon-based nanomaterials such as fullerenes (C_{60}) and carbon nanotubes (CNT) possess unique structural, mechanical, and electronic properties suited for numerous applications. In the biomedical field, due to their high hydrophobic and lipophilic characters, the carbon nanoparticles have the unique ability to easily penetrate cell membranes. Thus, they are of great interest for the intracellular delivery of therapeutic proteins, peptides, genes and vaccines.[1-9] For C_{60}, the uptake mechanism looks rather clear now. Several numerical[10-12] and experimental[13-14] works agree that monomeric neat fullerene placed in bulk water spontaneously enters the bilayer of mamalian cell within the hundred nanoseconds time scale. Monomeric neat C_{60} can cross the energy barrier at the lipid/water interface but quite often, fullerenes need to aggregate there in the first time.[15] Then, in the core of the lipid membrane, partitioning of fullerene molecules occurs.

With respect to C_{60}, CNT usually display lower cytotoxicity[16] but, so far, the CNT uptake into mammalian cells remain still a matter of debate. There is not yet in the literature a common opinion and sometimes conflicting results are presented. A very helpful analysis has been done recently by Raffa and co-workers.[17] It was shown that this disagreement is apparently due to the difference of tested samples. The cellular uptake of functionalized carbon nanotubes looks independent of functional groups and cell types but could be rather attributed to the differences in their physical properties like nanotube length and diameter.[18] The main conclusion is that the short nanotubes (*i.e.*, hundreds of nm in length) could act as tiny and straight "nanoneedles" able to easily penetrate the cell membrane,[7] and more efficiently than the longer ones (*i.e.*, few µm length), which display an energy-dependent endocytotic pathway. More precisely, Pantarotto *et al.* observed passive diffusion of peptide derivative single-walled carbon nanotubes (SWNT) and observed passive diffusion through living cells.[19] They found that incubation with cells in the presence of endocytosis inhibitors does not influence the cell penetration of functionalized carbon nanotubes (f-CNT). Furthermore, f-CNT show similar behavior when its incubation with cells is carried out at low temperature (4°C). The same research group also shows the ability of CNT to penetrate the plasma membrane by a similar process independent of energy, regardless of cell type or the functional group attached onto the CNT.[18] In addition, Raffa and co-workers showed that sub-1 µm length multi-walled carbon nanotubes (MWNT) are also easily internalized through an energy-independent pathway. They found the same trends obtained by Pantarotto *et al.* on SWNT.[19] Indeed, no difference was observed between 37°C and 4°C, and treating the cells with sodium azide, a well-known endocytosis inhibitor at a concentration of 5 mg/ml for

DRAFT ONLY

15 min.[17] They finally concluded that endocytosis cannot be evoked for this uptake process in their work. By contrast, endocytosis was clearly identified as the internalization pathway by the group of H.J. Dai when SWNT (length of hundreds of nm, diameters in the range of 1-5 nm) were used as intracellular transporters for proteins and DNA.[5, 20-21] Phagocytosis was also proposed as an uptake mechanism in mouse peritoneal macrophage-like cells incubated in a growth medium containing various concentrations of SWNT (*ca.* 1 nm average diameter, *ca.* 1 µm average length) in Pluronic surfactant.[22] Finally, C. Cheng and co-workers suggested that MWNT can enter human macrophage cells actively and passively via incomplete phagocytosis or impaling the membrane.[23]

At the light of these results, a clear understanding at the molecular level is necessary. However, to the best of our knowledge, no study has been reported prior to our investigation on the molecular aspects of interactions between f-CNT and cell membrane during its internalization. The few studies which have been done concerned either dissipative particle dynamics or coarse-grained or short constrained all-atom Molecular Dynamics simulations of single neat CNT (no functionalisation is considered) with model membranes.[24-27]

In the present study, we want to explore the uptake mechanism of different type of CNT by fully hydrated POPC membrane model. More precisely, we want to address three main questions, namely: (i) is the CNT uptake a passive diffusion or endocytosis like process ? (ii) how functionalizations participate in the uptake mechanism ? and (iii) what is the CNT length contribution in that process ?

RESULTS

We have performed large scale all-atom MD simulations, the largest being on the microsecond time scale, in order to reveal the precise manner by which CNT cross the membranes. We considered generally two main systems consisting of fully hydrated POPC bilayer and either one open (6,6)-CNT or one closed (6,6)-CNT, which have a diameter of around 1 nm. As presented in Figure 1, open CNT was tested in four separate configurations: **(1)** neat with C-atoms edges, **(2)** neat with H-ended (protonated) edges, **(3)** weakly functionalized (one functional per 130 carbon atoms) with C-atoms edges and **(4)** highly functionalized (one functional per 30 carbon atoms) with H-ended edges. Closed CNT was tested in three distinct sets: **(5)** neat and either **(6)** weakly or **(7)** highly functionalized configurations having one functional per 90 and per 30 carbon atoms, respectively. The functionalized CNT have the water-soluble ammonium derivate groups (f-CNT-NH_3^+) randomly dispersed on the whole surface, which is experimentally given by reaction with a

DRAFT ONLY

pyrrolidine ring through the 1,3-dipolar cycloaddition of azomethine ylides,[28] and was recently described in our previous work.

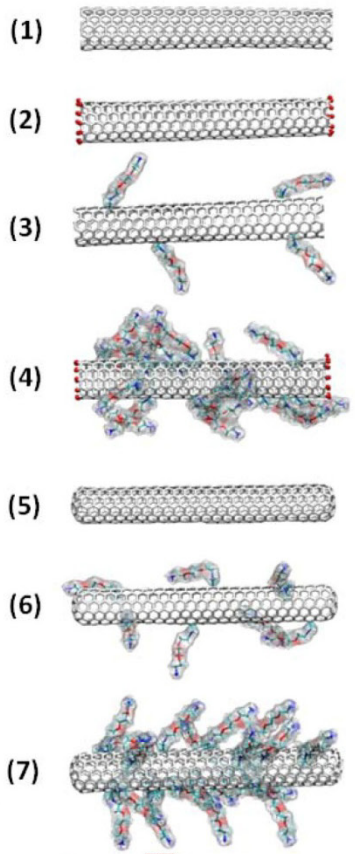

Figure 1 Different kinds of (6,6) CNT have been investigated depending on their aperture and their degree of functionalization. More description of each model can be find in text.

In the first step, we have tested the stability of each of the prepared CNT models in a pure water box before inserting them in the vicinity of the POPC lipid bilayer. Different initial configurations, consisting on CNT locations farther than 0.5 nm from the membrane surface and with different initial angles (0°, 45° and 90° with respect to the normal direction of the bilayer) exclude the possibility that the penetration mechanism can depend on the initial conditions, contrarily as it was recently reported from dissipative particle dynamics study with applied driving force.[27]

Irrespective of the type of CNT and on the concentration of amino-functionals, the nanotubes penetrate the lipid bilayer only by a passive diffusion mechanism, without any symptoms of membrane deformations that could lead to endocytosis hypothesis. Some examples observed in the case of closed CNT are shown in Figure 2. The "nanoneedle" mechanism, proposed in 2004 by Pantarotto *et al.*, is clearly present for all types of tested CNT models.[4] At the molecular level, this mechanism can be described by three successive

steps. The first one concerns the "landing and floating" of CNT onto the lipid bilayer, when the nanotube floats and rolls on the lipid head groups during a time. This time length seems to depend on the degree of functionalization. First phase stops when one or more lipid heads try to grab the CNT edge. At that time, the CNT rapidly acts as a "needle" and pricks the membrane without disturbing it much. It is finally followed by a "sliding" phase where the CNT simply slide into the lipid bilayer. These three sub-mechanisms are noticeably present for all kinds of tested CNT models.

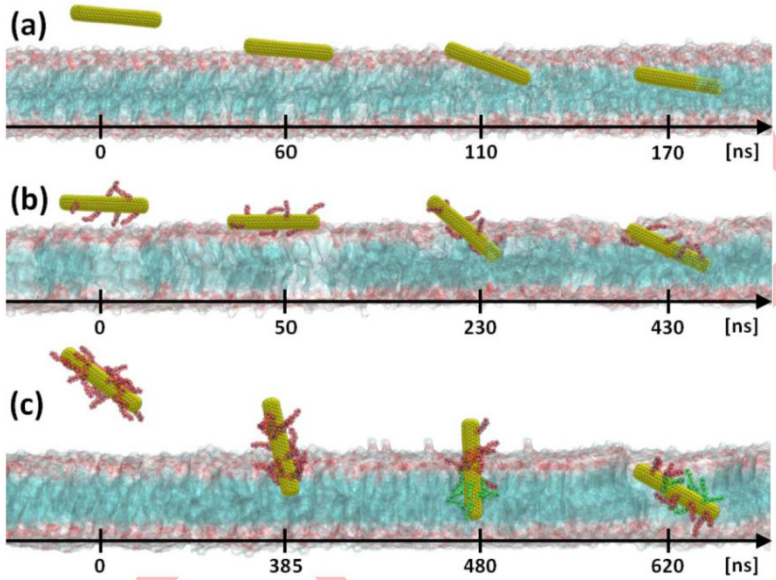

Figure 2 Uptake mechanisms obtained from unconstrained MD simulations with closed (6,6) CNT either **(a)** neat or **(b)** weakly functionalized or **(c)** highly functionalized.

To quantify our results, we have also generated a free energy profile of a neat closed CNT (model **(5)**) moving across the bilayer, using adaptive biasing force (ABF) method.[29-30] This effective but very time-consuming method confirms the nanoneedle mechanism. The profile shown in Figure 3 exhibits an attractive potential well of -24 kcal/mol located at the water/lipid interface. This one is certainly responsible for the attraction, landing and floating of the CNT on the lipid surface. The pricking process is represented by a 12 kcal/mol barrier at the polar head groups that CNT need to overcome in order to diffuse subsequently into the lipid tails. Finally, the large attraction created by a second well of -22 kcal/mol enlightens the last phase where CNT diffuse toward the hydrophobic lipid core of the membrane. Finally the membrane center present again an 12 kcal/mol barrier which could explain why in any of studied cases we could not observe a complete diffusion of CNT to the other side of the membrane. In spite of this, it could also be due to the too short length of tested CNT provoking its complete inclusion in the hydrophobic part of the bilayer. Computational limitations, however, do not permit to evaluate CNT longer than 5 nm in the reasonable time.

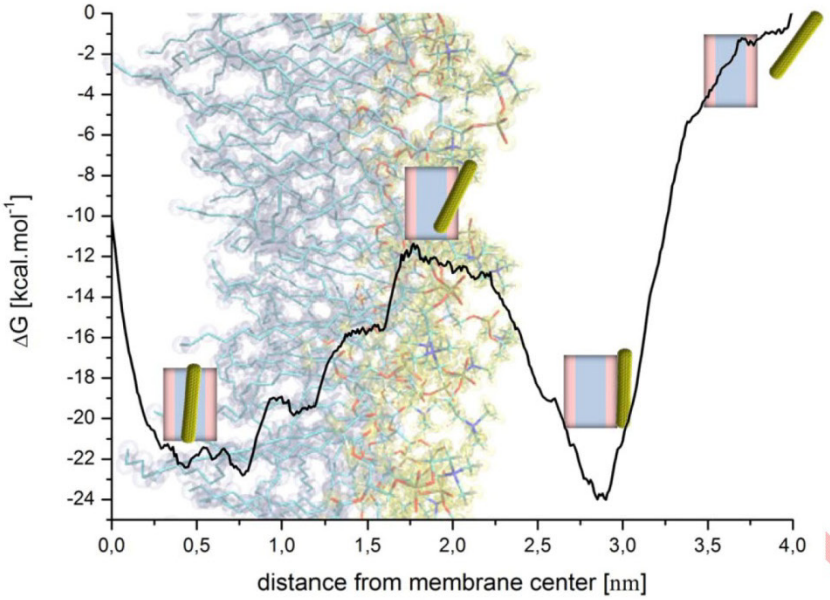

Figure 3 Free energy profile of (6,6) neat closed CNT passing across cell membrane, obtained using the ABF approach.

Even if the functionalized groups do not seem to influence the overall nanoneedle-like process, the sub-mechanisms, especially the "pricking" phase are directly linked with the amount of the functional groups. More the functionalized groups are attached on the CNT surface, more the translocation takes time and more the pricking angle (with respect to the surface of the membrane) is pronounced. In the case of lightly functionalized **(3)** and **(6)** CNT, penetration occurs with acute angles of picking. Highly functionalized **(4)** and **(7)** CNT present an almost perpendicular membrane picking, which likely seems to be a consequence of interactions between unfunctionalized CNT edges and lipid bilayer. The uncovered carbon atoms are probably more attracted by hydrophobic part of the membrane (more repulsed from water) and the lowest cost to cross the energetic barrier at the lipid/water interface can be achieved through the diffusion in the perpendicular configuration. Finally, it is worth to mention that protonated edges of the open CNT (models **(2)** and **(4)**) do not influence the molecular mechanism of the diffusion. Again, this kind of functionalization does not change the way CNT enter the bilayer, namely by passive diffusion.

At that point, it should be mentioned that after entering the membrane, and contrarily to what was observed experimentally, the positively charged ammonium groups stuck between lipid heads, due to simple charge-charge interactions with negatively charged phosphorous. This interaction stops the translocation and even the application of ionic transmembranal potential does not allow this translocation (it only substantially accelerates the whole process of diffusion). To solve this issue, we followed the hypothesis concerning the protonation/deprotonation process, which probably can occur on ammonium groups crossing

DRAFT ONLY

the membrane. In fact, some recent works based on local pKa measurements or calculations on the partitioning of amino-acids side chains into lipids bilayers argue that it is reasonable to expect that cationic residues like Arg in membrane proteins (once in the membrane) can change their protonation state.[31-32] However, we are aware that this mechanism, not yet confirmed for amino derivatives, could not be the single one to explain the easiest translocation of f-CNT confirmed experimentally, and that the charge transfers to the transmembrane proteins could also be an another argument.[33] Changes in protonation state are model by removing the hydrogen atom from the NH_3^+ head of the ammonium derivative group and by compensating the partial charges according to the Mulliken calculation scheme (for more details see Methods section). This procedure give immediately an uncharged CNT functional, permitting to switch the protonation state directly when running MD simulation. After the 400 ns of simulation on model **(7)**, with all positively charged functional, we started the functional by functional deprotonation once the charged residues were completely immersed into the membrane. As a consequence, CNT penetrate deeper the membrane core. After the next 140 ns CNT starts to touch the inner hydrophilic leaflet of the bilayer. At this time we also proceed to reprotonation of the amino groups being close to this membrane/water interface. During the total simulation time reaching 779 ns CNT completely immerse into the membrane as shown in Figure 1c. However, extremely short length of all tested CNT results in their complete inclusion in the hydrophobic part of the bilayer. In fact, used in experimental studies CNT have the length of at least a few tens of nanometers, which probably is long enough to not permit CNT completely immerse between lipid molecules. To solve this issue we decided to address a statistical MC model able to extent our MD result on longer nanotubes, and to predict final configuration of CNT crossing the membrane.

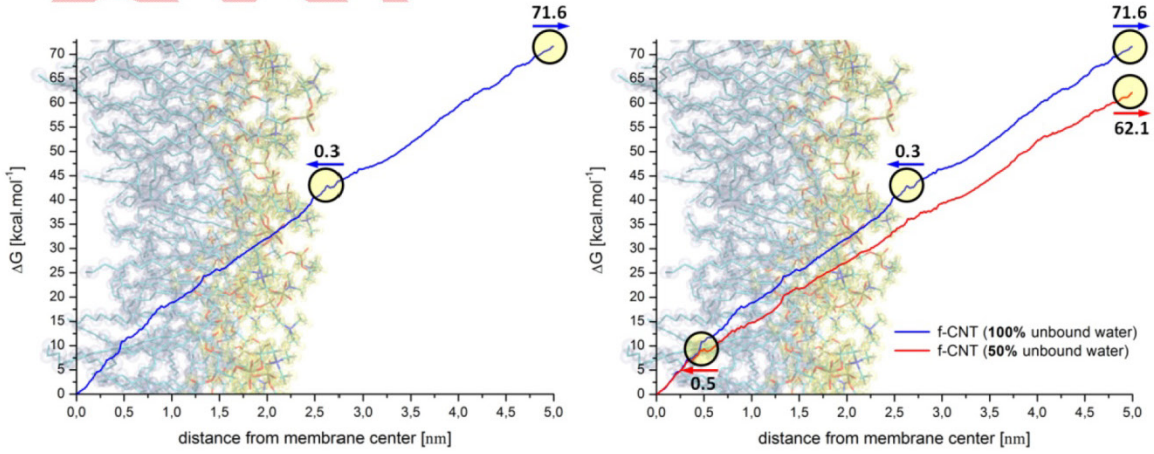

Figure 4 Free energy profiles of highly functionalized closed (6,6) CNT (model **(7)**) passing across cell membrane, obtained using Umbrella Sampling method. **(a)** symmetrical profile with marked entry and exit barriers, **(b)** asymmetrical profile for different environments with marked entry and exit barriers. 100% unbound water environment corresponds to extracellular media or nucleus, while 50% unbound water environment corresponds to cytoplasm.

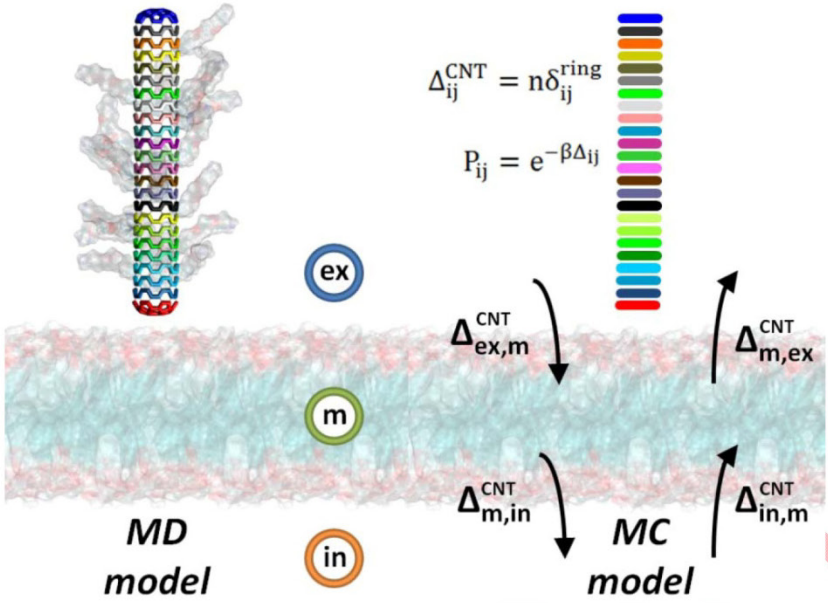

Figure 5 Monte Carlo (MC) statistical model issued directly from Molecular Dynamics (MD) simulation results.

We decided to found MC model on energy barriers extracted from the free energy profiles, obtained directly from previously generated MD trajectories of model **(7)** (f-CNT). Due to many consecutive runs with molecule in different protonation states and very long time of diffusion inside the membrane, we decided to use less consuming method than ABF, namely Umbrella Sampling method.[34] In accordance with profile shown in Figure 4a f-CNT going inside the membrane need to cross only 0.3 kcal/mol barrier, in comparison to those of 71.6 kcal/mol when living the membrane. We chose here a reference point (0 kcal/mol) in the membrane center to better visualize extracted energy barriers. In MC model shown in Figure 5 we consider three zones, which are extracellular side **(ex)**, membrane **(m)** and intracellular side **(in)**, respectively. Between each of the zones we attribute energy barriers $\Delta_{ij}^{CNT} = n\delta_{ij}^{ring}$ for the CNT diffusion, where *i* and *j* can be either **(ex)**, **(m)** or **(in)** (see arrows on Figure 5). Different f-CNT lengths are take into consideration as *n*-rings long f-CNT (*i.e.* *n* times 0.25 nm). The attributed ring barriers δ_{ij}^{ring} are those extracted directly from free energy profiles (Figure 4) and divided by number of 24 rings present in our 5 nm long f-CNT model (for example $\delta_{(ex),(m)}^{ring} = 0.3/24$ kcal/mol). We obtain thus a necessary energy for passing one f-CNT ring from one zone to another. During statistical equilibration (MC run) the probabilities of diffusion from one zone to another are calculated ring by ring. An average over a few millions samples predict a partition coefficient of f-CNT pricking passively and perpendicularly the lipid membrane. Results, with filled up at start the **(ex)** zone (*i.e.* f-CNT stayed initially outside the cell), are shown in Figure 6. Partition coefficient concerning the

DRAFT ONLY

f-CNT part staying outside the cell (see black curve on Figure 6), tends quickly to 100% for all f-CNT lengths being, which means that nanotube do not penetrate the cell.

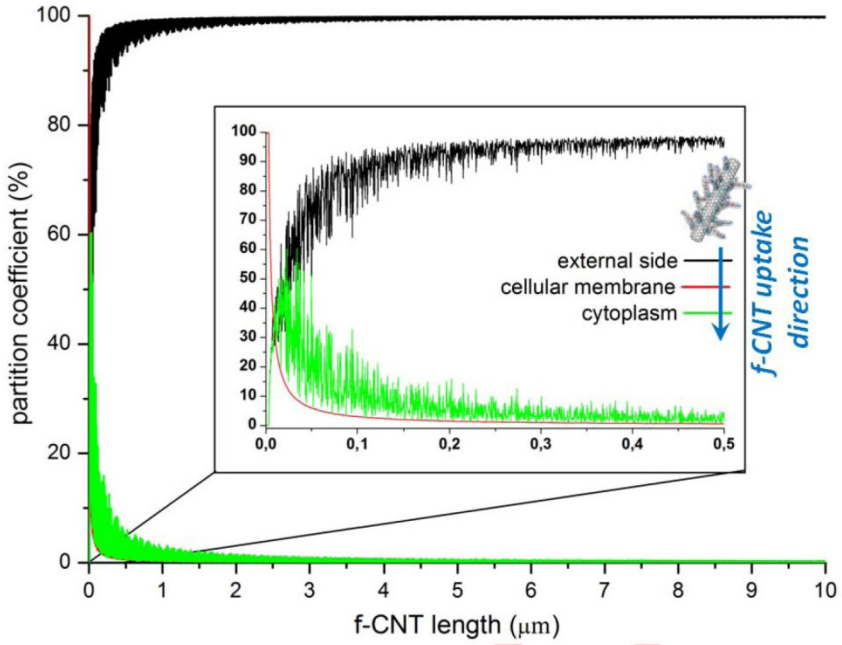

Figure 6 f-CNT partition coefficient between extracellular media and cytoplasm in function of f-CNT length. f-CNT was initially located outside the cell. Results are based on symmetrical free energy profile shown in Figure 4a.

Surprisingly, the first approach does not agree experimentally observed facts. Then, we realized that calculated profiles are usually considered as completely symmetrical for each lipid layer of the membrane, as we also done. In reality, it exist an important dissymmetry of the cell membrane due to the different reasons. We summarized possible factors inducing the cell membrane dissimetry in Table 1.

Table 1. Factors inducing cell membrane dissymetry

dissymmetry factor	references
composition in lipids	35-36
composition in proteins	37-38
cholesterol presence	39
lateral domains (rafts)	40
transmembrane potential	41-42
global viscosity	43-44
free/bound water molecules ratio*	45-47

*amount of the water molecules able to directly interact

In order to differentiate **(ex)** and **(in)** zones, and thus having an asymmetrical free energy profile, we decided to focus on only one dissymmetry factor, which let us to create the free energy profile dependent on only one variable. We chose the ratio between free and bound water molecules in each of the environments due to the important decrease of the

DRAFT

amount of unbound water inside the cell (*i.e.* able to free interact with CNT), which was reported to be 75-90% in comparison to the extracellular surrounding.[45-47] We numerically model this factor switching off randomly a half of interactions between water molecules and CNT during its uptake trajectory, which permits also to indirectly take into account the global viscosity differences in each side of the membrane. Found free energy profiles, using Umbrella Sampling on trajectories issued from MD simulations, for both environments are given in Figure 4b as a function of their distance from the central plane of the POPC bilayer. Now, basing on previous assumptions, we have different energetic situation. 5 nm long CNT passing from **(ex)** media (containing 100% unbound water molecules) to the membrane **(m),** needs to cross over still 0.3 kcal/mol barrier. Next, going through the membrane **(m)** to the **(in)** media (*i.e.* cytoplasm containing less unbound water molecules – here calculated as 50%), CNT cross over 62.1 kcal/mol barrier. In the opposite direction, from **(in)** by **(m)** to **(ex)**, the barriers to overcome are first 0.5 and then 71.6 kcal/mol.

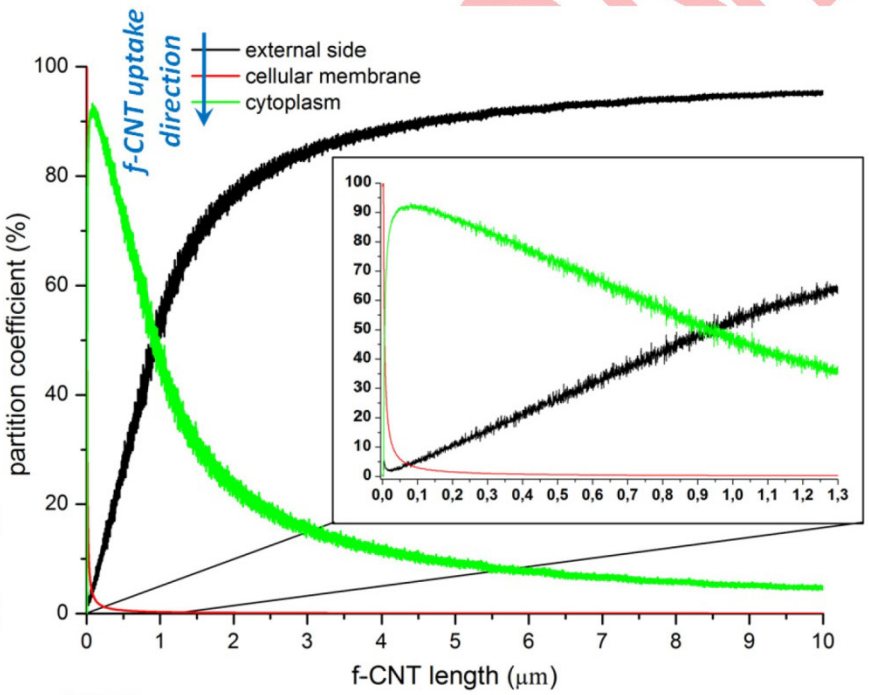

Figure 7 f-CNT partition coefficient between extracellular media and cytoplasm in function of f-CNT length. f-CNT was initially located outside the cell. Note that results are based on asymmetrical free energy profile shown in Figure 4b.

When this values are applied to our MC model we obtain the results (see Figure 7) being with excellent agreement with experimental observations of Raffa and coworkers, confirming that the sub-1 μm length CNT have strong ability to penetrate cells.[17] Results shown in Figure 7 present clearly that small f-CNT up to around 15 nm length will stuck inside the membrane, which completely agree with our observations issued from MD simulations for 5 nm long CNT. Moreover, f-CNT up 0,9 μm length will be statistically found

much more inside the cell (partition coefficient exceeding 50%) than outside. Finally, f-CNT much longer than 1 μm will almost totally stay outside the cell.

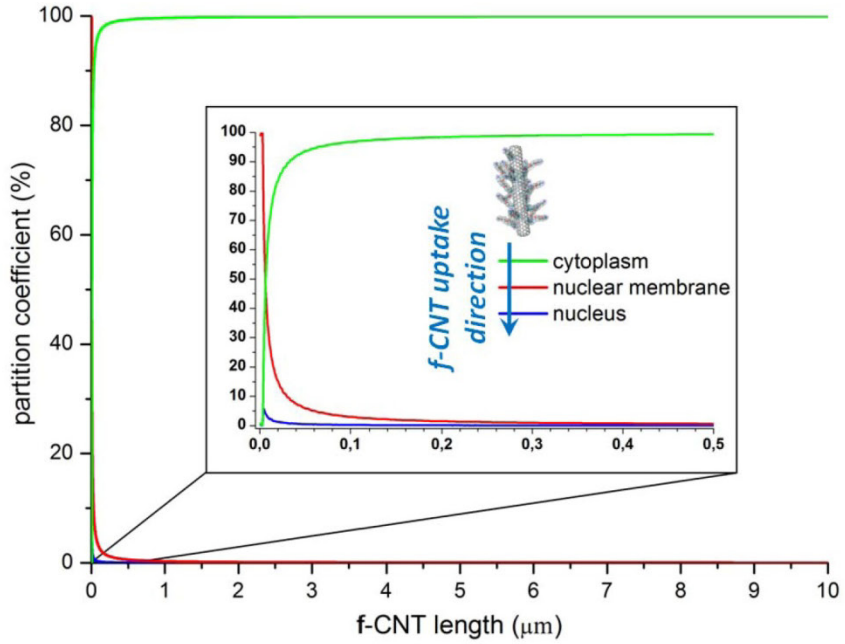

Figure 8 f-CNT partition coefficient between cytoplasm and nucleus in function of f-CNT length. f-CNT was initially located in the cytoplasm. Results are based on asymmetrical free energy profile shown in Figure 4b.

We tempted also to validate our MC model answering the crucial issue appearing for the CNT-based gene delivery. So far, experimental observations show that CNT cargo cannot penetrate the nuclear membrane, which has very different composition comparing to the cytoplasmic one. More surprisingly, the nuclear membrane contains the protein aggregates (nuclear pore complex - NPC) which can create individual pores with 10-20 nm in diameter leaving enough space to move CNT cargo across![48-49] As we have shown previously, the solvent plays a fundamental role in the uptake of f-CNT by the cell membrane separating the cytoplasm and the extracellular medium. Applying the same reasoning for the nuclear membrane, we find that the amount of water bound to macromolecules within the nucleus reveals also an important asymmetry, comparing to the intracellular media. Contrary to the cytoplasm, only 5% of water molecules are seems to be involved to direct interactions with nuclear macromolecules.[45-47] The nucleus environment is thus similar to the extracellular media, from this point of view. Basing still on the same free energy profile shown in Figure 4b but now locating initially f-CNT inside the cytoplasm we obtain the reverse situation, *i.e.* uptake form cytoplasm to the extracellular media or to the nucleus (assuming the similarity for the ratio of the free/bound water molecules amount). The MC results are completely different from the previous case as shown in Figure 8. Still very short f-CNT, less

DRAFT

than 15 nm length are embedded in the membrane. However, beyond this length, the proportion remaining in the cytoplasm is very important (90% against 10% in the nucleus). This result, being again in good agreement with experiment, ensured us in the validity of the proposed MC approach. It seems that the simple hydrophobic effect of f-CNT with respect to water can largely explain the experimental observations, so far remained unanswered.

In conclusion, unconstrained MD simulations on different models of open and closed, functionalized or not CNT, reveal a large propensity of passive uptake by phospholipid cell membrane. Functionalization does not seem to influence the general scheme of nanoneedle-like diffusion mechanism. The degree of functionalization define the pricking angle by which CNT penetrate the lipid bilayer. The extremely short length of studied CNT do not allow us to analyze the CNT length contribution in that process, which seems to be important.[17] The proposed here statistical approach using Monte Carlo simulations, directly based on the present MD results, tempt to solve the confronted numerical issue. The hydrophobic effect is likely the main driving force in the uptake mechanism of CNT, being in accordance with experimental observations, espetialy those in the field of CNT-based gene delivery. Novel research should thus pay particular importance to CNT functionalisations permitting the specific inclusion in the nuclei of cells.

METHODS

Molecular Dynamics Method: Unconstrained full atomistic MD simulations were performed using the equilibrated, fully hydrated palmitoyl-oleoyl-phosphatidylcholine (POPC) membrane model with a total simulation time reaching 3.7 μs (partial times are presented in Table 2). We consider the system consisting of 180 POPC units, 14,650 water molecules and one of the seven CNT models (shown in Figure 1) having 5 nm length and 1 nm diameter:

(1) neat open (6,6) CNT,

(2) protonated at edges open (6,6) CNT,

(3) functionalized open (6,6) CNT with 4 ammonium derivative groups,

(4) protonated at edges open (6,6) CNT functionalized with 20 ammonium derivative groups,

(5) neat closed (6,6) CNT,

(6) functionalized closed (6,6) CNT with 7 ammonium derivative groups,

(7) functionalized closed (6,6) CNT with 20 ammonium derivative groups,

DRAFT ONLY

The ammonium derivate groups (f-CNT-NH_3^+) are randomly dispersed on the whole surface of the nanotube and necessary simulation parameters are described above. The initial dimensions of the simulations cells of 70x74x124 $Å^3$ were chose to ensure the thickness of the water layer on both sides of the membrane equal to 86 Å (taking account periodic boundary conditions) in order to let enough space for used 53 Å long CNT. Moreover, systems **(2)**, **(4)** and **(7)** were simulated twice, either without any ions or contrarily, with Na^+ and Cl^- ions, redistributed in order to ensure a transmembranal potential as it was proposed by Delemotte *et al.*[50] All MD simulations have been carried out in the NPT ensemble using NAMD2.7b2,[51] a program targeted for massively parallel architectures. Short- and long-range forces were calculated every 1 and 2 time-steps respectively, with a time step of 2.0 fs. Long-range electrostatic forces were taken into account using the particle mesh Ewald (PME) approach.[52] The Langevin dynamics algorithm and the Langevin piston Nosé-Hoover method[53] were used to maintain 300 K temperature and 1 atm pressure in the system. At the temperature set for the study the bilayer is in the biologically relevant liquid crystal Lα phase.

The force field parameters for lipid were taken from CHARMM27[54] with the united atoms extension for acyl chains. The intra- and intermolecular potentials for water were taken from the TIP3P model [55]. For the carbon-carbon or carbon-water interactions in CNTs we follow the Bedrov description of Lennard-Jones potential [56-58] with σ_{CC}=3.895 Å, ε_{CC}=0.276 kJ mol^{-1} and σ_{CO}=3.580 Å, ε_{CO}=0.392 kJ mol^{-1} parameters. For the necessary potential parameters of the amino-derivative we followed the general procedure as described by Norrby and Brandt[59] based on construction of the Hessian matrix (the matrix of second derivatives of the energy with respect to geometry) for further use in the force field parameterization. The geometrical optimization of a single amino-derivative was performed using the Hartree-Fock approach with polarized continuum water model using integral equation formalism (IEFPCM) able to reproduce environmental effect of the solvent. The split-valence 6-31+G basis set was employed for all atoms and obtained Mulliken partial charges were applied to the molecular model.[60] Additionally, open nanotube's edges are fitted with the specific Mulliken partial charges distributions, accordingly to the results obtained from the quantum mechanics calculations with the same level of theory as for amino groups. This proceeding gives a supplementary (and naturally present due to carbon polarizability) charge-based functionalization inducing local electrostatic force coming from edge dipole moments of 5 D for neat open CNT **(1)** and **(3)** or 13.5 D for protonated open CNT **(2)** and **(4)**, respectively. All the *ab-initio* quantum calculations were performed using Gaussian 03 package software.[61]

DRAFT ONLY

Adaptive Biasing Force (ABF) Method: The free energy profiles were performed using NAMD software[51] with the ABF extensions integrated in the Collective Variables module[62] and under the same conditions as described for MD simulations. The minimal sampling was equal to 10'000 samples for each step along reaction coordinate under study, taken as a distance between center of mass (COM) of the neat closed CNT (model **(5))** and the COM of the lipid bilayer along the Z axis, with the step of 0.1 Å.

Umbrella Sampling Method: Corresponding free energy profiles were performed as described in ABF section above, but on previously generated MD trajectories of model **(7)**, and not as a separate run. The minimal sampling was equal to 10'000 samples for each step along reaction coordinate under study, taken as a distance between center of mass (COM) of the CNT carbon core and the COM of the lipid bilayer along the Z axis, with the step of 0.1 Å. Two water environments were considered. First, 100% water molecules freely interacted with all other molecules (*i.e.* f-CNT or lipids). Second, interactions between f-CNT and only 50% randomly chose water molecules were kept, while still 100% water molecules interacted with lipids. This intervention permitted to us to simulate an amount of bound water which was suppose to interact with cytoplasmic macromolecules, and thus being insensible to f-CNT presence.

Table 2. MD runs carried out

moleclular system	system description	total simulation time [ns]
(1)	neat open CNT	200
(2)	H-ended open CNT	443+20$_{TMP}$*
(3)	weakly functionalized open CNT	142
(4)	H-ended highly functionalized open CNT	466+108$_{TMP}$*
(5)	neat closed CNT	509
(6)	weakly functionalized closed CNT	423
(7)	highly functionalized closed CNT	779+600$_{TMP}$*

*supplementary run carried out with TransMembranal Potential (TMP)

DRAFT ONLY

Acknowledgement. This work was granted access to the HPC resources of the Mésocentre a regional computational center at the University of Franche-Comté .

BIBLIOGRAPHY

1. Ajayan, P. M., Nanotubes from carbon. *Chem. Rev.* **1999,** *99* (7), 1787-1799.
2. Da Ros, T.; Prato, M., Medicinal chemistry with fullerenes and fullerene derivatives. *Chem. Commun.* **1999,** (8), 663-669.
3. Baughman, R. H.; Zakhidov, A. A.; de Heer, W. A., Carbon nanotubes - the route toward applications. *Science* **2002,** *297* (5582), 787-792.
4. Pantarotto, D.; Singh, R.; McCarthy, D.; Erhardt, M.; Briand, J. P.; Prato, M.; Kostarelos, K.; Bianco, A., Functionalized carbon nanotubes for plasmid DNA gene delivery. *Angew. Chem. Int. Edit.* **2004,** *43* (39), 5242-5246.
5. Kam, N. W. S.; O'Connell, M.; Wisdom, J. A.; Dai, H. J., Carbon nanotubes as multifunctional biological transporters and near-infrared agents for selective cancer cell destruction. *Proc. Natl. Acad. Sci. USA* **2005,** *102* (33), 11600-11605.
6. Singh, R.; Pantarotto, D.; McCarthy, D.; Chaloin, O.; Hoebeke, J.; Partidos, C. D.; Briand, J. P.; Prato, M.; Bianco, A.; Kostarelos, K., Binding and condensation of plasmid DNA onto functionalized carbon nanotubes: Toward the construction of nanotube-based gene delivery vectors. *J. Am. Chem. Soc.* **2005,** *127* (12), 4388-4396.
7. Lacerda, L.; Raffa, S.; Prato, M.; Bianco, A.; Kostarelos, K., Cell-penetrating CNTs for delivery of therapeutics. *Nano Today* **2007,** *2* (6), 38-43.
8. Foldvari, M.; Bagonluri, M., Carbon nanotubes as functional excipients for nanomedicines: II. Drug delivery and biocompatibility issues. *Nanomed.-Nanotechnol.* **2008,** *4* (3), 183-200.
9. Partha, R.; Conyers, J. L., Biomedical applications of functionalized fullerene-based nanomaterials. *Int. J. Nanomed.* **2009,** *4*, 261-275.
10. Qiao, R.; Roberts, A. P.; Mount, A. S.; Klaine, S. J.; Ke, P. C., Translocation of C-60 and its derivatives across a lipid bilayer. *Nano Lett.* **2007,** *7* (3), 614-619.
11. Wong-Ekkabut, J.; Baoukina, S.; Triampo, W.; Tang, I. M.; Tieleman, D. P.; Monticelli, L., Computer simulation study of fullerene translocation through lipid membranes. *Nature Nanotech.* **2008,** *3* (6), 363-368.
12. Bedrov, D.; Smith, G. D.; Davande, H.; Li, L. W., Passive transport of C-60 fullerenes through a lipid membrane: A molecular dynamics simulation study. *J. Phys. Chem. B* **2008,** *112* (7), 2078-2084.
13. Sayes, C. M.; Fortner, J. D.; Guo, W.; Lyon, D.; Boyd, A. M.; Ausman, K. D.; Tao, Y. J.; Sitharaman, B.; Wilson, L. J.; Hughes, J. B.; West, J. L.; Colvin, V. L., The differential cytotoxicity of water-soluble fullerenes. *Nano Lett.* **2004,** *4* (10), 1881-1887.
14. Andreev, I.; Petrukhina, A.; Garmanova, A.; Babakhin, A.; Andreev, S.; Romanova, V.; Troshin, P.; Troshina, O.; DuBuske, L., Penetration of fullerene C60 derivatives through biological membranes. *Fuller. Nanotub. Car. N.* **2008,** *16* (2), 89-102.
15. Kraszewski, S.; Tarek, M.; Treptow, W.; Ramseyer, C., Affinity of C-60 Neat Fullerenes with Membrane Proteins: A Computational Study on Potassium Channels. *Acs Nano* **2010,** *4* (7), 4158-4164.
16. Bianco, A.; Prato, M., Can carbon nanotubes be considered useful tools for biological applications? *Adv. Mater.* **2003,** *15* (20), 1765-1768.
17. Raffa, V.; Ciofani, G.; Nitodas, S.; Karachalios, T.; D'Alessandro, D.; Masini, M.; Cuschieri, A., Can the properties of carbon nanotubes influence their internalization by living cells? *Carbon* **2008,** *46* (12), 1600-1610.
18. Kostarelos, K.; Lacerda, L.; Pastorin, G.; Wu, W.; Wieckowski, S.; Luangsivilay, J.; Godefroy, S.; Pantarotto, D.; Briand, J. P.; Muller, S.; Prato, M.; Bianco, A., Cellular uptake of functionalized carbon nanotubes is independent of functional group and cell type. *Nature Nanotech.* **2007,** *2* (2), 108-113.
19. Pantarotto, D.; Briand, J. P.; Prato, M.; Bianco, A., Translocation of bioactive peptides across cell membranes by carbon nanotubes. *Chem. Commun.* **2004,** (1), 16-17.
20. Kam, N. W. S.; Jessop, T. C.; Wender, P. A.; Dai, H. J., Nanotube molecular transporters: Internalization of carbon nanotube-protein conjugates into mammalian cells. *J. Am. Chem. Soc.* **2004,** *126* (22), 6850-6851.
21. Kam, N. W. S.; Liu, Z. A.; Dai, H. J., Carbon nanotubes as intracellular transporters for proteins and DNA: An investigation of the uptake mechanism and pathway. *Angew. Chem. Int. Edit.* **2006,** *45* (4), 577-581.
22. Cherukuri, P.; Bachilo, S. M.; Litovsky, S. H.; Weisman, R. B., Near-infrared fluorescence microscopy of single-walled carbon nanotubes in phagocytic cells. *J. Am. Chem. Soc.* **2004,** *126* (48), 15638-15639.
23. Cheng, C.; Muller, K. H.; Koziol, K. K. K.; Skepper, J. N.; Midgley, P. A.; Welland, M. E.; Porter, A. E., Toxicity and imaging of multi-walled carbon nanotubes in human macrophage cells. *Biomaterials* **2009,** *30* (25), 4152-4160.
24. Wallace, E. J.; Sansom, M. S. P., Blocking of carbon nanotube based nanoinjectors by lipids: A simulation study. *Nano Lett.* **2008,** *8* (9), 2751-2756.
25. Shi, X. H.; Kong, Y.; Gao, H. J., Coarse grained molecular dynamics and theoretical studies of carbon nanotubes entering cell membrane. *Acta Mech. Sinica* **2008,** *24* (2), 161-169.
26. Monticelli, L.; Salonen, E.; Ke, P. C.; Vattulainen, I., Effects of carbon nanoparticles on lipid membranes: a molecular simulation perspective. *Soft Matter* **2009,** *5* (22), 4433-4445.
27. Yang, K.; Ma, Y. Q., Computer simulation of the translocation of nanoparticles with different shapes across a lipid bilayer. *Nature Nanotech.* **2010,** *5* (8), 579-583.
28. Georgakilas, V.; Tagmatarchis, N.; Pantarotto, D.; Bianco, A.; Briand, J. P.; Prato, M., Amino acid functionalisation of water soluble carbon nanotubes. *Chem. Commun.* **2002,** (24), 3050-3051.
29. Rodriguez-Gomez, D.; Darve, E.; Pohorille, A., Assessing the efficiency of free energy calculation methods. *J. Chem. Phys.* **2004,** *120* (8), 3563-3578.
30. Darve, E.; Rodriguez-Gomez, D.; Pohorille, A., Adaptive biasing force method for scalar and vector free energy calculations. *J. Chem. Phys.* **2008,** *128* (14).
31. MacCallum, J. L.; Bennett, W. F. D.; Tieleman, D. P., Partitioning of amino acid side chains into lipid bilayers: Results from computer simulations and comparison to experiment. *Journal of General Physiology* **2007,** *129* (5), 371-377.
32. Yoo, J.; Cui, Q., Does arginine remain protonated in the lipid membrane? Insights from microscopic pK(a) calculations. *Biophysical Journal* **2008,** *94* (8), L61-L63.
33. Luecke, H.; Richter, H. T.; Lanyi, J. K., Proton transfer pathways in bacteriorhodopsin at 2.3 Angstrom resolution. *Science* **1998,** *280* (5371), 1934-1937.

PREVIEW ONLY

34. Torrie, G. M.; Valleau, J. P., Nonphysical sampling distributions in Monte Carlo free-energy estimation: Umbrella sampling *J. Comput. Phys.* **1977,** *23* (2), 187-199.
35. Dressler, V.; Haest, C. W. M.; Plasa, G.; Deuticke, B.; Erusalimsky, J. D., Stabilizing factors of phospholipid asymmetry in the erythrocyte membrane *BBA-Biomembranes* **1984,** *775* (2), 189-196.
36. Zachowski, A., Phospholipids in animal eukaryotic membranes - transverse asymmetry and movement. *Biochem. J.* **1993,** *294*, 1-14.
37. Rodriguezboulan, E.; Powell, S. K., Polarity of epithelial and neuronal cells. *Annu. Rev. Cell Biol.* **1992,** *8*, 395-427.
38. Nelson, W. J., Adaptation of core mechanisms to generate cell polarity. *Nature* **2003,** *422* (6933), 766-774.
39. Schroeder, F.; Frolov, A. A.; Murphy, E. J.; Atshaves, B. P.; Jefferson, J. R.; Pu, L. X.; Wood, W. G.; Foxworth, W. B.; Kier, A. B., Recent advances in membrane cholesterol domain dynamics and intracellular cholesterol trafficking. *P. Soc. Exp. Biol. Med.* **1996,** *213* (2), 150-177.
40. Devaux, P. F.; Morris, R., Transmembrane asymmetry and lateral domains in biological membranes. *Traffic* **2004,** *5* (4), 241-246.
41. Hille, B., *Ionic channels of excitable membranes*. 2nd ed.; Sinauer: Sunderland, MA, 1992.
42. Reiss, M. J.; Roberts, M. B. V.; Monger, G., *Advanced Biology*. Nelson Thornes Ltd: 2000; p 816.
43. Keith, A. D.; Snipes, W., Viscosity of cellular protoplasm. *Science* **1974,** *183* (4125), 666-668.
44. Lang, I.; Scholz, M.; Peters, R., Molecular mobility and nulceocytoplasmic flux in hepatoma-cells. *J. Cell Biol.* **1986,** *102* (4), 1183-1190.
45. Century, T. J.; Fenichel, I. R.; Horowitz, S. B., The concentrations of water, sodium and potassium in the nucleus and cytoplasm of amphibian oocytes. *J. Cell Sci.* **1970,** *7* (1), 5-&.
46. Pauser, S.; Zschunke, A.; Khuen, A.; Keller, K., Estimation of water-content and water mobility in the nucleus and cytoplasm of xenopus-laevis oocytes by NMR microscopy. *Magn. Reson. Imaging* **1995,** *13* (2), 269-276.
47. Ovadi, J.; Saks, V., On the origin of intracellular compartmentation and organized metabolic systems. *Mol. Cell. Biochem.* **2004,** *256* (1-2), 5-12.
48. Lamprecht, C.; Liashkovich, I.; Neves, V.; Danzberger, J.; Heister, E.; Rangl, M.; Coley, H. M.; McFadden, J.; Flahaut, E.; Gruber, H. J.; Hinterdorfer, P.; Kienberger, F.; Ebner, A., AFM imaging of functionalized carbon nanotubes on biological membranes. *Nanotechnology* **2009,** *20* (43).
49. Kang, B.; Yu, D. C.; Dai, Y. D.; Chang, S. Q.; Chen, D.; Ding, Y. T., Cancer-Cell Targeting and Photoacoustic Therapy Using Carbon Nanotubes as "Bomb" Agents. *Small* **2009,** *5* (11), 1292-1301.
50. Delemotte, L.; Dehez, F.; Treptow, W.; Tarek, M., Modeling membranes under a transmembrane potential. *J. Chem. Phys. B* **2008,** *112*, 5547-5550.
51. Phillips, J. C.; Braun, R.; Wang, W.; Gumbart, J.; Tajkhorshid, E.; Villa, E.; Chipot, C.; Skeel, R. D.; Kale, L.; Schulten, K., Scalable molecular dynamics with NAMD. *J. Comput. Chem.* **2005,** *26* (16), 1781-1802.
52. Darden, T.; York, D.; Pedersen, L., Particle mesh Ewald: An N.log(N) method for Ewald sums in large systems. *J. Chem. Phys.* **1993,** *98* (12), 10089-10092.
53. Feller, S. E.; Zhang, Y. H.; Pastor, R. W.; Brooks, B. R., Constant-Pressure Molecular-Dynamics simulation - the Langevin piston method. *J. Chem. Phys.* **1995,** *103* (11), 4613-4621.
54. Foloppe, N.; MacKerell, A. D., All-atom empirical force field for nucleic acids: I. Parameter optimization based on small molecule and condensed phase macromolecular target data. *J. Comput. Chem.* **2000,** *21* (2), 86-104.
55. Jorgensen, W. L.; Chandrasekhar, J.; Madura, J. D.; Impey, R. W.; Klein, M. L., Comparison of simple potential functions for simulating liquid water. *J. Chem. Phys.* **1983,** *79*, 926-935.
56. Li, L. W.; Davande, H.; Bedrov, D.; Smith, G. D., A molecular dynamics simulation study of C-60 fullerenes inside a dimyristoylphosphatidylcholine lipid bilayer. *J. Phys. Chem. B* **2007,** *111* (16), 4067-4072.
57. Li, L. W.; Bedrov, D.; Smith, G. D., A molecular-dynamics simulation study of solvent-induced repulsion between C-60 fullerenes in water. *J. Chem. Phys.* **2005,** *123* (20), 204504
58. Li, L. W.; Bedrov, D.; Smith, G. D., Water-induced interactions between carbon nanoparticles. *J. Phys. Chem. B* **2006,** *110* (21), 10509-10513.
59. Norrby, P. O.; Brandt, P., Deriving force field parameters for coordination complexes. *Coordin. Chem. Rev.* **2001,** *212*, 79-109.
60. Mulliken, R. S., Electronic population analysis on CAO-MO molecular wave functions .1. *J. Chem. Phys.* **1955,** *23* (10), 1833-1840.
61. Frisch, M. J.; Trucks, G. W.; Schlegel, H. B.; Scuseria, G. E.; Robb, M. A.; Cheeseman, J. R.; Montgomery, J. A.; Vreven, J., T. ; Kudin, K. N.; Burant, J. C.; Millam, J. M.; Iyengar, S. S.; Tomasi, J.; Barone, V.; Mennucci, B.; Cossi, M.; Scalmani, G.; Rega, N.; Petersson, G. A.; Nakatsuji, H.; Hada, M.; Ehara, M.; Toyota, K.; Fukuda, R.; Hasegawa, J.; Ishida, M.; Nakajima, T.; Honda, Y.; Kitao, O.; Nakai, H.; Klene, V.; Li, X.; Knox, J. E.; Hratchian, H. P.; Cross, J. B.; Adamo, C.; Jaramillo, J.; Gomperts, R.; Stratmann, R. E.; Yazyev, O.; Austin, A. J.; Cammi, R.; Pomelli, C.; Ochterski, J. W.; Ayala, P. Y.; Morokuma, K.; Voth, G. A.; Salvador, P.; Dannenberg, J. J.; Zakrzewski, V. G.; Dapprich, S.; Daniels, A. D.; Strain, M. C.; Farkas, O.; Malick, D. K.; Rabuck, A. D.; Raghavachari, K.; Foresman, J. B.; Ortiz, J. V.; Cui, Q.; Baboul, A. G.; Clifford, S.; Cioslowski, J.; Stefanov, B. B.; Liu, G.; Liashenko, A.; Piskorz, P.; Komaromi, I.; Martin, R. L.; Fox, D. J.; Keith, T.; Al-Laham, M. A.; Peng, C. Y.; Nanayakkara, A.; Challacombe, M.; Gill, P. M. W.; Johnson, B.; Chen, W.; Wong, M. W.; Gonzalez, C.; Pople, J. A. *Gaussian 03, Rev. C.02*, Gaussian, Inc.: Wallingford CT, 2004.
62. Henin, J.; Fiorin, G.; Chipot, C.; Klein, M. L., Exploring Multidimensional Free Energy Landscapes Using Time-Dependent Biases on Collective Variables. *J. Chem. Theory Comput.* **2010,** *6* (1), 35-47.

DRAFT ONLY

VI Conclusions et perspectives

Mon travail de thèse m'a conduit à considérer deux sujets étroitement liés. Le premier est relatif à la compréhension de la sélectivité des canaux ioniques à potassium. Dans le second, nous nous sommes intéressés au transport de nanostructures carbonées par les membranes cellulaires et notamment à leurs interactions avec ces canaux ioniques.

La sélectivité des canaux à potassium trouve son origine dans le filtre de sélectivité qui est une zone nanométrique comportant une séquence d'acides aminés bien spécifique. Hormis les hypothèses d'hydratation à respecter, de dynamique importante des groupements carbonyles et d'une taille de filtre adaptée spécifiquement aux ions K^+, nous avons mis en évidence que la polarisation des ions ainsi que des transferts de charge non-négligeables pouvaient aussi expliquer la sélectivité d'un canal ionique comme KcsA. En particulier, le calcul *ab initio* des charges partielles de MERZ-KOLLMAN montre clairement que la charge des ions potassium peut diminuer jusqu'à atteindre +0.8e alors que celle des ions sodium reste proche de l'unité. Cette charge dépend de la position des ions dans le filtre de sélectivité. Nous avons ainsi proposé un profil complet des charges pour Na^+ et K^+. Les calculs de dynamique moléculaire que nous avons effectués nous ont aussi permis de préciser et quantifier le mécanisme « knock-on » déclenchant la diffusion des ions dans le canal KcsA. En perspective à ce travail, il resterait à implémenter ce profil des charges dans la DM pour recalculer proprement la conduction des ions. Des modèles macroscopiques basés sur des équations de diffusion seraient bien adaptés. Ces études seront conduites par l'équipe ukrainienne de Kiev (S. YESSYLEVSKYY et V. KHARKYANEN) avec qui nous collaborons depuis longtemps. Une autre perspective à ce travail concerne un autre canal. Nous avons mis en évidence que pour KcsA le transfert de charge est important sur les ions K^+. Nous pensons que la sélectivité d'autres canaux comme la gramicidine A vis à vis du potassium et du sodium pourrait aussi être expliquée par ce point de vue. Ces études sont actuellement en cours. Elles seront faites majoritairement par une autre personne de l'équipe (M. TONGHTEP) dans le cadre d'une collaboration franco-thaïlandaise que nous développons depuis peu.

Dans le second volet de cette thèse, j'ai tenté de répondre à deux questions fondamentales. La première concernait l'élucidation des mécanismes de pénétration de nanostructures carbonées dans la membrane cellulaire. La seconde était relative à la toxicité des C60 et CNT par rapport aux protéines membranaires. Les simulations numériques m'ont permis d'apporter des réponses partielles à ces questions. L'étude par dynamique moléculaire des propriétés structurales,

dynamiques et énergétiques des C60 a montré une forte interaction de ceux-ci avec les canaux potassiques. Les sites et les énergies trouvées sont très voisins de ceux que l'on trouve pour des bloqueurs (TEA) ou pour des toxines d'animaux redoutables (scorpion, mygale). On peut donc craindre une forte toxicité des C60 vis-à-vis de ces protéines fonctionnelles. Les nanotubes de carbone sont moins toxiques vis-à-vis des protéines. En revanche, nous avons également montré que les CNT pouvaient diffuser de manière passive au travers de membranes modèles. Les résultats de la DM ont montré que les fonctionnalisations utilisées pour solubiliser les nanotubes dans l'eau n'empêchaient pas les tubes de rentrer dans la membrane, une fois le phénomène de déprotonation des espèces charges pris en compte. Le caractère hydrophobe des CNT semble être la clé du phénomène de transport. Il permet aussi d'expliquer pourquoi les CNT peuvent traverser les membranes cytoplasmiques allant vers le cytoplasme mais pas les membranes nucléaires. Il s'agit d'un travail d'une importance capitale car aucune expérience ne peut à ce jour donner une description microscopique des mécanismes impliqués dans la translocation de ces nanostructures à travers la membrane des cellules. Ces résultats ouvrent une voie nouvelle pour la délivrance de médicaments. On peut espérer un jour, fabriquer de nouveaux types de médicaments, dits « intelligents », utilisant les nanotubes de carbone comme vecteurs capables de reconnaître des cellules cancéreuses ou endommagées, de les pénétrer facilement, et de les réparer, ou au contraire de les détruire sélectivement.

En parallèle de l'étude des interactions entre les fullerènes et les canaux ioniques, nous avons aussi effectué des analyses préliminaires avec des CNT de différents diamètres. Nous avons estimé, par docking, les sites de liaisons des CNT les plus probables avec le canal fermé (KcsA) et ouvert (MthK) en considérant des nanotubes ouverts d'indices respectifs (6,6), (10,10) et (22,22). Tous les types de nanotubes étudiés semblent être capables de couvrir le pore de l'extérieur ainsi que de pénétrer le canal du côté intracellulaire une fois le canal ouvert. Ces résultats ne concluent en rien sur la perturbation du fonctionnement de ces protéines membranaires, et il faudra encore effectuer des simulations de DM identiques à celles effectuées pour les fullerènes afin de conclure et d'estimer les énergies libres des liaisons pour évaluer leur toxicité potentielle.

Jusqu'à présent, je ne me suis pas trop étendu sur les groupements fonctionnalisant les C60 ou les CNT. Il est clair que ceux-ci seront identifiés par rapport aux applications médicales envisagées. Il faudra surement porter une attention toute particulière aux peptides cationiques [163]. En effet, les médicaments basés sur les peptides cationiques pourraient être très profitables dans un avenir proche, compte tenu de la diminution du pouvoir des antibiotiques actuels et de la résistance de certains micro-organismes aux antibiotiques traditionnels. Nous avons remarqué que certains agents infectieux ou pathogènes n'ont pas acquis une résistance aux peptides cationiques alors qu'ils y sont exposés depuis longtemps. Ils n'ont pas pu acquérir une telle résistance jusqu'ici et dans ce cas leur

évolution n'est pas pertinente. Il y a plus de 600 peptides cationiques connus que l'on peut trouver dans différents organismes (du microbe à l'homme). Ils sont caractérisés par une gamme étendue d'activité anti-infectieuse comprenant des bactéries, parasites eukaryotiques, virus, et ils ont, en outre, une capacité à tuer les cellules néo-plastiques (activité anticancéreuse). Les peptides cationiques possèdent de telles propriétés parce qu'ils agissent, entre autres, avec les membranes bactériennes. Cependant, ils ne peuvent pas être facilement dirigés et véhiculés pour s'approcher des zones à traiter avec une grande exactitude. C'est pourquoi les CNT fonctionnalisés, envisagés comme vecteurs de médicaments pour les peptides cationiques, devraient être étudiés avec une attention particulière. À notre connaissance, peu d'expériences et aucun calcul n'ont été faits jusqu'ici. De telles études devraient avoir un impact important en particulier dans les communautés travaillant sur le traitement des cancers. Une autre voie serait d'utiliser les particules radioactives (émetteurs β) utilisées en radiologie nucléaire mais cette fois en les véhiculant à proximité des cellules malades. Ce travail est une des thématiques affichée dans la future équipe d'accueil que les membres de l'équipe ont décidé de créer.

Enfin, de plus en plus de groupes s'intéressent à la transfection de gènes, c'est-à-dire à l'introduction d'ADN exogène dans des cellules eucaryotes, non-médié par un virus, par opposition à la transduction. Elle est typiquement réalisée par l'ouverture transitoire de « trous » dans les cellules pour permettre l'entrée de molécules extracellulaires, comme un plasmide d'ADN par exemple. Une des dernières techniques directe de transfection est le « gene gun », dans lequel l'ADN est couplé à une nanoparticule d'or, qui est ensuite « tiré » directement dans le noyau des cellules-cibles. Etant donné le fort pouvoir des CNT à pénétrer la membrane cellulaire, il semblerait intéressant de complexer les structures carbonées fonctionnalisés avec de l'ADN pour réaliser la transfection. Nous avons déjà effectués quelques essais de simulation des CNT couverts d'un brin d'ADN pour vérifier son aptitude de traverser les membranes et les résultats préliminaires sont très encourageants. Un travail systématique devra être fait dans le futur en combinaison avec des études expérimentales.

VII Bibliographie

1. Whitesides, G.M., *The 'right' size in nanobiotechnology.* Nat. Biotechnol., 2003. **21**(10): p. 1161-1165.
2. LaVan, D.A., T. McGuire, and R. Langer, *Small-scale systems for in vivo drug delivery.* Nat. Biotechnol., 2003. **21**(10): p. 1184-1191.
3. Ferrari, M., *Cancer nanotechnology: Opportunities and challenges.* Nat. Rev. Cancer, 2005. **5**(3): p. 161-171.
4. Farokhzad, O.C., J.M. Karp, and R. Langer, *Nanoparticle–aptamer bioconjugates for cancer targeting.* Exp. Opin. Drug Delivery, 2006. **3**(3): p. 311-324.
5. Zhang, L., et al., *Nanoparticles in medicine: Therapeutic applications and developments.* Clin. Pharmacol. Ther., 2008. **83**(5): p. 761-769.
6. Langer, R., *Drug delivery and targeting.* Nature, 1998. **392**(6679): p. 5-10.
7. Langer, R., *New methods of drug delivery.* Science, 1990. **249**(4976): p. 1527-1533.
8. Glass, G., *Pharmaceutical patent challenges - Time for reassessment?* Nat. Rev. Drug Discov., 2004. **3**(12): p. 1057-1062.
9. Liong, M., et al., *Multifunctional inorganic nanoparticles for imaging, targeting, and drug delivery.* Acs Nano, 2008. **2**(5): p. 889-896.
10. Frisch, M.J., et al., *Gaussian 03*. 2004, Gaussian, Inc.: Wallingford CT.
11. Stewart, J.J.P. *MOPAC2007*. Stewart Computational Chemistry (2007); Available from: http//OpenMOPAC.net.
12. Bucher, D., et al. *Polarization effects and charge transfer in the KcsA potassium channel*. in *230th National Meeting of the American-Chemical-Society*. 2005. Washington, DC.
13. Bucher, D., et al., *Polarization effects and charge transfer in the KcsA potassium channel.* Biophys. Chem., 2006. **124**(3): p. 292-301.
14. Mulliken, R.S., *Electronic population analysis on CAO-MO molecular wave functions .1.* J. Chem. Phys., 1955. **23**(10): p. 1833-1840.
15. Singh, U.C. and P.A. Kollman, *An approach to computing electrostatic charges for molecules.* J. Comput. Chem., 1984. **5**(2): p. 129-145.
16. Besler, B.H., K.M. Merz, and P.A. Kollman, *Atomic charges derived from semiempirical methods.* J. Comput. Chem., 1990. **11**(4): p. 431-439.
17. Chirlian, L.E. and M.M. Francl, *Atomic charges derived from electrostatic potentials - a detailed study.* J. Comput. Chem., 1987. **8**(6): p. 894-905.
18. Breneman, C.M. and K.B. Wiberg, *Determining atom-centered monopoles from molecular electrostatic potentials - the need for high sampling density in formamide conformational-analysis.* J. Comput. Chem., 1990. **11**(3): p. 361-373.
19. Bayly, C.I., et al., *A well-behaved electrostatic potential based method using charge restraints for deriving atomic charges - the RESP model.* J. Phys. Chem., 1993. **97**(40): p. 10269-10280.
20. Reynolds, C.A., J.W. Essex, and W.G. Richards, *Atomic charges for variable molecular-conformations.* J. Am. Chem. Soc., 1992. **114**(23): p. 9075-9079.
21. van Gunsteren, W.F., *The role of computer-simulations techniques in protein engineering.* Prot. Eng., 1988. **2**(1): p. 5-13.

22. van Gunsteren, W.F. and H.J.C. Berendsen, *Computer simulation of molecular dynamics: methodology, applications, and perpectives in chemistry.* Angew. Chem. Int. Ed. Engl., 1990. **29**: p. 992-1023.
23. van Gunsteren, W.F., et al., *Molecular mechanics in biology: from structure to function, taking account of solvation.* Annu. Rev. Biophys. Biomol. Struct., 1994. **23**: p. 847-863.
24. Case, D.A., et al., *AMBER 8*. 2004, San Francisco: University of California.
25. Phillips, J.C., et al., *Scalable molecular dynamics with NAMD.* J. Comput. Chem., 2005. **26**(16): p. 1781-1802.
26. Weiner, S.J., et al., *A new force-field for molecular mechanical simulation of nucleic-acids and proteins.* J. Am. Chem. Soc., 1984. **106**(3): p. 765-784.
27. Berendsen, H.J.C., et al., *Molecular Dynamics and Protein Structure*. 1985, Western Springs: Polycrystal Book Service
28. Brooks, C.L., B.M. Pettitt, and M. Karplus, *Structural and energetic effects of truncating long ranged interactions in ionic and polar fluids.* J. Chem. Phys., 1985. **83**(11): p. 5897-5908.
29. van Gunsteren, W.F., P.K. Weiner, and A.J. Wikinson, eds. *Computer simulation of biomolecular systems*. 1993, ESCOM Leiden: Dordrecht.
30. Schreiber, H. and O. Steinhauser, *Molecular-dynamics studies of solvated polypeptides - Why the cutoff scheme does not work.* Chem. Phys., 1992. **168**(1): p. 75-89.
31. Aqvist, J. and T. Hansson, *On the validity of electrostatic linear response in polar solvents.* J. Phys. Chem., 1996. **100**(22): p. 9512-9521.
32. Aqvist, J. and T. Hansson, *Analysis of electrostatic potential truncation schemes in simulations of polar solvents.* J. Phys. Chem. B, 1998. **102**(19): p. 3837-3840.
33. Ashbaugh, H.S., S. Sakane, and R.H. Wood, *Reply to comment on "Electrostatic potentials and free energies of solvation of polar and charged molecules".* J. Phys. Chem. B, 1998. **102**(19): p. 3844-3845.
34. Hummer, G., et al., *Reply to comment on "Electrostatic potentials and free energies of solvation of polar and charged molecules".* J. Phys. Chem. B, 1998. **102**(19): p. 3841-3843.
35. Hummer, G., et al., *Electrostatic potentials and free energies of solvation of polar and charged molecules.* J. Phys. Chem. B, 1997. **101**(16): p. 3017-3020.
36. Ewald, P.P., *The calculation of optical and electrostatic grid potential.* Ann. Phys.-Leipzig, 1921. **64**(3): p. 253-287.
37. Allen, M.P. and D.J. Tildesley, *Computer Simulation of Liquids*. 1989, Oxford: Clarendon Press.
38. Darden, T., D. York, and L. Pedersen, *Particle mesh Ewald: An N.log(N) method for Ewald sums in large systems.* J. Chem. Phys., 1993. **98**(12): p. 10089-10092.
39. Berendsen, H.J.C., et al., *Molecular dynamics with coupling to an external bath.* J. Chem. Phys., 1984. **81**: p. 3684-3690.
40. Nielsen, S.O., et al., *Coarse grain models and the computer simulation of soft materials.* J. Phys.: Condens. Matter, 2004. **16**: p. R481-R512.
41. Lindahl, E. and M.S.P. Sansom, *Membrane proteins: molecular dynamics simulations.* Curr. Opin. Struct. Biol., 2008. **18**(4): p. 425-431.
42. Arkhipov, A., Y. Yin, and K. Schulten, *Four-scale description of membrane sculpting by BAR domains.* Biophys. J., 2008. **95**(6): p. 2806-2821.
43. Shelley, J.C., et al., *Simulations of phospholipids using a coarse grain model.* J. Phys. Chem. B, 2001. **105**(40): p. 9785-9792.
44. Marrink, S.J., A.H. Vries, and A.E. Mark, *Coarse grained model for semiquantitative lipid simulations.* J. Phys. Chem. B, 2004. **108**: p. 750-760.
45. Marrink, S.J., et al., *The MARTINI force field: Coarse grained model for biomolecular simulations.* J. Phys. Chem. B, 2007. **111**(27): p. 7812-7824.
46. Tozzini, V., *Coarse-grained models for proteins.* Curr. Opin. Struct. Biol., 2005. **15**(2): p. 144-150.
47. Lopez, C.F., et al., *Probing membrane insertion activity of antimicrobial polymers via coarse-grain molecular dynamics.* J. Chem. Theory Comput., 2006. **2**(3): p. 649-655.

48. Yefimov, S., et al., *Mechanosensitive membrane channels in action.* Biophys. J., 2008. **94**(8): p. 2994-3002.
49. Treptow, W., S.J. Marrink, and M. Tarek, *Gating motions in voltage-gated potassium channels revealed by coarse-grained molecular dynamics simulations.* J. Phys. Chem. B, 2008. **112**(11): p. 3277-3282.
50. Wallace, E.J. and M.S.P. Sansom, *Blocking of carbon nanotube based nanoinjectors by lipids: A simulation study.* Nano Lett., 2008. **8**(9): p. 2751-2756.
51. Wong-Ekkabut, J., et al., *Computer simulation study of fullerene translocation through lipid membranes.* Nat. Nanotech., 2008. **3**(6): p. 363-368.
52. Metropolis, N. and S. Ulam, *The Monte Carlo method.* J. Am. Stat. Assoc., 1949. **44**(247): p. 335-341.
53. Zwanzig, R.W., *Erratum: High-Temperature Equation of State by a Perturbation Method. I. Nonpolar Gases.* J. Chem. Phys., 1954. **22**(12): p. 2099-2099.
54. Zwanzig, R.W., *High-Temperature Equation of State by a Perturbation Method. I. Nonpolar Gases.* J. Chem. Phys., 1954. **22**(8): p. 1420-1426.
55. Kirkwood, J.G., *Statistical mechanics of fluid mixtures.* J. Chem. Phys., 1935. **3**(5): p. 300-313.
56. Torrie, G.M. and J.P. Valleau, *Nonphysical sampling distributions in Monte Carlo free-energy estimation: Umbrella sampling.* J. Comput. Phys., 1977. **23**(2): p. 187-199.
57. Lelievre, T., M. Rousset, and G. Stoltz, *Long-time convergence of an adaptive biasing force method.* Nonlinearity, 2008. **21**(6): p. 1155-1181.
58. Luzhkov, V.B. and J. Aqvist, *Mechanisms of tetraethylammonium ion block in the KcsA potassium channel.* Febs Lett., 2001. **495**(3): p. 191-196.
59. Luzhkov, V.B., et al., *Computational modelling of the open-state K(v)1.5 ion channel block by bupivacaine.* BBA-Proteins Proteom., 2003. **1652**(1): p. 35-51.
60. Hansson, T., J. Marelius, and J. Aqvist, *Ligand binding affinity prediction by linear interaction energy methods.* J. Comput. Aid. Mol. Des., 1998. **12**(1): p. 27-35.
61. Aqvist, J., V.B. Luzhkov, and B.O. Brandsdal, *Ligand binding affinities from MD simulations.* Accounts Chem. Res., 2002. **35**(6): p. 358-365.
62. Lin, Y., et al., *Advances toward bioapplications of carbon nanotubes.* J. Mater. Chem., 2004. **14**(4): p. 527-541.
63. Colvin, V.L., *The potential environmental impact of engineered nanomaterials.* Nat. Biotechnol., 2003. **21**(10): p. 1166-1170.
64. Ajayan, P.M., *Nanotubes from carbon.* Chem. Rev., 1999. **99**(7): p. 1787-1799.
65. Dresselhaus, M.S., G. Dresselhaus, and P. Avouris, eds. *Carbon Nanotubes: Synthesis, Structure, Properties, and Applications*. 2001, Springer: Berlin, New York.
66. Baughman, R.H., A.A. Zakhidov, and W.A. de Heer, *Carbon nanotubes - the route toward applications.* Science, 2002. **297**(5582): p. 787-792.
67. Hafner, J.H., C.L. Cheung, and C.M. Lieber, *Growth of nanotubes for probe microscopy tips.* Nature, 1999. **398**(6730): p. 761-762.
68. Yue, G.Z., et al., *Generation of continuous and pulsed diagnostic imaging x-ray radiation using a carbon-nanotube-based field-emission cathode.* App. Phys. Lett., 2002. **81**(2): p. 355-357.
69. Chen, R.J., et al., *Noncovalent sidewall functionalization of single-walled carbon nanotubes for protein immobilization.* J. Am. Chem. Soc., 2001. **123**(16): p. 3838-3839.
70. Besteman, K., et al., *Enzyme-coated carbon nanotubes as single-molecule biosensors.* Nano Lett., 2003. **3**(6): p. 727-730.
71. Guo, Z.J., P.J. Sadler, and S.C. Tsang, *Immobilization and visualization of DNA and proteins on carbon nanotubes.* Adv. Mater., 1998. **10**(9): p. 701-703.
72. Pantarotto, D., et al., *Functionalized carbon nanotubes for plasmid DNA gene delivery.* Angew. Chem. Int. Edit., 2004. **43**(39): p. 5242-5246.
73. Lacerda, L., et al., *Cell-penetrating CNTs for delivery of therapeutics.* Nano Today, 2007. **2**(6): p. 38-43.

74. Ajima, K., et al., *Enhancement of In Vivo Anticancer Effects of Cisplatin by Incorporation Inside Single-Wall Carbon Nanohorns.* Acs Nano, 2008. **2**(10): p. 2057-2064.
75. Ajima, K., et al., *Carbon nanohorns as anticancer drug carriers.* Mol. Pharm., 2005. **2**(6): p. 475-480.
76. Oberdorster, G., et al., *Principles for characterizing the potential human health effects from exposure to nanomaterials: elements of a screening strategy.* Part. Fibre Toxicol., 2005. **2**(8): p. 1-35.
77. Donaldson, K., et al., *Nanotoxicology.* Occup. Environ. Med., 2004. **61**(9): p. 727-728.
78. Tran, C.L., et al., *Inhalation of poorly soluble particles. II. Influence of particle surface area on inflammation and clearance.* Inhal. Toxicol., 2000. **12**(12): p. 1113-1126.
79. Donaldson, K. and C.L. Tran, *Inflammation caused by particles and fibers.* Inhal. Toxicol., 2002. **14**(1): p. 5-27.
80. Tasis, D., et al., *Soluble carbon nanotubes.* Chem. Eur. J., 2003. **9**(17): p. 4001-4008.
81. Georgakilas, V., et al., *Organic functionalization of carbon nanotubes.* J. Am. Chem. Soc., 2002. **124**(5): p. 760-761.
82. Pantarotto, D., et al., *Immunization with peptide-functionalized carbon nanotubes enhances virus-specific neutralizing antibody responses.* Chem. Biol., 2003. **10**(10): p. 961-966.
83. Singh, R., et al., *Binding and condensation of plasmid DNA onto functionalized carbon nanotubes: Toward the construction of nanotube-based gene delivery vectors.* J. Am. Chem. Soc., 2005. **127**(12): p. 4388-4396.
84. Klumpp, C., et al., *Functionalized carbon nanotubes as emerging nanovectors for the delivery of therapeutics.* BBA-Biomembranes, 2006. **1758**(3): p. 404-412.
85. Landau, S.I., E.L. Becker, and A. Manuila, eds. *International Dictionary of Medicine and Biology (Coenzymes and Cofactors).* 1986, John Wiley & Sons.
86. Bianco, A. and M. Prato, *Can carbon nanotubes be considered useful tools for biological applications?* Adv. Mater., 2003. **15**(20): p. 1765-1768.
87. Singh, R., et al., *Tissue biodistribution and blood clearance rates of intravenously administered carbon nanotube radiotracers.* Proc. Natl. Acad. Sci. USA, 2006. **103**(9): p. 3357-3362.
88. Da Ros, T. and M. Prato, *Medicinal chemistry with fullerenes and fullerene derivatives.* Chem. Commun., 1999(8): p. 663-669.
89. Friedman, S.H., et al., *Inhibition of the HIV-1 Protease by Fullerene Derivatives - Model-Building Studies and Experimental-Verification.* J. Am. Chem. Soc., 1993. **115**(15): p. 6506-6509.
90. Marchesan, S., et al., *Anti-HIV properties of cationic fullerene derivatives.* Bioorg. Med. Chem. Lett., 2005. **15**(15): p. 3615-3618.
91. Thakral, S. and R.M. Mehta, *Fullerenes: An introduction and overview of their biological properties.* Indian J. Pharm. Sci., 2006. **68**(1): p. 13-19.
92. Sayes, C.M., et al., *The differential cytotoxicity of water-soluble fullerenes.* Nano Lett., 2004. **4**(10): p. 1881-1887.
93. Sayes, C.M., et al., *Nano-C-60 cytotoxicity is due to lipid peroxidation.* Biomaterials, 2005. **26**(36): p. 7587-7595.
94. Oberdorster, E., *Manufactured nanomaterials (Fullerenes, C-60) induce oxidative stress in the brain of juvenile largemouth bass.* Environ. Health Perspect., 2004. **112**(10): p. 1058-1062.
95. Klumpp, C., et al., *Multifunctionalised cationic fullerene adducts for gene transfer: design, synthesis and DNA complexation.* Chem. Commun., 2007(36): p. 3762-3764.
96. Park, K.H., et al., *Single-walled carbon nanotubes are a new class of ion channel blockers.* J. Biol. Chem., 2003. **278**(50): p. 50212-50216.
97. Warheit, D.B., et al., *Comparative pulmonary toxicity assessment of single-wall carbon nanotubes in rats.* Toxicol. Sci., 2004. **77**(1): p. 117-125.
98. Lam, C.W., et al., *Pulmonary toxicity of single-wall carbon nanotubes in mice 7 and 90 days after intratracheal instillation.* Toxicol. Sci., 2004. **77**(1): p. 126-134.

99. Shvedova, A.A., et al., *Unusual inflammatory and fibrogenic pulmonary responses to single-walled carbon nanotubes in mice.* Am. J. Physiol.-Lung. C., 2005. **289**(5): p. L698-L708.
100. Mattson, M.P., R.C. Haddon, and A.M. Rao, *Molecular functionalization of carbon nanotubes and use as substrates for neuronal growth.* J. Mol. Neurosci., 2000. **14**(3): p. 175-182.
101. Shvedova, A.A., et al., *Exposure to carbon nanotube material: Assessment of nanotube cytotoxicity using human keratinocyte cells.* J. Toxicol. Env. Heal. A, 2003. **66**(20): p. 1909-1926.
102. Service, R.F., *American Chemical Society meeting: Nanomaterials show signs of toxicity.* Science, 2003. **300**(5617): p. 243-243.
103. Cui, D.X., et al., *Effect of single wall carbon nanotubes on human HEK293 cells.* Toxicol. Lett., 2005. **155**(1): p. 73-85.
104. Monteiro-Riviere, N.A., et al., *Multi-walled carbon nanotube interactions with human epidermal keratinocytes.* Toxicol. Lett., 2005. **155**(3): p. 377-384.
105. Bottini, M., et al., *Multi-walled carbon nanotubes induce T lymphocyte apoptosis.* Toxicol. Lett., 2006. **160**(2): p. 121-126.
106. Ramachandran, S., P.B.S. Kumar, and M. Laradji, *Lipid flip-flop driven mechanical and morphological changes in model membranes.* J. Chem. Phys., 2008. **129**(12).
107. Hille, B., *Ionic channels of excitable membranes*. 2nd ed. 1992, Sunderland, MA: Sinauer.
108. Purves, D., et al., *Neuroscience*. 2nd ed. 2001: Sinauer Associates Inc.
109. Siegel, G.J., et al., *Basic neurochemistry: molecular, cellular, and medical aspects*. 1999: Philadelphia: Lippincott-Raven.
110. Camerino, D.C., D. Tricarico, and J.F. Desaphy, *Ion channel pharmacology.* Neurotherapeutics, 2007. **4**(2): p. 184-198.
111. Verkman, A.S. and L.J.V. Galietta, *Chloride channels as drug targets.* Nat. Rev. Drug Discov., 2009. **8**(2): p. 153-171.
112. Camerino, D.C., et al., *Therapeutic Approaches to Ion Channel Diseases.* Adv. Genet., 2008. **64**: p. 81-145.
113. Bezanilla, F. and C.M. Armstrong, *Negative conductance caused by entry of sodium and cesium ions into potassium channels of squid axons.* J. Gen. Physiol., 1972. **60**(5): p. 588-608.
114. MacKinnon, R., *Potassium channels.* Febs Lett., 2003. **555**(1): p. 62-65.
115. Ashcroft, F.M., *Ion Channels and Disease* 1999: Academic Press.
116. Doyle, D.A., et al., *The structure of the potassium channel: molecular basis of K^+ conduction and selectivity.* Science, 1998. **280**: p. 69-77.
117. Zhou, Y., et al., *Chemistry of ion coordination and hydration revealed by a K^+ channel-FAB complex at 2.0 Ĺ resolution.* Nature, 2001. **414**: p. 43-48.
118. Kubo, Y., et al., *International Union of Pharmacology. LIV. Nomenclature and molecular relationships of inwardly rectifying potassium channels.* Pharmacol. Rev., 2005. **57**(4): p. 509-526.
119. Abraham, M.R., et al., *Channelopathies of inwardly rectifying potassium channels.* Faseb J., 1999. **13**(14): p. 1901-1910.
120. Jiang, Y.X., et al., *Crystal structure and mechanism of a calcium-gated potassium channel.* Nature, 2002. **417**(6888): p. 515-522.
121. Jiang, Y., et al., *The open pore conformation of potassium channels.* Nature, 2002. **417**: p. 523-526.
122. Long, S.B., E.B. Campbell, and R. MacKinnon, *Crystal structure of a mammalian voltage-dependent Shaker family K^+ channel.* Science, 2005. **309**: p. 897-903.
123. Noskov, S.Y. and B. Roux, *Importance of hydration and dynamics on the selectivity of the KcsA and NaK channels.* J. Gen. Physiol., 2007. **129**(2): p. 135-143.
124. MacKinnon, R., *Potassium channels and the atomic basis of selective ion conduction.* Bioscience Rep., 2004. **24**(2): p. 75-100.
125. Noskov, S.Y., S. Berneche, and B. Roux, *Control of ion selectivity in potassium channels by electrostatic and dynamic properties of carbonyl ligands.* Nature, 2004. **431**: p. 830-834.

126. Noskov, S.Y. and B. Roux, *Ion selectivity in potassium channels.* Biophys. Chem., 2006. **124**: p. 279-291.
127. Guidoni, L., V. Torre, and P. Carloni, *Potassium and sodium binding to the outer mouth of the K+ channel.* Biochemistry, 1999. **38**(27): p. 8599-8604.
128. Berneche, S. and B. Roux, *Energetics of ion conduction through the K+ channel.* Nature, 2001. **414**(6859): p. 73-77.
129. Guidoni, L. and P. Carloni, *Potassium permeation through the KcsA channel: a density functional study.* Biochimica et Biophysica Acta, 2002. **1563**: p. 1-6.
130. Burykin, A., M. Kato, and A. Warshel, *Exploring the origin of the ion selectivity of the KcsA potassium channel.* Proteins-Structure Function and Genetics, 2003. **52**(3): p. 412-426.
131. Taglialatela, M., et al., *Patterns of internal and external tetraethylammonium block in 4 homologous K+-channels.* Mol. Pharmacol., 1991. **40**(2): p. 299-307.
132. Guidoni, L. and P. Carloni, *Tetraethylammonium binding to the outer mouth of the KcsA potassium channel: implications for ion permeation.* J. Recept. Signal Trasnsduct. Res., 2002. **22**(1-4): p. 315-331.
133. Kutluay, E., B. Roux, and L. Heginbotham, *Rapid intracellular TEA block of the KcsA potassium channel.* Biophys. J., 2005. **88**(2): p. 1018-1029.
134. Oseguera, A.J., et al., *On the mechanism of TBA block of the TRPV1 channel.* Biophys. J., 2007. **92**(11): p. 3901-3914.
135. Yu, K.Q., et al., *Computational simulations of interactions of scorpion toxins with the voltage-gated potassium ion channel.* Biophys. J., 2004. **86**(6): p. 3542-3555.
136. Huang, P.T., Y.S. Shiau, and K.L. Lou, *The interaction of spider gating modifier peptides with voltage-gated potassium channels.* Toxicon, 2007. **49**(2): p. 285-292.
137. Li, L.W., D. Bedrov, and G.D. Smith, *A molecular-dynamics simulation study of solvent-induced repulsion between C-60 fullerenes in water.* J. Chem. Phys., 2005. **123**(20): p. 204504
138. Li, L.W., et al., *A molecular dynamics simulation study of C-60 fullerenes inside a dimyristoylphosphatidylcholine lipid bilayer.* J. Phys. Chem. B, 2007. **111**(16): p. 4067-4072.
139. Qiao, R., et al., *Translocation of C-60 and its derivatives across a lipid bilayer.* Nano Lett., 2007. **7**(3): p. 614-619.
140. Andreev, I., et al., *Penetration of fullerene C60 derivatives through biological membranes.* Fuller. Nanotub. Car. N., 2008. **16**(2): p. 89-102.
141. Bedrov, D., et al., *Passive transport of C-60 fullerenes through a lipid membrane: A molecular dynamics simulation study.* J. Phys. Chem. B, 2008. **112**(7): p. 2078-2084.
142. Li, L.W., D. Bedrov, and G.D. Smith, *Water-induced interactions between carbon nanoparticles.* J. Phys. Chem. B, 2006. **110**(21): p. 10509-10513.
143. Cherukuri, P., et al., *Near-infrared fluorescence microscopy of single-walled carbon nanotubes in phagocytic cells.* J. Am. Chem. Soc., 2004. **126**(48): p. 15638-15639.
144. Kam, N.W.S., et al., *Nanotube molecular transporters: Internalization of carbon nanotube-protein conjugates into mammalian cells.* J. Am. Chem. Soc., 2004. **126**(22): p. 6850-6851.
145. Lu, Q., et al., *RNA polymer translocation with single-walled carbon nanotubes.* Nano Lett., 2004. **4**(12): p. 2473-2477.
146. Pantarotto, D., et al., *Translocation of bioactive peptides across cell membranes by carbon nanotubes.* Chem. Commun., 2004(1): p. 16-17.
147. Bianco, A., et al., *Cationic carbon nanotubes bind to CpG oligodeoxynucleotides and enhance their immunostimulatory properties.* J. Am. Chem. Soc., 2005. **127**(1): p. 58-59.
148. Kam, N.W.S., Z.A. Liu, and H.J. Dai, *Carbon nanotubes as intracellular transporters for proteins and DNA: An investigation of the uptake mechanism and pathway.* Angew. Chem. Int. Edit., 2006. **45**(4): p. 577-581.
149. Lacerda, L., et al., *Carbon nanotube cell translocation and delivery of nucleic acids in vitro and in vivo.* J. Mater. Chem., 2008. **18**(1): p. 17-22.
150. Cai, D., et al., *Highly efficient molecular delivery into mammalian cells using carbon nanotube spearing.* Nat. Meth., 2005. **2**(6): p. 449-454.

151. Kam, N.W.S. and H.J. Dai, *Carbon nanotubes as intracellular protein transporters: Generality and biological functionality.* J. Am. Chem. Soc., 2005. **127**(16): p. 6021-6026.
152. Dumortier, H., et al., *Functionalized carbon nanotubes are non-cytotoxic and preserve the functionality of primary immune cells.* Nano Lett., 2006. **6**(7): p. 1522-1528.
153. Cheng, C., et al., *Toxicity and imaging of multi-walled carbon nanotubes in human macrophage cells.* Biomaterials, 2009. **30**(25): p. 4152-4160.
154. Raffa, V., et al., *Can the properties of carbon nanotubes influence their internalization by living cells?* Carbon, 2008. **46**(12): p. 1600-1610.
155. Porter, A.E., et al., *Direct imaging of single-walled carbon nanotubes in cells.* Nature Nanotech., 2007. **2**(11): p. 713-717.
156. Lamprecht, C., et al., *AFM imaging of functionalized carbon nanotubes on biological membranes.* Nanotechnology, 2009. **20**(43).
157. Kostarelos, K., et al., *Cellular uptake of functionalized carbon nanotubes is independent of functional group and cell type.* Nature Nanotech., 2007. **2**(2): p. 108-113.
158. Becker, M.L., et al., *Length-dependent uptake of DNA-wrapped single-walled carbon nanotubes.* Adv. Mater., 2007. **19**(7): p. 939-+.
159. Kang, B., et al., *Cancer-Cell Targeting and Photoacoustic Therapy Using Carbon Nanotubes as "Bomb" Agents.* Small, 2009. **5**(11): p. 1292-1301.
160. Century, T.J., I.R. Fenichel, and S.B. Horowitz, *The concentrations of water, sodium and potassium in the nucleus and cytoplasm of amphibian oocytes.* J. Cell Sci., 1970. **7**(1): p. 5-&.
161. Pauser, S., et al., *Estimation of water-content and water mobility in the nucleus and cytoplasm of xenopus-laevis oocytes by NMR microscopy.* Magn. Reson. Imaging, 1995. **13**(2): p. 269-276.
162. Ovadi, J. and V. Saks, *On the origin of intracellular compartmentation and organized metabolic systems.* Mol. Cell. Biochem., 2004. **256**(1-2): p. 5-12.
163. Hancock, R.E.W., *Cationic peptides: effectors in innate immunity and novel antimicrobials.* Lancet Infect. Dis., 2001. **1**(3): p. 156-164.

Resumé

Ce travail de thèse concerne l'étude théorique des mécanismes d'interaction de nanostructures à base de carbone avec les membranes cellulaires, constituant l'essentiel des cellules vivantes. Ce sujet très complexe compte tenu de la pluridisciplinarité de la thématique a été essentiellement réalisé à l'aide de simulations numériques. Nous avons volontairement partagé ce travail en deux parties distinctes. Nous avons d'abord étudié le fonctionnement des canaux ioniques à l'aide de la dynamique moléculaire et des études *ab-initio*. Ces canaux sont d'une part des protéines membranaires essentielles pour la fonction cellulaire, et d'autre part, elles constituent aussi des cibles thérapeutiques fréquentes dans la recherche des nouveaux médicaments. Dans une seconde partie, nous avons étudié le comportement d'espèces carbonées nus et fonctionnalisés tels que les fullerènes (C_{60}) et les nanotubes (CNT) en présence de la membrane cellulaire en analysant finement le mécanisme d'ingestion (ang. *uptake*) de ces vecteurs de médicaments potentiels par les membranes biologiques. Ces études en dynamique moléculaire sur des temps très longs (sub-1 µs) et sur des systèmes très vastes étaient aussi le challenge du point de vue informatique. Pour palier la problématique dans le temps limitée d'une thèse le développement des calculs parallèles de haute performance CPU/GPU a du être mis en place. Les résultats obtenus tentent de mettre en évidence le rôle toxique que peuvent présentées certaines nanostructures vis-à-vis des protéines membranaires précédemment étudiées. Ce travail de thèse ouvre naturellement la voie à l'étude des nanovecteurs biocompatibles pour la délivrance des médicaments.

Abstract

This thesis concerns the theoretical study of the interaction mechanisms of carbon-based nanostructures with cell membranes, being the essential compound of living cells. This very complex study of the multidisciplinary nature was essentially done using numerical simulations. We have voluntarily spitted this work in two distinct parts. First, we studied the membrane ion channels using molecular dynamics and *ab initio* approaches. These channel proteins being essential for cell function are also common therapeutic targets for new drugs design. Second, we studied the behavior of pristine and functionalized carbon species such as fullerenes (C_{60}) and nanotubes (CNT) in the presence of the cell membrane. The results focus mainly on passive uptake phenomenon of these potential drugs vectors by biological membranes. The molecular dynamics studies on a very long time scale (sub-1 microseconds) and on very large systems were also the challenge of the IT perspective. To solve the given problematic in the limited time of a single PhD the development of high performance parallel computing CPU/GPU had to be put in place. The obtained results tempt to highlight the toxic role of nanostructures versus previously studied membrane proteins. This thesis naturally opens the way for the study of biocompatible nanocarriers for drug delivery.